



**HAL**  
open science

# Tests d'Électrodynamique Quantique et Étalons de Rayons-X à l'Aide des Atomes Pioniques et des Ions Multichargés

Martino Trassinelli

► **To cite this version:**

Martino Trassinelli. Tests d'Électrodynamique Quantique et Étalons de Rayons-X à l'Aide des Atomes Pioniques et des Ions Multichargés. Physique Atomique [physics.atom-ph]. Université Pierre et Marie Curie - Paris VI, 2005. Français. NNT : . tel-00067768v1

**HAL Id: tel-00067768**

**<https://theses.hal.science/tel-00067768v1>**

Submitted on 8 May 2006 (v1), last revised 10 Aug 2009 (v2)

**HAL** is a multi-disciplinary open access archive for the deposit and dissemination of scientific research documents, whether they are published or not. The documents may come from teaching and research institutions in France or abroad, or from public or private research centers.

L'archive ouverte pluridisciplinaire **HAL**, est destinée au dépôt et à la diffusion de documents scientifiques de niveau recherche, publiés ou non, émanant des établissements d'enseignement et de recherche français ou étrangers, des laboratoires publics ou privés.



Thèse de doctorat de l'Université Paris VI  
Spécialité : Champs, Particules, Matières

*présentée par*

**Martino Trassinelli**

*Pour obtenir le grade de  
DOCTEUR de l'UNIVERSITÉ PARIS 6*

**Tests d'Électrodynamique Quantique et Étalons de Rayons-X  
à l'Aide des Atomes Pioniques et des Ions Multichargés**

**Quantum Electrodynamics Tests and X-rays Standards  
using Pionic Atoms and Highly Charged Ions**

*Soutenue le 12 Décembre 2005 devant le jury composé de :*

M. Christophe BLONDEL ..... *Examineur*  
M. Detlev GOTTA ..... *Membre invité*  
M. Paul INDELICATO ..... *Directeur de thèse*  
M. Benoît LOISEAU ..... *Rapporteur*  
M. Philippe RONCIN ..... *Examineur*  
M. Jean-Pierre ROZET ..... *Président du jury et rapporteur*  
M. Leopold M. SIMONS ..... *Membre invité*







*Alle mie nonne Lidia e Maria*



---

## Résumé

---

L'objet de cette thèse est de présenter une nouvelle mesure de la masse du pion en utilisant la spectroscopie X de l'hydrogène pionique et des résultats de spectroscopie de l'argon et du soufre héliumoides. La nouvelle masse du pion a été mesurée avec une précision 30% supérieure à la moyenne mondiale actuelle, c'est-à-dire égale à 1.7 ppm. Elle a été obtenue par spectroscopie de Bragg des transitions 5 -> 4 de l'azote pionique en utilisant les prédictions théoriques de QED. Je présente le calcul de la structure hyperfine et celui de la correction de recul du noyau pour les atomes pioniques au moyen d'une nouvelle méthode de perturbation de l'équation Klein-Gordon. Le spectromètre utilisé pour cette mesure a été caractérisé grâce aux transitions relativistes des atomes héliumoides produits dans un nouveau type de source d'ions à résonance cyclotronique des électrons. Les spectres haute statistique de ces ions permettent de mesurer les énergies de transition avec une précision de quelques ppm, ce qui permet de tester, avec un degré de précision jamais atteint, les prédictions théoriques. L'émission de rayons-X des atomes pioniques et des ions multichargés peut ainsi être utilisée pour la définition de nouveaux étalons de rayons-X de quelques keV.

**Mots-clefs :** Spectroscopie de rayons-X, masse du pion, atomes pioniques, ions multichargés, tests d'électrodynamique quantique, équation de Klein-Gordon.

---

## Abstract

---

The object of this thesis is to present a new measurement of the pion mass using pionic nitrogen X-ray spectroscopy and results on helium-like argon and sulphur spectroscopy. The new pion mass has been measured with an accuracy of 1.7 ppm, 30% better than the present world average value, and it is obtained from Bragg spectroscopy of 5 -> 4 pionic nitrogen transitions using the theoretical predictions provided by QED. I present the calculation of the hyperfine structure and recoil corrections for pionic atoms using a new perturbation method for the Klein-Gordon equation. The spectrometer used for this measurement has been characterized with the relativistic M1 transitions from he-like ions produced with a new device, the Electron-Cyclotron-Resonance Ion Trap. High statistics spectra from these ions enable to measure transition energies with a precision of some ppm that allows to compare theoretical predictions with experiment. X-ray emission from pionic atoms and multicharged ions can be used to define new types of X-ray standards for energies of a few keV.

**Keywords:** X-ray spectroscopy, pion mass, pionic atoms, highly charged ions, QED tests, Klein-Gordon equation.



---

# Contents

---

<b>Contents</b>	<b>i</b>
<b>Résumé de la thèse</b>	<b>vii</b>
Test d'Électrodynamique Quantique avec des atomes pioniques et des ions multichargés . . . . .	viii
Nouveaux étalons de rayons-X . . . . .	xi
Organisation de la thèse . . . . .	xiii
Sommaire des résultats . . . . .	xiv
Perspectives . . . . .	xvi
<b>1 Introduction</b>	<b>1</b>
1.1 Quantum Electrodynamics tests with pionic atoms and highly charged ions	2
1.2 New X-ray standard definition . . . . .	4
1.3 Organization of the thesis . . . . .	6
<b>I Pionic atoms</b>	<b>9</b>
<b>2 Hyperfine structure and recoil corrections in pionic atoms</b>	<b>11</b>
2.1 General characteristic of the Klein-Gordon equation . . . . .	12
2.2 Calculation of the Hyperfine Structure term . . . . .	15
2.3 Recoil corrections to the hyperfine structure energy term . . . . .	21
2.4 Numerical evaluation for some pionic atoms . . . . .	27
2.5 Conclusions and perspectives . . . . .	36
<b>3 Pionic atoms production and spectroscopy</b>	<b>39</b>
3.1 Pionic atoms production . . . . .	40
3.2 Atomic cascade . . . . .	43
3.3 X-ray Bragg crystal spectrometer . . . . .	44
3.4 Focal-plan position sensitive detector . . . . .	53
3.5 Data analysis . . . . .	56
3.6 Conclusions . . . . .	66
<b>4 Measurement of the charged pion mass</b>	<b>67</b>
4.1 Description of the set-up . . . . .	70
4.2 Beam-time operation and data collection . . . . .	72

4.3	Data analysis . . . . .	78
4.4	Discussion of the corrections . . . . .	83
4.5	Discussion of the systematic errors . . . . .	87
4.6	Final results . . . . .	90
4.7	Test of the Klein-Gordon equation . . . . .	92
<b>II Highly charged ions</b>		<b>93</b>
<b>5</b>	<b>Electron-Cyclotron-Resonance ion sources and traps</b>	<b>95</b>
5.1	General description of the Electron-Cyclotron-Resonance ion sources and traps . . . . .	97
5.2	Electron-Cyclotron-Resonance ion trap at the Paul Scherrer Institute . . . . .	102
5.3	Electron-Cyclotron-Resonance ion source at the Laboratoire Kastler Brossel	114
<b>6</b>	<b>Highly charged ion spectra and QED tests</b>	<b>125</b>
6.1	Helium-like ions spectra . . . . .	126
6.2	Data acquisition and analysis . . . . .	128
6.3	Results and comparison with theoretical predictions . . . . .	134
6.4	Outlook and further analysis . . . . .	136
<b>III Conclusion and appendices</b>		<b>143</b>
<b>7</b>	<b>Conclusion</b>	<b>145</b>
7.1	Results summary . . . . .	145
7.2	Outlook . . . . .	147
<b>Hyperfine structure in atomic and natural units</b>		<b>149</b>
<b>Non-relativistic transition probability calculation</b>		<b>151</b>
<b>Calculation of the lattice deformation for a spherically bent crystal</b>		<b>153</b>
<b>Measurement of the pixel distance and the CCD relative orientation (preprint article physics/0602159)</b>		<b>155</b>
<b>Bibliography</b>		<b>181</b>

---

# Remerciements

---

*Par où commencer? Quelle langue utiliser pour les remerciements? C'est dur! Bon j'adopterais la technique de "l'étudiant européen errant". Cette technique a été développée au sein du Laboratoire Kastler Brossel par les pionniers Francesco Intravaia et Riccardo Sapienza. Elle consiste dans l'utilisation de trois langues ou plus pour arriver à remercier efficacement toutes les personnes qui, directement ou indirectement, ont aidé au travail de thèse. J'essayerai de reproposez cette recette, en ajoutant l'allemand, la nouvelle langue que je suis entrain d'apprendre et qui reste, pour l'instant, très hermétique.*

*La liste des remerciements est longue, comme longue l'a été le travail de thèse effectué au sein du Laboratoire Kastler Brossel de Septembre 2002 à Décembre 2005.*

*Tout d'abord je remercie Franck Laloë de m'avoir accueilli au Laboratoire Kastler Brossel et qui a permis le début de ma thèse, et les membres du jury, qui ont permis qu'elle prenne fin. Je suis très reconnaissant aux rapporteurs Jean-Pierre Rozet et Benôit Loiseau, pour leur corrections et suggestions lors de la rédaction finale du manuscrit et aux autres membres : Christophe Blondel, Detlev Gotta, Philippe Roncin et Leopold Simons. Merci aussi à Torlief Ericson pour ses remarques intéressantes après la soutenance de thèse.*

*Je remercie très chaleureusement Paul Indelicato. Faire un thèse dans son groupe (surtout quand le groupe n'était que lui et moi) est le meilleur début dans la recherche qu'on puisse espérer. Sa double casquette de chercheur en physique théorique et en physique expérimentale est plus qu'unique, comme l'ont été sa générosité et sa disponibilité.*

*Durant ces quatre dernières années le groupe a grandi, et j'ai pu profiter de la compagnie des nouveaux membres du groupe. Merci à Éric-Olivier Le Bigot, mieux connu comme EOL, pour son aide informatique, pour les longues discussions sur la physique et sur nos classements secrets. Merci à Stéphane Boucart pour ses conseils de maître de la communication. Merci aux nouvelles doctorantes du groupe : Dina Attia et à son piège d'ion, et à Sophie St.. Scr.. Schlessler! Une des fondateurs de la bien connue QPD (Quantum Pion Dynamics). Un merci spécial pour Sophie pour la traduction en français de l'introduction de la thèse et pour les belles discussions "überhaupt".*

*Thank you to the post-doc and visitors than came in our group. Thank you to Thomas Jensen and Vladimir Yerokin for all the interesting discussion about exotic atoms cascades and QED, respectively. A special thank to Krzysztof Pachucki for the very useful discussion about perturbation methods for QED calculation that help me so much to investigate into the the recoil corrections in pionic atoms.*

*Et merci beaucoup à Bruno Manil, mon prédécesseur dans le group, pour son "hotline" qui m'a dépanné en cas de problèmes informatiques concernant les programmes d'analyse.*

*Le travail de thèse ne pouvait pas être plus agréable qu'avec l'atmosphère amicale de*

*l'antenne de Jussieu de l'LKB. En trois ans, plus que des relations de travail, ils sont nés des relations d'amitié. Merci à Julien Le Bars pour avoir eu toujours la patience d'écouter mes confiances et pour m'avoir donné, avec sa sensibilité, toujours de bons conseils. Grazie a Marco Romanelli (detto anche Martino Romanelli o Marco Trassinelli o Marcello Romanelli) compagno di avventure e sventure durante questi tre anni, ma ben più vecchio amico di Firenze, che mi ha aiutato a esportare la toscanità nel modo. Grazie a Riccardo Sapienza per la sua amicizia che dura oltre i confini di mezza europa e per la sua spinta e motivazione che mi ha dato nella ricerca e nell'arte. Grazie Francesco "toco" Intravaia per tutte le cene e "festazze" passate insieme a lui et tout le petit club de rue des Lombards. Encore un merci particulier à Sylvain Gigant, Vincent Delaubert, Rémy Hervé, Aurélien Dantan, Brahim Lamine, Olivier Arnault, Jean Cviklinski, Charles Leyder, FX (François-Xavier Dezael), Estefania Mirandes, Robert Kühn, Mathieu Melich e il resto della cricca italiana del laboratorio: Antonino Chiummo, Fabrizio Villa e le "new enries" Giuseppe Patera e Pier-Nicola Spinicelli (altra vecchia conoscenza dei bei tempi di Firenze). Merci aussi au reste de la grande famille des doctorants et post-docs: Senem Kilic, Vincent Josse, Olivier Sigwarth, Gaele Keller, Olivier Arcizet, Julien Laurat, Remi Battesti, Pierre Cladé, Thomas Caniard, Thomas Wellens, Augustin Baas et Laurent Lopez.*

*La famille de l'LKB ne se limite pas aux étudiants mais elle s'étend, bien sûr à tous les permanents du laboratoire avec lesquels j'ai eu le plaisir de travailler. Un merci particulier à François Nez et Amaury Mouchet pour toutes nos agréables discussions. Merci à tous les autres chercheurs du laboratoire pour leur disponibilité dans tous les moments. Merci à François Biraben (je n'oublierais pas facilement les rires que j'entendais de mon bureau!), Jean-Philippe Karr, Pier-François Cohadon (pour m'avoir aidé dans le choix de ma thèse), Alberto Bramati (per il suo umorismo tagliente), Nicolas Treps, Lucile Julien, Bernard Cagnac, Michel Pinard, Antoine Heidmann, Jean-Michel Courty, Dominique Delande, Benoît Grémaud, Thomas Coudreau, Laurent Hilico, Claude Fabre, Elisabethte Giacobino, Jean-Pierre Hermier, Agnès Maître, Catherine Schwob, Saida Guellati-Khélifa, Astrid Lambrecht et Serge Reynaud.*

*La thèse n'aurait pu voir le jour sans le soutien des autres membres du Laboratoire Kastler Brossel qui ne font pas forcément de la recherche. Tout d'abord merci à Monique Bonnamy et Lætitial Morel pour leur travail au secrétariat, sans lequel, même l'expérience physique la plus facile serait impossible. Je voudrais remercier en particulier Monique pour sa bonne humeur toujours présente et pour son désir, avec des personnes comme François Nez, de transformer le labo en une grande famille en cherchant à casser le train-train avec de gourmands goûts et d'autres choses encore (comme une jolie expo de "Trassinelli originali" organisé avec Riccardo et Julien). Merci aussi à l'atelier de mécanique et d'électronique de l'LKB et à tous les autres services techniques avec lesquels j'ai travaillé. Merci à Pascal Travers, Christophe Rafailac, Jaques Merot, Jean-Pierre Okpiz, Mohammed Boujrad pour avoir satisfait toutes les requêtes impossibles pour construire les pièces nécessaires à nos expériences. Merci aussi à Corinne Poisson, Serge Begon, Florence Thibout et José Romer. Un merci spéciale à Jacques Merot, maintenant INSP, sans lequel la source d'ion de Paris n'existerait pas. Merci Jacques pour sa bonne humeur et vos conseils sur les films et comiques français.*

*Pendant ma thèse j'ai travaillé pour de longues périodes en Suisse pour préparer et participer aux expériences au Paul Scherrer Institut. Pendant ces périodes j'ai eu le grand plaisir de travailler avec deux personnes exceptionnelles: Detlev Gotta et Leopold M. Si-*

*mons (Leo pour tout le monde). Ich danke Detlev für alle geführten Gespräche über Physik und vor allem über köstliches Essen und leckere Getränke; von ihm habe ich gelernt, präzise Resultate zu finden, mit einer Sicherheit und einer Reflektion, die nur eine sehr langsame und methodische Arbeitsweise ermöglichen können. Ich danke Leo, mir sowohl Begeisterung und Strenge in der Arbeit beigebracht zu haben als auch alle deutschen gastronomischen Spezialitäten (um die tollen Schnaps nicht zu erwähnen).*

*Thank you to the other member of the pionic atoms collaboration from the different countries: Hannes Zmeskal, Philipp Schmid, Alexander Gruber, João Veloso, Joaquim dos Santos, Nick Nelms and Dimis Anagnostopoulos. In particular I would like to like to tank the compagnons of long nights and days at the PSI, fighting with ions sources, charged pions and food machines: Albert Hirtl and Daniel Covita. Thank you to Maik Hennebach, my other “online help” during the beginning of my Ph.D. thesis, for all the time he spent to explain me all the experiment during my first visit at PSI. Infine grazie a Bruno Leoni per la sua precisione svizzera nella preparazione degli esperimenti. Thank to all the other people I met at the PSI. In particolare, grazie ad Aldissimo “sempreallegro” Antognini per le sue indimenticabili cene e le folli scorribande a Vienna, and to Franz Kottmann, Monsieur Dax (Andreas Dax), Paul Knowles Randolph Pohl and the Medames of the muonic hydrogen group: Françoise Mulhauser and Lidia Ludhova,*

*J’ai passé une autre bonne partie de ma thèse dans les sou-sol de Jussieu, en montant et travaillant sur la source d’ions SIMPA. Oui, les sou-sols de Jussieu ne sont pas le lieu le plus charmant du monde, mais on peut y travailler bien avec de chouettes personnes comme l’équipe de l’Institut des Nano-Science de Paris avec laquelle nous avons partagé la source. Je remercie Emily Lamour, Fabien Haranger et Nacer Adrouche avec lesquels c’était un vrai plaisir de travailler; et aussi aux “chefs” Dominique Vernhet et Jean-Pierre Rozet, toujours présents pour répondre aux questions et résoudre pas mal de problèmes.*

*Je remercie une deuxième fois Emily pour m’avoir aidé dans mes début dans l’enseignement de la physique aux étudiants de biologie pendant mon monitorat. De la même façon je remercie aussi les maîtres de conférence avec lesquels j’ai collaboré comme Samuel Gresillon, Bruno El-Bennich et Maria Barbi. Et naturellement je remercie tous mes étudiants qui ont eu la patience d’écouter leurs TD et TP avec un bon accent italien. En particulier je remercie ceux qui ont pu venir à ma soutenance de thèse (et à la fête de fin d’année naturellement). Ça a été un vrai plaisir de tenter d’enseigner la physique à ce groupe de biologistes.*

*Vu que on ne vit pas que de physique, je voudrais remercier tous mes amis qui m’ont fait penser à autre chose qu’à la science. Prima di tutto devo ringraziare Carlos e Ernesto, amici storici del mio arrivo a Parigi e compagni di feste e folli serate per tutti questi anni. Grazie a Simona e Costanza per tutte le belle cenate con gustose delizie come gli gnocchi fatti in casa e pasta all’avocado. Grazie a Domenico per il suo supporto con l’odiato/amato linux e per tutte le sue leccornie lucane gustate a casa sua. Merci à Lauren pour notre heureuse collocation dans la belle maison de rue Beaubourg durant deux ans et demi, et à toute sa chaleureuse famille en leur souhaitant le meilleur. Merci au “groupe du DEA” pour les fantastiques soirées dans tous ces années. Merci à François, Guillaume, Manu, Thihan, Bruno, Arnaud, Delphine, Jon et tous les autres. Grazie a Matilde per avermi aiutato in un brutto periodo coinciso con l’inizio della mia tesi. Merci aussi à tous les autres amis avec une mention particulière à tous ceux qui ont pu venir à voir ma soutenance, comme Anna (qui m’a appris les vertus des Platanos) et Jorissão (grasies por toudush i’ beei muum’ntch passade pairlanch portughich). Grazie alla mia famiglia, che si è fatta 1200*

*chilometri per ascoltare un soggetto inaccessibile in una lingua incomprensibile. Merci à tous ceux qui ont participé à la surprise finale après ma soutenance (et que je n'ai pas nommé encore): la trompette!! Merci à Pierone (disgraziato come ci si trova a Parigi), Hiromi, Valérie, Veronica, Chiara e Giulio, Chiarina, et Tristan.*

*Mais qui a organisé cette surprise? Mais c'est Cerise, qui a réussi à contacter tous mes amis et à organiser une collecte géante pendant des mois sans jamais se faire découvrir! Merci Cerise pour tout ton soutien pendant la période la plus difficile de ma vie. Et merci pour tout le reste qu'on ne peut pas écrire dans une thèse.*

*La thèse aurait été encore plus difficile sans trois choses qui ont été essentielles pour décompresser après mes longues journées de travail: le cour de dessin de Olga Rochard (merci pour tout ce que elle as réussi à faire sortir de mes mains et pour m'avoir fait redécouvrir le dessin oublié pour si longtemps!), l'Artusi, manuel essentiel pour s'amuser en lisant ses recettes de cuisine et se relaxer en les préparant, et les épisodes de Star Trek qui m'ont accompagné pendant les nombreuses nuits en Suisse.*

*Ancora più difficile sarebbe stato scrivere questa tesi se non mi fossi mai interessato alla fisica. Per questo devo ringraziare soprattutto tre persone. Primo tra tutti è Vanni Calamai (zio Vanni) che ha sempre risposto alle mie domande e stimolato fin da quando ero piccolo. Grazie poi a Nicola Radassao, per tutte le chiacchierate sulla fisica e fantascienza attorno a boccali di birra in fumose birrerie. Grazie infine alla Professoressa Rizzo che mi ha incoraggiato fin dai tempi del liceo artistico.*

*Finally, thank to Leslie, Linus and Steve, to provide the best tools to write this thesis.*

---

# Résumé de la thèse

---

La physique atomique, grâce à la précision des techniques qu'y ont été développées, et à la grande précision des calculs pouvant être atteinte, produit des résultats hautement utiles à d'autres domaines de la physique. La spectroscopie atomique permet de mesurer des constantes fondamentales, comme la constante de structure fine  $\alpha$  et la constante de gravitation  $G$  [1, 2]; mais aussi de mesurer les masses des particules, comme l'électron, l'antiproton et le pion [3, 4], et d'étudier les interactions fondamentales. Le but de cette thèse est de contribuer à résoudre un certain nombre de problèmes fondamentaux, en améliorant considérablement la précision des mesures. Je présente, en particulier, une nouvelle évaluation de la masse du pion, utilisant la spectroscopie des rayons-X émis par l'azote pionique, et de nouvelles mesures des transitions atomique de l'argon et du soufre héliumoides.

Les atomes et ions pioniques se forment lors de la capture d'une particule lourde par un noyau. Le pion de charge négative est un méson formé d'un anti-quark *anti-up* ( $\bar{u}$ ) et d'un quark *down* ( $d$ ). Lors de la capture du pion, les électrons de l'atome sont éjectés et l'on obtient un ion lourd très chargé avec des propriétés qui dépendent de la particule capturée. Les mesures sur les atomes pioniques permettent d'étudier l'interaction forte à basse énergie [5, 6] et d'évaluer la masse du pion chargé négativement [3, 7, 8].

La nouvelle mesure de la masse du pion que je présente est caractérisée par une précision de l'ordre de 1.5 ppm (part par million), bien meilleure que celle des mesures précédentes [3, 9]. Un effort expérimental et théorique considérable a été nécessaire pour l'obtenir : la masse du pion est mesurée par spectroscopie X des transitions  $5 \rightarrow 4$  dans l'azote pionique en utilisant les prédictions théoriques fournies par des calculs d'électrodynamique quantique (Quantum Electrodynamics : QED). Pour atteindre cette précision, des effets comme la polarisation du vide et les corrections de recul du noyau doivent être considérés pour l'évaluation correcte des niveaux atomiques. Une partie de mon travail de thèse est consacrée au calcul des corrections de recul et de la structure hyperfine dans les atomes pioniques. En particulier, je présenterais une nouvelle méthode perturbative pour l'équation de Klein-Gordon, qui décrit bien la dynamique des particules de spin-0, comme le pion. L'avantage de cette nouvelle technique est qu'elle tient compte des effets relativistes sans approximations. Avec le calcul de ces nouvelles corrections, nous attendons une précision de l'ordre de 0.2 ppm pour les prédictions théoriques des énergies des transitions  $5 \rightarrow 4$  dans l'azote pionique.

L'analyse précise du spectre de l'azote pionique nécessite une caractérisation détaillée du spectromètre à cristal de Bragg utilisé. Cette caractérisation a été obtenue en utilisant les émissions de rayons-X d'ions très chargés produits par un nouveau type de source d'ions à résonance cyclotronique des électrons (ECRIT : Electron-Cyclotron-Resonance

Ion Trap, où plus simplement source d'ions ECR). Dans cette source, les ions sont formés par des collisions électron-atome dans une bouteille magnétique. Les électrons sont accélérés par des microondes avec une fréquence résonante avec la fréquence du mouvement cyclotronique des électrons le long d'une surface équipotentielle du champ magnétique. Les ions créés, et les électrons sont piégés dans la bouteille magnétique. Les ions très chargés utilisés dans notre expérience sont formés par des noyaux dont la charge est 16–18 fois celle du proton ( $Z = 16 - 18$ ), et par quelques électrons qui sont soumis à un champ Coulombien du noyau fort.

Dans une ECRIT, pour des éléments comme le soufre et l'argon, la transition relativiste magnétique dipolaire  $M1 : 1s2s \ ^3S_1 \rightarrow 1s^2 \ ^1S_0$  est très intense et étroite, grâce à la très faible énergie cinétique des ions dans la source. Les transitions  $M1$  de ces éléments permettent une caractérisation systématique du cristal à courbure sphérique de notre spectromètre aux énergies où nous l'avons utilisé et donne ainsi une mesure précise de la fonction de réponse de l'instrument.

Hormis la caractérisation du spectromètre, l'un des plus importants résultats de ce projet était la mesure de haute précision d'une série de spectres de l'argon et du soufre. Avec une durée d'acquisition de 1–2 heures au maximum, nous avons obtenu de grands nombre d'événements sur les spectres des ions héliumoïdes et lithiuoïdes de ces éléments, et nous avons mesuré les énergies des transitions dans ces ions avec une précision de quelques dizaines de meV pour des photons d'environ 3 keV. Cette précision permet une comparaison détaillée et de tester les différentes prédictions théoriques disponibles avec l'expérience, et fourni un test sensible de l'Électrodynamique Quantique.

De la même façon, l'Électrodynamique Quantique peut être testée dans les atomes pioniques. L'analyse des énergies des transitions de l'azote pionique permet de comparer les mesures expérimentales de la structure fine aux prédictions théoriques avec une précision de l'ordre de 0.3%.

D'autre part, les rayons-X émis par ces atomes peuvent être utilisés comme nouveaux étalons d'énergie pour des photons de quelques keV.

Dans les sections suivantes je présenterai plus en détail ces deux aspects de la spectroscopie X des ions multichargés et des atomes pioniques : la possibilité de tester l'électrodynamique quantique et de définir des nouveaux étalons de rayons-X.

## Test d'Électrodynamique Quantique avec des atomes pioniques et des ions multichargés

L'électrodynamique quantique est la théorie qui décrit l'interaction entre le champ électromagnétique et la matière et reste à ce jour la théorie la mieux vérifiée en physique. La volonté de réunir relativité et mécanique quantique a émergé peu de temps après que cette dernière ait été formulée. Cependant, c'est seulement dans les années 1940 que l'on a été capable de former une théorie cohérente intégrant la relativité restreinte et la Mécanique Quantique. L'Électrodynamique Quantique décrit un champ quantique analogue au champ électrodynamique classique (théorie de Maxwell-Lorentz). La dualité onde-particule est maintenant totalement incorporée dans la théorie, et les particules chargées comme les photons sont traités comme des champs quantifiés, les plaçant ainsi sur le même plan. Les systèmes liés les plus élémentaires avec lesquels l'on peut tester la QED sont les systèmes hydrogénoïdes et ceux à peu d'électrons, formé par un noyau lourd et quelques particules

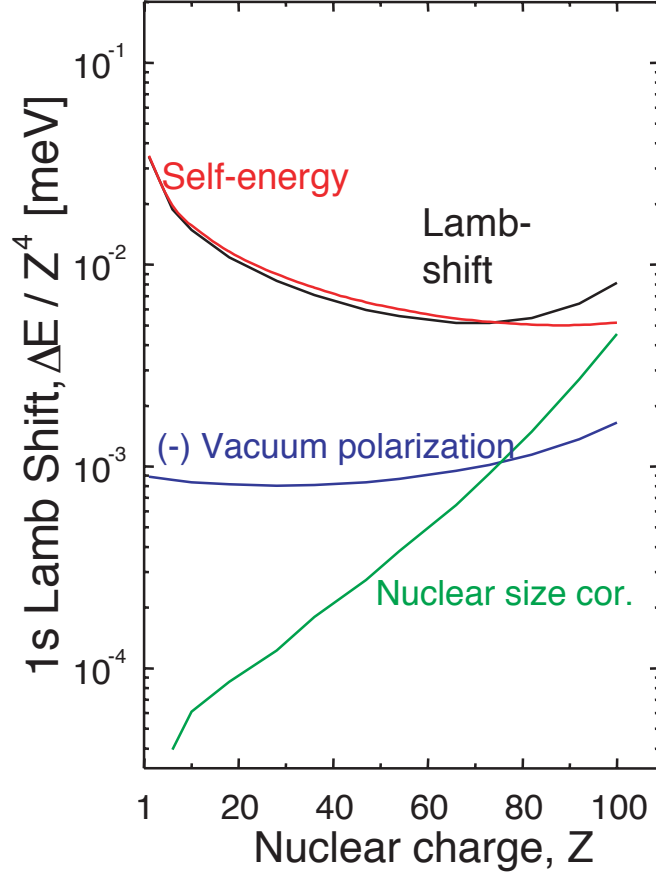


**Fig. 1** – Contribution du à la self-énergie, à la polarisation du vide et à la taille finie du noyau en dépendance de  $Z$ . Ce plot à été reproduit à partir de Réf. [10] en utilisant les valeurs publiées en Réf. [11].

liées. Comme décrit précédemment dans ce manuscrit, je m’intéresserai à deux systèmes. Le premier est l’azote pionique hydrogénoïde, où l’ensemble des électrons est remplacé par un pion de charge négative. Le deuxième exemple est celui composé d’ions à peu d’électrons, très chargés, avec une grande charge nucléaire ( $Z \sim 17$ ).

Mais pourquoi choisir particulièrement ces atomes ? Les atomes pioniques et les ions très chargés sont des objets intéressants car ils permettent de sonder des aspects de la structure atomique quantitativement différents de ce qu’on peut étudier avec des atomes “normaux”. Les atomes pioniques et les ions très chargés sont appropriés pour tester la QED car ils possèdent un rayon de Bohr caractéristique petit. En effet, le rayon de Bohr classique  $a_0$  est inversement proportionnel à la masse de la particule orbitant autour de la charge nucléaire  $Z$  :  $a_0 = \hbar / (mcZ\alpha)$  (où  $c$  est la vitesse de la lumière et  $\hbar$  est la constante de Planck). Une petite valeur du rayon de Bohr accroît la sensibilité aux phénomènes liés à l’électrodynamique quantique comme la polarisation du vide ou la self-énergie. Le pion chargé a une masse environ 270 fois plus grande que celle de l’électron. Dans ce cas, le rayon de Bohr et la longueur d’onde Compton de l’électron  $\hbar / (m_e c)$  sont du même ordre de grandeur, c’est-à-dire que le pion est très sensible à la distorsion du champ Coulombien due

à la création et à l'annihilation continuelle de paires électron-positron. Pour cette raison, les atomes pioniques ainsi que les atomes muoniques peuvent être utilisés pour vérifier avec plus de précision les corrections de QED comme la polarisation du vide [12, 13, 14], qui interviennent dans le domaine de la longueur d'onde Compton. De plus, ces atomes sont sensibles aux effets relativistes de la dynamique atomique. La "vitesse" caractéristique d'une particule dans un atome est  $\langle n|\hat{v}|n\rangle = Z \alpha c/n$ . Pour des ions avec  $Z \sim 17$ , cette vitesse atteint une valeur de  $\langle 1s|\hat{v}|1s\rangle \sim 0.12 c$  rendant la correction relativiste très grande.

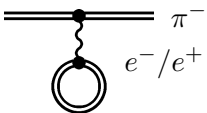
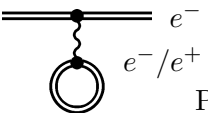
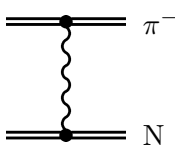
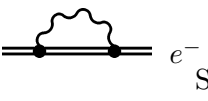
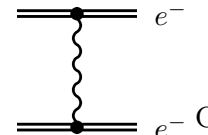
Contrairement au muon et à l'électron, le pion n'a pas de spin et sa dynamique est correctement décrite par l'équation de Klein-Gordon. Les prédictions de cette équation ont été bien moins testées que celles de l'équation de Dirac pour des particules possédant un spin égal et à  $1/2$  (comme l'électron ou le muon) [15]. Les mesures des transitions de l'azote pionique fournissent un test unique des prédictions de la mécanique quantique relativiste pour les particules de spin 0. En particulier, la différence d'énergie entre les transitions  $5g \rightarrow 4d$  et  $5f \rightarrow 4d$  permet de vérifier la structure fine telle que la prédit l'équation de Klein-Gordon avec une précision jusqu'alors jamais atteinte.

La spectroscopie de précision des rayons-X des ions très chargés peut conduire à une meilleure compréhension de problèmes fondamentaux qui ont émergé récemment : après plusieurs décennies de recherche de haute précision sur les ions héliumoïdes et hydrogénoïdes, on a encore peu de données pour comparer théorie et expérience. Comparés aux atomes pioniques, les ions très chargés avec  $Z = 15 - 20$  ne sont pas aussi sensibles à la polarisation du vide car le rayon de Bohr est encore trop grand comparé à la longueur d'onde Compton [16] et la contribution de QED au Lamb shift est dominée par la self-énergie (Fig. 1 et Table 1).

Actuellement, pour l'hélium il y a un fort désaccord ( 6 fois les barres d'erreurs combinées ) entre les calculs théoriques [17, 18, 19, 20] et les mesures récentes et très précises [21, 22, 23, 24]. Dans l'hélium et les éléments légers, la théorie utilise une expansion des équations Bethe-Salpeter en opérateur d'ordre  $1/c$  successif, et d'ordre  $Z\alpha$ . Pour les termes de correction qui dépendent de  $1/Z$ , comme la corrélation entre électrons liés, il faut utiliser des méthodes à tous les ordres, où des séries de diagrammes sont resommées. En revanche, pour les éléments lourds il faut utiliser les méthodes de QED à tous les ordres en  $Z\alpha$ , et la corrélation entre électron peut être calculée en utilisant la méthode de perturbation en  $1/Z$ .

Actuellement, plusieurs prédictions théoriques sont disponibles. Ces prédictions utilisent méthodes différentes comme le problème relativiste à n-corps (Relativistic Many-Body Problem Theory : RMBPT) [25, 26], la méthode de Dirac-Fock multi-configurée (Multi-Configuration Dirac-Fock : MCDF) [27, 28, 29] et méthodes mixtes de QED et problème à n-corps [30, 31, 32]. Chaque méthode utilise une approche différente pour les calculs, qui amène à des différences significatives dans leur prédictions. La difficulté de ces calculs est due à la présence de plusieurs particules interagissantes entre elles. Une possibilité de comprendre le motif de ces différences est l'étude détaillée des énergies de transitions d'éléments lourds à peu d'électrons. Seule la comparaison avec l'expérience peut vérifier la validité de ces méthodes pour différentes gammes de numéro atomique. C'est pourquoi la spectroscopie de rayons-X des ions multichargés est un outil unique pour tester les théories dont on dispose avec une précision de quelques ppm.

**Tab. 1** – Comparaison des différents aspects des atomes pioniques et ions multichargés avec  $Z \sim 15-20$ . Ces deux type de systèmes sont caractérisés par une différente sensibilité aux effets de QED, mais, dans la gamme de quelque keV, les rayons-X émis ont une largeur naturelle comparable.

ATOMES PIONIQUES	IONS MULTICHARGÉS
<b>Effet de QED dominant</b>	
 $\pi^-$ $e^-/e^+$ Polarisation du vide	 $e^-$ $e^-/e^+$ Polarisation du vide
 $\pi^-$ N Recul relativiste	 $e^-$ Self-énergie
	 $e^-$ $e^-$ Corrélation entre électrons
<b>Caractéristiques des ligne de transition</b>	
$\approx 5 - 100$ meV largeur ligne (largeur naturelle et élargissement Doppler)	
Précision des prédictions théoriques : 2.5 ppm	Précision des prédictions théoriques : < 1 ppm
<b>Taux de photons détectés (avec un spectromètre à cristal sphérique)</b>	
5 – 100 count/hour	1 – $8 \times 10^4$ count/hour

## Nouveaux étalons de rayons-X

Une fois la théorie précisément vérifiée, on peut admettre que la QED décrit correctement la dynamique des systèmes de particules chargées, à un certain niveau de précision. Dans cette hypothèse, les émissions de ces systèmes liés simples peuvent être utilisées comme étalons de longueur d'onde dans les rayons-X de basse énergie, comme cela est suggéré dans Réf. [33]. Actuellement, les raies X étalons de quelques keV sont obtenues en excitant les électrons du coeur des atomes, à l'aide d'électrons ou de photons. Dans de nombreux cas leurs énergies sont données avec une précision de l'ordre du ppm [34], ce qui ne veut pas forcément dire que ces étalons peuvent être effectivement utilisés à une telle précision. Pour des rayons-X issus des transitions du coeur dans les systèmes multi-électroniques, le centre de gravité des raies ne peut en effet pas être clairement attribué à une transition physique, et les raies sont élargies par l'effet Auger. Les processus de

shake-off<sup>1</sup> et de la création de lacunes supplémentaires produisent de nombreuses transitions satellites très proches en énergie de la transition de la raie de diagramme, qui ne peuvent pas être résolues. De plus, la forme de la raie des systèmes multi-électroniques dépend aussi des mécanismes d'excitation utilisés pour créer les trous dans les couches internes [35] et de l'environnement chimique (solide, métallique, vapeurs,...) [34]. À cause de tout cela, la largeur naturelle des étalons de rayons-X actuels est typiquement plus de 10 fois supérieure à la résolution des meilleurs spectromètres de rayons-X. Pour ce motif, les transitions du cœur ne sont pas appropriées pour déterminer la fonction d'appareil d'un tel spectromètre à haute résolution.

Contrairement aux raies de fluorescence, les atomes pioniques et les ions très chargés sont caractérisés par une largeur naturelle de l'ordre de 10 meV dans la gamme des énergies de quelques keV, et constituent un spectre de raies denses. Par exemple, la transition  $M1\ 1s2s\ ^3S_1 \rightarrow 1s^2\ ^1S_0$  dans l'argon héliumoïde a une largeur naturelle de  $10^{-10}$  fois l'énergie de transition. Des transitions dans les ions à un ou deux électrons peuvent être émises par un plasma dans un piège ou une source d'ion à résonance cyclotronique des électrons (ECRIT, ECRIS) [36]. L'énergie cinétique des ions dans un tel dispositif est faible, de 0.5 à 6 eV [37], donnant lieu à un élargissement Doppler de 5 à 18 ppm, c'est-à-dire de 0.07 à 0.28 eV pour l'argon. Cela permet d'effectuer des mesures d'une précision de moins d'un ppm ce qui correspond à la précision exigée par la théorie pour des ions à un électron dans cette gamme de  $Z$ . De même, les raies des atomes pioniques ont une largeur naturelle de quelques meV et d'autre part, différentes gammes d'énergies peuvent être connectées en utilisant la structure de Yrast de leur cascade de désexcitation : des transitions successives dans les mêmes atomes connectent différentes échelles d'énergies d'un rapport  $\approx [1/(n+1)^2 - 1/n^2]/[1/n^2 - 1/(n-1)^2]$  ce qui est environ de l'ordre de 0.5 pour  $n$  autour de 5. Par exemple, le néon pionique émet des photons avec une énergie de 2.7, 4.5 et 8.3 keV, qui correspondent aux transitions  $7 \rightarrow 6$ ,  $6 \rightarrow 5$  et  $5 \rightarrow 4$ , avec une largeur naturelle de 12 meV pour la transition  $6 \rightarrow 5$ .

Les niveaux d'énergies de ces systèmes peuvent être calculés à mieux qu'1 meV près, en ne tenant pas compte de l'incertitude sur la masse du pion et bénéficient des tests de grande précision de QED dans les atomes hydrogénoïdes et héliumoïdes [38].

La précision des prédictions des énergies de transition dans les atomes pioniques est limitée par l'incertitude expérimentale sur la masse du pion, qui est aujourd'hui de 2.5 ppm. Par exemple, dans la transition  $6h \rightarrow 5g$  de l'hélium pionique, cette erreur limite environ à 11 meV la précision de l'évaluation théorique [33]. C'est pour cette raison qu'en 2000 une nouvelle expérience a été démarrée, dans le but de mesurer la masse du pion négativement chargé avec une précision de l'ordre du ppm [7, 8]. Comme décrit dans le Ch. 4, nous avons atteint cet objectif avec la spectroscopie de la transition  $5 \rightarrow 4$  dans l'azote pionique.

Même si les transitions des ions pioniques et des ions très chargés ont des caractéristiques similaires dans la gamme d'énergie de quelques keV (valeurs des largeurs et des énergies des transitions), les sources disponibles de ces deux sortes d'étalons de rayons-X ont des taux d'émission très différents. Des rayons-X de hautes intensités peuvent facilement être obtenus avec des ions très chargés produits dans le plasma d'une source d'ion à résonance cyclotronique des électrons. En utilisant un spectromètre à cristal de Bragg courbe, nous avons environ 40 000 coups en 30 minutes dans la raie de transition  $M1\ 1s2s\ ^3S_1 \rightarrow 1s^2\ ^1S_0$  de l'argon héliumoïde. La production d'atomes pioniques est plus

<sup>1</sup>Relaxation de l'état initial vers un état propre de l'atome après l'enlèvement d'un électron.

difficile car les pions sont des particules lourdes avec un temps de vie court (26 ns). Seuls les accélérateurs de protons, avec une énergie suffisante, permettent de produire un faisceau secondaire de pions assez intense pour être utilisé pour la production d'atomes pioniques. Pour un faisceau de pions d'environ  $10^8$  pions/s, comme à l'Institut Paul Scherrer, il faut plusieurs semaines pour obtenir le même nombre d'événements dans la raie  $6 \rightarrow 5$  du néon pionique que dans la raie M1 de l'argon héliumoïde produite par une ECRIS en une demi-heure. Pour les atomes muoniques, le taux est significativement inférieur. C'est pourquoi les atomes muoniques ne peuvent être utilisés facilement comme étalons de rayons-X. À cause de cette différence de taux, les rayons-X des atomes pioniques et muoniques ne sont pas appropriés pour caractériser les spectromètres à cristal de Bragg, contrairement aux raies émises par des ions très chargés dans des ECRIS/ECRIT. La nouvelle ECRIT de l'Institut Paul Scherrer, décrite dans ce manuscrit, a été développée exactement dans cet but : la caractérisation du spectromètre à cristal courbé utilisé pour la spectroscopie des atomes pioniques.

## Organisation de la thèse

Dans la section précédente, j'ai présenté les deux propriétés des ions pioniques et électroniques très chargés : les deux systèmes peuvent être utilisés pour définir de nouveaux étalons de rayons-X, ainsi que pour tester l'électrodynamique quantique. Dans les chapitres suivants, je vais décrire le travail de recherche que j'ai réalisé dans ce domaine, travail qui consiste principalement en une contribution expérimentale à la spectroscopie X de haute précision. Celle-ci est complétée par un travail théorique de calcul d'énergies dans les atomes pioniques. Le manuscrit est divisé en deux parties principales. La première est consacrée aux atomes pioniques et la deuxième à la spectroscopie des ions très chargés.

Le chapitre 2 décrit le calcul des corrections de structure hyperfine et de recul pour les atomes pioniques. La structure hyperfine est calculée en utilisant une nouvelle méthode perturbative pour l'équation de Klein-Gordon. Les résultats ainsi obtenus sont vérifiés par une autre méthode utilisant un Hamiltonien de Breit-Pauli. Cette comparaison permet aussi de déduire les corrections de recul dans les atomes pioniques, qui présente des caractéristiques particulières du fait du spin 0 du pion. Le formalisme développé dans la première section du chapitre sert à calculer les niveaux d'énergies de l'hydrogène, du deutérium et de l'azote pionique. Les deux premiers atomes sont intéressants car leur spectroscopie permet d'étudier l'interaction forte à basse énergie [5, 6]. L'azote pionique est utilisé dans notre nouvelle mesure de précision de la masse du pion de charge négative et comme test de l'électrodynamique quantique pour les particules de spin 0.

Dans le chapitre 3, je présente le dispositif expérimental nécessaire à la production des atomes pionique et à la mesure précise des leurs caractéristiques par la spectroscopie X. J'y explique en détail le principe du spectromètre à cristal de Bragg qui sert à mesurer les énergies des transitions  $5 \rightarrow 4$  de l'azote pionique avec une résolution de quelques ppm. Cet instrument est le même que celui utilisé pour la spectroscopie des ions multi-chargés. Je vais présenter aussi l'analyse détaillée des données enregistrées par le détecteur de position du spectromètre, nécessaire à la reconstitution du spectre d'énergie.

Le chapitre 4 traite exclusivement de la mesure de la masse du pion négativement chargé. Dans ce chapitre je présente les mesures et une analyse détaillée des erreurs systématiques, aboutissant à une nouvelle valeur de la masse du pion d'une précision de

1.5 ppm. Les transitions  $5 \rightarrow 4$  de l'azote pionique sont aussi utilisées pour fournir le test le plus précis pour la prédiction de la structure fine par l'équation de Klein-Gordon.

Dans cette thèse, les spectres d'ions très chargés sont utilisés pour tester l'électrodynamique quantique dans les systèmes à quelques électrons et pour caractériser le spectromètre à cristal utilisé dans l'étude des atomes pioniques. Ces ions sont produits dans deux sources d'ions à résonance électron-cyclotron : l'une développée à l'institut Paul Scherrer en Suisse, l'autre située au Laboratoire Kastler Brossel à Paris dans le cadre du projet SIMPA (Source d'Ions Multichargés de Paris). Dans le chapitre 5, je vais premièrement expliquer le fonctionnement d'une source d'ion ECR, donner ses caractéristiques principales, et décrire les différents dispositifs. Je vais ensuite décrire le piège à ion ECR à l'Institut Paul Scherrer et la source d'ion ECR du Laboratoire Kastler Brossel. Ce dernier a été utilisé en particulier pour obtenir des spectres de haute précision de l'argon, du chlore et du soufre héliumoïdes.

Le chapitre 6 est consacré à l'analyse des spectres atomiques de l'argon et du soufre héliumoïdes. Les résultats fournissent la mesure la plus précise, utilisant la spectroscopie X, des énergies pour les  $Z$  moyens. Les valeurs mesurées sont comparées aux résultats expérimentaux précédents et aux prédictions théoriques. Dans la dernière partie du chapitre je présente un nouveau développement de l'analyse des données permettant d'accroître la précision.

Le chapitre 7 conclura le manuscrit. Comme dans la section suivante, j'y résume les résultats obtenus pendant ma thèse et j'y présente les perspectives et développements futurs envisageables à partir de ce travail.

## Sommaire des résultats

Le but de cette thèse était d'augmenter la précision de la spectroscopie X des atomes pioniques et des ions multichargés.

L'azote pionique a été utilisé pour fournir une nouvelle évaluation de la masse du pion chargé négativement. Celle-ci a nécessité une réduction de l'erreur des prédictions théoriques des énergies atomiques et une mesure précise des transitions  $5 \rightarrow 4$  de l'azote pionique.

Pour améliorer les calculs théoriques, basés sur l'équation de Klein-Gordon, il a été nécessaire d'aborder l'étude de nouvelles corrections à l'énergie. Pour cette raison, j'ai calculé la structure hyperfine dans les atomes pioniques, qui cause un déplacement de l'énergie de transition due à la différence entre les probabilités de transitions des sous-niveaux hyperfins. Le formalisme développé dans le Ch. 2 qui permet le calcul de la structure hyperfine a été comparés avec les prédictions utilisant le hamiltonien de Breit-Pauli pour un noyau de spin  $\frac{1}{2}$ . Cette comparaison a aussi permis de déduire des corrections de recul du noyau pour la structure hyperfine. Les résultats présentés dans le Ch. 2 ont été confirmés par les prédictions théoriques qui utilisent l'équation de Bethe et Salpeter pour une particule de spin- $\frac{1}{2}$ . Contrairement à ces deux approches théoriques, la méthode développée dans cette thèse peut être utilisée pour des valeurs arbitraires du spin nucléaire.

En utilisant ce dernier formalisme, il a été possible d'augmenter la précision des prédictions théoriques pour les atomes pioniques avec un nombre atomique  $Z$  petit et moyen. En particulier, nous avons calculé les énergies de transitions de l'azote pionique avec une précision de l'ordre de 0.2 ppm en produisant une contribution négligeable dans les erreurs

systématiques de la mesure de la masse du pion. De plus, les énergies électromagnétiques de transitions  $np \rightarrow 1s$  de l'hydrogène pionique ont été calculés avec une précision sans précédent qui mènent à une réduction d'environ 30% des erreurs systématiques de l'évaluation du déplacement dû à l'interaction forte de l'état fondamentale de l'hydrogène pionique.

Avec les nouvelles prédictions théoriques, la spectroscopie présentée dans le Ch. 4 fournit actuellement la valeur la plus précise de la masse du pion négativement chargé avec une erreur de 1.7 ppm, 32% en moins par rapport à l'incertitude de la moyenne mondiale (2.5 ppm).

La spectroscopie de l'azote pionique permet, de plus, de tester les prédictions de l'électrodynamique quantique pour une particule spin-0 dans un système lié. En mesurant la différence d'énergie entre les transitions parallèles  $5g \rightarrow 4f$  et  $5f \rightarrow 4d$ , il a été possible de tester la validité de l'équation de Klein-Gordon avec une précision de l'ordre de 0.6%.

Cette nouvelle valeur de la masse du pion ne cause pas aucune réduction de l'erreur du déplacement dû à l'interaction forte parce que la transition  $6 \rightarrow 5$  dans l'oxygène pionique a été utilisée comme ligne de référence pour la transition  $3p \rightarrow 1s$  dans l'hydrogène pionique. Cependant, une réduction de l'incertitude de la masse du pion produit une augmentation de la précision des étalons de rayons-X en utilisant les transitions des atomes pioniques. La précision des prédictions de ces transitions est en effet limitée par l'erreur expérimentale de la masse du pion.

Une précision accrue de la masse du pion a été obtenue grâce à l'amélioration des techniques expérimentales. En particulier, nous utilisons la transition de l'oxygène muonique comme ligne de référence à la place de raies de fluorescence, et nous avons caractérisé précisément le spectromètre à cristal utilisé dans l'expérience.

La mesure de la fonction de réponse du spectromètre a été possible par le développement d'un nouveau piège d'ion à résonance cyclotronique des électrons pour la production des ions multichargés. Les transitions relativistes  $M1\ 1s2s\ ^3S_1 \rightarrow 1s^2\ ^1S_0$  dans l'argon, le chlore et le soufre héliumoïdes ont été utilisés pour l'étude systématique du spectromètre à cristal courbe. Cette étude a permis, entre autres, le développement et le test de la simulation Monte Carlo de l'instrument et des programmes de d'ajustement de courbes, utilisés dans l'analyse des spectres.

La simulation et les programmes d'analyses constituent un ensemble d'outils pour l'étude approfondie des spectres X. Ces outils ont permis d'utiliser le profil de raie adapté pour la mesure de la masse du pion et pour l'évaluation du déplacement dû à l'interaction forte de l'état fondamentale de l'hydrogène pionique, mais aussi pour la mesure des transitions des ions héliumoïdes.

Les ions multichargés produits dans le piège à ion ECR ont été utilisés pour tester l'électrodynamique en champ fort de plus de la caractérisation du spectromètre. L'analyse préliminaire des spectres de l'argon et du soufre héliumoïdes fournit l'évaluation la plus précise, de l'ordre de 10 meV, des énergies des transitions  $1s2p\ P \rightarrow 1s^2\ ^1S_0$  par rapport à la transition  $M1\ 1s2s\ ^3S_1 \rightarrow 1s^2\ ^1S_0$  utilisant la spectroscopie X, avec une réduction des incertitudes d'un facteur 3 à 10 par rapport aux expériences précédentes. En particulier, ces nouvelles mesures permettent de tester précisément les prédictions théoriques sur les ions multichargés avec quelques électrons.

## Perspectives

La méthode de perturbation de l'équation Klein-Gordon a été utilisée pour le calcul de la structure hyperfine due au moment magnétique nucléaire, mais elle peut aussi être utilisée pour un type différent de perturbation. Pour les atomes pioniques avec une grande valeur de  $Z$ , le moment quadripolaire électrique peut être non négligeable. L'effet d'une tel moment peut être évalué facilement en utilisant la même méthode de perturbation. Dans ce cas, la structure hyperfine due au moment quadripolaire peut être prédite en utilisant le développement multipolaire du potentiel électrostatique pour calculer l'opérateur de perturbation correspondant. De la même manière, les effets dus à l'interaction forte peuvent être pris en compte en introduisant le potentiel optique [39, 40] comme perturbation.

Ces deux applications sont très importantes pour le calcul des niveaux atomiques des atomes pioniques lourds où les effets relativistes, pris en compte automatiquement par l'équation de Klein-Gordon, sont importants.

Une amélioration additionnelle de ce formalisme sera l'introduction de la taille finie du pion et du noyau dans la formule de la structure hyperfine. Une approche correcte au problème nécessite une modification de l'expression du potentiel vecteur pour prendre en compte la distribution spatiale du moment magnétique nucléaire qui conduit à la correction Bohr-Weisskopf [41, 42].

Comme écrit ci-dessus, l'analyse des ions héliumoïdes présentée dans cette thèse est seulement préliminaire. Plusieurs améliorations doivent être apportés pour augmenter la précision de la mesure. Actuellement, la majeure source d'incertitude est l'évaluation de la distance cristal-détecteur dans le spectromètre à rayons-X. En plus, le modèle de profil de ligne utilisé jusqu'à présent ne tient pas compte de la déformation des pics dans les spectres X pour les réflexions de Bragg lorsque la raie est sur une partie du détecteur en dehors du point focal du spectromètre. Une analyse plus correcte est en cours. Cette nouvelle étude simule le profil le plus adapté pour chaque pic dans le spectre X et elle utilise les nouvelles fonctions de la simulation Monte Carlo pour tenir compte des mesures récentes des angles de coupe des cristaux (angle entre la surface du cristal et les plans cristallins) utilisés dans les expériences.

Cette analyse sera étendue aux spectres des ions moins chargés comme les transitions lithiomoïdes et bérylliumoïdes. L'étude de ces transitions nécessitera un effort supplémentaire pour étudier correctement la contribution des transitions satellites due principalement à la complexité des mécanisme de population de niveaux atomiques. Pour cette raison, il est nécessaire de faire une étude des caractéristiques des spectres en fonction de la puissance injectée des microondes et de la pression du gaz dans la chambre du plasma dans le piège à ion ECR. Une telle étude a déjà été commencée en utilisant la source à ion ECR SIMPA à Paris. L'installation SIMPA est actuellement équipée d'un spectromètre à cristal de graphite mosaïque qui, de part sa résolution en énergie limitée, ne peut pas distinguer ces transitions satellites. Cependant, un nouveau spectromètre à double cristal plan est en construction dans le groupe. Cet instrument est caractérisé par une résolution en énergie de 0.27 eV pour des rayons-X de 3 keV en utilisant Si(111), et il peut mesurer la valeur absolue des énergies de transition, comme la transition  $M1 \ 1s2s \ ^3S_1 \rightarrow 1s^2 \ ^1S_0$  dans l'argon héliumoïde, avec un erreur inférieure à 0.5 ppm, qui permettra de tester les différentes prédictions théoriques pour les ions très chargé à quelques électrons avec une précision sans précédents.

# Chapter 1

---

## Introduction

---

*Nulla dies sine linea*

---

Pliny the Elder, Natural History. Book xxxv. Sect. 84

Atomic Physics, thanks to the precision of the techniques that it enables to use, and to the possibility of very accurate *ab initio* calculations, leads to results that are highly needed in other fields. Atomic spectroscopy enables to measure fundamental constants as the fine structure constant  $\alpha$  and the gravitation constant  $G$  [1, 2]; but also to measure the particle masses, as the electron, the antiproton and the pion mass [3, 4], and to study the fundamental interaction. The aim of this thesis is to contribute to solve a number of fundamental problems, by improving considerably the measurement precision. In particular, I present a new measurement of the pion mass using pionic nitrogen X-ray spectroscopy and recent results on helium-like argon and sulphur spectroscopy.

Pionic atoms and ions are formed when a heavy particle is captured on an atomic nucleus. The negatively charged pion is a meson formed by a anti-quark *anti-up* ( $\bar{u}$ ) and a quark *down* ( $d$ ). In the process, many or all electrons of the atom are ejected and one obtains a highly charged heavy ion, with properties that depend on the captured particle. Measurements in pionic atoms leads to strong-interaction studies at very low energy [5, 6] and, in addition, to accurate negatively charged pion mass evaluation [3, 7, 8].

The new pion mass measurement that I present is characterized by an accuracy in the order of 1.5 ppm, much better than the previous measurements [3, 9]. To obtain such precision, a considerable experimental and theoretical effort was required: the pion mass is measured by X-ray spectroscopy of  $5 \rightarrow 4$  pionic nitrogen transitions using the theoretical predictions provided by Quantum Electrodynamics (QED) calculations. To reach this precision, effects as the vacuum polarization and recoil corrections have to be taken into account for the correct evaluation of the atomic levels. A part of my Ph.D. work is dedicated to the calculation of the recoil correction and of the hyperfine structure in pionic atoms. In particular, I will present a new perturbation method for the Klein-Gordon equation, which describes the dynamics of spin-0 particles, as the pion. The advantage of this new technique consist to take into account relativistic effects without approximations. With the calculation of these new corrections, we can reach a precision of 0.2 ppm for the theoretical predictions of the  $5 \rightarrow 4$  pionic nitrogen transition energies.

The precise analysis of the pionic nitrogen spectra requires an accurate characterization of the Bragg crystal spectrometer we used. This characterization has been obtained using the X-ray emission from highly charged ions produced with an Electron-Cyclotron-Resonance Ion Trap (ECRIT). Highly charged ions studied in this manuscript are composed of a nucleus with a charge 16–18 times higher than the proton charge ( $Z = 16 - 18$ ), and few orbiting electrons in presence of a strong nuclear Coulomb field.

In the ECRIT, for elements like sulphur and argon, the relativistic  $M1$  transition  $1s2s\ ^3S_1 \rightarrow 1s^2\ ^1S_0$  is very bright and very narrow, due to the very low kinetic energy of the ions in the source. The  $M1$  transitions from these elements enable for a systematic characterization of the spherically bent crystal of our X-ray spectrometer and thus allow for the precise measurement of the response function of the instrument.

Apart from the characterization of the spectrometer, one of the most important results of this project was in a series of high-precision measurement of the X-ray spectra of argon and sulphur. With 1–2 hours maximum acquisition time, we obtained high-statistics spectra of He- and Li-like ionic states of these elements and we measured transition energies of these ions with a precision of few tens of meV for 3 keV photons. This precision allows to compare and to test accurately the different available theoretical predictions with the experiment, and it provides a sensitive test of QED.

In the same way, Quantum Electrodynamics can be tested in pionic atoms. The analysis of pionic nitrogen enables to compare the experimental measurement of the fine structure to the theoretical predictions with a precision in the order of 0.3%.

In addition, the X-rays emitted from these atoms can be used to define new wavelength standards for the energy range of few keV.

In the following sections, I will present in detail these two features of the X-ray spectroscopy of multicharged ions and pionic atoms: the possibility to test Quantum Electrodynamics and to define new X-ray standards.

## 1.1 Quantum Electrodynamics tests with pionic atoms and highly charged ions

Quantum Electrodynamics (QED) is the theory that describes the interaction between light and matter, and it has been, up to now, the best tested theory in physics. The effort to merge Quantum Mechanics and relativity was initiated, soon after Quantum Mechanics was formulated. However, it is only during the 1940s that it was possible to satisfy the requirement of relativity in a consistent manner. Quantum Electrodynamics is a quantum field equivalent of the classical electrodynamics (Maxwell-Lorentz theory). The wave-particle duality is now fully incorporated into the theory; and charged particles and photons are treated as quantized fields, placing them in the same footing.

The most elementary bound systems where we can test QED are hydrogen-like and few-electron atoms, formed by a heavy nucleus and few orbiting particles. As written above, in this manuscript I will focus on two systems. The first one is the H-like pionic nitrogen, where all the electrons are replaced by a negatively charged pion. The second example is represented by few electrons highly charged ions, with a nuclear charge  $Z \sim 17$ .

But why do we choose these particular atoms? Pionic atoms and highly charged ions are interesting objects as they enable to probe aspects of atomic structure that are quantitatively different from what can be studied in electronic or “normal” atoms. Pionic and

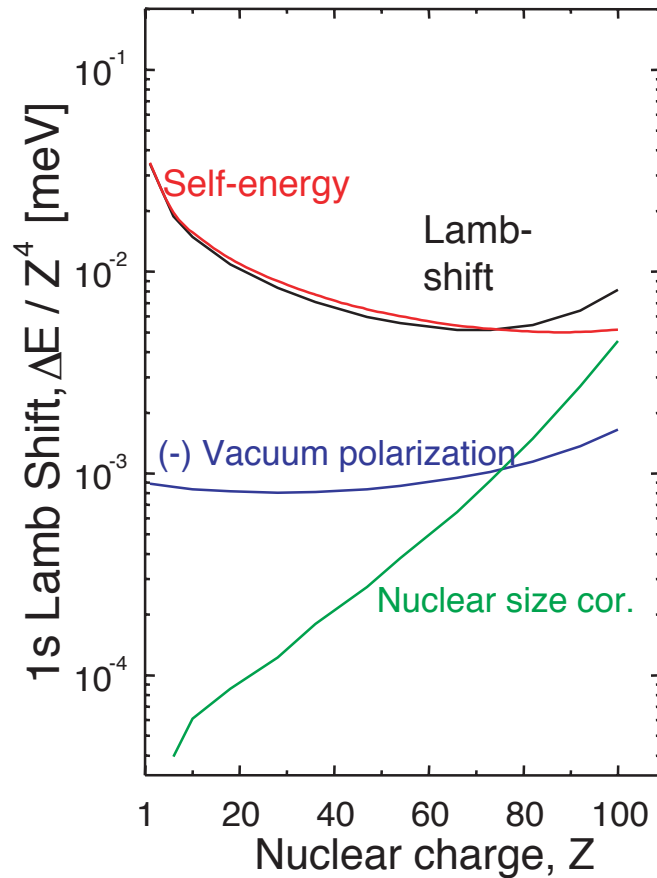


**Figure 1.1** – Contribution of the self-energy, of the vacuum polarization and of the nuclear finite size against the atomic number  $Z$ . This plot has been reproduced from Ref. [10], which uses the values published in Ref. [11].

highly charged atoms are interesting system to test QED because both of them have a small characteristic Bohr radius. The classic Bohr radius  $a_0$  is, in fact, inversely proportional to the orbiting particle mass  $m$  and to the nuclear charge  $Z$ :  $a_0 = \hbar/(mcZ\alpha)$  ( $c$  is the speed of light and  $\hbar$  is the Planck constant). A small value of the Bohr radius corresponds to a larger sensitivity to Quantum Electrodynamics effects as vacuum polarization and self-energy. The charged pion has a mass about 270 times larger than the electron mass. In this case, the Bohr radius and the electron Compton length  $\hbar/(m_e c)$  are of the same order of magnitude, i.e., the pion is sensitive to the distortion of the Coulomb field due to the continuous creation and annihilation of electron-positron pairs. For this reason pionic atoms, as muonic atoms, can be used to test QED corrections such as the vacuum polarization [12, 13, 14], which has a range in the order of the Compton wavelength. Moreover, these atoms are sensitive to relativistic effects in the atomic dynamics. The characteristic “velocity” of a particle in an atom is  $\langle n|\hat{v}|n\rangle = Z\alpha c/n$ . For ions with  $Z \sim 17$ , this velocity reaches a value  $\langle 1s|\hat{v}|1s\rangle \sim 0.12 c$  making relativistic correction very large.

Contrary to the muon and the electron, the pion has no spin and its dynamics is well described, in the leading order, by the Klein-Gordon equation. The predictions of this

equation have been much less tested than the predictions for particles with spin equal to  $1/2$  (as the electron and the muon) [15]. For this reason, the measurement of pionic nitrogen transition energies provides in addition an unique test for Relativistic Quantum Mechanics for spin-zero particles. In particular, the measurement of the energy difference between the  $5g \rightarrow 4f$  and  $5f \rightarrow 4d$  transitions allows to test the fine structure as predicted by the Klein-Gordon equation with unprecedented accuracy.

Precise X-ray spectroscopy of highly charged ions may lead to a better understanding of a fundamental problem that arose recently: after several decades of high-precision work on He and helium-like ions, there are still difficulties in comparing theory and experiment. Contrary to pionic atoms, highly charged ions with  $Z = 15 - 20$  are not so sensitive to the vacuum polarization because the Bohr radius is still too large compared to the electronic Compton wavelength [16] and the QED contribution to the Lamb shift is dominated by the self-energy (Fig. 1.1 and Table 1.1).

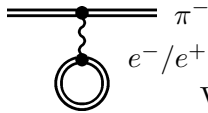
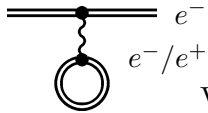
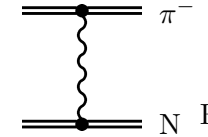
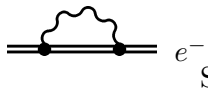
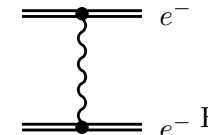
At present, in helium there is a strong disagreement (six times the combined error bars) between the calculations [17, 18, 19, 20] and recent very accurate measurements [21, 22, 23, 24]. In He and light elements, the theory makes use of an expansion of the Bethe and Salpeter equations in operators of successive orders in  $1/c$ , and  $Z\alpha$ . For correction terms that depends on  $1/Z$ , as the binding electron correlation, one uses all-orders methods, in which series of diagrams are summed up. In opposite, for heavier elements, all-orders methods have to be used for correction terms that depend on  $Z\alpha$ , and the electron correlation can be calculated using a perturbation expansion on  $1/Z$ .

At present, different theoretical predictions are available that use different methods as the relativistic many-body problem theory (RMBPT) [25, 26], the Multi-Configuration Dirac-Fock (MCDF) method [27, 28, 29] and methods that use QED calculation and many-body problem theory together [30, 31, 32]. Each technique uses a different approach for the calculation, leading to significant differences in their predictions. The difficulty of these calculations is due to the presence of several particles interacting each other. One way to understand this very important discrepancy, is then to study more accurately heavier elements. Only the comparison with experience can test the validity of these methods for different ranges of  $Z$ . For this reason, precise X-ray spectroscopy of multi-charged ions is a unique tool to test the available theories with an accuracy of some ppm.

## 1.2 New X-ray standard definition

Once theory has been accurately tested, we can assume that QED describe correctly systems consisting of interacting light and particles, to a certain level of accuracy. With this assumption, X-rays from these simple bound systems could be used as wavelength standards in the low-energy X-rays range, as suggested in Ref. [33]. Presently, standard X-ray lines in the few keV range are made by exciting innershell transitions in neutral atoms with either electrons or photons. In a number of cases their energies are given with a precision close to 1 ppm [34], which does not necessarily means that these standards can be used to such an accuracy because of the complex line structure. For X-rays originating from innershell transitions in multi-electron systems, the center of gravity of the line cannot be unambiguously attributed to a physical transition and the lines have a broadening due the Auger effect. Shake-off processes and open outer shells lead to numerous satellite transitions very close in energy to the diagram line, which can not be resolved. Moreover,

**Table 1.1** – Comparison of different aspects of pionic atoms and of highly charged ions with  $Z \sim 15 - 20$ . These two systems are characterized by a sensitivity to different QED effects but, in the range of few keV, their X-ray transitions are characterized by a similar natural width.

PIONIC ATOMS	HIGHLY CHARGED IONS
<b>Dominant QED effects</b>	
 $\pi^-$ $e^-/e^+$ Vacuum polarization	 $e^-$ $e^-/e^+$ Vacuum polarization
 $\pi^-$ N Relativistic recoil	 $e^-$ Self-energy
	 $e^-$ $e^-$ Electronic correlation
<b>Transition lines characteristics</b>	
$\approx 5 - 100$ meV line width (natural width and Doppler broadening)	
Accuracy theoretical values: 2.5 ppm    Accuracy theoretical values: < 1 ppm	
<b>Rate of detected photon (spherically bent crystal spectrometer)</b>	
5 – 100 count/hour	1 – $8 \times 10^4$ count/hour

the line shape of multi-electronic system depends also on the excitation mechanism used to create the innershell vacancies [35] and on the chemical environment (solid, metallic vapors, ...) [34]. In addition, the natural width of the current X-ray standard is typically more than 10 times larger than the resolution of the best X-ray spectrometers. Hence, innershell transitions are unsuitable to determine the response function of such apparatus.

Contrary to fluorescence radiation, pionic and highly charged atom transitions are characterized by a natural width on the order of 10 meV in the few keV range, and provide a dense set of lines in this energy range. As an example, the  $1s2s\ ^3S_1 \rightarrow 1s^2\ ^1S_0$   $M1$  transition in He-like argon has a natural width of  $10^{-10}$  times the transition energy. Transition in one- and two-electron ions can be emitted by a plasma in an Electron-Cyclotron-Resonance ion sources or trap (ECRIS, ECRIT) [36]. The ion energy in such a device ranges from  $\approx 0.5$  to 6 eV [37], giving rise to a Doppler Broadening in the 5 to 18 ppm, i.e., 0.07 to 0.28 eV for argon. This allows for measurements below 1 ppm, which corresponds to the expected accuracy (typically 1 meV) of the theory for one electron ions in this range of  $Z$  but would be very demanding for two electron systems. Similarly, pionic atoms have a natural

width of a few meV and in addition, different energy ranges can be connected by exploiting the Yrast structure of the their de-excitation cascade: successive transitions in the same atom connect different energy scales in ratios  $\approx [1/(n+1)^2 - 1/n^2]/[1/n^2 - 1/(n-1)^2]$ , which are roughly of the order of 0.5 for  $n$  around 5. For instance, pionic neon provides photon energies of 2.7, 4.5 and 8.3 keV corresponding, respectively, to the  $7 \rightarrow 6$ ,  $6 \rightarrow 5$  and  $5 \rightarrow 4$  transitions, with a natural width of 12 meV for the  $6 \rightarrow 5$  transition. Level energies of these systems can be calculated nowadays from first principles to better than 1 meV, excluding the uncertainty of the pion mass, benefiting from the high-accuracy tests of QED in hydrogen and hydrogen-like atoms [38].

The precision of the transition energies prediction in pionic atoms is limited at present by the experimental error in the pion mass value, which is  $\approx 2.5$  ppm. As an example, in the  $6h \rightarrow 5g$  pionic helium transition, this error limits to about 11 eV the accuracy of the theoretical evaluation [33]. For this reason, in 2000, a new experiment was started, with the goal to measure the negatively charged pion mass with an accuracy in the order of 1 ppm [7, 8]. As described in Ch. 4, we accomplished this objective by X-ray spectroscopy of the  $5 \rightarrow 4$  transition in pionic nitrogen.

Even, if pionic atoms and highly charged ions transitions have similar characteristics in the few keV range (width and energy value), The available sources for these two kinds of X-ray standards have a very different emission rate. High X-rays intensities can be easily obtained from highly charged ions produced in the plasma of an Electron-Cyclotron-Resonance ion source. Using a curved Bragg crystal spectrometer, it is possible to obtain about 40 000 counts in 30 minutes in the  $1s2s \ ^3S_1 \rightarrow 1s^2 \ ^1S_0$  M1 transition of He-like argon. The production of pionic atoms is more difficult because pions are unstable particles. Only proton accelerators, with a sufficient energy, can provide a secondary pion beam that can be used to produce pionic atoms. For a pion beam of about  $10^8$  pion/s as at the Paul Scherrer Institut, it requires several weeks to obtain the same number of count in the  $6 \rightarrow 5$  pionic neon transition than in the He-like argon M1 line from an ECRIS in half-an-hour. For muonic atoms the rate is even significantly lower. and they can not easily used as X-ray standard. Due to this rate difference, X-rays from pionic and muonic atoms are unsuitable to characterize Bragg crystal spectrometers, contrary to highly charged ions radiation.

### 1.3 Organization of the thesis

In this introduction, I have shown the common features of pionic and highly charged ions: both systems can be used to define new precise X-ray standard and they can be used to test Quantum Electrodynamics as well. In the following chapters, I will present the research work I have done in this field, which consists principally in an experimental contribution to high precision X-ray spectroscopy. This work is completed with a theoretical study consisting in pionic atoms energies calculations. The manuscript is divided in two main parts. The first part is dedicated to pionic atoms and the second is devoted to highly charged ions spectroscopy.

The chapter 2 is dedicated to the calculation of the hyperfine structure and recoil corrections for pionic atoms. The hyperfine structure is calculated using a new perturbation method for the Klein-Gordon equation. The results obtained by this method are checked with an other method using the Breit-Pauli Hamiltonian. This comparison allows also to

investigate the recoil corrections in pionic atoms, which presents particular characteristics due to the spin-zero nature of the pion. The formalism developed in the first sections of the chapter is used to calculate the energy levels of pionic hydrogen, deuterium and nitrogen. The first two atoms are interesting because their spectroscopy enables to study the strong interaction force at low energy. Pionic nitrogen is used in our new precision measurement of the negatively charged pion and as new test of Quantum Electrodynamics for spin-zero particles.

In the chapter 3, I will describe the experimental set-up required to produce excited pionic atoms and to measure accurately their characteristics by X-ray spectroscopy. I will describe in detail the Bragg crystal spectrometer used to measure pionic nitrogen transition energies with an accuracy of a few ppm. This instrument is the same spectrometer than will be used also for highly charged ions spectroscopy. In particular, I will present the data analysis required to reconstruct the energy spectra from the CCD recorded data.

The chapter 4 is exclusively devoted to the charged pion mass measurement. In this chapter, I will present the experiment and a detailed analysis of systematic errors, showing that the new measurement of the pion mass has an accuracy of 1.5 ppm. The  $5 \rightarrow 4$  pionic nitrogen transitions are also used to provide the most accurate test to date for the Klein-Gordon equation prediction for the fine structure.

In this thesis, highly charged ions spectra are used for two different tasks: to test Quantum Electrodynamics in few-electrons systems and to characterize the crystal spectrometer used for the pionic atoms study. These ions are produced in two Electron-Cyclotron-Resonance (ECR) ion sources: one developed at the Paul Scherrer Institut in Switzerland and one installed at the Laboratoire Kastler Brossel in Paris. In chapter 5, I will first describe how an ECR ion source works, give its main characteristics, and describe these different apparatus. I will then describe the ECR ion source of the Laboratoire Kastler Brossel and the ECR ion trap at the Paul Scherrer Institut. This last one has been used, in particular, to obtain high-precision spectra of helium-like argon, chlorine and sulphur.

The chapter 6 is dedicated to the analysis of the atomic spectra of He-like argon and sulphur. The results provide the most precise measurement for medium-Z He-like ions energies using X-ray spectroscopy. The measured values are compared to the older experimental results and theoretical predictions. In the last part of the chapter I will present a new development of the data analysis for an additional increase of the result accuracy.

Chapter 7 will conclude the manuscript. I will summarize the results obtained during my Ph.D. thesis and I will present the outlook and future developments one can envision from the presented work.



# **Part I**

## **Pionic atoms**



## Chapter 2

---

# Hyperfine structure and recoil corrections in pionic atoms

---

*... dico che quanto alla verità di che ci danno cognizione le dimostrazioni matematiche, ella è l'istessa che conosce la sapienza divina; ma vi concederò bene che il mondo col quale Iddio conosce le infinite proporzioni, delle quali noi conosciamo alcune poche, è sommamente più eccellente del nostro, il quale procede con discorsi e con passaggi di conclusione in conclusione,..*

---

Galileo Galilei, Dialogo Sopra i Due Massimi Sistemi del Mondo, Firenze 1932

### Introduction

In this chapter, I present the calculation of the hyperfine structure (HFS) and the recoil correction for pionic atoms. The pion is a boson with spin equal to zero. The Klein-Gordon equation (KG) is the correct equation to describe a charged boson in the Coulomb field of the nucleus. If we consider the interaction between the nuclear magnetic moment and the magnetic field created by the orbiting pion, we have to add an additional hyperfine term in the equation. This term is obtained using a multipole development of the electromagnetic field using the precise approach shown in references [42, 43]. Non-relativistic calculation for the pionic atom hyperfine structure can be found in Refs. [39, 44, 45]. Differently from this methods, I will present a formalism where the energy corrections are calculated in a completely relativistic framework as a perturbation correction of the KG equation, alternative to the methods presented in Refs. [46, 47, 48, 49]. At present, theoretical prediction for HFS including relativistic corrections can be found only for spin- $\frac{1}{2}$  nucleus [50, 51]. The calculations presented here are not restricted to this case and they can be used for an arbitrary value of the nucleus spin.

In Sec. 2.2 we develop the formalism to evaluate the energy correction. In Sec. 2.3 we calculate the hyperfine structure using the Breit-Pauli Hamiltonian. This formalism

enables to test the HFS relativistic calculation and to derive additional recoil corrections. In Sec. 2.4 we present the detailed energy level evaluation for some particular choice of pionic atoms: pionic hydrogen and pionic nitrogen. These systems have a particular interest due to the ongoing experiments at the Paul Scherrer Institut in Switzerland [5, 7].

## 2.1 General characteristic of the Klein-Gordon equation

During the period 1925-1926, the scientific community was ready to formulate a relativistic equation to describe matter wave packets, and several reputed scientists contributed to its formulation. The Klein-Gordon equation was probably formulated for the first time by Erwin Schrödinger in mid December 1925, before he derived his more famous non-relativistic equation. It is only in June 1926 that Schrödinger submitted the relativistic version, after the submission at the end of April of an equivalent version of the KG equation by Oskar Klein. De Broglie presented independently a complete version of the KG equation in July 1926, after the submission of the paper on relativistic wave mechanics by Vladimir Fock (beginning of June 1926) and before Walter Gordon's paper (September 1926). During the same period, other physicists, like Pauli and Dirac, stated the KG equation<sup>1</sup>. Even though the KG equation was considered by many physicists, it didn't play an important role in the development of Quantum Mechanics. The non-linear nature of the equation prevented an easy interpretation in a more general Quantum Mechanical picture. The Klein-Gordon equation reappeared in the 1930's and Yukawa used it for his nuclear interaction theory, which predicted the existence of a spin-0 particle ("U-quantum") [53].

What are the principal characteristics of the Klein-Gordon equation? The simplest relativistic quantum mechanics equation for a free particle must reproduce the expression of the kinetic energy in the special relativity framework:

$$E = \sqrt{\mathbf{p}^2 c^2 + m^2 c^4}, \quad (2.1)$$

where  $\mathbf{p}$  and  $m$  are the momentum and the mass of the particle, respectively. If we apply the canonical quantization, we have to associate  $\mathbf{p}$  and  $E$  to the corresponding operators:

$$\begin{cases} E \rightarrow i\hbar \frac{\partial}{\partial t} \\ p_i \rightarrow -i\hbar \frac{\partial}{\partial r_i} \end{cases} . \quad (2.2)$$

In the previous formula the variable  $r_i$  is the  $i$ -th spatial component of the quadri-vector coordinate  $x = (ct, \mathbf{r})$ . In this case, Eq. (2.1) in terms of operator acting on the wavefunction  $\Psi(x)$  becomes:

$$i\hbar \frac{\partial}{\partial t} \Psi(x) = \sqrt{-\hbar^2 c^2 \nabla^2 + m^2 c^4} \Psi(x) \quad (2.3)$$

This expression cannot directly be used because the presence of the square-root operator. If we expand it, we obtain all powers of the Laplacian operator and it will lead to a non-local theory. In addition, relativistic invariance is not clearly exhibited since there is a

---

<sup>1</sup>More detailed historical information about the KG equation can be found in Ref. [52]

lack of symmetry between the space and time coordinates. We can avoid these difficulties by using the quadratic form of Eq. (2.1):  $E^2 = \mathbf{p}^2 c^2 + m^2 c^4$ . In this case we have:

$$-\hbar^2 \frac{\partial^2}{\partial t^2} \Psi(x) = -\hbar^2 c^2 \nabla^2 \Psi(x) + m^2 c^4 \Psi(x), \quad (2.4)$$

which in the covariant form becomes<sup>2</sup>:

$$(\hbar^2 c^2 \partial^\nu \partial_\nu + m^2 c^4) \Psi(x) = 0, \quad (2.6)$$

equivalent to

$$(\hbar \square + m^2 c^2) \Psi(x) = 0. \quad (2.7)$$

For the study of pionic atoms, we are interested in the KG equation with the presence of an external electromagnetic potential  $A_\nu$ . The Klein-Gordon equation for a particle with a charge equal to  $-e$  and mass  $\mu$  in the presence of an electromagnetic field is obtained applying the minimal coupling  $p_\nu \rightarrow p_\nu + eA_\nu(x)$ . The minimal coupling is the simplest coupling with the electromagnetic field, which respects the gauge invariance and which is used in classical relativistic mechanics to describe the interaction of a point-like particle with an applied field [54]. We have:

$$\mu^2 c^2 \Psi(x) = \left\{ \frac{1}{c^2} [i\hbar \partial_t + eV(x)]^2 + [i\hbar \partial_i - eA_i(x)] [i\hbar \partial^i - eA^i(x)] \right\} \Psi(x). \quad (2.8)$$

In particular, we consider an atomic system composed of a negatively charged boson and of a nucleus with a positive charge equal to  $Ze$ . In this case, in the previous equation  $\mu$  indicate the reduced mass of the system and we can substitute to  $A^\nu$  the Coulomb potential  $(V(r), 0)$ , where:

$$V(r) = \frac{Ze}{4\pi\epsilon_0} \frac{1}{r}, \quad (2.9)$$

with  $r = |\mathbf{r}|$  (the module of the spatial part of the quadri-vector coordinate) and  $\epsilon_0$  is the electric permittivity of the free space<sup>3</sup>. In this case the energy of the system is:

$$E_{(0)}^{nl} = \frac{\mu c^2}{\sqrt{1 + \frac{(Z\alpha)^2}{\left[ n - l - 1/2 + \sqrt{(l + 1/2)^2 - (Z\alpha)^2} \right]^2}}}, \quad (2.11)$$

<sup>2</sup>In this chapter we use the following metric tensor:

$$g_{\mu\nu} = \left\{ \begin{array}{cccc} 1 & & & \\ & -1 & & \\ & & -1 & \\ & & & -1 \end{array} \right\}. \quad (2.5)$$

With this notation we have:  $\partial_i \partial^i = \partial_t^2$  and  $\partial_i \partial^i = -\sum_{i=1}^3 \partial_i^2$ .

<sup>3</sup>With this notation the fine structure constant is

$$\alpha = \frac{e^2}{4\pi\epsilon_0 \hbar c} = \frac{e^2}{4\pi} \sqrt{\frac{\mu_0}{\epsilon_0}}, \quad (2.10)$$

where  $\mu_0$  is the magnetic permeability of the free space

where  $n$  and  $l$  denote the principal and angular momentum quantum numbers, respectively, The energy  $E_{(0)}$  can be decomposed in the mass energy  $\mu c^2$  and the binding energy  $\mathcal{E}_{(0)}^{nl}$ :  $E_{(0)}^{nl} = \mu c^2 + \mathcal{E}_{(0)}^{nl}$ . In reality, the mass energy is  $\mathcal{M}c^2$ , where  $\mathcal{M}$  is the total mass of the system: pion and nucleus. However, if we apply the leading recoil correction to the KG equation, we have to consider a particle, with mass  $\mu$ , the reduced mass of the system, orbiting around to a nucleus with infinite mass. A more detailed discussion about recoil corrections will be developed in Sec. 2.3.

If we expand  $\mathcal{E}_0$  in function of the parameter  $Z\alpha$  we obtain:

$$\mathcal{E}_0^{nl} = -\mu c^2 \frac{(Z\alpha)^2}{2n^2} - \mu c^2 \frac{(Z\alpha)^4}{n^3} \left[ \frac{1}{2(l+1/2)} - \frac{3}{8n} \right] + \mathcal{O}[(Z\alpha)^6]. \quad (2.12)$$

The first term is the classical energy expression for the Schrödinger equation for hydrogen atom. The lower correction term, due to the relativistic effects, is of the order of  $\mu(Z\alpha)^4$  which correspond to a relative correction of  $(Z\alpha)^2 \simeq 5 \times 10^{-5} \times Z^2$ .

For a bound system, the eigenfunction can be decomposed in a time-dependent part and a spatial-dependent part. The spatial-dependent part, as in the non-relativistic wavefunction, can be written as the product of spherical harmonics (the angular momentum eigenfunctions) with a function that depends only on  $|\mathbf{r}| = r$ :

$$\Psi(x) = \exp(-iE^n t/\hbar) \varphi_{nl}(\mathbf{r}) \equiv \exp(-iE^n t/\hbar) Y_l^m(\theta, \phi) \psi_{nl}(r). \quad (2.13)$$

Using  $\tilde{\psi}_{nl}(\rho) = (2K_{nl})^{3/2} \psi_{nl}(r)$ , the normalized radial part can be written as a function of the dimensionless variable  $\rho = 2K_{nl}r$  [40, 55]:

$$\tilde{\psi}_{nl}(\rho) = \sqrt{\frac{(n-l-1)!}{2[n + \sqrt{(l+1/2)^2 - (Z\alpha)^2} - l - 1/2] \Gamma[n + 2\sqrt{(l+1/2)^2 - (Z\alpha)^2} - l]}} \times \rho^{\sqrt{(l+1/2)^2 - (Z\alpha)^2} - 1/2} e^{-\rho/2} L_{n-l-1}^{2\sqrt{(l+1/2)^2 - (Z\alpha)^2}}(\rho), \quad (2.14)$$

where the function  $L_n^a(x)$  are the associated Laguerre polynomials. The parameter and  $K_{nl}$  is given by:

$$K_{nl} = \frac{\mu c Z \alpha}{\hbar} \times \frac{1}{\left[ n - l - 1/2 + \sqrt{(l+1/2)^2 - (Z\alpha)^2} \right] \sqrt{1 + (Z\alpha)^2 \left[ n - l - 1/2 + \sqrt{(l+1/2)^2 - (Z\alpha)^2} \right]^{-2}}}. \quad (2.15)$$

We remark that  $K_{nl}$  is directly connected to a typical radius  $r_0 = 1/(nK_{nl})$ , the equivalent of the Bohr radius  $a_0 = \hbar/(\mu c Z \alpha)$ .

The functions  $\Psi_{nl}$ , defined in Eqs. (2.13) and (2.14), are normalized to 1:

$$\int \varphi_{nl}^*(\mathbf{r}) \varphi_{nl}(\mathbf{r}) d\mathbf{r}^3 \equiv \int \psi_{nl}^*(r) \psi_{nl}(r) r^2 dr = 1. \quad (2.16)$$

However, differently to the non-relativistic case, we can have:

$$\int \psi_{n'l'}^*(r) \psi_{nl}(r) dr^3 \neq 0 \text{ with } n' \neq n, l' \neq l \quad (2.17)$$

because the probability density (and the scalar product) has a different definition for spin-0 particles. In the non-relativistic case, the probability density is defined as  $\rho(r) = |\varphi(\mathbf{r})|^2$ . In the relativistic case for spin-0 particles we have [40, 54]:

$$\rho(r) = i \left( \Psi^*(x) \frac{\partial \Psi}{\partial t}(x) - \frac{\partial \Psi^*}{\partial t}(x) \Psi(x) \right). \quad (2.18)$$

In the case of pionic atoms, the previous equation becomes [46, 47, 49]:

$$\rho(r) = 2i\varphi^*(\mathbf{r}) (E + eV(\mathbf{r})) \varphi(\mathbf{r}). \quad (2.19)$$

It is interesting to compare these expressions with the non-relativistic wavefunction  $\tilde{\psi}_{nl}(\rho)_{NR}$  and with the Bohr radius  $a_0$ . In particular, it is possible to develop  $\tilde{\psi}_{nl}(\rho)$  and  $r_0$  in power series of  $Z\alpha$ ,

$$\tilde{\psi}_{nl}(\rho) = \tilde{\psi}_{nl}(\rho)_{NR} \left\{ 1 + \left[ \frac{25}{36} - \frac{\gamma}{3} - \frac{\ln(\rho)}{3} \right] (Z\alpha)^2 + \mathcal{O}[(Z\alpha)^4] \right\}, \quad (2.20)$$

$$r_0 = a_0 \left\{ 1 + \left[ \frac{1}{2(l+1/2)n} - \frac{1}{2n^2} \right] (Z\alpha)^2 + \mathcal{O}[(Z\alpha)^4] \right\}, \quad (2.21)$$

where  $\gamma = 0.5772\dots$  is the Euler-Mascheroni constant. We remark that the non-relativistic limit of the Klein-Gordon energy and wavefunction gives, as expected, the Schrödinger equation energy and wavefunction. In particular, we can use Eq. (2.20) and (2.21) to write the relativistic expectation values of  $r^n$  ( $n \neq 0$ ) in function to the non-relativistic ones:

$$\langle nl|r^n|nl \rangle = \langle nl|r^n|nl \rangle_{NR} \{ 1 + \mathcal{O}[(Z\alpha)^2] \} \quad (2.22)$$

We will use this result to compare HFS energy levels calculation from different methods.

## 2.2 Calculation of the Hyperfine Structure term

### Perturbation approach to the Klein-Gordon equation

The hyperfine interaction in pionic atoms can be calculated taking into account the vector potential due to the nuclear magnetic moment in Eq. (2.8). Additional terms appear in the KG equation due to the presence of  $A_i(\mathbf{r})$ .

$$\mu^2 c^2 \Psi(x) = \left\{ \frac{1}{c^2} [i\hbar \partial_t + eV(r)]^2 + \hbar^2 \nabla^2 - \hat{W}(\mathbf{r}) \right\} \Psi(x), \quad (2.23)$$

with

$$\hat{W}(\mathbf{r}) = +ie\hbar [\partial_i A^i(\mathbf{r}) + A_i(\mathbf{r}) \partial^i] - e^2 A^i(\mathbf{r}) A_i(\mathbf{r}). \quad (2.24)$$

We can rewrite, Eq. (2.23) as:

$$\left\{ \frac{1}{c^2} [E + eV(r)]^2 + \hbar^2 \nabla^2 - \mu^2 c^2 - \hat{W}(\mathbf{r}) \right\} \varphi_{nl}(\mathbf{r}) = 0, \quad (2.25)$$

where

$$\Psi(x) = \exp(-iE^n t/\hbar) \varphi_{nl}(\mathbf{r}). \quad (2.26)$$

We note that in the case without perturbation  $\Psi_0(x) = \exp(-iE_0^nl/\hbar) \varphi_0^{nl}(\mathbf{r})$  is eigenfunction of the angular momentum operator. In this case the spherical coordinates the kinetic energy term can be written as:

$$\hbar^2 \nabla^2 \rightarrow \frac{\hbar^2}{r} \frac{\partial^2}{\partial r^2} r - \hbar^2 \frac{L^2}{r^2}, \quad (2.27)$$

where the dimensionless angular momentum operator is defined by  $\mathbf{L} = -i\mathbf{r} \times \vec{\nabla}$ .

If we want to solve this expression using perturbation methods, we have to apply a variable change to obtain an equation linear in the energy. For this propose, we consider the new variables  $E_r$ , the relativistic energy, and  $\mu_r$  the relativistic reduced mass [56]:

$$\begin{cases} E_r = \frac{E^2 - \mu^2 c^4}{2\mu_r c^2} \\ \mu_r = \frac{E}{c^2} \end{cases}. \quad (2.28)$$

It is interesting to note that  $\mu_r$  can be expressed as function of the relativistic parameter  $\gamma = (1 - v^2/c^2)^{-1/2}$ :  $\mu_r = \mu\gamma$ . With this new variables, Eq. (2.25) becomes:

$$\left[ E_r + eV(r) + \frac{e^2 V^2(r)}{2\mu_r c^2} + \frac{\hbar^2 \nabla^2}{2\mu_r} - \frac{W(\mathbf{r})}{2\mu_r} \right] \varphi_{nl}(\mathbf{r}) = 0. \quad (2.29)$$

This equation can be written in the standard form for the perturbation treatment.

$$\left[ \hat{H}_0(r) + \hat{W}(\mathbf{r}) \right] \varphi_{nl}(\mathbf{r}) = E_r^{nl} \varphi_{nl}(\mathbf{r}), \quad (2.30)$$

where

$$\hat{H}_0(r) = -\frac{\hbar^2 \nabla^2}{2\mu_r} - \frac{e^2 V^2(r)}{2\mu_r c^2} - eV(r) \quad (2.31)$$

is the zero order Hamiltonian<sup>4</sup> and

$$\hat{W}(\mathbf{r}) = \frac{+ie\hbar [\partial_i A^i(\mathbf{r}) + A_i(\mathbf{r}) \partial^i] + e^2 A^i(\mathbf{r}) A_i(\mathbf{r})}{2\mu_r} \quad (2.32)$$

is the perturbation operator. Considering the energy perturbation development  $E_r^{nl} = E_r^{nl(0)} + E_r^{nl(1)} + \dots$  we can calculate the first order energy correction:

$$E_r^{nl(1)} = \langle nl | \hat{W} | nl \rangle = \langle nl | \frac{\hat{W}}{2\mu_r} | nl \rangle, \quad (2.33)$$

where the average value of an generic operator  $O$  is defined by:

$$\langle nl | O | nl \rangle \equiv \langle O \rangle \equiv \int \varphi_{nl}^*(\mathbf{r}) O(\mathbf{r}) \varphi_{nl}(\mathbf{r}) d\mathbf{r}^3 \quad (2.34)$$

<sup>4</sup>With the Coulomb potential  $V(r) = \frac{Ze}{4\pi\epsilon_0} \frac{1}{r}$  the equation  $\hat{H}_0(r) \psi_{nl}(r) = E \psi_{nl}(r)$  provide the energies presented in Eq. (2.11).

and the functions  $\varphi_{nl}(\mathbf{r})$  are normalized to 1 (see Eq. 2.16). We can now calculate the correction for the real energy  $E = E_{(0)} + E_{(1)} + \dots$ . Using Eq. (2.28) we obtain:

$$E_{(1)} = \frac{c^2 \langle W \rangle}{E_{(0)} \left( 1 + \frac{\mu^2 c^4}{E_{(0)}^2} \right)}. \quad (2.35)$$

The next step is to evaluate the expected value of the operator  $\hat{W}$  for a generic KG wavefunction  $|nl\rangle$ . In the following section we will show how to perform this calculation.

### Perturbation term calculation

The expression for  $W(\mathbf{r})$  is derived using the multipole development of the vector potential  $\mathbf{A}(\mathbf{r})$ . This development is obtained in the Coulomb gauge following the procedure described in Ref. [42]. We neglect here the effect due to the finite size on the operator of the nucleus, i.e., the spatial distribution into the nucleus of the magnetic moment [41].  $\mathbf{A}(\mathbf{r})$  is decomposed as a sum of scalar products between  $\hat{\mathbf{M}}^k$ , spherical tensor operator of rank  $k$ , and vector spherical harmonics  $\mathbf{C}^{kk}$  (for a definition of vector spherical harmonics and their properties, see Refs. [42, 57, 58]):

$$\mathbf{A}(\mathbf{r}) = -i \frac{\mu_0}{4\pi} \sum_k \left( \frac{k+1}{k} \right)^{1/2} r^{-k-1} \mathbf{C}^{kk} \circ \hat{\mathbf{M}}^k. \quad (2.36)$$

The symbol “ $\circ$ ” indicate here the general scalar product between tensor operators in order to distinguish it from the ordinary scalar product between vectors “ $\cdot$ ”.  $\hat{\mathbf{M}}^k$  operate only on the nuclear part of the wave function.  $\mathbf{C}^{kk}$  and  $\hat{\mathbf{M}}^k$  are defined in spherical coordinate as <sup>5</sup>:

$$M_q^k = \mu_N \vec{\nabla}_N (r_N^k C_q^k) \cdot \left( \frac{2}{k+1} g \mathbf{l}_N \right), \quad (2.39)$$

$$\mathbf{C}_q^{kk} = [k(k+1)]^{-1/2} (\mathbf{l} C_q^k), \quad C_q^k = \left( \frac{4\pi}{2k+1} \right)^{1/2} Y_q^k(\theta, \phi). \quad (2.40)$$

In the formula above the operators designed with  $N$  act only on the nuclear wavefunction part. The operator  $\mathbf{l}$  acts only on  $C_q^k$ .  $\mu_N$  is the nuclear magneton:  $\mu_N = e\hbar/2m_p c$ . The hyperfine structure due to the magnetic dipole interaction is obtained by taking into account the first magnetic multipole term. In this case we have:

$$\mathbf{A}(\mathbf{r}) = -i \frac{\mu_0}{4\pi} \sqrt{2} r^{-2} \mathbf{C}^{11} \circ \hat{\mathbf{M}}^1. \quad (2.41)$$

<sup>5</sup>Spherical coordinates are defined by the unit vectors:

$$\begin{cases} \mathbf{e}_0 = \mathbf{e}_z \\ \mathbf{e}_{\pm} = \mp \frac{1}{\sqrt{2}} (\mathbf{e}_x \pm \mathbf{e}_y) \end{cases}. \quad (2.37)$$

The components of a generic vector  $\mathbf{v}$  in this base are:  $v_q = \mathbf{v} \cdot \mathbf{e}_q$ . The scalar product between two vectors  $\mathbf{v}$  and  $\mathbf{u}$ , is defined by:

$$\mathbf{v} \cdot \mathbf{u} = \sum_q (-1)^q v_q u_{-q} \equiv \sum_q v^q u_q. \quad (2.38)$$

Using this expression, we can rewrite the perturbation term  $W(\mathbf{r})$  from Eq. (2.23) as:

$$W(\mathbf{r}) = W_1(\mathbf{r}) + W_2(\mathbf{r}), \quad (2.42)$$

where

$$W_1(\mathbf{r}) = +i\hbar e [2A_i(\mathbf{r})\partial^i + [\partial_i, A^i(\mathbf{r})]], \text{ and } W_2(\mathbf{r}) = -e^2 A^i(\mathbf{r})A_i(\mathbf{r}). \quad (2.43)$$

$W_2$  is a second order correction and there is no corresponding operator in the Dirac equation.

We start to study the operator  $W_1$ . Firstly, we note that  $[\partial_i, A^i(\mathbf{r})] = -\vec{\nabla} \cdot \mathbf{A}(\mathbf{r}) = 0$  because we are using the Coulomb gauge. In this case we have:

$$\hat{W}_1(\mathbf{r}) = +2i\hbar e A_i(\mathbf{r})\partial^i = -2i\hbar e \mathbf{A}(\mathbf{r}) \cdot \vec{\nabla} = -e\mu_0\hbar \frac{\sqrt{2}}{2\pi} r^{-2} (\mathbf{C}^{11} \cdot \vec{\nabla}) \circ \hat{M}^1. \quad (2.44)$$

If we use the property of the spherical tensor [42, 57], we can demonstrate that:

$$\mathbf{C}_q^{11} \cdot \vec{\nabla} = -\frac{r^{-1}}{\sqrt{2}} L_q, \quad (2.45)$$

where  $L_q$  is the dimensionless angular momentum operator in spherical coordinates. The perturbation operator can be written as a scalar product in spherical coordinate of the operator  $\hat{T}$  acting on the orbital wavefunction, and the nuclear operator  $\hat{M}^1$ :

$$\hat{W}_1(\mathbf{r}) = \frac{e\mu_0\hbar}{2\pi} r^{-3} (\mathbf{L} \circ \hat{M}^1) = \hat{T} \circ \hat{M}^1 \quad \text{with} \quad T_q = \frac{e\mu_0\hbar}{2\pi} r^{-3} L_q. \quad (2.46)$$

The wavefunction is the results of the convolution product of the nuclear wavefunction  $|Im_I\rangle$  and the pion wavefunction  $|nlm\rangle$  and the total wavefunction is built using the angular momenta addition properties:

$$|nlm\rangle \otimes |Im_I\rangle \rightarrow |nIIFM\rangle, \quad (2.47)$$

where  $I$  and  $m_I$  are the spin of the nucleus and its z-axis component, respectively,  $F$  is quantum number relative to the total angular momentum of the system, and  $M$  is the quantum number relative to the z-axis component.  $F$  respects the triangular inequality  $|l - I| \leq F \leq |l + I|$  and  $M = m + m_I$ . The expected value of the operator  $\hat{W}_1$  can be evaluated using the scalar product properties in spherical coordinates [57, 59]:

$$\langle n'l'IIF'M' | \hat{W}_1 | nIIFM \rangle = (-1)^{l+I+F} \delta_{FF'} \delta_{MM'} \delta_{II'} \left\{ \begin{matrix} F & I & l' \\ 1 & l & I \end{matrix} \right\} \langle n'l' || T || nl \rangle \langle I || M^1 || I \rangle, \quad (2.48)$$

where  $\left\{ \begin{matrix} \phantom{F} & \phantom{I} & \phantom{l'} \\ \phantom{1} & \phantom{l} & \phantom{I} \end{matrix} \right\}$  indicate the Wigner 6-j symbol<sup>6</sup>. The reduced operator  $\langle n'l' || T || nl \rangle$  can be calculated by a particular choice of the quantum numbers  $m$  and  $q$  using the Wigner-Eckart theorem:

$$\langle n'l' || T || nl \rangle = \frac{(-1)^{l-m}}{\left( \begin{matrix} l & 1 & l' \\ -m & q & m' \end{matrix} \right)} \langle n'l'm' | T_q | nlm \rangle, \quad (2.49)$$

<sup>6</sup>For the definition of the 6-j symbol see Ref. [57, 59] and the website <http://mathworld.wolfram.com/Wigner6j-Symbol.html>.

where  $\begin{pmatrix} l & m & l' & m' \\ l & 1 & l & 1 \\ -1 & 0 & 1 & \end{pmatrix}$  indicate the Wigner 3-j symbol<sup>7</sup>.  $\langle n'l' || T || nl \rangle$  can be calculated with a particular value of  $m$ ,  $m'$  and  $q$ . In particular, except for the case  $l=0$ , we can use the values  $m = m' = 1$  and  $q = 0$ . In that case, the 3-j symbol in the denominator is always different to zero and:

$$\begin{aligned} \langle n'l' || T || nl \rangle &= \frac{(-1)^{l-1}}{\begin{pmatrix} l & 1 & l \\ -1 & 0 & 1 \end{pmatrix}} \langle n'l' 1 | T_0 | nl 1 \rangle = \\ &= \sqrt{l} \sqrt{l+1} \sqrt{2l+1} \frac{e\mu_0 \hbar}{2\pi} \langle n'l' 1 | r^{-3} L_z | nl 1 \rangle = \\ &= \delta_{ll'} \sqrt{l} \sqrt{l+1} \sqrt{2l+1} \frac{e\mu_0 \hbar}{2\pi} \langle n'l | r^{-3} | nl \rangle. \end{aligned} \quad (2.50)$$

In the case  $l' = 0$  (or  $l = 0$ ), the term  $\langle n'(l' = 0)(m' = 0) | T_q | nlm \rangle = 0$  for any value of  $q$ .

The nuclear operator can be related to the magnetic moment on the nucleus by  $\langle II | M_0^1 | II \rangle = \mu_I \mu_N$ .  $\mu_I$  is the nuclear dipole momentum in units of nuclear magneton ( $\mu_N = e\hbar/2m_p c$ ). We have:

$$\langle I || M^1 || I \rangle = \frac{\mu_I \mu_N}{\begin{pmatrix} I & 1 & I \\ -I & 0 & I \end{pmatrix}}. \quad (2.51)$$

Considering Eq. (2.46), the total expression for  $W_1(\mathbf{r})$  becomes:

$$\begin{aligned} \langle n'l' IF' M' | W_1 | nl IFM \rangle &= \\ &= \delta_{FF'} \delta_{MM'} \delta_{ll'} \mu_I \mu_N \frac{e\mu_0 \hbar}{2\pi} \frac{F(F+1) - I(I+1) - l(l+1)}{2I} \langle n'l | r^{-3} | nl \rangle. \end{aligned} \quad (2.52)$$

We note  $\langle nl IFM | W_1 | nl IFM \rangle = 0$  for  $l = 0$  (then  $I = F$ ), as expected.

To find the final expression of the HFS energy shift, we have to evaluated the contribution of the operator  $W_2(\mathbf{r}) = -e^2 A^i(\mathbf{r}) A_i(\mathbf{r})$  in the  $\langle W \rangle$  diagonal terms. Using Eq. (2.41), we have:

$$\langle nl IFM | W_2 | nl IFM \rangle = +2 \left( \frac{e\mu_0}{4\pi} \right)^2 \langle nl IFM | (r^{-2} \mathbf{C}^{11} \circ \hat{\mathbf{M}}^1) \cdot (r^{-2} \mathbf{C}^{11} \circ \hat{\mathbf{M}}^1) | nl IFM \rangle. \quad (2.53)$$

We are in presence of 3 independent scalar products: two scalar product between the tensor  $\mathbf{C}^{11}$  and the vector  $\hat{\mathbf{M}}^1$ , and the scalar product between the vectorial operators  $\mathbf{C}^{11} \circ \hat{\mathbf{M}}^1$ .

The “.” scalar product in  $W_2$  can be decomposed using the properties of the reduced matrices of a generic operator product  $X(K)$ , of rank  $K$ , between non-commutating tensor operators  $U(k)$  and  $V(k)$  of rank  $k$ . For our case, this scalar product correspond to a tensor product with  $K = 0$ , and  $k = 1$ :

$$X(0) = U(1) \cdot V(1) = (r^{-2} \mathbf{C}^{11} \circ \hat{\mathbf{M}}^1) \cdot (r^{-2} \mathbf{C}^{11} \circ \hat{\mathbf{M}}^1), \quad (2.54)$$

$$U(1) = V(1) = (r^{-2} \mathbf{C}^{11} \circ \hat{\mathbf{M}}^1). \quad (2.55)$$

<sup>7</sup>For the definition of the 3-j symbol see Ref. [57, 59] and the website <http://mathworld.wolfram.com/Wigner3j-Symbol.html>.

In this case we have [57]:

$$\langle nlIF||X(0)||nlIF\rangle = \sum_{F'} \left\{ \begin{array}{ccc} 1 & 1 & 0 \\ F & F & F' \end{array} \right\} \langle nlIF||U(1)||nlIF'\rangle \langle nlIF'||V(1)||nlIF\rangle. \quad (2.56)$$

$\mathbf{V}$  and  $\mathbf{U}$  are scalar products between commutative tensor operators, and its reduced matrix  $\langle F'||V||F\rangle$  can be calculate applying again the Wigner-Eckart theorem:

$$\langle nlIF'||V||nlIF\rangle = \frac{\langle nlIF'F'|V_0|nlIFF\rangle}{\left( \begin{array}{ccc} F' & 1 & F \\ -F' & 0 & F \end{array} \right)}. \quad (2.57)$$

The component  $q = 0$  of  $\mathbf{V}$  and  $\mathbf{U}$  is [58]:

$$V_0 = U_0 = r^{-2}(\mathbf{C}^{11} \circ \hat{\mathbf{M}}^1)_0 = r^{-2} \sum_q (-1)^q \frac{q}{\sqrt{2}} C_q^1 M_{-q}^1. \quad (2.58)$$

Using again the tensor operator properties, it is possible to decompose the  $V_0$  and  $U_0$  matrix elements:

$$\langle nlIF'F'|V_0|nlIFF\rangle = r^{-2}(-1)^{l+I+F} \delta_{FF'} \delta_{MM'} \left\{ \begin{array}{ccc} F & I & l \\ 1 & l & I \end{array} \right\} \langle nl||r^{-2} \frac{q}{\sqrt{2}} C_q^1||nl\rangle \langle I||M^1||I\rangle. \quad (2.59)$$

The reduced matrix  $\langle ||r^{-2}qC_q^1/\sqrt{2}||\rangle$  has to be the same for any choice of  $q$ . In fact, if we choose  $q = 1$  or  $0$  we have the same result. For  $q = 0$ , the reduced matrix is clearly equal to zero, and for  $q = 1$  as well<sup>8</sup>. This result implies that also the reduced matrices of  $U$  and  $V$  are always equal to zero. As a consequence, the diagonal elements  $\langle A^i(\mathbf{r})A_i(\mathbf{r})\rangle = 0$  for any wavefunction, i.e.,  $W_2$  doesn't contributes to the HFS energy shift.

Finally, the final expression for the HFS energy correction is:

$$E_{(1)}^{nlF} = \frac{\mu_I \mu_N \epsilon \mu_0 \hbar}{2\pi \mu \left( 1 + \frac{\mathcal{E}_0^{nl}}{\mu c^2} \right) \left[ 1 + \left( 1 + \frac{\mathcal{E}_0}{\mu c^2} \right)^{-2} \right]} \left[ \frac{F(F+1) - I(I+1) - l(l+1)}{2I} \right] \langle nl|r^{-3}|nl\rangle. \quad (2.61)$$

We remark that this formula is obtained by a perturbation approach of the KG equation. For this reason, all the relativistic effects are automatically included in Eq. (2.61).

For the expression of the HFS correction term in atomic units see Appendix 7.2.

<sup>8</sup> If we take  $q = 1$  we have  $\langle ||r^{-2}q/\sqrt{2}C_q^1||\rangle = \langle ||r^{-2}C^1||\rangle/\sqrt{2}$ . Using the reduced matrix of the spherical harmonics  $C_q^1$  we have:

$$\langle nl||r^{-2}C^1||nl\rangle = (-1)^l(2l+1) \left( \begin{array}{ccc} l & 1 & l \\ 0 & 0 & 0 \end{array} \right) \langle nl|r^{-2}|nl\rangle. \quad (2.60)$$

The value of the 3-j symbol is zero for any choice of  $l$ , i.e.,  $\langle ||r^{-2}C^1||\rangle = 0$ .

### Non-relativistic limit

In this section we will compare the precedent HFS relativistic formula with the non-relativistic expression calculated from the Schrödinger equation.

If we consider the hyperfine interaction between the nuclear magnetic moment  $\boldsymbol{\mu}_N$  and the orbital moment (dimensionless), we have to add the perturbation term in the non-relativistic Hamiltonian [60, 61]:

$$\hat{W}_{NR}(\mathbf{r}) = \frac{\mu_0 e \hbar}{4\pi\mu} \frac{1}{r^3} \mathbf{L} \cdot (\mu_I \boldsymbol{\mu}_N). \quad (2.62)$$

The first order correction to the energy  $E_1^{NR}$  can be calculated using the theory of time-independent perturbation:

$$E_1^{NR} = \langle \psi_{nl} | \hat{W}_{NR} | \psi_{nl} \rangle, \quad (2.63)$$

where  $|\psi_{nl}\rangle$  is the eigenfunction of Schrödinger equation without perturbations terms. Following the same procedure than in the previous sections, we obtain<sup>9</sup>

$$E_1^{NR} = \mu_I \mu_N \frac{e\mu_0 \hbar}{4\pi\mu} \frac{F(F+1) - I(I+1) - l(l+1)}{2I} \langle nl | r^{-3} | nl \rangle_{NR}. \quad (2.64)$$

This equation can be compared with (2.61): if  $c \rightarrow \infty$  (non-relativistic limit) Eq. (2.61) becomes equivalent to Eq. (2.64) as expected.

The term  $\langle nl | r^{-3} | nl \rangle_{NR}$  can be explicitly written as function of the wavefunction quantum numbers [60]:

$$\langle nl | r^{-3} | nl \rangle = \frac{(Z\alpha)^3}{n^3(l+1)(l+1/2)l} \frac{\mu^3 c^3}{\hbar^3} \quad (2.65)$$

With this equality Eq. (2.64) becomes:

$$\langle \hat{W}^{NR} \rangle_{NR} = \mu_I \mu_N \frac{e(Z\alpha)^3}{n^3} \frac{\mu_0 \mu^2 c^3}{4\pi \hbar^2} \frac{F(F+1) - I(I+1) - l(l+1)}{I(l+1)(2l+1)l} \quad (2.66)$$

## 2.3 Recoil corrections to the hyperfine structure energy term

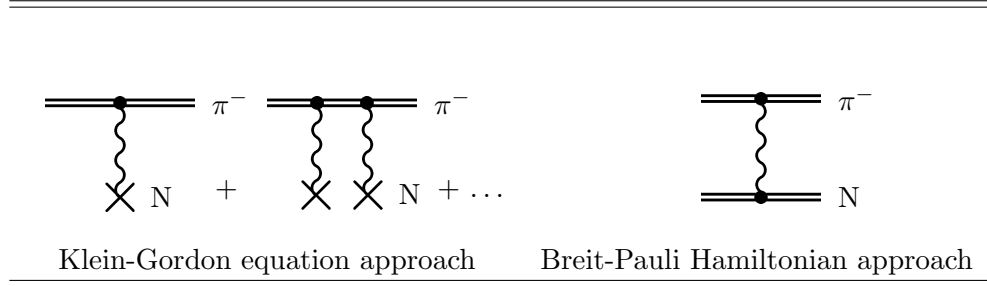
The Klein-Gordon equation can perfectly describe the one-body system of a spin-less point-like particle in presence of an external electromagnetic potential. A more accurate description for pionic atoms requires a two-body QED approach to the problem. The Schrödinger equation for hydrogen-like atoms can be reduced to one-body problem by a simple variable change using the reduces mass  $\mu$  instead the orbiting particle mass (electron, pion, ...). The QED treatment for a two-body system requires, in contrast, additional recoil corrections. These terms can be calculated by a perturbation approach using the Breit-Pauli Hamiltonian [60], which provides the exact mass dependence of the

<sup>9</sup>In Ref. [60] the equivalent formula in atomic units is

$$\hat{W}^{NR} = \mu_0 \mu_N g [F(F+1) - I(I+1) - l(l+1)] r^{-3},$$

where  $\hat{M}^1 = \mu_N g \mathbf{I}$ .  $\mu_N$  is the nuclear magneton,  $\mathbf{I}$  is the spin operator and  $g$  is the giromagnetic factor for the nucleus. With this definition  $gI = 1$  for a pure Dirac particle and about 2.8 for the proton (Ref. [60] page 109). This definition cause the absence of  $I$  in the denominator in the formula above compared to (2.64).

**Table 2.1** – Feynman diagrams relative to the Klein-Gordon equation approach and to the Breit-Pauli Hamiltonian approach.



contribution to the energy levels of order  $(Z\alpha)^4$ . In this case, the relativistic and recoil corrections are calculated as perturbation to the zero-order Hamiltonian  $\hat{H}_0$ , which have as the eigenvalues the energies  $E_0^n$ :

$$\hat{H}_0 = \frac{\mathbf{p}^2}{2\mu} - \frac{Ze^2}{r}, \quad (2.67)$$

the corresponding eigenvalues of which are:

$$E_0^n = -\frac{\mu(Z\alpha)^2}{2n^2}. \quad (2.68)$$

For these last two formulas, and the rest of the chapter, I use the natural units:  $c = \hbar = 1$ . Correction to  $E_0^n$  can be calculated by the addition of other perturbation terms to  $\hat{H}_0$  as the Breit-Pauli Hamiltonian additional operators and, eventually, the vacuum polarization operator, and the particle finite size term [16].

The Breit-Pauli Hamiltonian predictions take into account Feynman diagrams for two-body QED with an exchange of one photon between the two interacting particles, the pion and the nucleus in our case. In opposite, Klein-Gordon equation calculations take into account the exchange of one or more photons between the pion and fixed electromagnetic source (see Table 2.3).

In this section we will evaluate firstly the energy levels using the Breit-Pauli Hamiltonian. Secondly, we will compare the Breit-Pauli Hamiltonian results with the relativistic calculations. By the comparison of these predictions, we will determine the recoil correction for the KG equation.

### Breit-Pauli Hamiltonian for spin-0 and spin- $\frac{1}{2}$ particle

The expression of the Breit-Pauli Hamiltonian  $\hat{H}_{BP}^f$  can be found in classical textbooks [60, 62]. In particular, in the article of W.A. Barker and F.N. Glover [63] it can be found a generic expression of the Breit-Pauli Hamiltonian for two spin- $\frac{1}{2}$  particles with mass  $m$  and  $M$ , with charge  $-e$  and  $Ze$  and with anomalous magnetic moments  $k_I$  and  $k_{II}$ , respectively. The anomalous magnetic moment are defined by:

$$(\mu_N \mu_I)_I = \frac{-e\hbar}{2m}(1 + k_I) \quad (\mu_N \mu_I)_{II} = \frac{Ze\hbar}{2m}(1 + k_{II}). \quad (2.69)$$

This form of Hamiltonian is very useful because it can easily be adapted to an atomic system with a nucleus with an anomalous magnetic moment. The Hamiltonian is:

$$\hat{H}^f = \hat{H}_0^f + \hat{H}_{BP}^f, \quad \text{with} \quad \hat{H}_{BP}^f = \hat{H}_{RC}^f + \hat{H}_{SO}^f + \hat{H}_{SS}^f, \quad (2.70)$$

where  $\hat{H}_0^f$  is given in Eq. (2.67).  $\hat{H}_{RC}^f$  contains the first order relativistic and recoil corrections, and the transverse photon contribution.  $\hat{H}_{SO}^f$  and  $\hat{H}_{SS}^f$  contain the spin-orbit interaction and the spin-spin (and tensor) interaction, respectively:

$$\begin{aligned} \hat{H}_{RC}^f &= -\frac{\mathbf{p}^4}{8M^2} - \frac{\mathbf{p}^4}{8m^2} \\ &+ \frac{\pi e^2}{2M^2}(1+2k_I)\delta(\mathbf{r}) + \frac{\pi e^2}{2m^2}(1+2k_{II})\delta(\mathbf{r}) - \frac{e^2}{2mM} \frac{\mathbf{p}^2}{r} - \frac{e^2}{2mM} \mathbf{r} \left( \frac{\mathbf{p} \cdot \mathbf{r}}{r^3} \right) \cdot \mathbf{p}, \end{aligned} \quad (2.71)$$

$$\begin{aligned} \hat{H}_{SO}^f &= \frac{e^2}{2mM}(1+k_I)\boldsymbol{\sigma}_I \cdot \left( \frac{\mathbf{p} \times \mathbf{r}}{r^3} \right) + \frac{e^2}{4m^2}(1+2k_I)\boldsymbol{\sigma}_I \cdot \left( \frac{\mathbf{p} \times \mathbf{r}}{r^3} \right) \\ &+ \frac{e^2}{2mM}(1+k_{II})\boldsymbol{\sigma}_{II} \cdot \left( \frac{\mathbf{p} \times \mathbf{r}}{r^3} \right) + \frac{e^2}{4M^2}(1+2k_{II})\boldsymbol{\sigma}_{II} \cdot \left( \frac{\mathbf{p} \times \mathbf{r}}{r^3} \right), \end{aligned} \quad (2.72)$$

$$\hat{H}_{SS}^f = -\frac{e^2}{4mM}(1+k_I)(1+k_{II}) \left[ \frac{\boldsymbol{\sigma}_I \cdot \boldsymbol{\sigma}_{II}}{r^3} - \frac{3(\boldsymbol{\sigma}_I \cdot \mathbf{r})(\boldsymbol{\sigma}_{II} \cdot \mathbf{r})}{r^5} - \frac{8\pi}{3}\boldsymbol{\sigma}_I \cdot \boldsymbol{\sigma}_{II}\delta(\mathbf{r}) \right] \quad (2.73)$$

In this expressions we do not consider corrections higher that order  $\mu(Z\alpha)^4$ .  $\boldsymbol{\sigma}_I$  and  $\boldsymbol{\sigma}_{II}$  are the spin operator of the two particles (spin  $\mathbf{s}_i = \frac{1}{2}\boldsymbol{\sigma}_i$ ). The first two terms in Eq. (2.71) comes from the Taylor expansion on  $p^2/m$  of formula of the relativistic energy. The third and fourth represent the Darwin terms and they are valid for spin- $\frac{1}{2}$  particles. The last two terms come from the transverse photon contribution.

In the case of pionic atoms, the previous formulas become simpler because the pion has no spin. In fact, for spin-0 particles there is no Darwin term in the perturbation development of the Hamiltonian [16, 64, 65]. The Breit-Pauli Hamiltonian becomes:

$$\hat{H}_{BP} = \hat{H}_{RC} + \hat{H}_{SO}, \quad (2.74)$$

where

$$\hat{H}_{RC} = -\frac{\mathbf{p}^4}{8M^3} - \frac{\mathbf{p}^4}{8m^3} + \frac{\pi e^2}{2M^2}(1+2k)\delta(\mathbf{r}) - \frac{e^2}{2mM} \frac{\mathbf{p}^2}{r} - \frac{e^2}{2mM} \mathbf{r} \left( \frac{\mathbf{p} \cdot \mathbf{r}}{r^3} \right) \cdot \mathbf{p}, \quad (2.75)$$

$$\hat{H}_{SO} = \frac{e^2}{2mM}(1+k)\boldsymbol{\sigma} \cdot \left( \frac{\mathbf{p} \times \mathbf{r}}{r^3} \right) + \frac{e^2}{4M^2}(1+2k)\boldsymbol{\sigma} \cdot \left( \frac{\mathbf{p} \times \mathbf{r}}{r^3} \right). \quad (2.76)$$

$k$  and  $\boldsymbol{\sigma}$  are the anomalous magnetic moment and spin operator of the nucleus, respectively.

The recoil corrections terms are more apparent if we introduce the reduced mass in Eq. (2.75) using the relationship:

$$-\frac{1}{m^3} - \frac{1}{M^3} = -\frac{1}{\mu^3} + \frac{3}{m^2M} + \frac{3}{mM^2}. \quad (2.77)$$

In this case, we have:

$$\hat{H}_{RC} = -\frac{\mathbf{p}^4}{8\mu^3} + \frac{3\mathbf{p}^4}{8m^2M} + \frac{3\mathbf{p}^4}{8mM^2} + \frac{\pi e^2}{2M^2}(1+2k)\delta(\mathbf{r}) - \frac{e^2}{2mM} \frac{\mathbf{p}^2}{r} - \frac{e^2}{2mM} \mathbf{r} \left( \frac{\mathbf{p} \cdot \mathbf{r}}{r^3} \right) \cdot \mathbf{p} \quad (2.78)$$

Table 2.2 – Expectation operator values.

Operator	Expectation value
$\mathbf{p}^4$	$-\frac{3\mu^4\alpha^4}{n^4} + \frac{4\mu^4\alpha^4}{n^3(l+1/2)}$
$\frac{e^2\mathbf{p}^2}{r}$	$-\frac{\mu^3\alpha^4}{n^4} + \frac{2\mu^3\alpha^4}{n^3(l+1/2)}$
$\pi e^2\delta(\mathbf{r})$	$\frac{\mu^3\alpha^4}{n^3}\delta_{l,0}$
$e^2\mathbf{r}\left(\frac{\mathbf{p}\cdot\mathbf{r}}{r^3}\right)\cdot\mathbf{p}$	$\frac{\mu^3\alpha^4}{n^4} - \frac{\mu^3\alpha^4}{n^3(l+1/2)} + \frac{2\mu^3\alpha^4}{n^3}\delta_{l,0}$
$e^2\boldsymbol{\sigma}\cdot\left(\frac{\mathbf{p}\times\mathbf{r}}{r^3}\right)$	$-\frac{\mu^3\alpha^4}{n^3}\left(\frac{2}{F+1/2} - \frac{2}{l+1/2}\right)(1-\delta_{l,0})$

The perturbation term effects are calculated using the  $\Psi_{n,l,F}$  wavefunction expected values for the different operators resumed in Table 2.3: The relativistic energy corrections are:

$$\langle nlF|\hat{H}_{RC}|nlF\rangle = \frac{\mu(Z\alpha)^4}{n^3} \left[ \frac{3}{8n} - \frac{1}{2(l+1/2)} - \frac{\mu^2}{8nmM} + \frac{\mu^2}{mM}\delta_{l,0} + (1+2k)\frac{\mu^2}{2M^2}\delta_{l,0} \right]. \quad (2.79)$$

The hyperfine term is:

$$\langle nlF|\hat{H}_{SO}|nlF\rangle = -\frac{\mu(Z\alpha)^4}{n^3} \left( \frac{1}{F+1/2} - \frac{1}{l+1/2} \right) \left[ \frac{\mu^2(1+k)}{mM} + \frac{\mu^2(1+2k)}{2M^2} \right] (1-\delta_{l,0}). \quad (2.80)$$

Equations (2.79) and (2.80) can be obtained directly using the Bethe-Salpeter equation for a spin-0 and spin- $\frac{1}{2}$  particle as shown in Refs. [50, 51]. Starting from Ref. [63] we have in addition a clear dependency on the anomalous nuclear magnetic moment of the nucleus. The first two terms in Eq. (2.79) can be found by the  $Z\alpha$  development of the Klein-Gordon atomic energy formula (see Eq. (2.11)). The last term is the recoil correction due the Zitterbewegung term (Darwin term) of spin- $\frac{1}{2}$  nucleus and, in particular, it is absent for the nuclear spin equal to 0 or 1 [16, 64, 65]. For these nuclear spins, Eq. (2.79) becomes:

$$\langle nlF|\hat{H}_{RC}|nlF\rangle = \frac{\mu(Z\alpha)^4}{n^3} \left[ \frac{3}{8n} - \frac{1}{2(l+1/2)} - \frac{\mu^2}{8nmM} + \frac{\mu^2}{mM}\delta_{l,0} \right]. \quad (2.81)$$

We notice also that Eq. (2.80) is valid only for a nuclear spin equal to 1/2.

It is interesting re-write Eq. (2.79) and (2.80) using the equality

$$\frac{1}{\mu^2} = \frac{1}{m^2} + \frac{1}{M^2} + \frac{2}{mM}. \quad (2.82)$$

After some simplification we have:

$$\begin{aligned} \langle nlF | \hat{H}_{BP} | nlF \rangle = \frac{\mu(Z\alpha)^4}{n^3} & \left[ \frac{3}{8n} - \frac{1}{2(F+1/2)} - \frac{\mu^2}{8nmM} - \frac{\mu^2}{2m^2} \delta_{l,0} + k \frac{\mu^2}{M^2} \delta_{l,0} + \right. \\ & \left. - \left( \frac{1}{F+1/2} - \frac{1}{l+1/2} \right) \frac{\mu^2(1+2k)}{2M^2} (1 - \delta_{l,0}) \right]. \end{aligned} \quad (2.83)$$

In Eq. (2.83) the first two terms can be found by the  $Z\alpha$  development of the Dirac atomic energy formula (see Eq. (2.84)). The fourth term is due to the absence of the Zitterbewegung operator for the pion (more precisely, it is due to the absence of the compensation with the transverse photon contribution). The fifth term is due to the anomalous magnetic moment of the nucleus.

It is interesting to note than  $\hat{H}_0 + \hat{H}_{BP}$ , in the limit  $m \rightarrow \infty$  (infinite massive boson), reproduces the Dirac atomic energy formula:

$$E_{nlF}^D = \frac{\mu c^2}{\sqrt{1 + \frac{(Z\alpha)^2}{[n - F - 1/2 + \sqrt{(F+1/2)^2 - (Z\alpha)^2}]^2}}}. \quad (2.84)$$

In opposite, when  $M \rightarrow \infty$  (infinite massive fermion),  $\hat{H}_0 + \hat{H}_{BP}$  reproduces the Klein-Gordon atomic energy formula (Eq. (2.11)).

### Comparison between Klein-Gordon hyperfine structure and Breit-Pauli Hamiltonian

As remembered in the precedent paragraphs, the Klein-Gordon equation, valid for one-body problem, doesn't treat correctly the mass dependency. In opposite, the Breit-Pauli Hamiltonian provides the exact mass dependency up to the order  $(Z\alpha)^4$  but doesn't include relativistic corrections higher than order  $(Z\alpha)^4$ .

To clarify the mass dependency and the relativistic contributions we can compare the corrections provided by different methods using developments up to order  $(Z\alpha)^4$  for a spin-0 particle orbiting around a heavier spin- $\frac{1}{2}$  nucleus. The energy contributions calculated with the different methods are compared in Table 2.3, where we consider only the corrections to the leading energy  $\mathcal{E}_0 = \mu \frac{(Z\alpha)^2}{2n^2}$  up to order  $(Z\alpha)^4 (\mu^2/M^2)$ . The values in Table 2.3 have to be multiplied by  $\mu(Z\alpha)^4/n^3$  in order to obtain the energy correction.

In the formulas in Table 2.3 we wrote all the mass dependences using the reduced mass  $\mu$  and total mass  $\mathcal{M}$  of the system. To easily compare the different formula we wrote the nuclear magnetic moment as function of the nuclear anomalous magnetic moment  $k$ :

$$\mu_N \mu_I = \frac{Ze\hbar}{2M} (1+k), \quad (2.85)$$

where  $M$  is the mass of the nucleus. The nuclear magnetic moment can also write more conventionally using the giromagnetic factor  $g$ :

$$\mu_N \mu_I = \mu_N g I \quad (2.86)$$

**Table 2.3** – Comparison between the different approach for relativistic, recoil and HFS corrections for a bound system with a spin-0 particle and a spin- $\frac{1}{2}$  nucleus. The relativistic correction for the Klein-Gordon equation are obtained by the development of Eq. (2.11). In the table we didn't show the multiplicative factor  $\mu(Z\alpha)^4/n^3$  common to all the corrections.

	Relativistic corr.	Recoil corr.	HFS corr.
Non-rel. HFS Eq. (2.66)			$\left(\frac{\mu}{\mathcal{M}} + \frac{\mu^2}{\mathcal{M}^2}\right)(1+k)$ $\times \frac{F(F+1) - I(I+1) - l(l+1)}{2I(l+1)(2l+1)l}$
Breit-Pauli H Eqs. (2.79), (2.80) <sup>10</sup>	$\frac{3}{8n} - \frac{1}{2(l+1/2)}$	$-\frac{\mu}{8n\mathcal{M}} + \frac{\mu}{\mathcal{M}}\delta_{l,0}$ $+\frac{\mu^2}{\mathcal{M}^2}(1+2k)\delta_{l,0}$	$\left(\frac{\mu}{\mathcal{M}}(1+k) + \frac{\mu^2}{2\mathcal{M}^2}(1+2k)\right)$ $\times \frac{F(F+1) - I(I+1) - l(l+1)}{2I(l+1)(2l+1)l}$
KG + Rel. HFS Eqs. (2.11), (2.87)	$\frac{3}{8n} - \frac{1}{2(l+1/2)}$		$\left(\frac{\mu}{\mathcal{M}} + \frac{\mu^2}{\mathcal{M}^2}\right)(1+k)$ $\times \frac{F(F+1) - I(I+1) - l(l+1)}{2I(l+1)(2l+1)l}$

With this notation, the relativistic HFS Eq. (2.61) in natural units becomes:

$$E_{(1)}^{nlF} = (1+k) \frac{Z\alpha}{\mu M \left(1 + \frac{\mathcal{E}_0}{\mu}\right) \left[1 + \left(1 + \frac{\mathcal{E}_0}{\mu}\right)^{-2}\right]} \left[ \frac{F(F+1) - I(I+1) - l(l+1)}{I} \right] \langle nl|r^{-3}|nl \rangle. \quad (2.87)$$

In addition in Table 2.3 we used the relationship

$$\frac{\mu}{M} \simeq \frac{\mu}{\mathcal{M}} + \frac{\mu^2}{\mathcal{M}^2} + \mathcal{O}\left(\frac{\mu^3}{\mathcal{M}^3}\right) \quad \text{and} \quad \frac{\mu}{mM} = \frac{1}{\mathcal{M}}. \quad (2.88)$$

For the HFS correction with the Breit-Pauli Hamiltonian we used the equivalence of the angular dependence in Eq. (2.80) and (2.66) for a nuclear spin  $I = 1/2$ .

Comparing the different formulas we can notice a difference between the Breit-Pauli Hamiltonian and KG correction terms in the HFS contribution. More precisely, the Breit-Pauli Hamiltonian and the relativistic HFS energies differ by a term proportional to  $(Z\alpha)^4(\mu^2/\mathcal{M}^2)$ .

To take into account correctly the relativistic corrections, it is suitable to use the perturbation calculated with the KG equation. A correct treatment of the recoil requires the extra terms coming from the Breit-Pauli Hamiltonian, which can be identified as a recoil correction of the relativistic energy formula.

By a combination of the two methods, it is possible to obtain the HFS and recoil corrections up to order  $(Z\alpha)^5(\mu/\mathcal{M})$  including relativistic correction in all orders in  $(Z\alpha)$  for pionic atoms with a spin- $\frac{1}{2}$  nucleus:

$$E^{nlF} = E_{(0)}^{nl} + E_{\text{Rec}}^{nl} + E_{\text{HFS}}^{nlF} + E_{\text{HFS-Rec}}^{nlF}, \quad (2.90)$$

where  $E_{(0)}^{nl}$  is the KG energy (Eq. (2.11)).  $E_{\text{HFS}}^{nlF}$  is the hyperfine structure terms given in Eq. (2.87).  $E_{\text{Rec}}^{nl}$  and  $E_{\text{HFS-Rec}}^{nlF}$  are the recoil correction deduced from the comparison with the Breit-Pauli Hamiltonian results:

$$E_{\text{Rec}}^{nl} = \mu \frac{(Z\alpha)^4}{n^3} \left[ -\frac{\mu}{8n\mathcal{M}} + \frac{\mu}{\mathcal{M}} \delta_{l,0} + \frac{\mu^2}{\mathcal{M}^2} (1+2k) \delta_{l,0} \right], \quad (2.91)$$

$$E_{\text{HFS}}^{nlF} = (1+k) \frac{Z\alpha}{\mu M (1 + \frac{\varepsilon_0}{\mu}) \left[ 1 + (1 + \frac{\varepsilon_0}{\mu})^{-2} \right]} \left[ \frac{F(F+1) - I(I+1) - l(l+1)}{I} \right] \langle n'l | r^{-3} | nl \rangle, \quad (2.92)$$

$$E_{\text{HFS-Rec}}^{nlF} = -\mu \frac{(Z\alpha)^4}{n^3} \frac{\mu^2}{2\mathcal{M}^2} \frac{F(F+1) - I(I+1) - l(l+1)}{2I(l+1)(2l+1)l}. \quad (2.93)$$

As written before, for a spin-0 or spin-1 nuclei the Darwin term is not present [16, 64, 65] and  $E_{\text{Rec}}^{nl}$  becomes:

$$E_{\text{Rec}}^{nl} = \mu \frac{(Z\alpha)^4}{n^3} \left[ -\frac{\mu}{8n\mathcal{M}} + \frac{\mu}{\mathcal{M}} \delta_{l,0} \right] \quad (2.94)$$

For other nuclear spins, the equivalent of the Darwin term is unknown at present, as it is unknown the recoil correction to HFS for nuclear spins different to 1/2.

The precedent corrections reproduce, for a spin- $\frac{1}{2}$  nucleus, the result contained in Ref. [51], up to order  $(Z\alpha)^5(\mu^2/\mathcal{M}^2)$ , which is obtained using the Bethe-Salpeter equation. In addition, following the indication of Ref. [63], Eq. (2.90) takes into account the anomalous momentum of the nucleus reproducing the results contained in Ref. [50], which also uses the Bethe-Salpeter equation. Furthermore, as written below, the relativistic corrections are automatically included because we used the Klein-Gordon equation. For this reason, Eq. (2.90) is particularly adapted for pionic atoms with  $Z \gg 1$ . For higher values of  $Z$ , relativistic corrections become more important. In contrast, due to the heavier nuclear mass, recoil corrections are smaller. The important feature of Eq. (2.90) is the simple dependence on the spin value of the nucleus. The nuclear spin is simply taken into account by the use of the appropriate value of  $I$  and  $\mu_N$ . In contrast, the formulas in Refs. [50, 51] are valid only for a spin- $\frac{1}{2}$  nucleus.

## 2.4 Numerical evaluation for some pionic atoms

In this section, I present the HFS calculation for a selected choice of pionic atoms. In addition, we will study the Z-dependence on the hyperfine splitting for stable atoms. In particular, I will show detailed calculations for some of interest for experiment in pionic hydrogen, deuterium and nitrogen. The eigenfunction and eigenvalue for a spin-0 particle are calculated resolving numerically the Klein-Gordon differential equation.

The energy values are calculated using a Fortran90 code developed by P. Indelicato and J.-P. Desclaux [27, 28, 29]. This code takes into account, in addition to the HFS contributions, other important corrections, such as the vacuum polarization, the self-energy of the pion, the finite size of the nucleus and of the pion, etc.

**Table 2.4** – Energy (in eV) contribution for the selected levels in pionic hydrogen. The first error take into account the accuracy of the proton radius and the evaluation of the next order QED corrections. The second is due to the accuracy of the pion mass ( $\pm 2.5$  ppm).

	1s	2p	3p	4p	2p-1s	3p-1s	4p-1s
Coulomb	-3235.0520	-808.7423	-359.4409	-202.1853	2426.3097	2875.6111	3032.8667
Self Energy	0.0015	0.0000	0.0000	0.0000	-0.0015	-0.0015	-0.0015
Vac. Pol. (Uehling)	-3.2408	-0.0358	-0.0114	-0.0049	3.2050	3.2294	3.2359
Vac. Pol. Wichman-Kroll	0.0000	0.0000	0.0000	0.0000	0.0000	0.0000	0.0000
Vac. Pol. Loop after loop	-0.0049	0.0000	0.0000	0.0000	0.0049	0.0049	0.0049
Vac. Pol. Källén-Sabry	-0.0244	-0.0003	-0.0001	0.0000	0.0240	0.0243	0.0243
Relativistic Recoil	0.0541	-0.0003	-0.0001	0.0000	-0.0544	-0.0541	-0.0541
Total	-3238.2665	-808.7787	-359.4524	-202.1903	2429.4878	2878.8141	3036.0763
Hyperfine structure							
F=1/2	0	-0.0052	-0.0015	-0.0006			
F=3/2	0	0.0026	0.0008	0.0003			
HFS Recoil F=1/2	0	0.0001	0.0000	0.0000			
HFS Recoil F=3/2	0	0.0000	0.0000	0.0000			
Splitting	0	0.0077	0.0023	0.0010			
Shift (statistical population)					0.0000	0.0000	0.0000
Error					$\pm 0.0012$	$\pm 0.0012$	$\pm 0.0012$
Error due to the pion mass					$\pm 0.0062$	$\pm 0.0072$	$\pm 0.0076$

**Table 2.5** – Hyperfine transitions energy and transition rate in pionic hydrogen.

Transition	F-F'	Trans. rate ( $s^{-1}$ )	Trans. E (eV)	Shift (eV)	HFS rec. corr. (eV)
$2p \rightarrow 1s$	1/2-1/2	$4.99 \times 10^{10}$	2429.48270	-0.00519	0.00009
	3/2-1/2	$9.98 \times 10^{10}$	2429.49035	0.00260	-0.00005
$3p \rightarrow 1s$	1/2-1/2	$1.33 \times 10^{10}$	2878.81255	-0.00154	0.00003
	3/2-1/2	$2.66 \times 10^{10}$	2878.81482	0.00077	-0.00001
$4p \rightarrow 1s$	1/2-1/2	$0.54 \times 10^{10}$	3036.07562	-0.00065	0.00001
	3/2-1/2	$1.08 \times 10^{10}$	3036.07658	0.00032	-0.00001

### Calculation of the energy levels of pionic hydrogen and deuterium

One of the important applications of the formulas deduced in the previous sections is the calculation of the HFS in pionic hydrogen and deuterium. These atomic systems are particularly interesting because they allow to measure the strong interaction effects between pion and proton, and pion and deuteron in a simple bound system [5, 6]. In the pionic hydrogen and deuterium ground state, strong interaction shows up as an energy shift and a line broadening in the  $np \rightarrow 1s$  transitions. For  $p$ -states or higher values of  $l$ , these effects are considerably reduced. The evaluation of the shift requires Quantum Electrodynamics (QED) theoretical calculation of the  $1s$  and  $np$  levels in the ideal case of the presence of the electromagnetic interaction only.

The most recent evaluation of the strong interaction shift in pionic hydrogen can be found in Ref. [66] and is:

$$\epsilon_{1s} = (7.120 \pm 0.008 \begin{smallmatrix} +0.008 \\ -0.009 \end{smallmatrix}) \text{ eV}. \quad (2.95)$$

The first error is the statistical error and the second is due to systematic effects. The shift  $\epsilon_{1s}$  is obtained by subtraction of the older evaluation of the  $3p \rightarrow 1s$  QED transition energy [67]:  $E_{QED} = (2878.808 \pm 0.006) \text{ eV}$ . The systematic errors are dominated by the uncertainty in the theoretical prediction, which is due to the accuracy of the theoretical evaluation. The error of the pion mass measurement doesn't contribute because the energy of the  $3p \rightarrow 1s$  transition is measured taking as reference the pionic oxygen  $6 \rightarrow 5$  transition.

To increase the theoretical accuracy, the calculation of the HFS and the recoil correction evaluation were necessary.

The HFS causes a splitting of the transition line. As shown in Table 2.5 and 2.7, this splitting is on the order of some meV, smaller than the resolution of the best available X-ray spectrometer, which is around 0.4 eV in this energy range (see Chapter 3 for details). However, due to the differences in the transition probabilities and populations of the HFS sub-levels, the main value of the transition line can be shifted. For this reason we calculated, in addition to the HFS splitting, the transition probability for the different  $np$  sub-level states to evaluate a possible shift. We assume a statistical population of the sub-levels proportional to their multiplicity:  $2F + 1$  and the transition probabilities are calculated using the non-relativistic formula shown in Appendix 7.2. The relativistic correction to the transition probabilities is estimated to be small. The difference between

**Table 2.6** – Energy (in eV) contribution for the selected levels in pionic deuterium. The first error take into account the accuracy of the deuteron radius and the evaluation of the next order QED corrections. The second is due to the accuracy of the pion mass ( $\pm 2.5$  ppm).

	1s	2p	3p	4p	2p-1s	3p-1s	4p-1s
Coulomb	-3458.4709	-864.6996	-384.3108	-216.1746	2593.7712	3074.1601	3242.2963
Self Energy	0.0018	0.0000	0.0000	0.0000	-0.0018	-0.0018	-0.0018
Vac. Pol. (Uehling)	-3.7292	-0.0453	-0.0143	-0.0062	3.6839	3.7149	3.7230
Vac. Pol. Wichman-Kroll	0.0000	0.0000	0.0000	0.0000	0.0000	0.0000	0.0000
Vac. Pol. Loop after loop	-0.0058	0.0000	0.0000	0.0000	0.0057	0.0058	0.0058
Vac. Pol. Källén-Sabry	-0.0279	-0.0004	-0.0001	-0.0001	0.0275	0.0278	0.0279
Relativistic Recoil	0.0208	-0.0002	0.0000	0.0000	-0.0210	-0.0208	-0.0208
Total	-3462.2111	-864.7455	-384.3253	-216.1808	2597.4656	3077.8859	3246.0303
Hyperfine structure							
F=0	0	-0.0010	-0.0003	-0.0001			
F=1	0	-0.0005	-0.0001	-0.0001			
F=2	0	0.0005	0.0001	0.0001			
Splitting F=2-0	0	0.0015	0.0004	0.0002			
Shift (statistical population)					0.0000	0.0000	0.0000
Error					$\pm 0.0014$	$\pm 0.0014$	$\pm 0.0014$
Error due to the pion mass					$\pm 0.0065$	$\pm 0.0077$	$\pm 0.0081$

**Table 2.7** – Hyperfine transition energies and transition rate in pionic deuterium. The error due to the unevaluated HFS recoil correction is presented in the last column.

$2p \rightarrow 1s$	0-1	$2.03 \times 10^{10}$	2597.46463	0.00099	0.00003
	1-1	$1.52 \times 10^{10}$	2597.46513	0.00050	0.00002
	2-1	$10.16 \times 10^{10}$	2597.46612	-0.00050	-0.00002
$3p \rightarrow 1s$	0-1	$0.54 \times 10^{10}$	3077.88557	0.00029	0.00001
	1-1	$0.41 \times 10^{10}$	3077.88571	0.00015	0.00000
	2-1	$2.71 \times 10^{10}$	3077.88601	-0.00015	0.00000
$4p \rightarrow 1s$	0-1	$0.22 \times 10^{10}$	3246.03019	0.00012	0.00000
	1-1	$0.17 \times 10^{10}$	3246.03026	0.00006	0.00000
	2-1	$1.10 \times 10^{10}$	3246.03038	-0.00006	0.00000

non-relativistic calculation and relativistic ones valid for fermions are, in fact, less than 1% [67].

Due to the spin-0 nature of the pion, the  $ns$  states have no splitting because there is no fine structure ( $j = 0$ ) and there is one possible eigenvalue of the operator  $\mathbf{F} = \mathbf{L} + \mathbf{I}$  ( $F = I$ ). For this reason, transition to  $ns$  levels are not affected by HFS line splitting because there is a complete compensation between the transition probability values and the statistical population effect (see Tables 2.4 and 2.6).

A detailed evaluation of the energy levels is presented in Tables 2.5 and 2.7. In Table 2.8 the evaluation of the  $3p \rightarrow 1s$  transition energy is compared, to the older evaluation presented in Ref. [68] and to the precision of the experimental measurement.

For this calculation we used the world average pion mass from Ref. [69]. References [69, 70] have been used for mass, magnetic moment and radius values of the nucleus. The *Coulomb* term in the table includes the non-relativistic recoil correction using the reduced mass on the KG equation. The pion and nucleus finite size contribution are also included in this term. About the QED corrections, the vacuum polarization contribution are evaluated including the Ueling potential, *Ueling* and *Loop after Loop* in Table 2.4, in the Coulomb potential in the non-perturbed KG equation [28], and calculating and higher order correction: *Wichman-Kroll* and *Källén-Sabry* [71, 72] as perturbation. The self-energy is calculated using the formula in Ref. [73] including the recoil correction. A new evaluation of this term is in progress in the group.

The calculations presented in this section do not take into account higher QED corrections as second order recoil effects and feynman diagrams with vacuum polarization **and** self-energy (see Fig. 2.1). The contribution from these terms has been evaluated considering the formula for a spin- $\frac{1}{2}$  orbiting particle. Higher order of recoil correction has been evaluated about 0.4 meV for the  $np \rightarrow 1s$  transitions (Fig. 2.1, top)[74]. Vacuum polarization and self-energy mixed diagrams (Fig. 2.1, bottom) contribute with a correction in the order of 50  $\mu\text{eV}$  for the diagram with the vacuum polarization loop in the nuclear photon line [75], and 5  $\mu\text{eV}$  for the diagram with the vacuum polarization loop inside the self-energy loop [16]. However, the largest systematic error contribution of these calculations is due to the error of the proton and deuteron size [70], which introduce an error of 1.1 meV for the pionic hydrogen  $np \rightarrow 1s$  transitions and 1.3 meV for the pionic deuterium  $np \rightarrow 1s$  transitions. The accuracy of the numerical calculation has been evaluated about

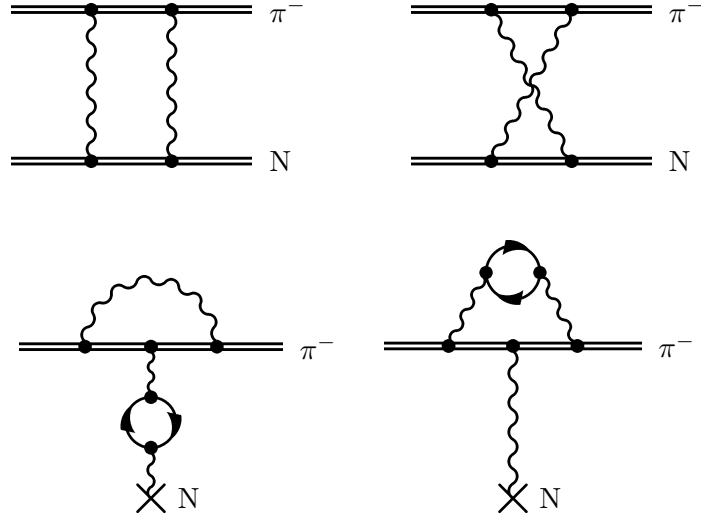


**Figure 2.1** – Diagrams relative to the unevaluated QED contributions: second order recoil correction (up), and vacuum polarization and self-energy mixed diagrams (down). Their effects are estimated using the available formulas for spin- $\frac{1}{2}$  particles.

few tens of  $\mu\text{eV}$ . From this new evaluation of the QED transition energies we obtain a new evaluation of the strong interaction shift of the ground state:

$$\epsilon_{1s} = (7.114 \pm 0.008 \begin{smallmatrix} +0.005 \\ -0.007 \end{smallmatrix}) \text{ eV}. \quad (2.96)$$

that correspond to a reduction of a factor of about 30% on the systematic effects (the first error is the statistical error and the second is due to systematic effects).

For pionic deuterium it was not possible to evaluate the recoil correction for the HFS because the nuclear spin is equal to 1 and the correspondent formula for the correction is unknown. However it is possible to evaluate the contribution using the formula valid for spin- $\frac{1}{2}$  nuclei. The corrections are in the order of some tens of  $\mu\text{eV}$  (see Table 2.7).

### Calculation of the energy levels of pionic nitrogen

The transitions between  $n = 5$  and  $n = 4$  in pionic nitrogen are interesting because they are used for the precise measurement of the pion mass [3, 7, 8]. For these transitions, strong interaction effects between pion and nucleus are negligible, and the level energies are directly dependent to the reduced mass of the atom (see Sec. 4.4). The precise measurement of  $5g \rightarrow 4f$  transition and the QED predictions allow for the measurement of the pion mass.

The accuracy of the theoretical calculation has to be better than 1 ppm and, in particular, the evaluation of the HFS shift is required. The measurement of the  $5g \rightarrow 4f$  and  $5f \rightarrow 4d$  transitions enables also to test the Klein-Gordon equation, i.e., the Relativistic Quantum Mechanics predictions for a spin-0 particle (for more detail, see Chapter 4). As for the pionic hydrogen case, the HFS in pionic nitrogen can not be resolved with the actual X-ray spectrometers. But contrary to the  $np \rightarrow 1s$ , the  $5 \rightarrow 4$  transitions can be effected by a line shift due to the presence of several HFS sub-levels in the final state of the transition.

In this section we study in particular the transitions  $5g \rightarrow 4f$  and  $5f \rightarrow 4d$ , which are the more relevant for the interpretation of the experimental data ( $5d \rightarrow 4p$  is already too

**Table 2.8** – Comparison between the previously estimation and this work. The calculation are obtained using the pion mass world average [69]. All the energies are in eV.

	F=1/2	F=3/2	Schröder <i>et al.</i> [68]
Coulomb	2875.6111	2875.6111	2875.613
Self-energy	-0.0015	-0.0015	
Vac. Pol (Uelhing)	3.2294	3.2294	3.235
Higher order Uelhing	0.0000	0.0000	
Wichmann and Kroll	0.0049	0.0049	
Källén-Sabry	0.0243	0.0243	
Rel. Recoil+Darwin term	-0.0541	-0.0541	-0.047
Hyperfine Structure	-0.0015	0.0008	
Hyperfine Structure Recoil	0.0000	0.0000	
$\alpha^3$ VP corrections			0.018
Vertex			-0.007
Pion recoil			-0.004
Total energy	2878.8126(12)	2878.8148(12)	2878.808(8)
Experiement	2885.928(8)		
Differences	7.1154	7.1132	7.120

sensitive to the strong interaction effects as explained in Sec. 4.4). For these calculations we used the nitrogen nuclear mass value from Ref. [76]. In Table 2.9, all the energy contributions to these transition are shown. As expected, we observe that the recoil corrections are, in this case, considerably smaller than in the pionic hydrogen case. The QED effects are also reduced because we are looking to levels with a higher value of the principal quantum number  $n$ , which reduce considerably these effects even when we have an higher value of  $Z$  ( $Z=7$ ).

In Fig. 2.2 and in Table 2.4 I represent all the HFS transitions with the associated transition rates. Using these values, it is possible to calculate the expected shift for the transitions. For transitions  $5g \rightarrow 4f$  and  $5f \rightarrow 4d$  we obtain 0.27 and 0.85 eV, respectively. These values correspond to a correction to the pion mass between 0.06 and 0.21 ppm. The accurate description of the pion mass measurement is presented in Chapter 4

The accuracy of these calculations is limited by the Feynman diagram contributions we do not take into account. The largest contribution comes from the unevaluated diagram with the vacuum polarization loop in the nuclear photon line [75], the associated correction is estimated in the order of 1 meV for pionic nitrogen  $5 \rightarrow 4$  transitions. As for the pionic deuterium, it was not possible to calculate the recoil correction to the HFS for pionic nitrogen, and the introduced error is in the order of few tens of  $\mu\text{eV}$  (see Table 2.4).

### General behavior of the hyperfine structure correction over $Z$

The relativistic effects in the HFS formula (Eq. (2.61)) are very small for low values of  $Z$ . As we saw in Sec. 2.3, the relativistic HFS expression, differs from the non-relativistic one by terms of order  $(Z\alpha)^6$ .

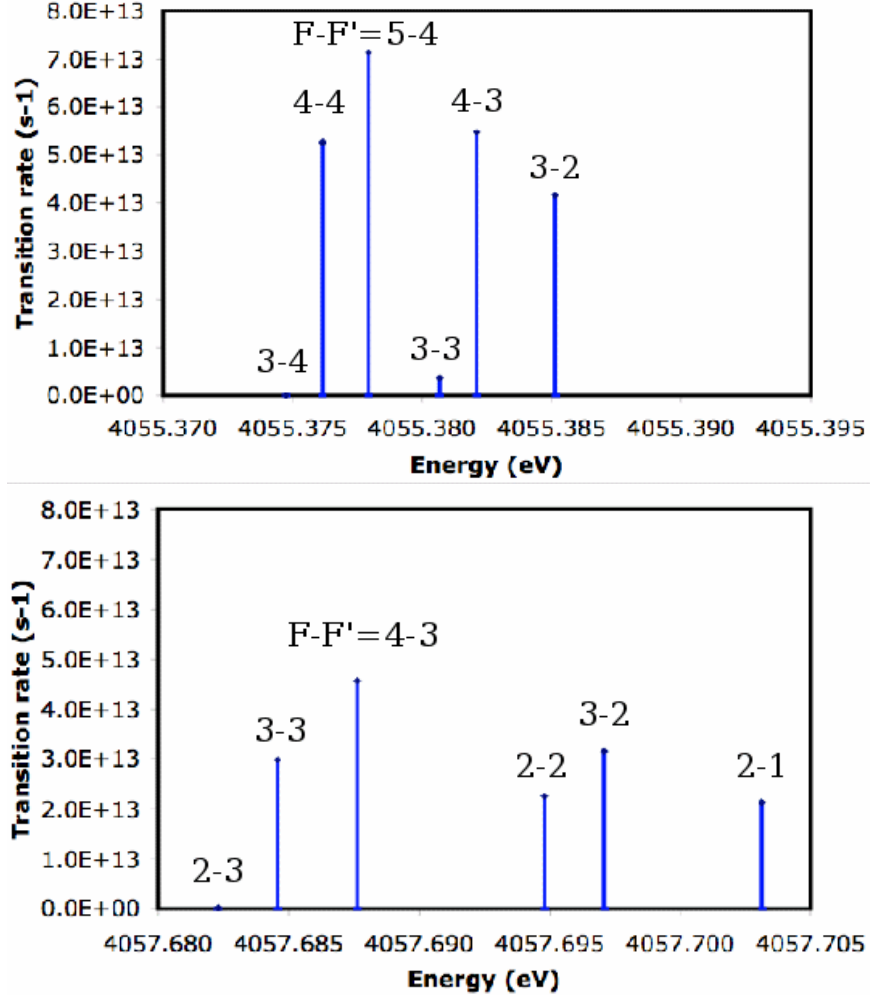


**Figure 2.2** – Visualization of the HFS transition with the relative value of the transition probability for  $5g \rightarrow 4f$  transition (top) and  $5f \rightarrow 4d$  transition (bottom).

In particular, using Eq. (2.85) and (2.66), we note that for the non-relativistic case, the HFS splitting normalized to the binding energy and to the nuclear magnetic moment, depends linearly on  $Z\alpha$ . Any deviation to this linear dependence in the Klein-Gordon HFS can be caused only by relativistic effects.

To study the behavior of the normalized HFS splitting  $(E_{F=3/2}^{2p} - E_{F=3/2}^{2p})/(\mathcal{E}_0\mu_I)$  for the relativistic case, we calculated the HFS for a selected choice of pionic atoms with a stable nucleus of spin 1/2. The results are summarized in Table 2.4. For these calculations we used the nuclear mass values from Ref. [76], the nuclear radii from [70, 77] and the nuclear magnetic moments from Ref. [78].

For higher  $Z$  values the non-linear dependence on  $Z\alpha$  appears as we can see in Fig. 2.4. This non-linearity comes from the two different parts of Eq. (2.61): the non-trivial dependency on  $\mathcal{E}_0$  in the denominator and the expectation value  $\langle nl|r^{-3}|nl\rangle$ .

I remind that the HFS evaluation didn't take into account the magnetic moment dis-

**Table 2.9** – Energy (in eV) contribution for the selected levels in pionic nitrogen. The first error take into account the evaluation of the next order QED corrections. The second is due to the accuracy of the pion mass ( $\pm 2.5$  ppm).

	5g	5f	4f	4d	5g-4f	5f-4d
Coulomb	-7206.7927	-7207.0315	-11260.9107	-11261.7504	4054.1180	4054.7189
Self Energy	0.0000	0.0001	0.0001	0.0003	-0.0001	-0.0003
Vac. Pol. (Uehling)	-0.2237	-0.7544	-1.4722	-3.7013	1.2485	2.9470
Vac. Pol. Wichman-Kroll	0.0002	0.0004	0.0009	0.0014	-0.0007	-0.0010
Vac. Pol. two-loop Uehling	-0.0001	-0.0005	-0.0009	-0.0042	0.0008	0.0038
Vac. Pol. Källén-Sabry	-0.0021	-0.0068	-0.0137	-0.0293	0.0116	0.0225
Relativistic Recoil	-0.0020	-0.0020	-0.0048	-0.0048	0.0028	0.0028
HFS Shift					-0.0008	-0.0022
Total	-7207.0203	-7207.7947	-11262.4013	-11265.4883	4055.3801	4057.6914
Error					$\pm 0.0011$	$\pm 0.0011$
Error due to the pion mass					$\pm 0.010$	$\pm 0.010$

**Table 2.10** – Hyperfine transition energies and transition rate in pionic nitrogen. The error due to the unevaluated HFS recoil correction is presented in the last column.

Transition	F-F'	Trans. rate ( $s^{-1}$ )	Trans. E (eV)	Shift (eV)	Error (eV)
$5f \rightarrow 4d$	4-3	$4.57 \times 10^{13}$	4057.68762	-0.00605	0.00004
	3-2	$3.16 \times 10^{13}$	4057.69708	0.00341	-0.00002
	3-3	$2.98 \times 10^{13}$	4057.68457	-0.00910	0.00006
	2-1	$2.13 \times 10^{13}$	4057.70313	0.00946	-0.00006
	2-2	$2.25 \times 10^{13}$	4057.69479	0.00112	-0.00001
	2-3	$0.01 \times 10^{13}$	4057.68229	-0.01138	0.00007
$5g \rightarrow 4f$	5-4	$7.13 \times 10^{13}$	4055.37793	-0.00304	0.00002
	4-3	$5.47 \times 10^{13}$	4055.38210	0.00113	-0.00001
	4-4	$5.27 \times 10^{13}$	4055.37616	-0.00481	0.00003
	3-2	$4.17 \times 10^{13}$	4055.38514	0.00417	-0.00003
	3-3	$0.36 \times 10^{13}$	4055.38068	-0.00029	0.00000
	3-4	$0.01 \times 10^{13}$	4055.37474	-0.00623	0.00004

**Table 2.11** – HFS splitting values between the levels  $F=1/2$  and  $F=3/2$  in the  $2p$  orbital for elements with spin  $\frac{1}{2}$  nucleus

Element	Z	$2p$ energy (eV)	HFS splitting (eV)
$H$	1	-808.7787	0.0078
${}^3He$	2	-3541.2220	-0.0797
${}^{13}C$	6	-33118.8146	0.5492
${}^{15}N$	7	-45162.7278	-0.3531
${}^{19}F$	9	-74865.0787	7.0101
${}^{31}P$	15	-209040.5553	14.1428
${}^{57}Fe$	26	-631953.8459	5.9258
${}^{77}Se$	34	-1083389.6254	77.0744
${}^{89}Y$	39	-1083389.6254	-29.3757
${}^{107}Ag$	47	-2066710.1251	-40.1706
${}^{129}Xe$	54	-2714230.8480	-390.2880
${}^{183}W$	74	-4931103.2073	116.3326
${}^{202}Pb$	82	-5940088.8608	705.0580

tribution inside the nucleus, which could contribute significantly to the HFS splitting, especially for high values of  $Z$ .

## 2.5 Conclusions and perspectives

In this chapter we demonstrate a new perturbation method for the Klein-Gordon equation. In particular we applied this technique to the calculation of the hyperfine structure of pionic atoms. The major advantage of this method is the simple dependence of the formulas on the nuclear spin, which reproduces for  $c \rightarrow \infty$  the non-relativistic results. Moreover, the

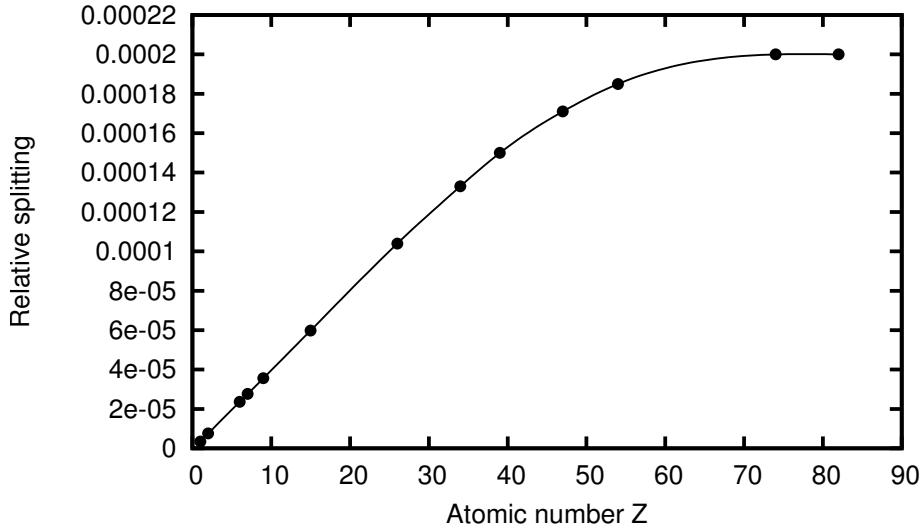


**Figure 2.3** – Value of relative splitting  $(E_{F=3/2}^{2p} - E_{F=3/2}^{2p})/(\mathcal{E}_0\mu_I)$  for different values of  $Z$ . Nuclear masses, radii and magnetic moments values have been obtained from Ref. [76, 77, 70, 78].

relativistic effects are naturally included in the expression because we used the Klein-Gordon equation. Nevertheless, the calculation of the relativistic recoil corrections was necessary due to the high value of the pion-nucleus mass ratio for low  $Z$  atoms. Using the Breit-Pauli Hamiltonian, it was possible to calculate the exact mass dependence up to order  $(Z\alpha)^4$  for atoms with a spin- $\frac{1}{2}$  nuclei. These recoil corrections have been confirmed by the Bethe-Salpeter predictions [50, 51]. For spin-0 and spin-1 nuclei we could evaluate only partially the recoil correction, without the possibility to calculate the recoil correction to the hyperfine term.

A natural development of the formalism shown in the previous sections will be the introduction of the pion and the nucleus finite size in the HFS formula. Eq. (2.36) and (2.41) are in fact valid only for a magnetic moment for a point-like nucleus. A correct approach to the problem requires a modified expression of the vector potential to include the spatial distribution of the nuclear magnetic moment that leads the Bohr-Weisskopf correction and enables to take into account the hyperfine anomaly in pionic atoms [41, 42].

For low  $Z$  atoms, the electric quadrupole interaction effect is negligible. For this reason in this chapter we took into account only the first term of the multipole expansion of the vector potential. However, for heavier nuclei this term is important due to the relevant nuclear quadrupole moment. As proposed in Ref. [44], the quadrupole splitting measurement in pionic atoms allows to measure the quadrupole moment of heavy nuclei [39, 45]. Using the formulas presented in this chapter, it is possible to calculate the quadrupole splitting by multipole expansion of the Coulomb potential. Compared to the method proposed in Ref. [44], the formalism developed in the previous sections takes into account automatically all the relativistic corrections, which are important for high  $Z$  pionic atoms. These are the reasons why the quadrupole interaction, with the effect of the distribution of the magnetic moment, will be a natural development of the studies presented in the previous sections.



# Chapter 3

---

## Pionic atoms production and spectroscopy

---

### Introduction

Charged pions are unstable particles with a lifetime of only 26 ns [69]. However, such a short lifetime does not prevent a negatively charged pion from being captured in ordinary matter and to form a bound system. Even before the discovery of the pion in 1947 [79, 80], Enrico Fermi and other scientists predicted the existence of mesic atoms: bound systems composed of a normal nucleus and of an orbiting pion or muon instead of the electron [81, 82]. The experimental evidence for the production of mesic atoms came only in 1951 by the detection, in photographic emulsions, of traces of electrons, which were ejected from the atoms by Auger de-excitation after the capture of the exotic particle [83]. It is only in 1952 that X-radiation from pionic atoms was detected for the first time [84]. From these years until now, pionic atoms have been the object of many experiments. The unique features of these systems allow for a large variety of investigation as the study of the hadronic interaction at threshold, and the measurement of the pion characteristics. Low energy strong interaction effect between the nucleus and the pion can be evaluated by the measurement of the atomic energy levels. In particular, strong interaction properties of pionic hydrogen ground state allows for the study of the scattering length of the hadronic reactions  $\pi^- + p \rightarrow \pi^- + p$  and  $\pi^- + p \rightarrow \pi^0 + n$  [85, 86, 87, 88, 89]. Moreover, X-ray spectroscopy of atomic levels not affected by hadronic influences enables the accurate measurement of the pion mass (see Chapter 4).

In this chapter I will present the techniques that are necessary to produce and to detect pionic atoms. In Sec. 3.1 we will see how we can capture charged pions and produce pionic atoms. In Sec. 3.2 I will present the cascade processes in pionic atoms, which allow to the emission of X-rays. Section 3.3 is dedicated to the description of the Bragg crystal spectrometer we used in the experiments described in this manuscript. Finally, the focal plan detector of the spectrometer, and the data acquisition and analysis are presented in Sec. 3.4.

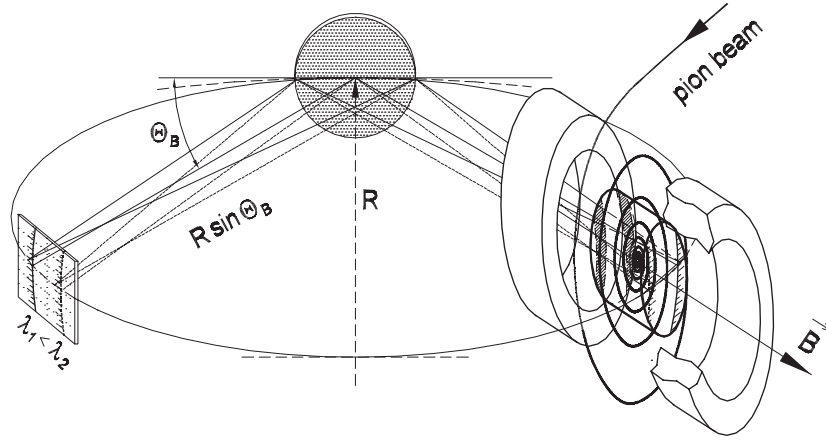


**Figure 3.1** – The Johann-type crystal spectrometer set-up. X-rays with different energies are reflected by the crystal with different angles, therefore they form different lines in the position sensitive detector.

## 3.1 Pionic atoms production

### Pion production

Due to the charged pions short lifetime, precise pionic atoms spectroscopy requires a pion beam for a continuous production of the pionic atoms. In our experiment (see Figs. 3.1 and 3.2) we used the pion beam provided by the Paul Scherrer Institut<sup>1</sup> (PSI). The PSI facilities provide the most intense pion beam in the world. The pions are produced by collision of the proton beam with a carbon target. The kinetic energy of the protons is 590 MeV/c and the beam current is up to 1.9 mA. From the target, the pions are collected in a secondary beam and transported to the experimental area  $\pi E5$  (see Fig. 3.2) where the pions are captured by the cyclotron trap (see following subsection). The pion momentum can be varied between 30 and 120 MeV/c. The optimal value for the pionic trap is 110 MeV/c. At this setting, we have the highest intensity of the captured pions using the cyclotron trap: 1–3% of the incoming pions ( $4 \times 10^9 \pi^-/s$ ). The muons produced by the decay of the pions in the cyclotron trap can be trapped as well, and allow for the formation of muonic atoms.

The absorption of pions in matter causes a high neutron background in the pionic atoms production area (about  $150 n/(mA s cm^2)$ ). A concrete shielding around the pion interaction zone and around the spectrometer is necessary to prevent secondary Compton background in the position sensitive detector of the spectrometer.

### Cyclotron trap

The cyclotron trap captures and slows down the pions from the beam, and it is composed principally of a pair of super-conducting coils and of a series of plastic degrader. The super-

<sup>1</sup>Villigen, Switzerland. Web site: <http://www.psi.ch>

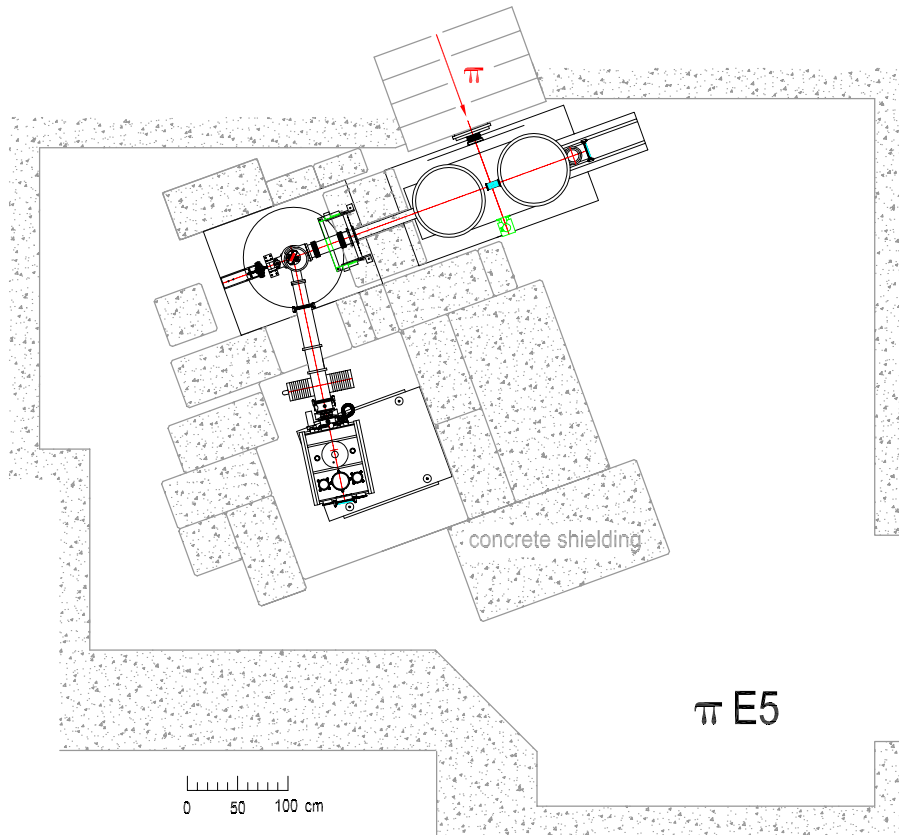


**Figure 3.2** – Setup of the experiment during the 2002 measurement. The pion beam (at the top of the picture) is decelerated into the cryogenic gas target inside the cyclotron trap. X-rays from pionic atoms are reflected onto the CCD detector array by the Bragg crystal.

conducting split-coil magnet [90] creates a strong magnetic field perpendicular to the pion beam, up to 4 Tesla. The pions are forced onto a circular path by the magnetic field and they are slowed down by collisions with plastic degraders along their trajectory (see Figs. 3.1 and 3.3). The loss of kinetic energy corresponds to a reduction of the trajectory curvature radius and allows the pion to reach the central target chamber (see Figs. 3.3 and 3.4). Due to the short pion lifetime ( $2.6 \times 10^{-8} s$ ), the degraders characteristics have to be optimized to decelerate the pions as fast as possible. At a pressure of 1 bar in the target cell, about 1–3% of the pion from the beam are stopped in the gas.

### Target chamber

The target cell (Fig. 3.3 right) is a thin-walled Kapton chamber, cylindrical in shape with a diameter of 60 mm, positioned on the axis of the cyclotron trap magnetic field. The chamber can be filled with different gas types up to a pressure of about 1.4 bar. The target density can be changed by cooling down the gas with cryogenics methods. It is possible to reach temperatures of the order of 20°K, with the possibility to obtain a liquid hydrogen target [66]. The target window facing the crystal has to be thin enough not to absorb the low energies X-rays emitted by the pionic and muonic atoms. This is accomplished by

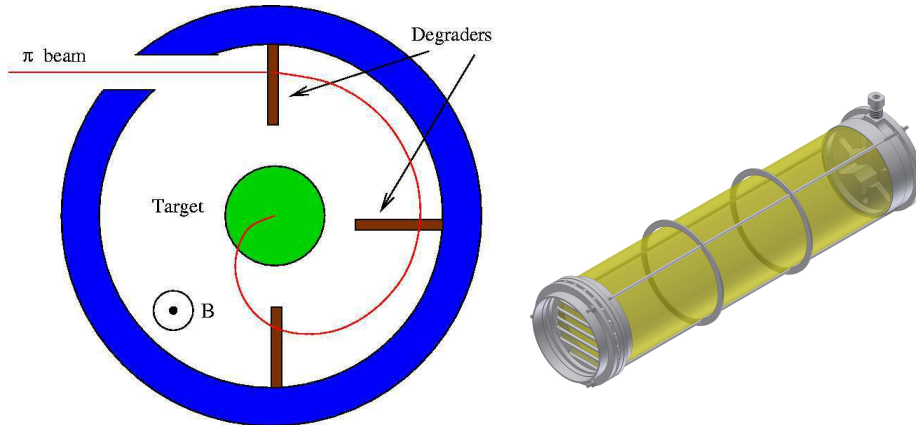


**Figure 3.3** – Left: schematic of the cyclotron trap. The incoming pions are forced onto a circular path by the magnetic field  $\mathbf{B}$  and they are slowed down by the collision with plastic degraders along their trajectory. Right: drawing of the target chamber. The metallic structure is made in aluminum and the walls of the gas cell are made by Kapton foils. The cell can contain gas mixtures up to a pressure of about 1.4 bar.

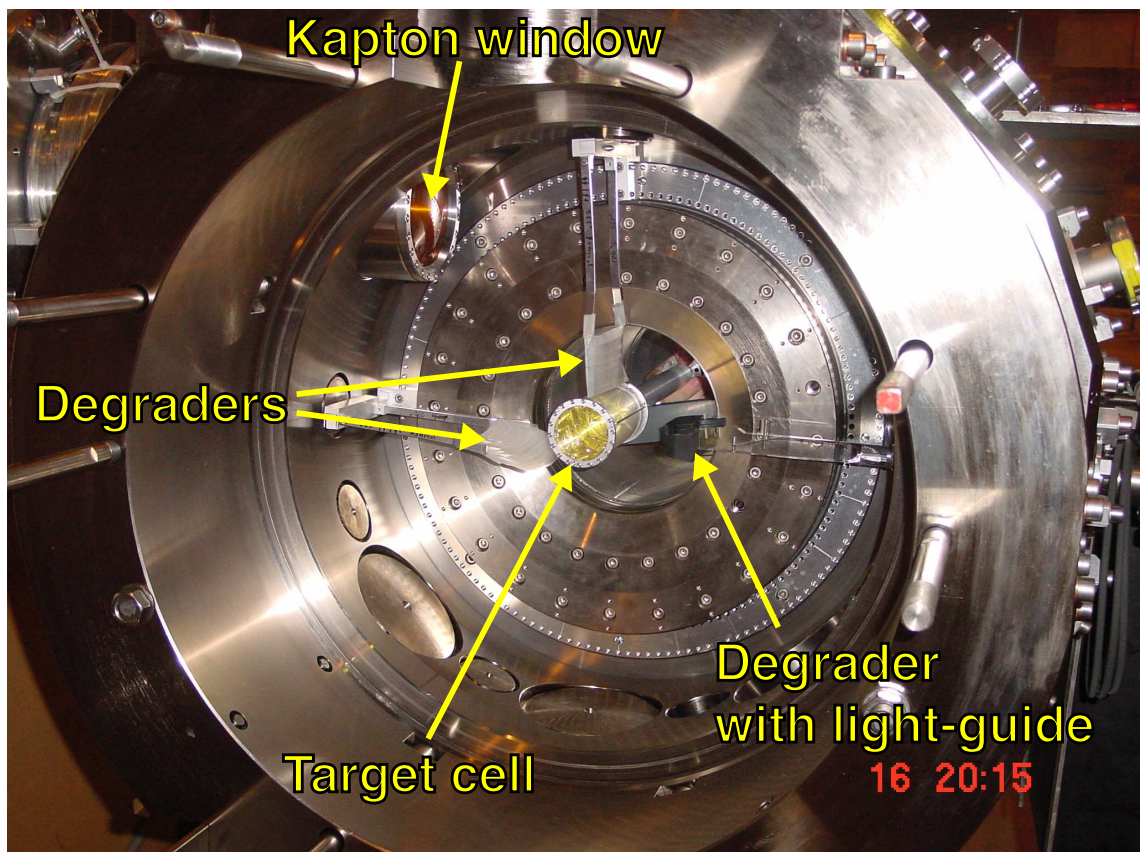


**Figure 3.4** – Photograph of the cryogenic target within the cyclotron trap. The pion beam enters through the Kapton window in the upper left corner. The plastic degraders are also visible: two formed by plastic foils (up and right to the target) and the third one connected to a scintillator to monitor the incoming pions at the left of the target.

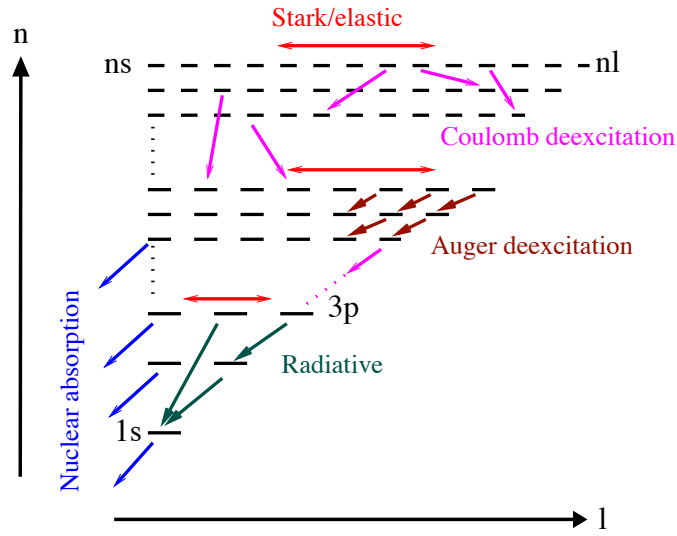


**Figure 3.5** – Cascade processes in pionic atoms. The predominance of one process over another depends on the quantum numbers  $n$  and  $l$ .

reinforcing the very thin Kapton foil ( $7.5 \mu\text{m}$ ) against pressure by a stabilizing structure.

### 3.2 Atomic cascade

In the target cell, pions are captured by the atoms in a highly excited state where the overlap of the outermost electron and pion wavefunctions are maximal, i.e., where the characteristic radius  $r_n = n^2 \hbar / (mcZ\alpha)$  of the wavefunctions are similar:

$$\frac{n_i^2 \hbar}{m_\pi c Z \alpha} \sim \frac{n_e^2 \hbar}{m_e c Z \alpha} \rightarrow n_i \sim n_e \sqrt{m_\pi / m_e} \sim n_e \times 16. \quad (3.1)$$

$n_i$  is the initial principal quantum number of the captured pion and  $n_e$  is the principal quantum number of the most external electron of the atom (for hydrogen and helium  $n_e = 1$ ). This rule of thumb has been confirmed by the experiments and more accurate calculations [91, 92, 93, 94, 95].

Different processes, illustrated in Fig. 3.6, take place when pionic atom de-excites to lowest states. For atoms with  $Z > 2$ , there are two principal de-excitation mechanisms: Auger emission and radiative decay. For pionic hydrogen and helium, there are other important cascade processes as the Stark mixing and the Coulomb de-excitation. For pionic atoms with  $Z > 2$  the Auger emission is dominant at the beginning of the cascade process, and the ejection of the electrons proceeds shell by shell as soon as the energy difference between the pionic atom levels exceeds the ionization energy for an electron. Transitions with  $\Delta l = \pm 1$  and with minimal energy difference are favored because the transition probability  $\Gamma_{\text{Auger}}$  is proportional to  $1/\sqrt{\Delta E}$  [96].

After complete depletion of the electron shell, we have a pure radiative cascade. The transition probability between orbitals depends on the transition energy as  $\Gamma_X \propto (\Delta E)^3$

(see Appendix 7.2), where  $\Delta E \propto \left( \frac{1}{n_f^2} - \frac{1}{n_i^2} \right)$ , with  $n_i > n_f \geq 1$ . For this reason, transitions with  $\Delta n = n_i - n_f$  as big as possible are favored. In addition, in light pionic atoms the selection rules impose  $\Delta l = \pm 1$ . Due to these characteristics of the radiative decay, the population of the states with maximum angular momentum is strongly enhanced.

In the final part of the cascade, the hadronic interaction between the pion and the nucleus causes an energy shift of  $\epsilon_{nl}$  of the atomic levels and open a capture channel, which reduces the lifetime of the energy level. This reaction is due to the overlap between the pion and nucleus wave functions and it is observable as a line broadening  $\Gamma_{nl}$  in the X-ray transition, which is larger in the low-angular-momentum states.

For pionic hydrogen, another important mechanism in the cascade process is the Stark mixing. During the collision with other atoms, the presence of an external Coulomb field  $\mathbf{E}$  mixes the states  $|nlm\rangle$  due to non-vanishing matrix element  $\langle nlm | \hat{\mathbf{E}} | n'l'm' \rangle$  [97]. The contribution of s- and p-states increases the reaction probability between the pion and the nucleus in high-angular-momentum states. When the target density increases, collision probability between atoms increases and Stark mixing effect reduces drastically X-ray yields because pion capture from the nucleus becomes more probable than radiative de-excitation during the collisions.

Another possible non-radiative cascade process for pionic hydrogen is the Coulomb de-excitation. It occurs when, during a collision between pionic hydrogen and another atom, the energy released  $\Delta E$  from transition  $n_i \rightarrow n_f$  is converted into kinetic energy. The increase in the pionic hydrogen velocity introduces a Doppler broadening in the X-ray transitions. This phenomena is very important for the ongoing experiment at PSI which has the goal to measure the strong interaction width and shift of the pionic hydrogen ground state [5, 6]. The Doppler broadening produced by the Coulomb de-excitation has to be evaluated accurately for the strong interaction broadening measurement.

More details on the cascade processes in pionic and other exotic atoms can be found in Refs. [98, 99, 100, 101, 102].

### 3.3 X-ray Bragg crystal spectrometer

The energy of the X-rays emerging from the target cell is measured using crystal spectrometry techniques. Similarly to the diffraction grating spectroscopy for visible light, crystal spectroscopy uses the constructive interference of photons that interact with a regular pattern. In visible spectroscopy, this pattern is represented by the parallel slits or steps of the grating, which are regularly spaced. In the case of X-rays, the regular pattern is constituted by the atoms regularly arranged in the crystal planes. As we can see in Fig. ?? (left), an X-ray that interacts with a crystal, can be scattered from the electrons coming from different planes. The X-rays emerging from different planes have the same phase if the length difference  $s$  between their paths is a multiple of the X-ray wavelength. This condition can be satisfied only for a precise value of the X-ray incident angle. Considering crystal planes spaced by a distance  $d$  and an X-rays with an incident angle  $\Theta_B$  (the Bragg angle), the path difference  $s = 2d \sin \Theta_B$ . There is a constructive interference between the two reflection if  $d$  and  $\Theta_B$  respect the Bragg law:

$$n\lambda = 2d \sin \Theta_B, \quad (3.2)$$

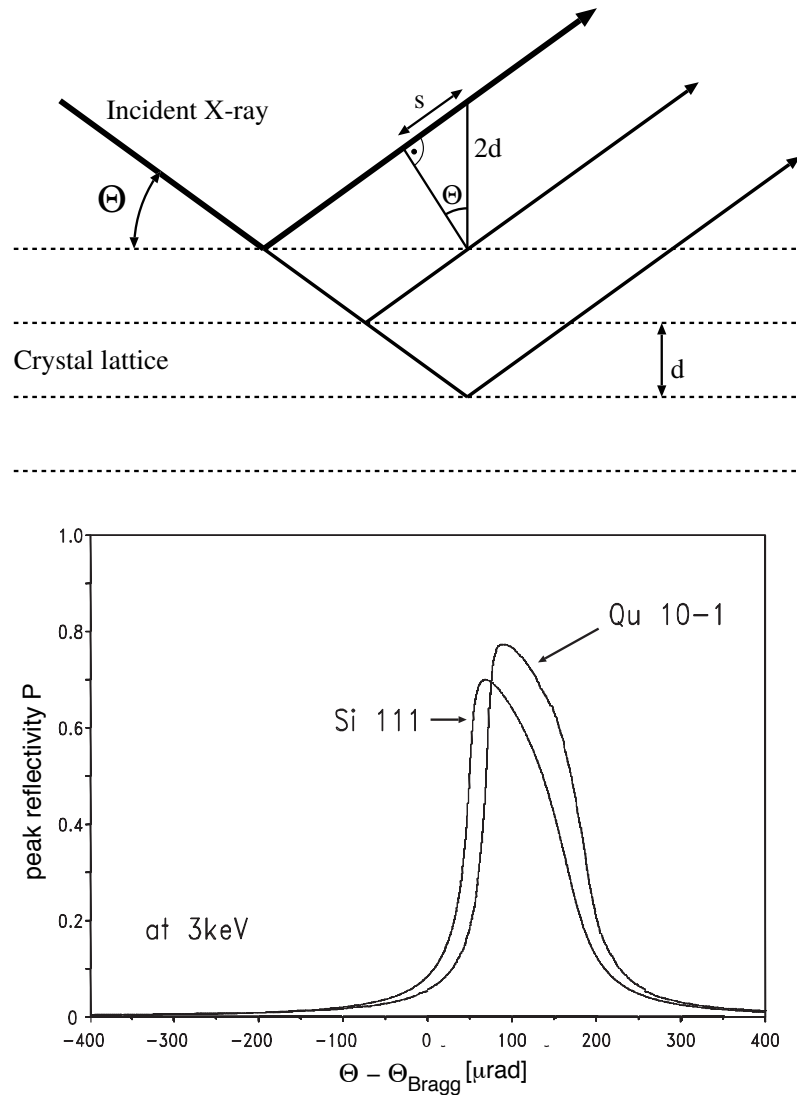


**Figure 3.6** – Top: Bragg reflection with a plane crystal. Reflected X-rays interfere constructively if their optical retardation  $s = 2d \sin \Theta$  is equal to a multiple of their wave length  $\lambda$ . Bottom: Rocking curves of two crystals (Si(111) and Qz(10 $\bar{1}$ )) used in the experiment, derived from the XOP program written at ESRF [103]. Compared to the Bragg angle, the centroid of the rocking curve is shifted because the refraction index inside the crystal is significantly different from vacuum.

where  $n$  is the order of diffraction (an integer number) and  $\lambda$  is the wavelength of the incident X-ray, related to the photon energy by the relationship  $E = hc/\lambda$  ( $h$  is the Planck constant and  $c$  is the speed of light).

According to Eq. (3.2), an incident photon with a determinate energy can be reflected by the crystal only for precise values of its incident angle: the Bragg angles. However, for real crystals, we have a reflection for a finite angle range around the correspondent Bragg angle. This is due to the multiple scattering of the X-rays between internal planes [104]. Taking into account this phenomenon and the photon absorption inside the crystal, the

rocking curve of a crystal has a non trivial shape as it is shown in Fig. ?? (bottom). The width of the rocking curve corresponds to the intrinsic resolution of the crystal  $\omega_f$ , which defines the energy resolution of the crystal spectrometer. In the few keV range, quartz or silicon crystals are the best materials suitable for Bragg spectroscopy. Their intrinsic resolution  $\omega_f$  of perfect plane crystal allows for a relative energy resolution

$$\frac{\Delta E}{E} = \left| \frac{\Delta \Theta_B}{\tan \Theta_B} \right| = \left| \frac{\omega_f}{\tan \Theta_B} \right| \quad (3.3)$$

on the order of  $\Delta E/E \approx 10^{-4}$  (Bragg angle  $\approx 30^\circ - 40^\circ$ ). Two examples of rocking curve for silicon (111) and quartz (10. $\bar{1}$ ) crystals are shown in Fig. ?? (bottom). Rocking curves for perfect crystal, i.e., without lattice imperfections, can be calculated by the XOP program written at ESRF [103].

### The Johann-type crystal spectrometer

Plane crystals can be used for X-ray spectroscopy, but they are not adapted for low intensity X-rays sources as pionic atoms. If we dispose of a spatial extended source, it is possible to use horizontally bent crystals to increase the intensity of the Bragg spectrometer. In the Johann spectrometer setup [105], one uses a bent crystal with curvature radius  $R$ . The position sensitive detector and the X-ray source have to be positioned at the distance  $R \sin \Theta_B$  from the crystal (see Fig. 3.1) on the Rowland circle: an imaginary circle tangent to the crystal and with a diameter equal to  $R$ . The X-rays from the source placed on (or near) the Rowland circle, will be reflected according to the Bragg law from the full crystal area and focused to a point on the opposite side of the Rowland circle, where a position sensitive detector can be placed to measure the position of the Bragg reflections.

A extended source is required because the energy range visible by the detector depends directly on the source size. As we can see in Figs. 3.1 and 4.2, X-rays with different energies comes from different zones of the source and they are focalized as spatial separated lines in the focal-plane. The use of spherical bent crystals instead of cylindrical ones allows for an additional focusing property in the vertical direction which reduces the height of the image in the detector. In this case we can use as position sensitive detector a compact device such Charge-Coupled Devices (CCD). The two-dimensional position information from the detector allows to reconstruct the energy spectrum [106].

### Measurement of the energy difference between two lines

The evaluation of the energy difference corresponds to the measurement of the Bragg angle difference, i.e., the line position on the position sensitive detector and it can be easily calculated using basic geometry. If we consider the coordinate system (x,y) as in Fig. 4.2, the two lines are detected at the position  $x_A$  and  $x_B$ . The detector cross the Rowland circle at the point with coordinate  $x_F$ , and the Bragg angle for line A is:

$$\Theta_A = \Theta_F + \arctan \left( \frac{x_A - x_F}{D} \right) \approx \Theta_F + \frac{x_A - x_F}{D} + \mathcal{O} \left[ \left( \frac{x_A - x_F}{D} \right)^3 \right], \quad (3.4)$$

where  $\Theta_F$  is the Bragg angle of the focus position and  $D$  is the crystal-detector distance. The energy corresponding to the line in  $x_A$  can be calculated using the Bragg formula

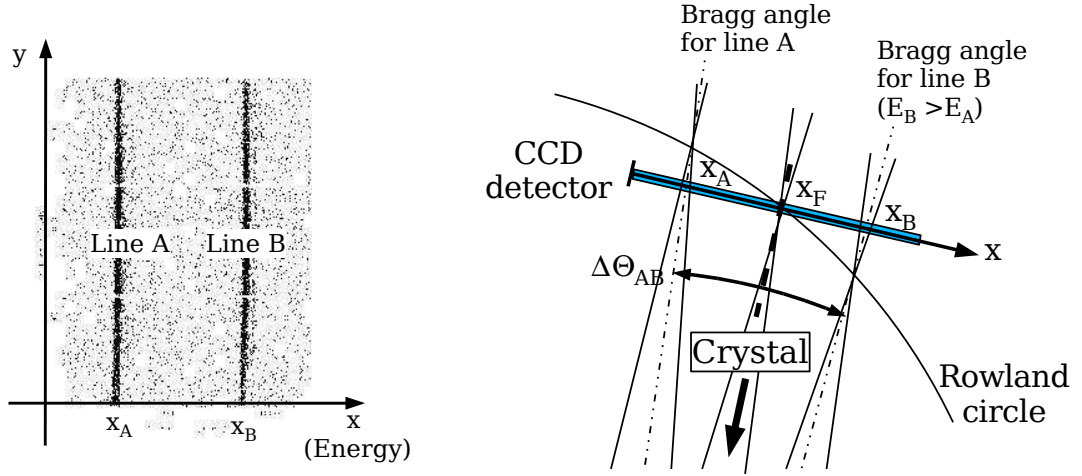


**Figure 3.7** – Left: visualization on the two-dimensional sensitive detector of two transition with different energy. The transition with higher energy has a smaller Bragg angle, i.e. a smaller value of the x-coordinate on the image. The lines presented in this image corresponds to the  $5g \rightarrow 4f$  transition in muonic oxygen (left) and pionic nitrogen (right) for the pion mass measurement presented in Ch. 4. Right: scheme of the line position in the spectrometer. By the measurement of the lines position on the detector, it is possible to calculate their energy difference (see text).

(Eq. (3.2)). If we look at the first order Bragg reflection we have:

$$E_A = \frac{hc}{2d \sin \Theta_A}. \quad (3.5)$$

In our spectrometer the angle  $\Theta_F$  can be evaluated only approximately, and for this reason we cannot measure absolute energies. However, we can measure with high precision the energy difference between two transitions. One transition has to be taken as reference if we want evaluate the absolute energy of one of the line. Considering line A as reference with energy  $E_A$ , and line B corresponding to the unknown energy  $E_B$ , the difference between their Bragg angle,  $\Delta\Theta_{AB}$ , is:

$$\Delta\Theta_{AB} = -\arctan\left(\frac{x_A - x_F}{D}\right) + \arctan\left(\frac{x_B - x_F}{D}\right) \approx -\frac{x_A - x_B}{D} + \mathcal{O}\left[\left(\frac{x_{A,B} - x_F}{D}\right)^3\right]. \quad (3.6)$$

The energy  $E_B$  can be evaluated using once again the Bragg formula:

$$\begin{aligned} E_B &= \frac{hc}{2d \sin \Theta_B} = \frac{hc}{2d \sin(\Theta_A + \Delta\Theta_{AB})} \\ &= \frac{hc}{2d(\sin \Theta_A \cos \Delta\Theta_{AB} + \cos \Theta_A \sin \Delta\Theta_{AB})} \\ &= E_A \frac{1}{\cos \Delta\Theta_{AB} + \cot \Theta_A \sin \Delta\Theta_{AB}} \end{aligned} \quad (3.7)$$

which correspond to an energy difference  $\Delta E_{AB}$ :

$$\begin{aligned} \Delta E_{AB} &= E_A \left( 1 - \frac{1}{\cos \Delta\Theta_{AB} + \cot \Theta_A \sin \Delta\Theta_{AB}} \right) \\ &\approx E_A \left\{ -\cot \Theta_A \Delta\Theta_{AB} + \mathcal{O} \left[ (\Delta\Theta_{AB})^2 \right] \right\} \\ &\approx E_A \left\{ \cot \Theta_A \left( \frac{x_A - x_B}{D} \right) + \mathcal{O} \left[ \left( \frac{x_{A,B} - x_F}{D} \right)^2 \right] \right\}, \end{aligned} \quad (3.8)$$

where the angle  $\Theta_A$  is the Bragg angle relative to the energy  $E_A$ :  $\Theta_A = \arcsin \left( \frac{2d E_A}{hc} \right)$ . From this formula we can deduce the important dispersion relationship:

$$\frac{dE}{E} = \frac{d\Theta}{\tan \Theta} = -\frac{dx}{D \tan \Theta}. \quad (3.9)$$

As we can notice a precise energy measurement requires the precise evaluation of the position of the reflected X-ray and an accurate value of the crystal-detector distance.

### Energy resolution of the spectrometer

The energy resolution of the Johann-type crystal spectrometer depends, of course, on the intrinsic crystal resolution  $\omega_f$  according to Eq. (3.3). Differently from flat crystal spectrometers, the energy resolution depends also on the crystal and sources finite sizes [107]. The total energy resolution can be written as:

$$\frac{\Delta E}{E} = \left( \frac{\Delta E}{E} \right)_{\text{CRY-INT}} + \left( \frac{\Delta E}{E} \right)_{\text{CRY-W}} + \left( \frac{\Delta E}{E} \right)_{\text{CRY-H}} + \left( \frac{\Delta E}{E} \right)_{\text{SRC-H}}, \quad (3.10)$$

where

- the term  $(\Delta E/E)_{\text{CRY-INT}}$  is given by Eq. (3.3),
- the term  $(\Delta E/E)_{\text{CRY-W}}$  depends on the horizontal crystal size  $b$  as:

$$\left( \frac{\Delta E}{E} \right)_{\text{CRY-W}} = \frac{b^2}{8R^2} \cot^2 \Theta_B, \quad (3.11)$$

- the term  $(\Delta E/E)_{\text{CRY-H}}$  depends on the vertical crystal size  $a$  as:

$$\left( \frac{\Delta E}{E} \right)_{\text{CRY-H}} = \frac{a^4}{64R^4} \cot^3 \Theta_B \quad (3.12)$$

and may be ignored for large values of  $R$ ,

- the term  $(\Delta E/E)_{\text{SRC-H}}$  depends on the vertical dimension of the source  $z$  as:

$$\left( \frac{\Delta E}{E} \right)_{\text{SRC-H}} = \frac{z^2}{4R^2 \sin 2\Theta_B}. \quad (3.13)$$



**Figure 3.8** – Silicon crystal attached to the glass support and crystal holder. The holder has a step-by-step motor to adjust the crystal angle relative to the horizontal axis.

### Particular characteristics of our spectrometer

In the spectrometer we used for our experiment, the crystals have a diameter of 100 mm and a radius of curvature of 3 m. The crystals are about 0.3 mm thick and they are attached to concave spherical glass lenses by adhesion forces (see Fig. 3.8).

The crystal, the detector and the intermediate connecting pipes of the spectrometer are in vacuum to avoid X-ray absorption. The adjustment of the spectrometer to different Bragg angles can be done online with linear steps moved by two stepping motor controlled remotely. One step changes the relative angle between the crystal and the detector  $\Theta_{CRY}$ . The other changes the relative angle  $\Theta_{ARM}$  between the crystal and detector ensemble and the cyclotron trap, i.e., the X-ray source, keeping  $\Theta_{CRY}$  unchanged (see Fig.3.9). The distance between the crystal and the detector can be changed online to adjust to the optimal focal condition with the CCD on the Rowland circle. The distance crystal-cyclotron trap is fixed for each set-up. The adjustment of  $\Theta_{CRY}$  allows to select of the energy range visible by the detector. The adjustment of  $\Theta_{ARM}$  allows to scan the target to optimize the X-ray rate.

### Spectrometer aberrations and corrections

#### Refractive index in the crystal

An important correction which has to be taken into account is due to a more correct relationship between the X-ray energy and the Bragg angle. The Bragg law, as stated in Eq. (3.2), is not completely exact because it doesn't take into consideration the deviation

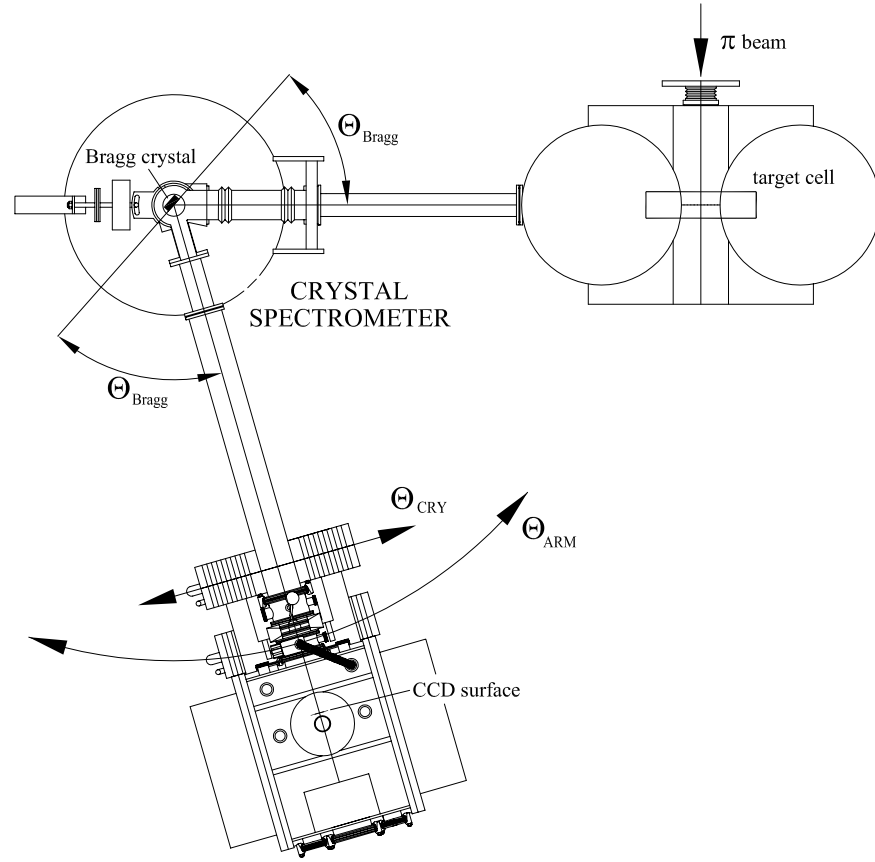


**Figure 3.9** – Top view of the spectrometer. The angles  $\Theta_{\text{CRY}}$  and  $\Theta_{\text{ARM}}$  define the spectrometer setting. The Bragg angle is taken between the crystal plane and the direction of the incident and reflected X-ray.

due to the index of refraction inside the crystal. Assuming that the simple Bragg equation holds in the interior of the crystal and that the usual optical principles of refraction apply, the refractive index correction is easily derived [108]. Inside the crystal the X-ray wavelength changes from  $\lambda$  to  $\lambda'$  and the Bragg angle becomes  $\Theta'_B$ . The Bragg law inside the crystal becomes:

$$n\lambda' = 2d \sin \Theta'_B. \quad (3.14)$$

The wavelengths  $\lambda$  are  $\lambda'$  related to refractive index  $n_r$  by the relationship (see also Fig. 3.10):

$$n_r = \frac{\lambda}{\lambda'} = \frac{\cos \Theta_B}{\cos \Theta'_B} = 1 - \delta, \quad (3.15)$$

where  $\delta$  is the decrement of the index of refraction and it is of the order  $10^{-6}$  for few keV X-rays. Eliminating the index of refraction  $n_r$  and primed variables from equations (3.14) and (3.15) leads to the corrected Bragg law:

$$n\lambda = 2d \sin \Theta_B \sqrt{1 - \frac{2\delta - \delta^2}{\sin^2 \Theta_B}} \approx 2d \sin \Theta_B \left(1 - \frac{4d^2\delta}{n^2\lambda^2}\right). \quad (3.16)$$

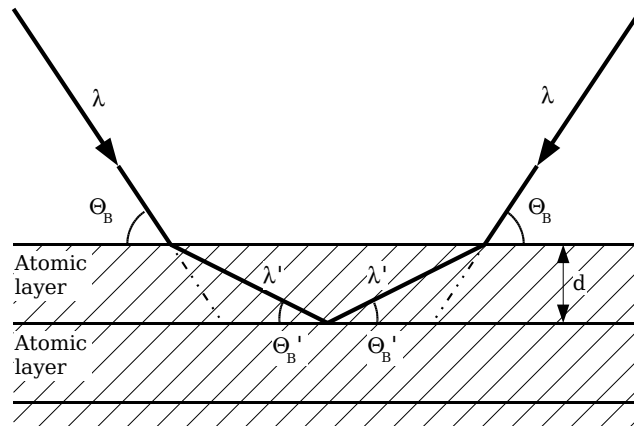


**Figure 3.10** – Effect of the index of refraction. The incident X-ray is refracted inside the crystal. Consequently, the Bragg law, valid in vacuum condition, changes.

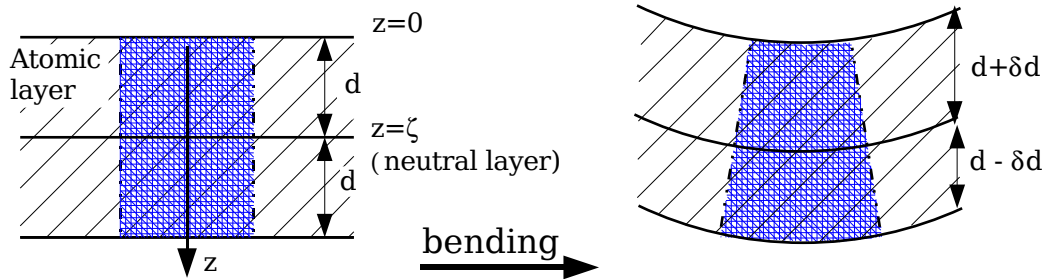


**Figure 3.11** – Effect of the bending deformation. The distance  $d$  between crystal planes change in function of their position with respect to the neutral layer ( $z = \zeta$ ). Due to the conservation of the crystal volume, the  $d$ -spacing increase for crystal planes with  $z < \zeta$  and decrease for crystal planes with  $z > \zeta$ .

### Crystal lattice deformation

For spectrometer used in Johann geometry (and curved crystal spectrometer), the positive radius of curvature of the crystal causes a deformation of the lattice constant  $d$  increasing the separation toward the rear of the crystal and decreasing it toward the front (Fig. 3.11).

The middle layer (defined as the neutral layer) of the crystal will retain the original  $d$  spacing. The relative change in the lattice constant is given by [109]:

$$\frac{\Delta d}{d} = -\frac{2\nu}{1-\nu} \frac{z(E) - \zeta}{R}, \quad (3.17)$$

where  $\nu$  is the Poisson's ratio<sup>2</sup> for the crystal material,  $z$  is the extinction length at the energy of interest and  $\zeta$  is the distance from the neutral layer to the surface of the crystal

<sup>2</sup>When a sample of material is stretched in one direction, it tends to get thinner in the other two

with radius curvature  $R$ . This formula is valid for a isotropic elasticity model. In the general case, the  $\nu/(1 - \nu)$  ratio is substitute to a more complex expression that depends on the elements of the compliance coefficients . Crystals have an anisotropic elasticity and the deformation of the lattice distance depends on the orientation of the bent surface with respect to the crystal planes, as explained in Appendix 7.2.

The small change of the crystal lattice distance  $d$  causes a correction of the Bragg angle that depends on the X-ray energy. Using the Bragg law from Eq. (3.2) we can easily calculate such correction:

$$\Delta\Theta_{\text{LDC}} = -\frac{\Delta d}{d} \tan \Theta_B. \quad (3.18)$$

### Penetration depth correction

There is a simple geometrical aberration caused by the change in the incident angle that the X-rays undergoes on penetrating the crystal, This results in a change in Bragg angle, which can depends on the average penetration depth  $z$  of the X-ray [109, 110]:

$$\Delta\Theta_{\text{PDC}} \approx \frac{z(E)}{R} \cot \Theta_B. \quad (3.19)$$

### Johann broadening

In the Johann-type spectrometer, the crystal surface is tangent to the Rowland circle only in its middle point. For this reason, this spectrometer geometry is affected by an intrinsic aberration. In principle, it is possible to eliminate this aberration using a crystal with lattice planes with a curvature radius  $R$  and with a surface with a curvature radius  $R/2$  (Johanson-type spectrometer). In practice, it is impossible to realize a crystal with these characteristics with the required precision, and it is easier to use the Johann configuration taking into account the required corrections. The principal aberration is due to the horizontal extension of the crystal  $b$ . X-rays incident on the lateral sides of the crystal are reflected with a slightly different angle that X-rays incident on the central part as shown in Fig. 3.12. This angle difference is always positive and causes an asymmetric shape of the focalized line on the detector. The asymmetry produces a shift  $\Delta\Theta_J$  of the Bragg angle, which, for crystals with circular aperture, is [105]:

$$\Delta\Theta_J = \frac{b^2}{32R \tan^2 \Theta_B}. \quad (3.20)$$

### Measurement and simulation of the spectrometer response function

The spectrometer aberration and the quality of the different crystal have been recently studied accurately using a particular intense X-ray source. During 2003 and 2004, after some modification of the cyclotron trap, we set-up an Electron-Cyclotron-Resonance Ion Trap (ECRIT) to produce He-like ions [111]. The  $1s2s \ ^3S_0 \rightarrow 1s^2 \ ^1S_0$   $M1$  transitions from He-like argon, chlorine and sulphur have been used to test the spectrometer components. The theoretical value of these transitions can be predicted with a precision of

---

directions. Poisson's ratio ( $\nu$ ), named after Simeon Poisson, is a measure of this tendency. It is defined as the ratio of the strain normal to the applied load divided by the strain in the direction of the applied load. For a perfectly incompressible material, the Poisson's ratio would be exactly 0.5. Most practical engineering materials have  $\nu$  between 0.0 and 0.5. Definition provided by Wikipedia: <http://wikipedia.org>.

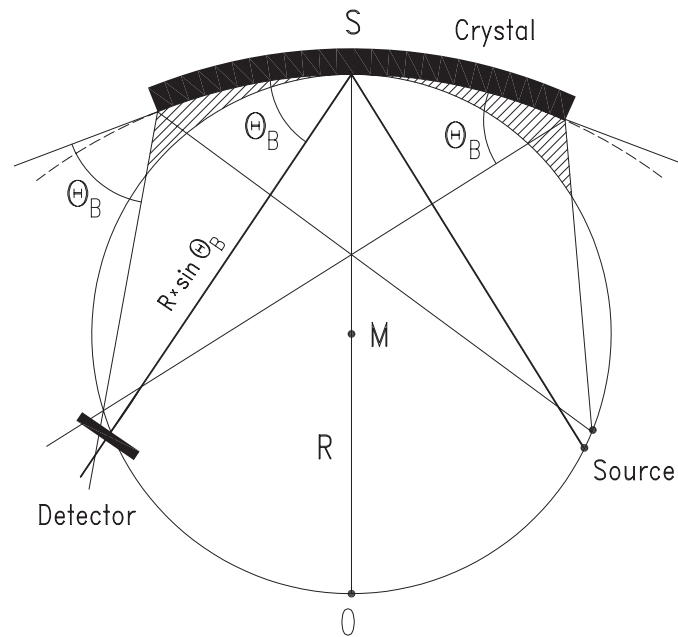


**Figure 3.12** – The Johann setup for Bragg spectroscopy. The crystal bending radius  $R = SO$  is the diameter of the Rowland circle (with the center at  $M$ ) on which the focusing condition  $R \sin \Theta_B$  is fulfilled. X-rays reflected from the lateral sides of the crystal are focalized in a different point on the Rowland circle than the X-rays reflected from the central side of the crystal. This effect causes a shift of the line centroid to smaller values of Bragg angle (higher energies).

few meV from Quantum Electrodynamics (QED) calculations, and they are characterized by a width of some meV, much less than the spectrometer resolution (around 0.4 eV). Systematic focal scans and aperture changes on the crystal surface allow to determinate completely the characteristic of the crystals and to measure the response function of the spectrometer. This experimental work was coupled with a Monte Carlo simulation of the spectrometer, which allows for a complete understanding of this instrument (see also Sec. 6 and Ref. [112]).

The use of the Monte Carlo X-ray tracking routine allows for the simulation of the response function for an arbitrary position of the CCD array with respect to the spectrometer focal plan. This enables to take into account the Johann aberration and, if necessary, the line defocusing effect, for the correct measurement of the Bragg reflection position.

### 3.4 Focal-plan position sensitive detector

#### CCD detector characteristics

The position of the reflected X-rays is measured by an array of 6 CCDs placed on the Rowland circle. The position sensitive detector used in our experiment has been developed jointly between the University of Leicester and the Paul Scherrer Institut using the CCD of

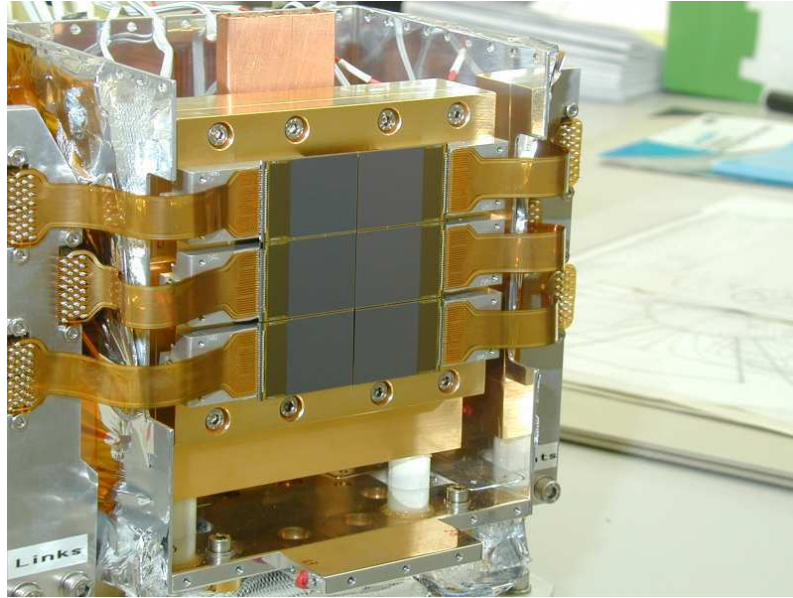


**Figure 3.13** – Photo of the CCD detector array. The read-out connections are visible at the external side of each chip.

type CCD22. The charged-coupled device CCD22 has been developed jointly by University of Leicester and Marconi Applied Technologies (formerly EEV) for the European Photon Imaging Camera (EPIC) on board of the X-ray telescope for the XMM-Newton spatial mission. A standard CCD is sensitive to X-rays in the energy range of few keV, but has very poor quantum efficiency (QE) at low energies (due to the absorption in the electrode structure) and at high energies (due to the limited depletion depth). The device CCD22 has been designed to overcome these limitations. Each CCD has an image area of  $600 \times 600$  pixels of  $40 \times 40 \mu\text{m}^2$  made on a silicon substrate,  $300 \mu\text{m}$  thick, with a depleted region of about  $30 \mu\text{m}$ . Each pixel is defined by an open-electrode structure. In a standard CCD, the three electrodes (required for any charged-coupled device) are nominally the same width, approximately  $1/3$  of the pixel size. In this case the electrode structure covers the whole of the pixel surface and provides a barrier to low energy X-rays, reducing the detection efficiency. As shown in Fig. 3.14, in the CCD22 the width of electrodes 1 and 2 are reduced substantially, whilst electrode 3, although much wider, is etched away, leaving a tapered T-shape structure. For this reason, the detector characterizing dimension is the distance between the center of adjacent pixels rather than the pixel size commonly used. This CCD type has a good quantum efficiency for 0.1-10 keV X-rays, with a maximum of about 90% for 1-5 keV photons when cold at  $-100^\circ\text{C}$  and used in photon counting mode (see Fig 3.15). The energy resolution for each pixel is about 160 eV at 3 keV. More detailed informations can be found in Ref. [113, 114] and in Appendix 7.2.

### Data acquisition

The position sensitive detector is usually calibrated with one radioactive  $^{55}\text{Fe}$  source temporary placed in front of the CCD array. The signal from each CCD of the detector

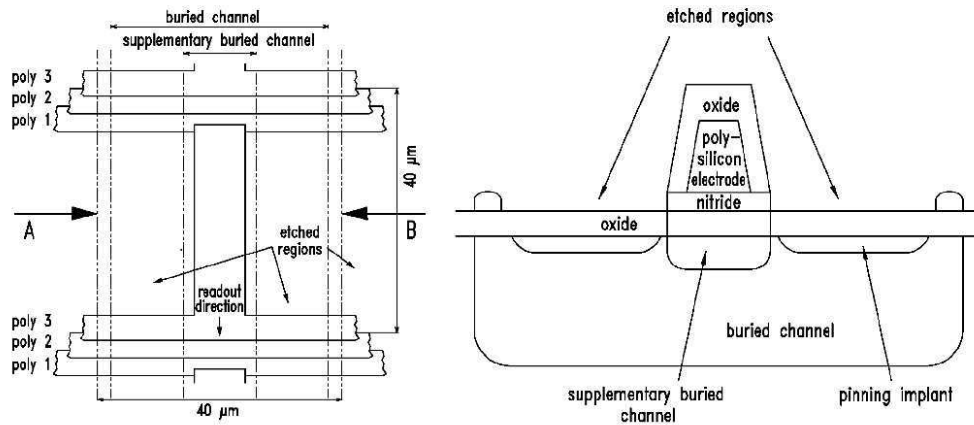


**Figure 3.14** – Schematic of CCD22 pixel and enlarged cross-section view through A-B. The etched (open) regions in the enlarged poly-silicon electrode (Poly 3) reduce absorption in the overlying electrode structure, improving low-energy X-ray quantum efficiency.

consists on ensemble of charges collected in different pixels in the CCD chip acquisition zone. The signal collection is operated during a finite period, i.e., frame, with a duration that can be changed in conformity of the experimental condition. At the end of this period, the charge deposited in the pixels are transferred, which occurs in 20–30 ms, in the storage zone of the chip. From the this zone, the signals are readout and converted in digital signal in about 30 s. The exposure time for each CCD frame used for pionic atoms spectroscopy is in the order of 1 minute (30 seconds of data integration plus 30 seconds read-out). This allows to have only 1-10 % of the image area illuminated by background events. The charge deposited in each pixel is decoded in 12 bits. For each pixel, a set of 5 bytes is recorded on the file: 3 for the position and 2 for the charge. The 6 CCDs are read out by a Visual Basic program running on a Windows95 PC. The data are usually stored in files in packets of 30-60 frames (equivalent to 15-30 min. data acquisition). The raw data files are transferred to a Linux PC to operate the necessary online analysis. Backup copies are made regularly on the computers of the collaboration institutes.

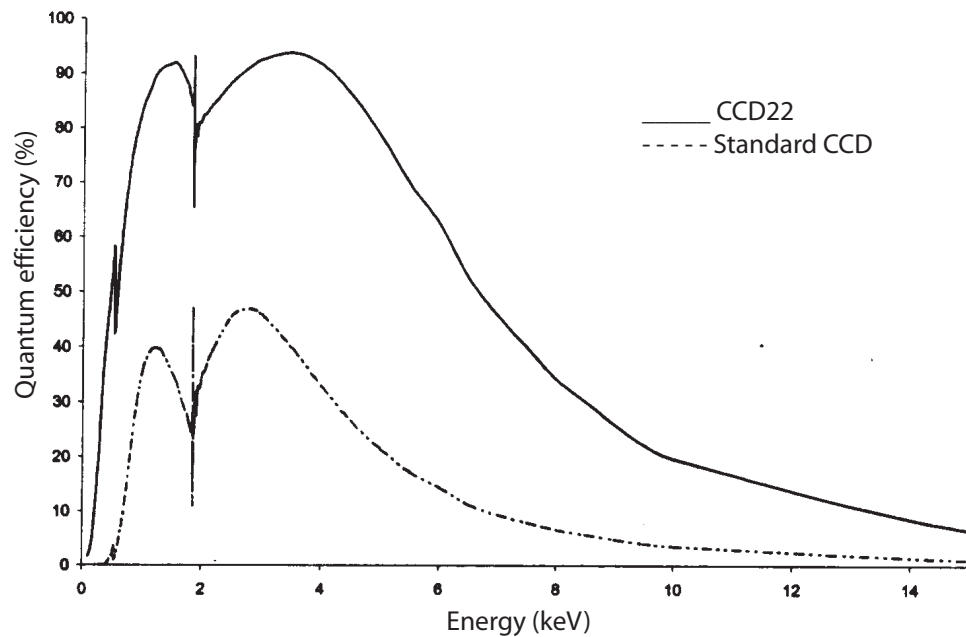


**Figure 3.15** – Quantum efficiency of the open-electrode CCD22 and of a standard front-illuminated CCD.

### 3.5 Data analysis

#### High precision energy spectra production

In X-ray crystal spectroscopy, the position of each spectral line on the focal-plane detector depends strongly on the energy of the detected X-rays. For this reason, the spatial analysis of the events distribution on the CCD array allows to obtain a final one-dimensional position spectrum that provides high accuracy energy spectra with a resolution of about 0.2–0.4 eV. The direct analysis of the charge deposited in each pixel enables to built low-resolution energy spectra with an energy resolution of about 160 eV at 3 keV. The low-resolution energy spectrum can be used to apply energy cuts for the events recorded by the position sensitive detector and to increase peak-to-background ratio on the final high-accuracy energy spectrum.

The raw data from the CCD array are read and analyzed using a Fortran program created by the collaboration members. To avoid possible programming errors, we developed two independent versions of this program: one carried by our group in Paris called CCDM and one by our collaborators from the Forschungszentrum Jülich (Jülich, Germany) called CSDCLUSTER. Both programs have as objective the reconstruction of the final one-dimensional position spectra from the two-dimensional data recorded by the CCD array. To reach this goal, three important steps have to be accomplished:

- *Discrimination between background and pionic atoms X-ray events.* Raw data are characterized by a high background signal. The increase in the signal-to-background

ratio is required to perform accurate measurements of the spectral lines.

- *Reconstruction of the two-dimensional events distribution on the detector.* The 6 CCDs, which constitute the position sensitive detector are spatially separated and they are oriented with slightly different angles. For each event, the raw information from a CCD has to be corrected to reconstruct the real two-dimensional position taking into account the relative orientation of each CCD.
- *Curvature correction and projection of the two-dimensional data distribution to obtain the final position spectrum.* A monochromatic X-ray source reflected by a Bragg crystal, produces a curved line on a flat detector. The line parameters depend on the angle and distance between the crystal and the detector, and on the characteristic of the crystal surface (flat, cylindrically curved, spherically curved, ...). This curvature has to be taken into account before the projection of the two-dimensional data to obtain the final one-dimensional position spectrum.

The completion of each of these steps is essential to obtain the final position spectrum from the data collected by the CCD detector array.

### Cluster analysis and energy cuts

The detection of the pionic atoms X-rays is affected by a strong background. This background is caused from the intense radiation produced by the interaction between pion and ordinary matter. Most of the pions from the beam are, in fact, absorbed in solid matter to form radioactive nuclei. The new nuclei, produced in an excited state, de-excite principally by emission of several neutrons and  $\gamma$ -rays:



where  $i$  is the number of ejected neutrons and  $A$  and  $A'$  are the nucleus types before and after the absorption of the pion, respectively. The neutrons can interact with matter as well and produce a secondary  $\gamma$ -ray background from nuclear de-excitation:



The neutrons are mostly stopped by the concrete shielding between the cyclotron trap and the detector (see Fig. 3.2). In opposite, the secondary  $\gamma$ -ray background can easily reach the detector.

High energetic particles can penetrate deeply in the chips and they can create electron-hole pairs into the depletion region, which is about  $30 \mu\text{m}$  thick, and beyond it. Charge generated in the depletion region is usually contained within the pixel where the X-ray interaction occurred. Charge generated deeper in the CCD substrate (field-free region) tends to diffuse further where some may be lost due to recombination and the rest is eventually collected in several pixels. For this reason, gamma photons penetrate beyond the depletion region of the CCD, and produce a signal involving clusters of several pixels by charge splitting in the silicon substrate. In contrast, 3-4 keV X-rays emitted by pionic atoms excite normally only one or two pixels in the CCDs. The charge distribution analysis, cluster analysis, is necessary to distinguish the signal from background events. Before the beginning of my Ph.D. thesis, the pixel analysis was based on the pattern recognition

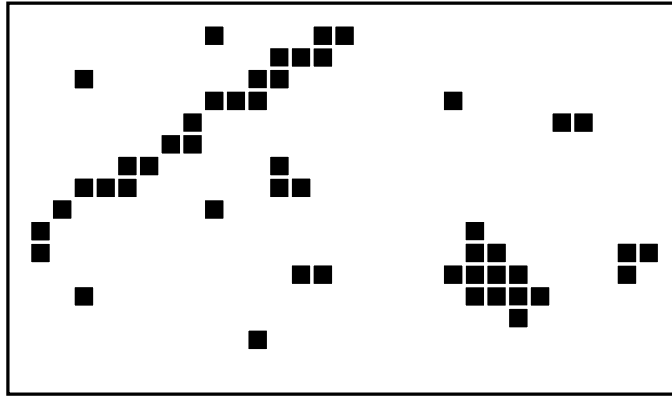


**Figure 3.16** – Typical charge distribution on the CCD pixels. The cluster analysis separates proper X-rays (isolated or paired events) from background events (clustered events or tracks).

of the cluster. For each pixel with a charge greater than a fixed threshold, the eight surrounding pixels were checked against fixed patterns. Events with one charged pixel (called type 1 event), two adjacent charged pixels (type 2) or two diagonally adjacent charged pixels (type 2B), were stored. All the other cases were discarded. This algorithm was developed and applied independently in the Paris analysis program CCDM (by Bruno Manil) [115], and in the Jülich analysis program CSD (the older version of CSDCLUSTER). This algorithm was sufficiently adapted for 2–4 keV X-rays but not for fluorescence X-rays used to monitor the spectrometer stability. Photons from the  $Zn K\alpha$  line have an energy of 8.64 keV and produce in the CCDs clusters of principally 5–15 pixels. Only a small part of this X-rays could be detected using this cluster analysis. For cluster of this size, there are so many possible forms that pattern recognition is too involved to provide a workable solution.

To increase the detection efficiently of X-rays with energy of about 5–12 keV, our collaboration developed a new cluster analysis. The new algorithm has been developed for the program CSDCLUSTER during the Maik Henneback's Ph.D. thesis [66] (period 2000–2003), and independently for the program CCDM during my Ph.D..

Differently from the old version, the new cluster analysis is not based on pattern recognition and it can be explained with the help of Fig. 3.17. As the old algorithm, the new algorithm checks the pixels row by row for deposited charges in each CCD (Fig. 3.17 a)). When the pixel charge is above a selected threshold, its charge and position are stored, and the pixel gets a zero charge value in the program memory array. Next, the algorithm starts to check all the four directly adjacent pixels for the presence of a deposited charge, and it continues recursively (Fig. 3.17 b) and c)). When no more adjacent charged pixels can be found, the total charge of the cluster is calculated adding the single pixel charges. The cluster two-dimensional position is evaluate by a weighted average, using the deposited charge as weight. The program continues to seek for pixels with a deposited charge ignoring the already checked pixels that have their charge set to zero (Fig. 3.17 d)).

Position coordinates are in pixels and they are expressed by integer numbers. In contrast, the cluster barycenter can assume non-integer values. The position of the event within the pixel grid (coordinates in integer numbers) is chosen assuming an isotropic

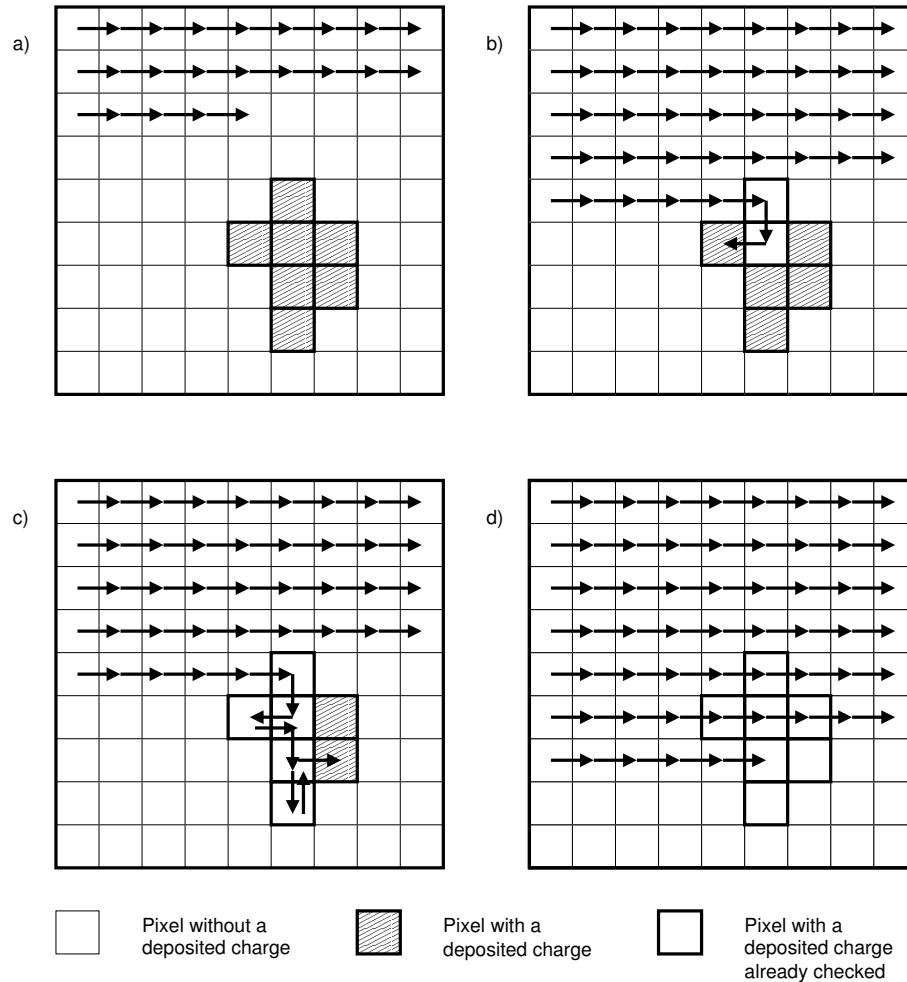


**Figure 3.17** – The new analysis cluster. a) The pixels are checked row by row for deposited charges. b) When a deposited charge is found, the pixel assume a charge equal to zero in the program memory array and the algorithm continue to check all the four directly adjacent pixels. c) The algorithm continues to check the pixels forming the clusters until no more adjacent charged pixel can be found. At this point, the position, the total energy and the pixel number of the cluster are stored. d) The program continue to check for charged pixels. The pixels already checked are ignored because their charged has been set to zero.

event distribution and determining the exact position of a single event randomly for both x- and y-coordinate. To be more clear, we can study the 1-dimension case: if the position of the cluster barycenter is  $x=1.3$ , the position of the event will be  $x=1$  in the 70% of the cases and it will be  $x=2$  in the 30% of the cases.

The new cluster analysis had to be included in the main program by addition of some Fortran and C subroutine. The core of the recursive algorithm has been written in C because it showed better performances than the equivalent code written in Fortran90.

The number of pixels, position, and total charge of the clusters are stored to be used for additional analysis. In the energy spectrum visualization, it is possible to select only clusters with a certain number of pixels. In pionic atoms data, this allows to a first strong reduction of the background as it is possible to observe in Fig. 3.18. The selection of the cluster energy range, allows for an additional background reduction, and leads to high values of the signal-to-background ratio, typically of the order of 300. Compared with the old algorithm, the new algorithm enables the detection of about 4-6% more photons: 1% comes from the detection of 3-pixels-events, and 3-4% comes from the correct treatment of the diagonally adjacent pixels considered now as two single events.

The advantage of the new cluster analysis is more evident for 8-9 keV X-rays detection. Only 20% of the  $Zn K\alpha$  photons were detectable by the old algorithm. The correct treatment of the clusters with high number of pixels, allows to gain a factor of 5 in the number of detected photons [66].

### Two-dimensional plot reconstruction

Cluster analysis provides two-dimensional position in pixels for each event relative to the detecting CCD. In the ideal case we had perfect aligned and adjacent CCDs, we could use this information to determinate the real events distribution on the whole array. In reality, there are gaps between CCD of the order of 0.3 mm, and the chips are slightly misaligned, with relative orientations of 1-6 mrad. The real two-dimensional position of the events is reconstructed applying an appropriate coordinate change for each CCD. Position coordinates are in pixels and they are expressed by integer numbers. After the rotation and the translation of the reference frame, position coordinates can assume non-integer values. The events position is redistributed within the pixel grid applying the same method used for the cluster position (see previous subsection).

The relative position and orientation of the CCDs have been measured twice using two different methods. The first method used the image of an aluminum mask illuminated by an X-ray fluorescent source [66]. The second method used the image of a nanometric grid illuminated by a light source. Both techniques are described in the preprint of the article in Appendix 7.2.

### Curvature correction and high resolution energy spectrum production

As I explained in Sec. 3.3, the crystal spectrometer produces curved lines on the detector, which correspond to X-ray transitions with different energy. To determine accurately the line width and position, a curvature correction has to be applied to the two-dimensional plot before to project the event distribution on the x-axis (for the accurate energy measurement). The lines shape is parameterized with a parabolic function  $x = A + By + Cy^2$ . The coefficients A, B and C are calculated by a linear fit to a selected spectral line. The

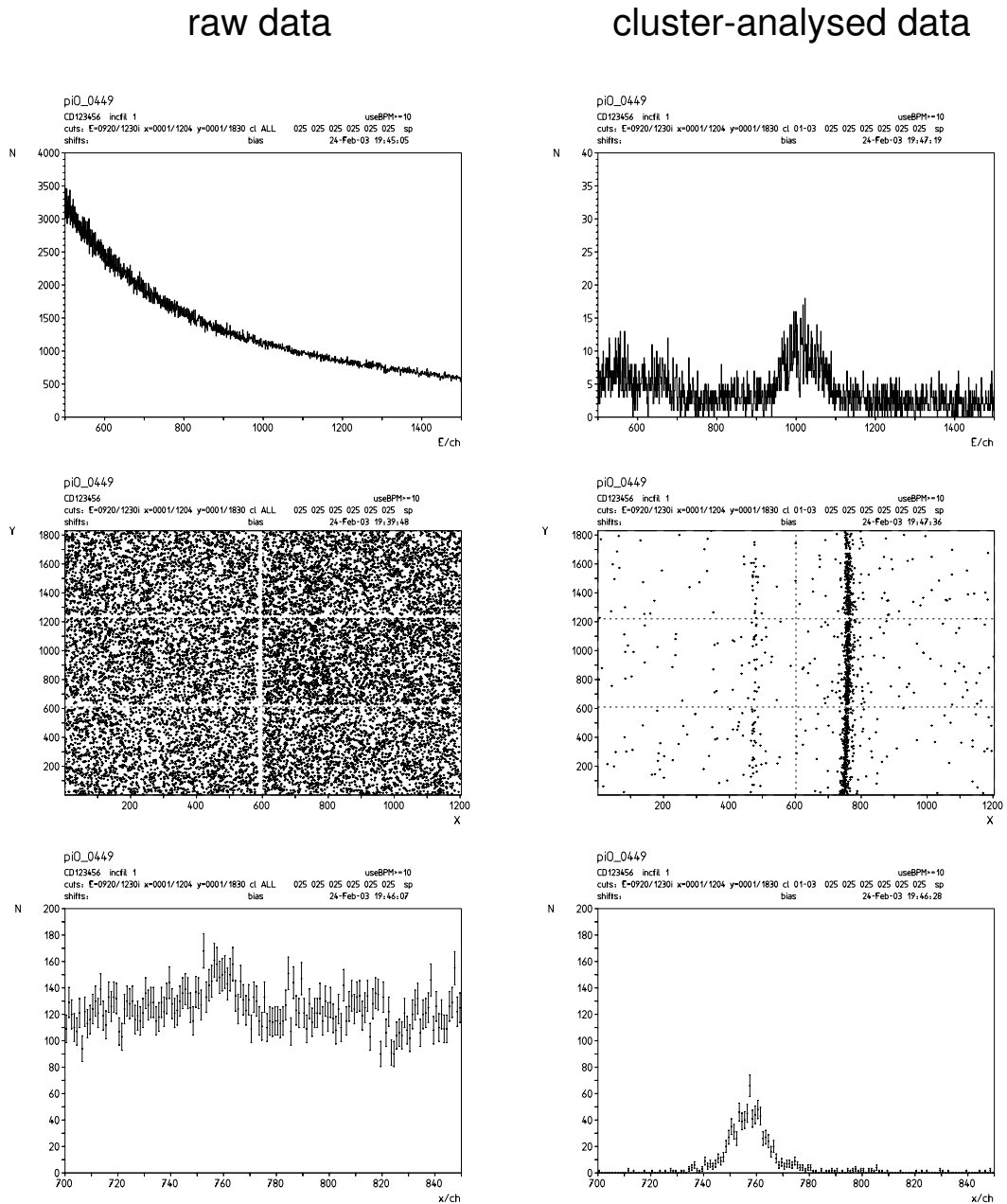


**Figure 3.18** – 10 hours worth of  $\pi^0$  data from 2002 shown without (left column) and with (right column) cluster analysis. The spectra are direct printouts of the data analysis software.  $N$  is the number of events. Upper row: energy spectra. Middle row: 2D plot of the data. Lower row: x-position spectra. For the cluster analyzed 2D and x-position plot, energy cuts are applied.

value of the parameters A, B and C are not significantly sensitive to the line position on the CCD array and they can be obtained choosing the brightest line in the two-dimensional plot. The zone around the line is divided in several horizontal slices. For each slice, the centroid is calculated. The position of the centroids is used to perform a  $\chi^2$ -fit to determine the parabola parameters. The influence of the background events in the fit results is minimized applying a recursive method. For successive fits, only events than are horizontally close enough to the previously calculated parabola are taken into account. In this way the selected zone is curved and it follows the tendency of the line intensity maximum. After some iteration, the result converges and gives the final parabola parameters. The width of the fit interval is set by the user.

The curvature correction is applied by changing the events position from  $(x_i, y_i)$  to  $(x_i - By_i - Cy_i^2, y_i)$ . The events position is redistributed within the pixel grid applying the same method used for the cluster repositioning. After the curvature correction, the detected events are distributed in the two-dimensional plot along a straight line, and their position can be projected into the x-axis to obtain one-dimensional plot. The different lines are visualized on the projection as different peaks the position of which can be measured by a fit. The effect of the curvature correction in the two- and one-dimensional plot is shown in Fig. 3.19.

### Fit of the one-dimensional plot

After the CCD orientation and curvature corrections, the program CCDM provides, as final results, an one-dimensional plot, that correspond to the projection on the x-axis of the two-dimensional X-ray distribution on the detector. Peaks in this plot represent the spectral lines detected by the CCD array. The position of such peaks depends on the corresponding transition energies, which are measured precisely performing a fit of these peaks.

But which profile should we use to measure the peak position? In first approximation, as usual, the Gaussian distribution can be used to take into account the results of the different error sources as imperfections of the crystal, Doppler broadening, crystal response function, mechanical instabilities of the spectrometer. . . For low statistic data, the Gaussian profile is sufficient to describe the line profile but it start to be unsuitable for a more accurate analysis.

As an example, in pionic hydrogen spectra, the strong interaction manifests itself as an evident broadening into the  $n p \rightarrow 1s$  transitions. This broadening comes from the instability of the 1s level of such atom due to the possible reaction between the pion and the nucleus. The ground level is unstable with a lifetime in the order of 0.4 fs, which correspond to a linewidth of about 0.8 eV, significantly larger than the spectrometer resolution of about 0.4 eV. In this case the instability of the ground level has to take into account using a Lorentzian profile to fit the peak, instead to the Gaussian profile. More precisely, a more adapted profile for this problem is the convolution of a Lorentzian and a Gaussian profile: the Voigt profile. The Voigt profile is well adapted to fit spectra, with energy level lifetime sufficiently short to produce an observable natural linewidth as in some cases of pionic atoms transitions.

To take into account the precise spectrometer response function and/or a more complicated velocity distribution of the atoms, a more generic profile has to be used. This profile

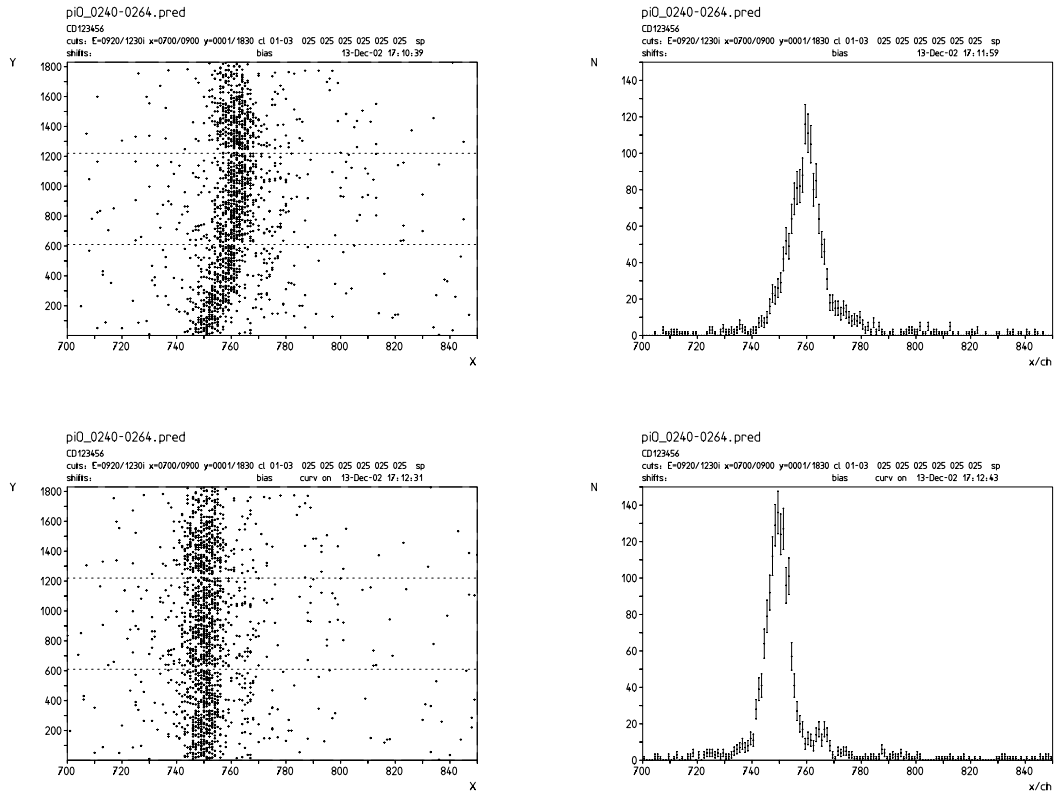


**Figure 3.19** –  $\pi O$  data from 2002 shown before (upper row) and after curvature correction (lower row). On the left side there are the 2D plot and on the right side there are the x-position plot.

**Table 3.1** – Profile types to use to fit transition lines characterized by different aspects

Profile used by the fit	Transition line characteristics
Gaussian	Simple fit for any instrument resolution
Lorentzian	Transition lines with short lifetime
Lorentzian $\otimes$ Gaussian $\rightarrow$ Voigt	Short lifetime and other effects
Spline	Johann aberration, defocusing, . . .
Spline $\otimes$ Gaussian	Johann aberration, defocusing, . . . and other effects

can be provided by a simulation or by real measurement interpolated with splines<sup>3</sup> to be used for the fit. For our proposal, the specific profile comes from a Monte Carlo simulation of the crystal spectrometer described in Sec. 5.2. This simulation can take into account also the effect of an arbitrary velocity distribution of the X-ray source. This feature is essential to consider the effects of the Coulomb explosions and the radiative cascade in pionic atoms. In particular, multicharged ion spectra analysis, described in Chapters 5 and 6, requires adapted spectrometer response functions to fit correctly the transition lines in the atomic spectra. The typical linewidth and Doppler broadening in these spectra are so small that, in this case, the line profiles is very sensitive to the response function and focal condition of the crystal spectrometer. More details about the simulation program and ions spectroscopy analysis can be found in Sec. 5.2 and Ch. 6, respectively. To take into account additional resolution degradation, due to crystal imperfection as example, the spline profiles can convoluted with a Gaussian distribution.

All these requirements for a fit program are fulfilled by the program used in our group: FIT6. FIT6 is a Fortran77 and Fortran90 program developed by P. Indelicato with some additional features added by me. In particular, this program can use Gaussian, Lorentzian and Voigt profiles. In addition, I added few routines to fit with a generic line profile provided by an external data file using the spline interpolation. The spline can also be convoluted with a Gaussian distribution (see following section for more details). The fit is performed by  $\chi^2$  minimization using the Levenberg-Marquardt method presented in the book Numerical Recipes for Fortran77 [116]. An equivalent program is available in the collaboration: FITIT. Like FIT6, the program FITIT can use the theoretical profiles provided by the Monte Carlo simulation convoluted with a Gaussian distribution to fit the one-dimensional spectra. Differently from FIT6, this program can additionally determine the parameters of the Doppler broadening and it can fit several peaks with a fixed position between them. The fit is obtained minimizing the  $\chi^2$ , using MINUIT libraries [117]. More details about FITIT and the Monte Carlo routines can be found in Ch. 5 and 6. This program, developed by Leopold Simons will be used, in particular, for the measurement of the pion mass (Ch. 4).

The fit of the one-dimensional plot provides the peak position in pixels. To obtain the corresponding energy differences, two principal informations are required: the exact distance between the detector and the crystal center, and the distance between pixels in the CCDs. The crystal-detector distance is unambiguously determined by the experimental set-up. The average pixel distance at the working detector temperature has been recently measured with an error of 15 ppm. The description of this measurement is described in Appendix 7.2.

### Data fitting using an arbitrary simulated profiles

The program FIT6 can use simulated or measured profiles provided as an histogram in an ASCII file. When the fit is performed, this histogram is read and interpolated to adjust the simulated profile to the real profile. This requires two principal steps:

- Interpolation of the data describing the simulated profile.

---

<sup>3</sup>A spline is a special function defined piecewise by polynomials. In interpolating problems, spline interpolation is often preferred to polynomial interpolation because it yields similar results, even when using low degree polynomials.

- Use of the interpolated profile for the  $\chi^2$  minimization.

The histogram provides a finite set of data points, which have to be interpolated to extract a continue function to use for the fit. The simulated or measured profile is normally affected by statistical data fluctuation of the histogram values, proportional to its square root. A normal interpolation using simple splines is not adapted because it does not consider the statistical nature of the data fluctuation. For this reason, it has to be applied a spline fit of the simulated histogram.

In FIT6, we used a particular type of splines for the interpolation: the B-splines. Given  $m + 1$  knots  $t_i$  in  $[0,1]$  with

$$t_0 < t_1 < \dots < t_m, \quad (3.23)$$

a B-spline of degree  $n$  is a parametric curve

$$\mathbf{S} : [0, 1] \rightarrow \mathbb{R}^2 \quad (3.24)$$

composed of basis B-splines of degree  $n$

$$\mathbf{S}(t) = \sum_{i=0}^{m+1} \mathbf{P}_i b_{i,n}(t), \quad t \in [0, 1]. \quad (3.25)$$

The  $P_i$  are called control points or de Boor points. A polygon can be constructed by connecting the de Boor points with lines, starting with  $P_0$  and finishing with  $P_n$ . This polygon is called the de Boor polygon.

The  $m - n$  basis B-splines of degree  $n$  can be defined using the Cox-de Boor recursion formula:

$$b_{j,0}(t) := \begin{cases} 1 & \text{if } t_j \leq t < t_{j+1} \\ 0 & \text{otherwise} \end{cases} \quad (3.26)$$

$$b_{j,n}(t) := \frac{t - t_j}{t_{j+n} - t_j} b_{j,n-1}(t) + \frac{t_{j+n+1} - t}{t_{j+n+1} - t_{j+1}} b_{j+1,n-1}(t). \quad (3.27)$$

When the knots are equidistant we say the B-spline is uniform otherwise we call it non-uniform<sup>4</sup>. In our case we used a cubic B-spline, i.e.,  $n = 3$ , which guarantee the continuity of the derivative in each point of the considered interval.

The fit and the evaluation of the B-splines is obtained using subprograms from the SLATEC Common Mathematical Library<sup>5</sup>, in particular using the subroutines `defc.f`, for the fit, and `dbvalu.f` to calculate the value of the spline and its first derivative.

The B-spline obtained from the fit of the simulated data is normalized and parameterized to be used by the  $\chi^2$  minimization subroutine. The function implemented for the fit is in the form:

$$\text{Bspline}(x) = a \text{Nspline}(x - x_0), \quad (3.28)$$

where  $a$ , and  $x_0$  are the parameters to fit, and `Nspline` is the normalized B-spline, i.e., with the integral normalized to 1. The partial derivatives of the B-spline necessary for the

<sup>4</sup>Definition provided by Wikipedia: <http://wikipedia.org>.

<sup>5</sup><http://www.netlib.org/slatec/>.

fit are:

$$\frac{\partial \text{Bspline}}{\partial a}(x) = \text{Nspline}(x - x_0), \quad (3.29)$$

$$\frac{\partial \text{Bspline}}{\partial x_0}(x) = a \frac{\partial \text{Nspline}}{\partial x_0}(x - x_0), \quad (3.30)$$

where  $\partial \text{Nspline}/\partial x$  is provided by the subroutine `dbvalu.f`.

The implementation by FIT6 of the convolution of the B-spline with a Gaussian requires an additional parameter to take into account the width of the Gaussian distribution. In this case the function implemented for the fit is:

$$C(x) = \int_{-\infty}^{\infty} \frac{1}{\sqrt{2\pi}\sigma} e^{-\frac{(x-\tilde{x})^2}{2\sigma^2}} a \text{Nspline}(\tilde{x} - x_0) d\tilde{x}, \quad (3.31)$$

where  $\sigma$  is the width of the Gaussian distribution.

In this case, the calculation of the derivative is given by the formulas:

$$\frac{\partial C}{\partial a}(x) = \int_{-\infty}^{\infty} \frac{1}{\sqrt{2\pi}\sigma} e^{-\frac{(x-\tilde{x})^2}{2\sigma^2}} \text{Nspline}(\tilde{x} - x_0) d\tilde{x}, \quad (3.32)$$

$$\frac{\partial C}{\partial x_0}(x) = \int_{-\infty}^{\infty} \frac{1}{\sqrt{2\pi}\sigma} e^{-\frac{(x-\tilde{x})^2}{2\sigma^2}} a \frac{\partial \text{Nspline}}{\partial x_0}(\tilde{x} - x_0) d\tilde{x}, \quad (3.33)$$

$$\frac{\partial C}{\partial \sigma}(x) = \int_{-\infty}^{\infty} \frac{1}{\sqrt{2\pi}\sigma^2} \left( \frac{(x-\tilde{x})^2}{\sigma^2} - 1 \right) e^{-\frac{(x-\tilde{x})^2}{2\sigma^2}} a \text{Nspline}(\tilde{x} - x_0) d\tilde{x}. \quad (3.34)$$

### 3.6 Conclusions

In this chapter I described the pionic production and the X-ray spectrometer for high precision X-ray measurement. In Ch. 4 and 6 we will see how we can use such instrument for two particular cases: the measurement of the pion mass (Ch. 4) and highly charged ions spectroscopy (Ch. 6).

# Chapter 4

---

## Measurement of the charged pion mass

---

*La cucina è una bricconcella; spesso e volentieri fa disperare, ma dà anche piacere, perché quelle volte che riuscite o che avete superata una difficoltà provate compiacimento e cantate vittoria.*

---

Pellegrino Artusi, *La Scienza in Cucina e l'Arte di Mangiar Bene*, Firenze 1891

### Introduction

In 1928, with the development by Paul Dirac of the relativistic quantum field theory, the electromagnetic force between charged particles had been understood on the basis of electromagnetic potentials and fields describing exchange of photons. Following the idea of the deep connection between exchanges of particles and energy potential, the Japanese physicist Hideki Yukawa attempted to describe the strong interaction force between nucleons with the introduction of a new particle [53]. Due to the strong interaction short range, this particle had a non-zero mass and the predicted value was between that of the electron and proton masses (for this reason the new particle was called meson from middle, in Greek).

It is only in 1947 that Powell, Lattes and Occhialini obtained the photographic evidence of the existence of a new particle (see Fig. 4.1) showing a heavier particle decaying in a lighter one [79, 80]. This heavier particle fulfilled the requirement of Yukawa's prediction and it was called  $\pi$ -meson or pion. The light particle produced by the disintegration of the pion was called  $\mu$ -meson or muon.

Yukawa estimated the pion mass to 200 times the electron mass ( $\approx 110$  MeV). Counting the photographic emulsion grain in the particle trajectory, Powell and his group estimated the pionic and muonic mass ratio about 1.5. The first direct measurement of the pion mass came when it was possible to produce pions with proton accelerators measuring the deflection trajectory of the pion in a magnetic field. Stearns and his collaborators

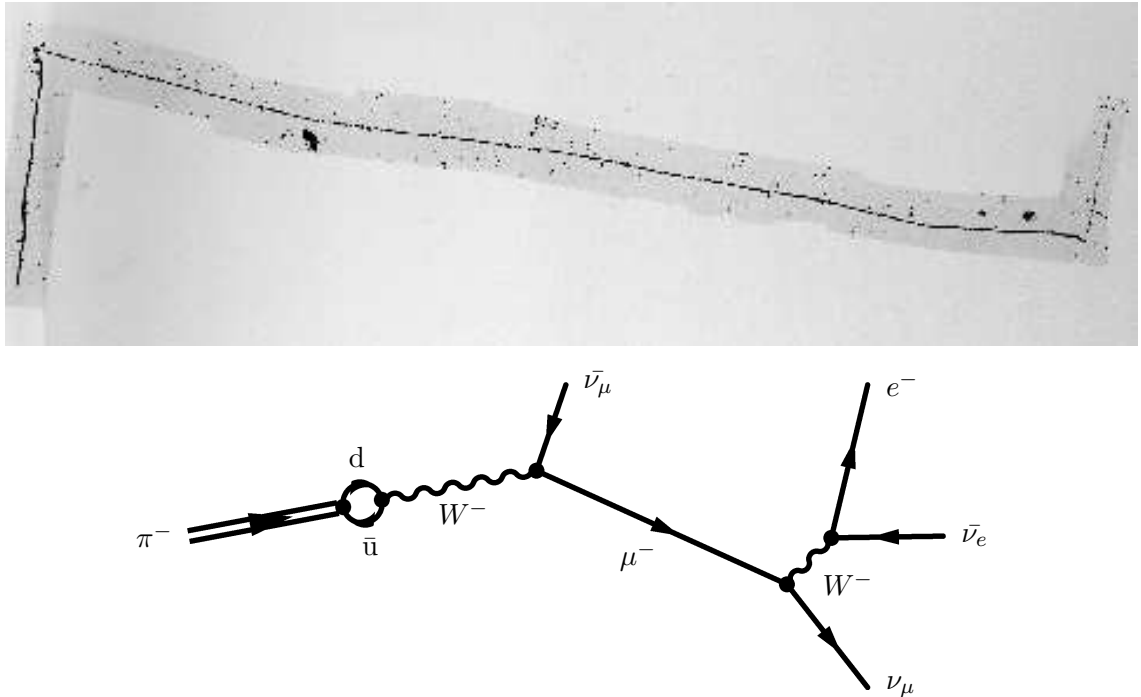


**Figure 4.1** – Top: the picture shows the particle tracks left in a photographic emulsion during the decay of a pion. The pion enters moving upwards from the bottom left, and comes to rest. It decays to produce a muon, which travels to the right. The muon track becomes increasingly dense as the muon slows down, and eventually stops. The muon then decays to an electron, producing the final track leaving at the top right. Bottom: Feynman diagram corresponding to the subsequent pion and muon decay.

performed the first mass measurement using pionic atoms in 1954 [118]. The  $4f \rightarrow 3d$  X-rays emitted by light pionic atoms were measured with the critical absorption edge technique. The pion mass was estimated between 272.2 and 273.3 times the electron mass.

With the increase of the pion beam intensities, it was possible to measure pionic atoms X-rays with crystal spectrometers (which have a very low efficiency but high resolution). The first measurement was performed using pionic calcium and titanium obtaining  $m_\pi = 139.577 \pm 0.013 \text{ MeV}/c^2$  [119]. Since then, the pion mass has been re-measured several times using this technique with increased precision [120, 121, 122]. The most precise value to date has been obtained by Jeckelmann and his collaborator in 1986. With the measurement of the  $4f \rightarrow 3d$  transition in pionic magnesium, they evaluate the pion mass with an accuracy to the level of 2.6 ppm [123].

It is possible to estimate the charged pion mass using a different method: studying the positive charged pion disintegration. Measuring the muon momentum in the decay  $\pi_{\text{at rest}}^+ \rightarrow \mu^+ \nu_\mu$  [124, 125], it is possible to measure a lower limit value of the pion mass assuming  $m_{\nu_\mu}^2 \geq 0$ . The experiment performed in 1991 [124] gives a pion mass lower limit equal to 139.569 29 MeV, which was in complete disagreement with the value of “Jeckelmann1986” [123]. A too low value of the pion mass gives, in fact, a negative neutrino square mass.

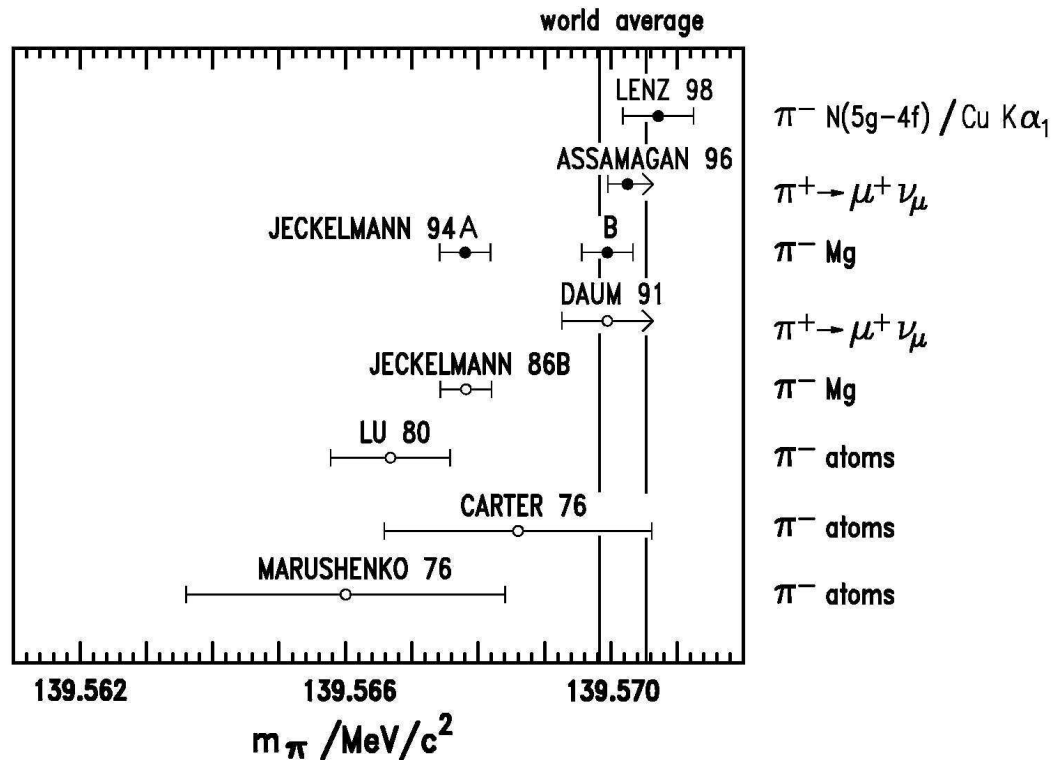


**Figure 4.2** – The most recent results of the charged pion mass. The world average [69] is indicated by the vertical band and it is derived from  $\pi Mg$  (solution B) and  $\pi N$  experiments. The references of older experiments can be found in the text and in Ref. [69].

After a reanalysis of the data obtained in 1986, two possible pion mass values were proposed by Jeckelmann in Ref. [9], based on the assumption that a prevalent part of the pionic atoms had one or two remaining electrons in the K-shell, solution A and B, respectively. Only solution B was in agreement with the pion mass lower limit evaluated using the pion decay from Ref. [124]. Assamagan and his collaborators obtained in 1996 a new pion mass lower limit: 139.570 08 MeV [125], which is compatible with the solution B of Ref. [9].

The actual accepted value [69] is the result of the average of the solution B of Ref. [9] and the new value obtained by a more recent experiment in 1998 [3], and it has a relative error of 2.5 ppm (see Fig. ??). Pionic magnesium was created by interaction of the pion beam with a solid target. The high density of the target allows for the possibility of the electron capture by the pionic atom. In contrast, due to the use of a gaseous target (nitrogen), this effect was negligible in the experiment performed in 1998 [3].

The present uncertainty of the pion mass, reduces the accuracy of the pionic atoms X-ray standard [33] to 2.5 ppm, the pion mass error [69], since, pionic atoms energy levels can be calculated using QED with a precision  $\lesssim 1$  ppm. For this reason, an improvement of the accuracy of such standards requires a reduction of the pion mass error.

In this chapter I will present a new pion mass experiment performed during 2000-2005

period. As in the experiment performed in 1998, we used a gaseous target [3], composed of nitrogen to avoid a possible electron recapture from the pionic atoms. The evaluation of the pion mass is obtained from the measurement of pionic nitrogen  $5g \rightarrow 4f$  transition energy. The measurement of the 4 keV X-ray was performed using the crystal spectrometer described in Sec. 3.3. The experimental data were acquired at the Paul Scherrer Institut in a nine-week period in Spring 2000. During my Ph.D thesis I could participate to the final data analysis, which required the complete study of systematic effects.

The details of the experimental set-up are described in Sec. 4.1. The acquisition and analysis of the experimental data are described in Sec. 4.2 and 4.3. In Sec. 4.4 and 4.5, I will present the corrections and the systematic errors investigation required for the precise evaluation of pion mass. In Sec. 4.6, the final result of the new pion mass measurement is presented. Section 4.7 is dedicated to the test of the Klein-Gordon equation using the evaluation of the energy difference between the  $5g \rightarrow 4f$  and  $5f \rightarrow 4d$  pionic nitrogen transitions.

## 4.1 Description of the set-up

The general description of the Bragg crystal spectrometer and the data acquisition process can be found in Chapter 3. In this section I will describe the specific features of the set-up for the pion mass measurement.

Our crystal spectrometer can measure only energy differences. For this reason, determination of the energy of the pionic nitrogen  $5g \rightarrow 4f$  transition requires a calibration line. For this propose, we used the muonic oxygen  $5g \rightarrow 4f$  transition. Muonic oxygen was produced using a nitrogen-oxygen gas mixture. The muon are created by the pion disintegration and they are trapped by the magnetic bottle along the cyclotron trap axis and they are slowed down by the interaction with Mylar windows of the target. The muons sufficiently slow are captured by the gas in the cell to allow for the formation of muonic oxygen and muonic nitrogen. In the optimal condition, 2-3% of the incoming pions are stopped within the target chamber. About 10% of the muons produced by the decay of the pions are trapped. To check the stability of the spectrometer we used the copper  $K\alpha$  lines. The Cu  $K\alpha$  lines were produced using a copper fluorescence target illuminated by a W anode X-ray tube. The copper target was positioned at the same place as the gas cell. The Cu  $K\alpha$  lines were measured in second order of diffraction from the crystal because their energy are almost double of the  $5g \rightarrow 4f$  muonic oxygen transition energy.

### Target chamber

The target cell used in this experiment was 266 mm long with a diameter of 60 mm and it has, as particularity, a stabilizing structure for the end window with a honeycomb shape (see Fig. 4.3). To enable the formation of muonic oxygen, the target cell was filled with a gas mixture with 90% of oxygen and 10% of nitrogen at a pressure of 1000–1400 mbar, to take into account the ratio  $\sim 10 : 1$  between the trapped pion and muon quantities in the target. Assuming a yield of 40% and 30% for the pionic nitrogen and muonic oxygen 5-4 transition, the expected X-ray rate is in the same order of magnitude for both atomic species.

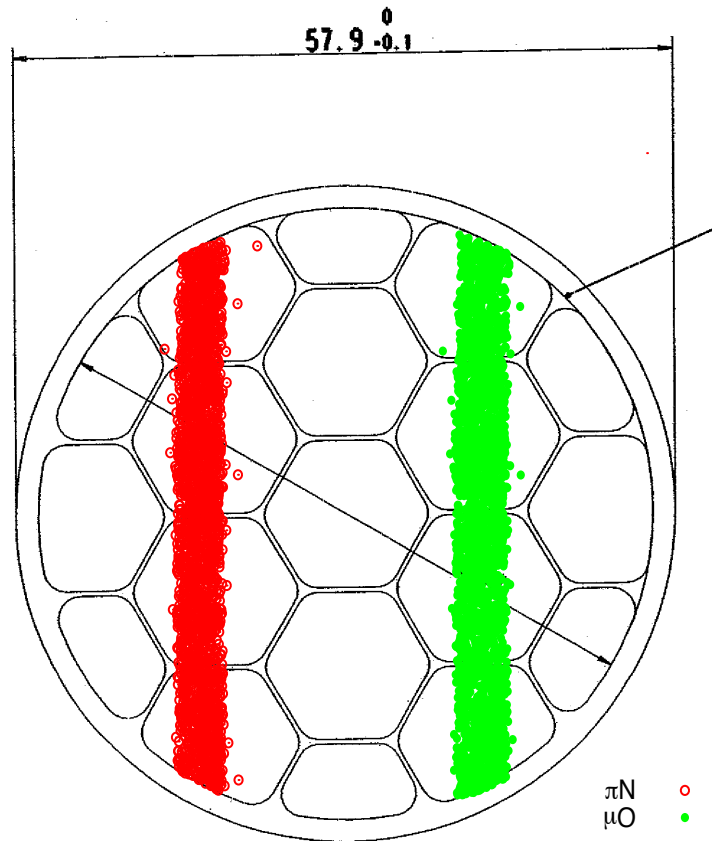


**Figure 4.3** – Honeycomb support on the end of the target cell superimposed to the simulation of the X-rays apparent source on the target window corresponding to the Bragg reflection of pionic nitrogen and muonic oxygen X-rays detected on the CCD array. See also Fig. 4.5.

### Spectrometer

For the measurement of the 4 keV X-rays, we used a spherically bent silicon crystal with a radius of curvature of  $2981.31 \pm 0.33$  mm (measured by ZEISS<sup>1</sup> with mechanical methods). The crystal has a diameter of 100 mm and a thickness of  $290 \mu\text{m}$ . We use the (220) planes for the Bragg reflection assuming the crystal plane spacing recommended by CODATA 2002 [70]:  $2d_{(220)} = 0.384\,031\,193$  nm at  $22.5^\circ\text{C}$ . The correspondent Bragg angle for 4 keV is about  $53^\circ$ . The energies of pionic nitrogen and muonic oxygen  $5g \rightarrow 4f$  lines differ by only 32 eV, which corresponds to a Bragg angle difference of  $\approx 36'$ , i.e., a separation of  $\approx 30$  mm between the two Bragg reflections on the detector, equivalent to about 623 pixels.

Changes to the crystal lattice structure at the edge of the crystal can cause poor quality reflection in this region. For this reason, the apparent crystal size was reduced by placing an aluminum mask with a 90 mm diameter circular aperture in front of the crystal.

<sup>1</sup><http://www.zeiss.com/>

## 4.2 Beam-time operation and data collection

Data was taken continuously over a period of nine weeks in Spring 2000. The measurement comprises the system optimization, calibration data and system stability data. The experimental period was organized as following:

- **Week 1.** Experimental apparatus set-up.
- **Week 2.** Target scan, adjustment of the crystal tilt angle, measurement of the spectrometer dispersion with the Cu  $K\alpha$  line ( $\Theta_{\text{CRY}}$  scan), focus check.
- **Week 3.** Dispersion with Cu  $K\alpha$ . Pionic nitrogen and muonic oxygen data acquisition.
- **Week 4-7.** Pionic nitrogen and muonic oxygen data acquisition. Calibration check with Cu  $K\alpha$  line.
- **Week 8.** Measurement of the spectrometer dispersion with pionic nitrogen transition.
- **Week 9.** Pionic neon data acquisition for spectrometer resolution and crystal-detector distance measurements.

In the following paragraph I will describe more in details the single operations. For additional information see also N. Nelms Ph.D. thesis [114].

### Spectrometer and target optimization

The optimal target cell position and the optimal pion beam line parameters have been obtained by filling the target chamber with neon at 1 bar and measuring the X-ray count rate against the target position, the plastic moderator thickness and the quadrupole line currents. X-rays from the pionic and muonic neon  $3 \rightarrow 2$  transitions at  $\approx 40$  KeV were measured with a germanium detector. This transition was used because, at this energy, there is no self-absorption within the target gas and the X-ray count depends solely upon stop volume. The final parameters adjustment has been done filling the target with oxygen and measuring the pionic and muonic oxygen  $5 \rightarrow 4$  transitions to evaluate the effect of the X-ray absorption within the target gas before they can escape from the chamber.

Once the pionic and muonic atoms production have been optimized, the most favorable parameters of the spectrometer have to be determined. The spectrometer optimization consisted of two operations. The first is to determine the crystal tilt angle, and the second is a target scan (see Fig. 4.5) to find the center portion of the target.

As mentioned in Sec. 3.3, the crystal holder has a stepping motor to adjust the crystal angle relative to the horizontal axis (see Fig. 3.8). A correct value of the tilt angle provides a balanced reflection at the detector, i.e., with a similar proportion of X-rays on the top and bottom CCDs of a column. The target chamber was filled with nitrogen at a pressure of 1000 mbar. With the pionic nitrogen  $5g \rightarrow 4f$  line reflected onto one column of the CCD array, we recorded, for different tilt angles, the number of X-rays detected by the top and the bottom CCDs. The dependency of the detected X-ray on the tilt angle allows for the determination of the optimal position for a correct detector illumination. We found a tilt angle equal to  $+0.35^\circ$ .

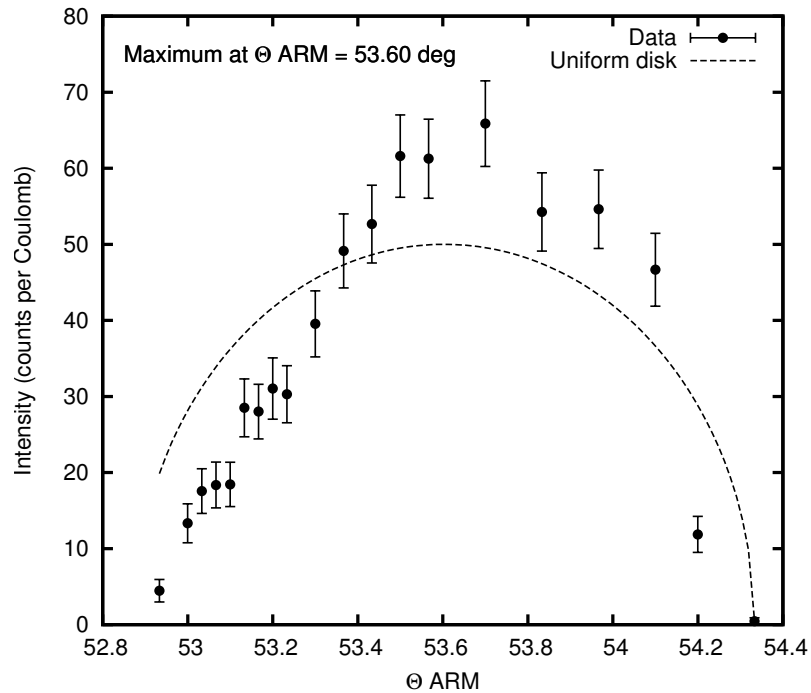


**Figure 4.4** – Target scan results. Plot of count rate against spectrometer arm angle  $\Theta_{ARM}$ . The real data are compared with the fit results assuming a uniform intensity distribution from the circular window of the target. The width of the target window correspond to  $1,46^\circ$  on the plot. The intensity decrease in correspondence with  $\Theta_{ARM} \approx 53.1^\circ$  and  $53.3^\circ$  is due to the honeycomb structure of the window (Fig. 4.3).

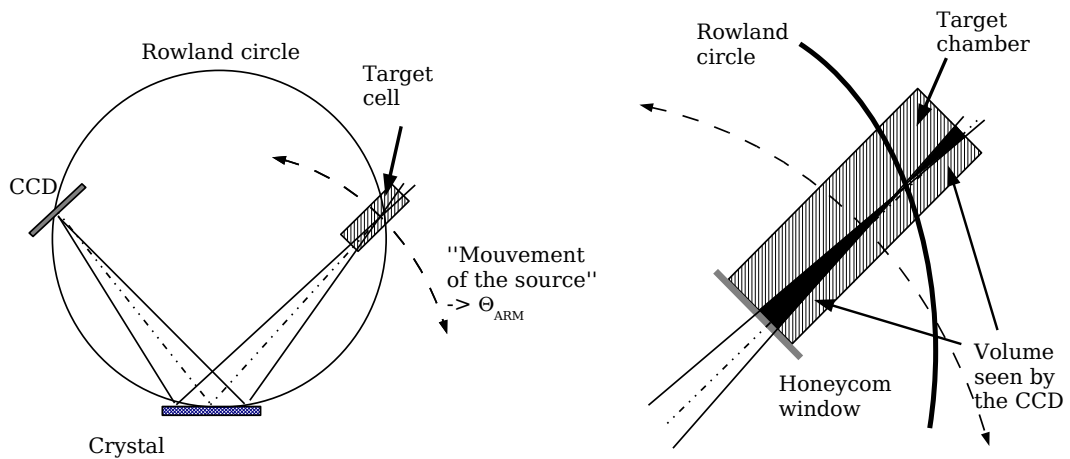


**Figure 4.5** – Scan of the target. The change of the angle  $\Theta_{ARM}$  on the spectrometer is equivalent to change the zone of the target cell that emit the photons detected by the CCD array. The volume of this zone depends on the set-up geometry: the distance between the center of the target chamber with respect to the Rowland circle. The projection of this volume on the honeycomb window defines the apparent sources simulated in Fig. 4.3.

Since the stop distribution has a finite radius, we change the the angle between the crystal and the target keeping the detector-crystal angle fixed, i.e. changing  $\Theta_{ARM}$  value, to determine where the edges of the target occurred to ensure the spectrometer was looking at the optimal central region of the cell (Fig. 4.4). I remember that changing  $\Theta_{ARM}$  correspond to collect on the CCD detector X-rays coming from different part of the target volume. This measurement enables to choose the positions of the X-rays apparent source on the target window, correspondent to the Bragg reflection of the pionic nitrogen and muonic oxygen X-rays on the detector, with respect to the honeycomb structure of the target window. These positions have been chosen to be equally distant from the window center, and in the middle of the honeycomb cell as we can see in Fig. 4.3.

### Data acquisition

Simultaneous reflection from pionic nitrogen and muonic oxygen were recorded, with one line on each column of the CCD array (see Fig. 4.2) for a total period of 5 weeks. At the end of this period we had about 8500 counts in the pionic nitrogen lines and about 9000 counts in the muonic oxygen lines. At regular intervals throughout the beam-time, the target chamber was withdrawn and replaced by a copper fluorescence target illuminated by a X ray tube. Cu  $K\alpha_1$  and Cu  $K\alpha_2$  lines spectra where recorded to check the stability of the spectrometer apparatus. The Cu  $K\alpha$  lines were measured in second order (using the Si (440) planes) and have a Bragg angle very similar to the muonic oxygen  $5g \rightarrow 4f$  transition (see Table 4.1).

### Spectrometer dispersion measurement

For the analysis of the pionic and muonic atom spectra, we must characterize the spectrometer. This means that the dispersion and the resolution of the instrument has to be measured.

The spectrometer dispersion has been evaluated with two different methods: either by direct measurement of the crystal-detector distance and by taking specific X-ray dispersion measurements. During the beam-time, two set of X-ray dispersion measurement were taken: using the  $5g \rightarrow 4f$  pionic nitrogen transition and the copper fluorescence  $K\alpha$  line. In each case, a high statistic measurement of the reflection was recorded at six separate positions across the CCD array by adjusting the crystal angle ( $\Theta_{CRY}$ ). The arm angle was also adjusted for each position to ensure that the spectrometer viewed the same part of the target, i.e., changing  $\Theta_{CRY}$  and  $\Theta_{ARM}$  simultaneously with the relationship in the angle change  $\delta\Theta_{CRY} = -\delta\Theta_{ARM}$ . Unfortunately, a mechanical instability in the arm movement caused a distortion of the spectrometer tube, which resulted in a slight rotation of the CCD cryostat. As consequence, this method of spectrometer dispersion measurement results useless and the final detector distance has been evaluated measuring directly the mechanic components and measuring the focal distance for neon and pionic nitrogen with the analysis of the line shape using the Monte Carlo simulation described in Sec. 5.2. The mechanic component survey measurement gives the result  $D = 2388.1 \pm 0.2$  mm. The focal scan with pionic neon gave a focal distance  $D(Ne) = 2140.82 \pm 0.37$  mm ( $D$  is different because the X-ray energy is in this case, about 4.5 keV), where the error is the quadratic sum of the fit error and the systematic error due to the accuracy of the radius of curvature of the crystal. The analysis of the pionic nitrogen line shape provided a third

**Table 4.1** – Energies and Bragg angles of the atomic transitions involved on the pion mass measurement. The pionic nitrogen energies have been calculated in Ch. 2. The muonic oxygen energies have been provided by Ref. [67] using the muon mass from Ref. [69]. The copper  $K\alpha$  Bragg angles have been calculated using the values in Ref. [126] and adjusting the energy value using the CODATA 2002 recommended value for  $\hbar c = 197.326\,968$  Mev/fm. The corrected Bragg angle have been calculated using the XOP program [103] and they take into account the correction due to the refraction index of the material. The silicon (220) crystal had a radius of curvature of  $2981.31 \pm 0.33$  mm (value measured mechanically from the crystal surface) and  $2d_{(220)} = 0.384\,031\,193$  nm at  $22.5^\circ\text{C}$  [70]. Pionic and muonic X-rays were reflected in the  $2^{nd}$  order of diffraction ((220) plane) and the copper K-lines in the  $4^{th}$  order of diffraction ((440) plane). See Eq. 3.2. The calculation of the pionic nitrogen levels is presented in Sec. 2.4. The strong interaction shift is evaluated in Sec. 4.4.

Transition	Relative intensity	Natural abundance (%)	Energy (eV)	Corrected Bragg angle
$\mu^{16}\text{O } 5g_{7/2} \rightarrow 4f_{7/2}$	1	99.756	4023.50794	$53^\circ 21' 51''$
$\mu^{16}\text{O } 5g_{9/2} \rightarrow 4f_{7/2}$ 1 K el.	35	99.756	4022.82300	$53^\circ 22' 39''$
$\mu^{16}\text{O } 5g_{9/2} \rightarrow 4f_{7/2}$	35	99.756	4023.75025	$53^\circ 21' 35''$
$\mu^{16}\text{O } 5g_{7/2} \rightarrow 4f_{5/2}$ 1 K el.	27	99.756	4023.37341	$53^\circ 22' 01''$
$\mu^{16}\text{O } 5g_{7/2} \rightarrow 4f_{5/2}$	27	99.756	4024.29836	$53^\circ 20' 57''$
$\mu^{16}\text{O } 5f_{5/2} \rightarrow 4d_{5/2}$	1	99.756	4025.39564	$53^\circ 19' 41''$
$\mu^{16}\text{O } 5f_{7/2} \rightarrow 4d_{5/2}$	20	99.756	4025.80308	$53^\circ 19' 13''$
$\mu^{16}\text{O } 5f_{5/2} \rightarrow 4d_{3/2}$	14	99.756	4026.99219	$53^\circ 17' 52''$
$\mu^{18}\text{O } 5g_{7/2} \rightarrow 4f_{7/2}$	1	0.205	4026.66923	$53^\circ 18' 14''$
$\mu^{18}\text{O } 5g_{8/2} \rightarrow 4f_{7/2}$	35	0.205	4026.91324	$53^\circ 17' 57''$
$\mu^{18}\text{O } 5g_{7/2} \rightarrow 4f_{5/2}$	27	0.205	4027.46417	$53^\circ 17' 19''$
$\pi^{14}\text{N } 5g \rightarrow 4f$ 1 K el.	35	99.64	4054.92528	$52^\circ 46' 17''$
$\pi^{14}\text{N } 5g \rightarrow 4f$	35	99.64	4055.38012	$52^\circ 45' 47''$
$\pi^{14}\text{N } 5f \rightarrow 4d$ QED	35	99.64	4057.69379	$52^\circ 43' 12''$
$\pi^{14}\text{N } 5f \rightarrow 4d$ QED + $\epsilon_{4d}$	35	99.64	4057.70089	$52^\circ 43' 12''$
$\pi^{14}\text{N } 5d \rightarrow 4p$ QED	27	99.64	4061.94796	$52^\circ 38' 29''$
$\pi^{14}\text{N } 5d \rightarrow 4p$ QED + $\epsilon_{4p}$	27	99.64	4063.087	$52^\circ 37' 23''$
$\pi^{15}\text{N } 5g \rightarrow 4f$		0.36	4058.24019	$52^\circ 42' 36''$
$\pi^{15}\text{N } 5f \rightarrow 4d$		0.36	4060.55549	$52^\circ 40' 01''$
$\text{Cu}K\alpha_{22}$			8027.98600	$53^\circ 32' 40''$
$\text{Cu}K\alpha_{12}$			8045.36000	$53^\circ 22' 39''$

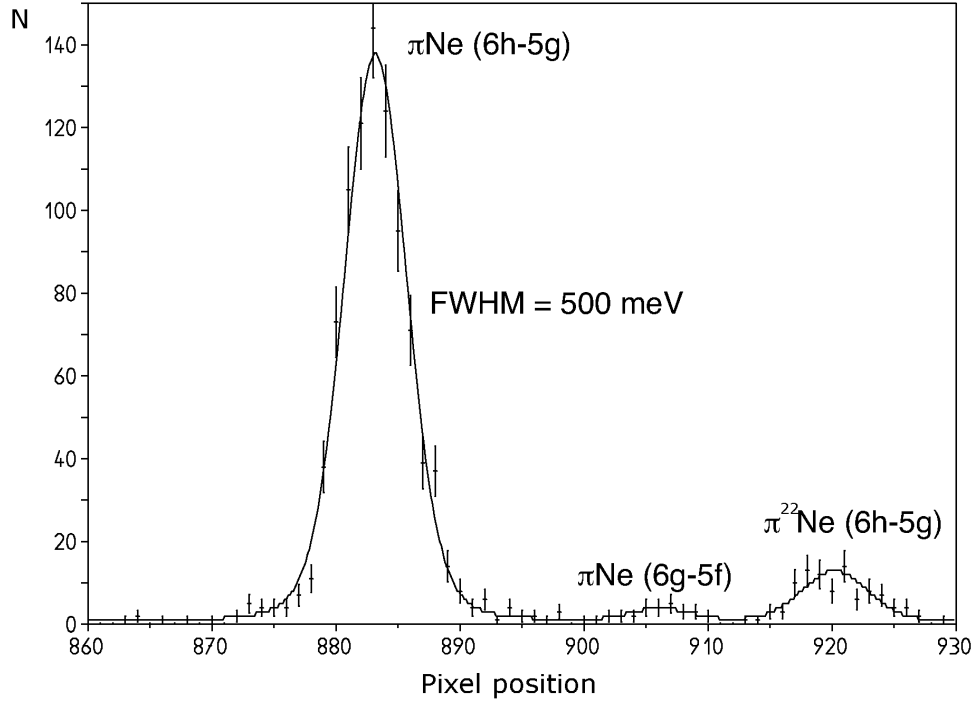


**Figure 4.6** – One-dimensional position spectrum of pionic neon  $6h \rightarrow 5g$  transitions. The spectrometer resolution (FWHM) is about 500 meV. The  $6h \rightarrow 5g$  line for the naturally occurring  $^{22}\text{Ne}$  isotope is also visible.

estimation of the crystal-detector distance by giving a deviation to the assumed position of  $+0.34 \pm 0.52$  mm, where the error is the quadratic sum of the fit error and the systematic error due to the accuracy of the radius of curvature of the crystal. All three methods agree inside two standard deviations and combining all three results we obtained:

$$D = 2388.192 \pm 0.166 \text{ mm.} \quad (4.1)$$

### Spectrometer response function and focal position measurement

During the beam-time, the spectrometer resolution was evaluated by taking a high statistics measurement of pionic neon  $6h \rightarrow 5g$  transition ( $\approx 4.5$  keV). Neon was chosen because it is a monoatomic gas and consequently does not suffer from the Doppler broadening due to Coulomb explosion during the pionic atoms formation (see Sec. 4.3).

We obtained the spectrometer resolution by taking a set of 7 high statistic spectra with different values of the crystal-detector distance. The spectrometer resolution was estimated by measuring the Full Width Half Maximum (FWHM) of the pionic neon transition peak, which was equal to  $\approx 500$  meV (see Fig. 4.6). This value has to be compared to the theoretical resolution of a perfect crystal obtained from a Monte Carlo simulation, which is equal to 330 meV. The difference between these values is caused by imperfections of the crystal, which can be taken into account by the simulation, convoluting the response function of a perfect crystal with a Gaussian distribution with  $\sigma = 56 \mu\text{rad}$ .

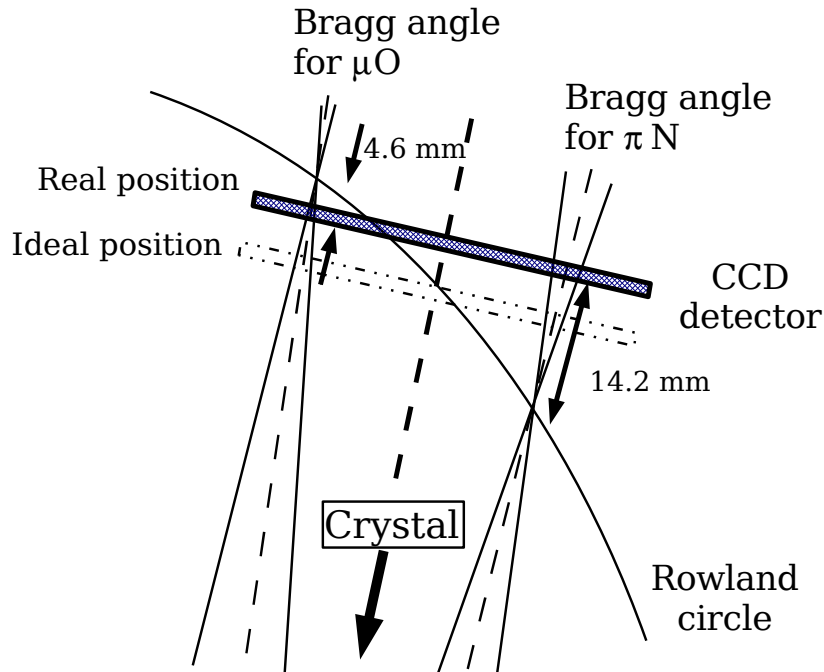


**Figure 4.7** – Position of the CCD array with respect to the Rowland circle. From the pionic neon focal scan, it was possible to evaluate the distance between the detector plane and the focal position of pionic nitrogen and muonic oxygen. It results a distance of 4 mm for the muonic oxygen  $5g \rightarrow 4f$  transition, and 15 mm for the pionic nitrogen  $5g \rightarrow 4f$  transition.

The precise value of the radius of curvature of the Si(220) crystal, has been obtained in spring 2005 by measuring mechanically the crystal surface. The measured value is  $R = 2981.31 \pm 0.33$  mm, which is significantly different from the nominal value  $R = 2982.5$  mm. This new value is in agreement with the radius of curvature evaluated from the analysis of the multicharged ion spectra obtained in August 2005 (see also Sec. 5.2) and it is used to measure the pionic neon focal distance, which enables to determine exactly the position of the detector plane with respect to the Rowland circle in the pion mass measurement set-up. From this analysis, described more accurately in Sec. 5.2, it results that, during the data acquisition, the pionic nitrogen focal position was at 14.2 mm from the detector into the crystal direction, and the muonic oxygen was at about 4.6 mm in the opposite direction as showed in Fig. 4.7, instead of the estimated distance of 9.4 mm for both lines (closer and further to the crystal, respectively). This information is essential for the fit of the one-dimensional spectrum because it allows to take into account the line defocusing effect which can introduce a shift of the peak centroid.

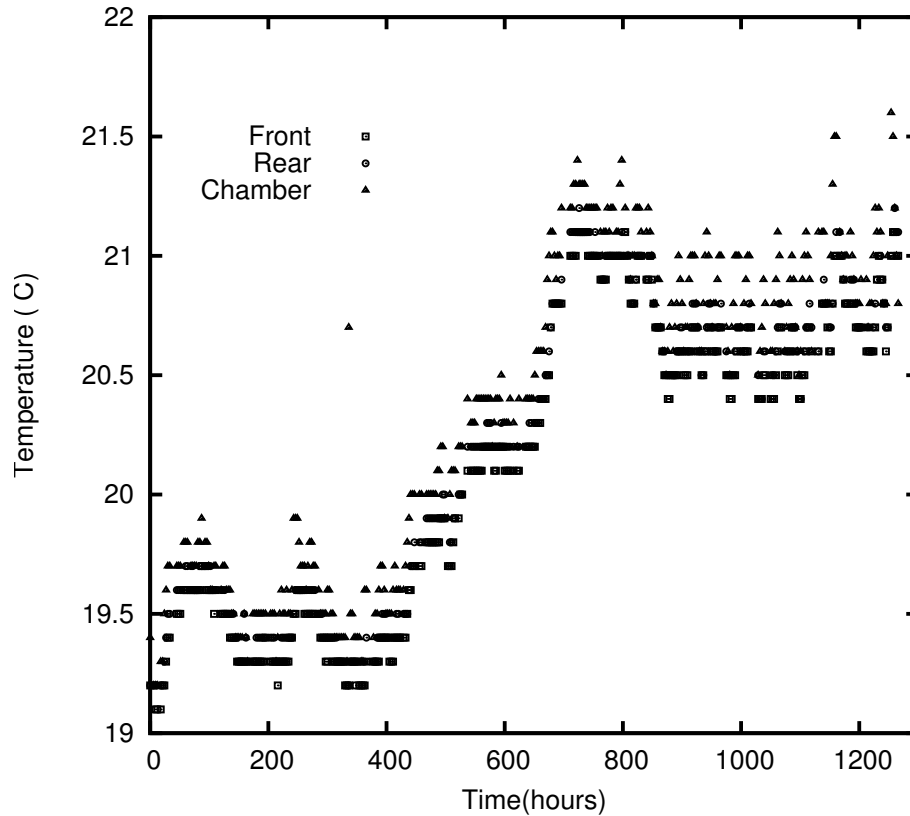


**Figure 4.8** – Crystal and housing temperature variation over the duration of the beam time. The period when simultaneous pionic nitrogen and muonic oxygen were recorded starts at  $hour=330$  and stops at  $hour=990$ .

### 4.3 Data analysis

#### Analysis of the raw data

The data from the CCD array have been analyzed using the program CSDCLUSTER to produce the one-dimensional spectrum necessary for the evaluation of the angular distance between the pionic nitrogen and muonic oxygen Bragg reflections. The value of the energy cut and cluster analysis parameters have been chosen to optimize the peak-to-background ratio, i.e., the accuracy of the fit of the one-dimensional spectrum. The curvature correction parameters have been calculated from the fit of the pionic nitrogen line. The choice of the line for this calculus does not affect the final results as we will see in Sec. 4.5.

During the data acquisition, the crystal temperature was passively monitored using three Platinum Resistance Thermometers (PRT), one at the front of the crystal, at the back and one outside the crystal chamber.

The temperature of the crystal changed slowly, with a maximum variation of  $2^{\circ}\text{C}$  (see Fig. 4.8). In correspondence to this variation, the crystal d-spacing varied and a corresponding correction has to be applied to analyze the data acquired at different temperatures. To perform such corrections, the data have been grouped in four set corresponding to similar temperatures. Each set has been analyzed independently producing four one-

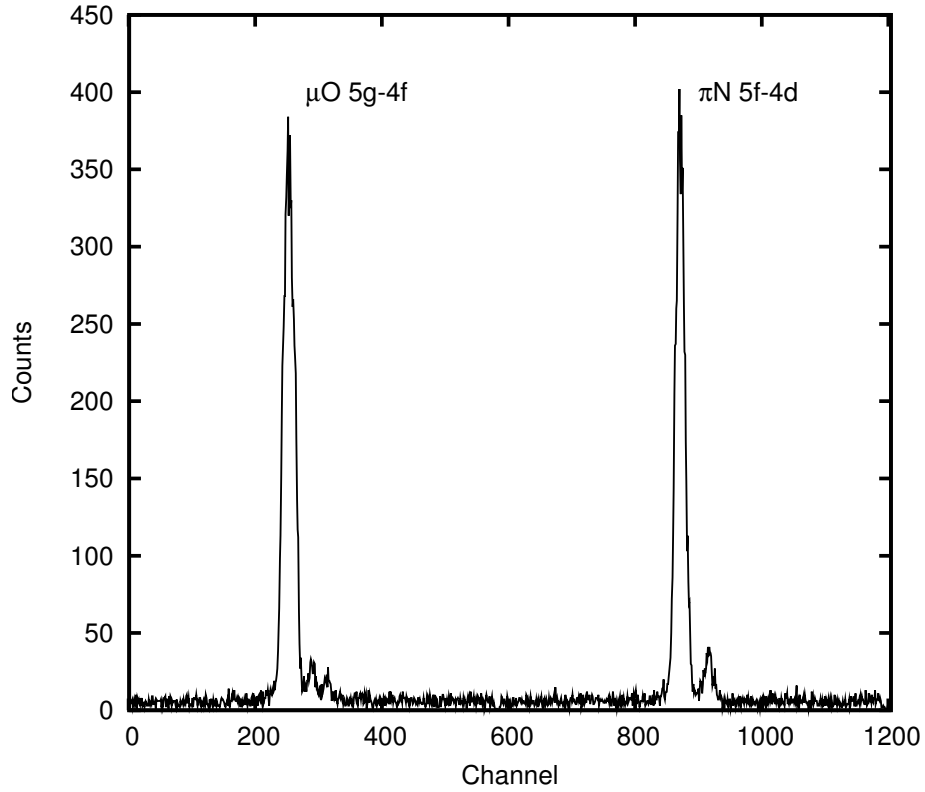


**Figure 4.9** – Spectrum position of the  $5 \rightarrow 4$  pionic nitrogen and muonic oxygen.

dimensional position spectra to measure the distance between the pionic nitrogen and muonic oxygen lines.

Using the data from the pionic nitrogen dispersion measurement, it was possible in addition to produce a high statistics spectrum of the  $5 \rightarrow 4$  pionic nitrogen transitions (Fig. 4.10) that has been used for the test of the Klein-Gordon equation.

### Characteristics of the one-dimensional spectrum

The characteristics of the  $5 \rightarrow 4$  transitions for pionic nitrogen and muonic oxygen are quite different. These differences are principally due to spin of the orbiting particle, which determines the fine structures of the transition. The muonic oxygen  $5g \rightarrow 4f$  transition is split into three different lines due to the spin of the muon:  $5g_{9/2} \rightarrow 4f_{7/2}$ ,  $5g_{7/2} \rightarrow 4f_{7/2}$  and  $5g_{7/2} \rightarrow 4f_{5/2}$ , which have theoretical intensity ratios of 35:1:27 [60, 67]. The presence of the naturally occurring oxygen isotope  $^{18}\text{O}$  (0.205%) makes a noticeable contribution from  $\mu^{18}\text{O}$   $5g_{9/2} \rightarrow 4f_{7/2}$  and  $5g_{7/2} \rightarrow 4f_{5/2}$  transitions. No fine structure splitting due to the spin occurs in the case of pionic nitrogen. As for the muonic oxygen, the parallel transition  $5f \rightarrow 4d$  has to be taken into account as well as the contribution from the naturally occurring  $^{15}\text{N}$  (0.36%)  $5g \rightarrow 4f$  transition. All the transition energies are presented in Table 4.1.

The profile of the peaks on the one-dimensional spectrum depends on the response function of the spherically bent crystal spectrometer. This response function is defined

by the rocking curve of the crystal, by the position of the CCD detector with respect to the focal position of the peak and by the Johann and other aberration described in Sec. 3.3. As discussed in the previous section, the focal position of the pionic nitrogen and muonic oxygen lines were different (Fig. 4.7). For this reason, the corresponding peaks were characterized by a different response function. I remember that the Johann broadening produces an asymmetry of the peak and that depends on the crystal aperture.

Contrary to the pionic neon, muonic oxygen and pionic nitrogen are subject to the Coulomb explosion during their formation [127]. Oxygen and nitrogen in the target cell are in form of diatomic molecules. As the electrons are ejected during the de-excitation of the exotic atoms, the ionization reaches a level where the Coulomb repulsion between nuclei forces the fragment of the molecule apart, causing a Doppler shift in the observable transition energy. This results in a symmetric broadening of the response function. Consequently, the FWHM of the pionic nitrogen and muonic oxygen is of the order 800 meV, compared to only 500 meV for pionic neon.

Cascade models predict that complete ionization has a high probability in the case of pionic nitrogen and muonic oxygen. Yet there is a small probability (2-3%) that one or two K-shell electrons remain [3].

## Analysis of the one-dimensional spectrum

### Model of the line profile

The fit of the peaks of the one-dimensional spectra has been performed using FITIT, a program similar to FIT6 developed by L. Simons, and using Monte Carlo simulations of the Bragg spectrometer as described in Sec. 5.2. The focal scan with pionic neon provides the measurement of the position of the Rowland circle with respect to the detector in the experimental set-up, and the additional Gaussian broadening of the response function, which takes into account the crystal imperfections. Using this information, the Monte Carlo simulation provides the best adapted response function for the muonic oxygen and pionic nitrogen peaks. The use of the Monte Carlo X-ray tracking routine enables to include the Johann aberrations and the response function deformation due to the defocusing in the line model of the fit. In addition, it can take into account the effect of the circular shape of the target window on the peak position. This curved shape can, in fact, modify the line barycenters, and thus, the distance between Bragg reflections. The reliability of this simulation has been accurately tested using He-like ions X-rays as described in Sec. 5.2.

### Doppler broadening, intensity ratio and K-shell electron contamination

The fit of the pionic nitrogen high statistics spectrum, using the dispersion measurement data, provides an accurate evaluation of the Doppler broadening parameters and the ratio intensity  $I$  between parallel transitions with an relative error of 0.75% and 1.7% respectively. In particular we measured:

$$\frac{I(5f \rightarrow 4d)}{I(5g \rightarrow 4f)} = 0.0673 \pm 0.0017. \quad (4.2)$$

These values have been used for the fit of the position of pionic nitrogen in the mixed spectrum with muonic oxygen. These spectra are in fact characterized by a statistics

six times smaller. Fixing some of the fit parameters reduces the uncertainty on the peak position evaluation in the mixed spectrum. In addition, the high statistic spectrum enabled to estimate the probability to have a remaining K-shell electron to be smaller than 0.16%. For this reason in the fit of the pionic nitrogen and muonic oxygen peak position, we did not consider the contribution of the atoms with a remaining electron in the K-shell.

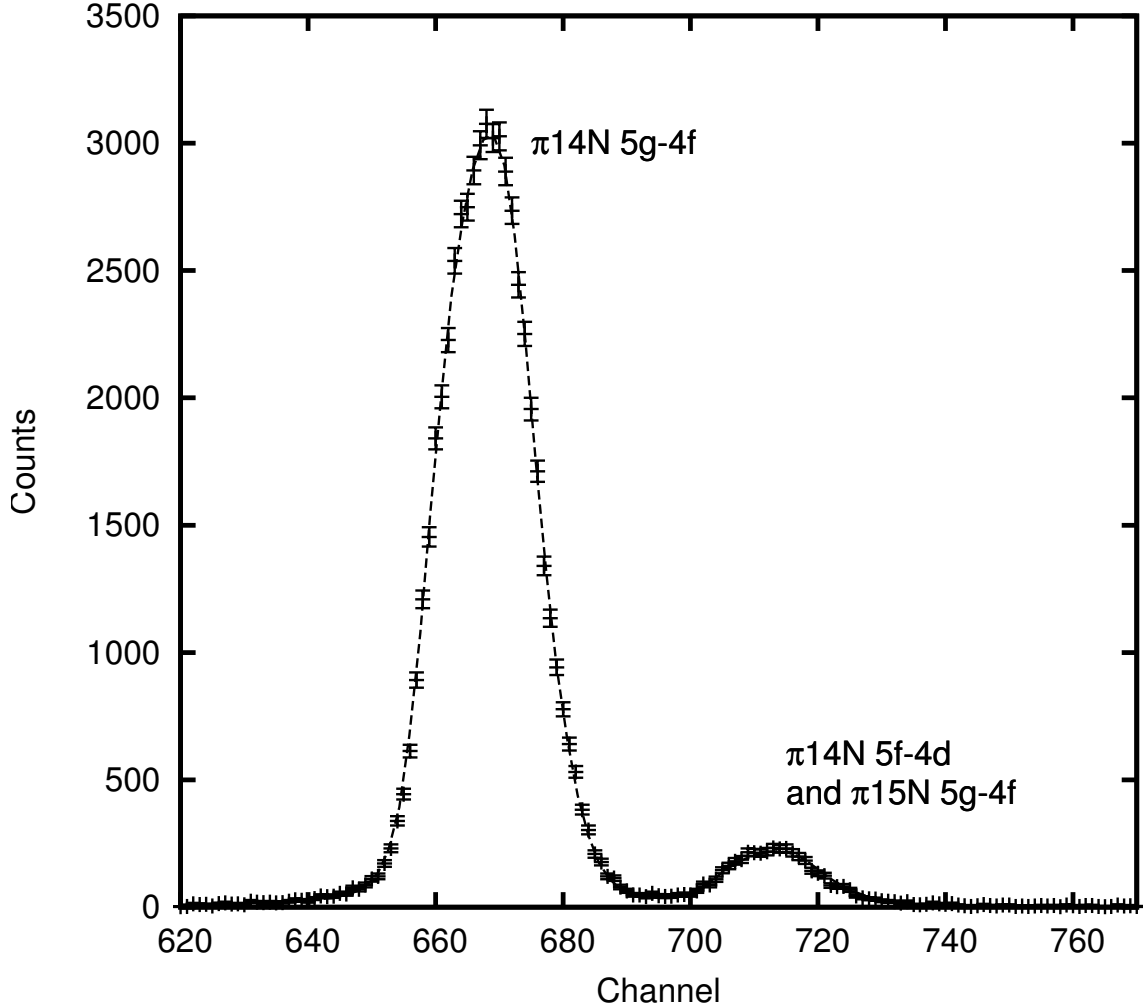


**Figure 4.10** – High statistic spectrum for pionic nitrogen  $5 \rightarrow 4$  transitions. From the fit of this spectrum, it was possible to obtain an accurate measurement of the Doppler broadening, due to the Coulomb explosion, and of the intensity ratio between parallel transitions. In addition, it was possible to estimate the abundance of pionic nitrogen atoms with a remaining K-shell electron to be smaller than 0.16%. One pixel correspond to 52 meV.

#### Fit of the pionic nitrogen and muonic oxygen mixed spectra

For the pionic nitrogen, the Doppler broadening parameters and the parallel transition ratio intensity were fixed to the values obtained from the high statistics spectrum (Fig. 4.10). The intensity ratio between  $\pi^{14}\text{N}$ ,  $\pi^{15}\text{N}$  and between  $\mu^{16}\text{O}$ ,  $\mu^{18}\text{O}$  transitions were fixed taking into account the naturally abundancy of the two pairs of isotopes. For muonic

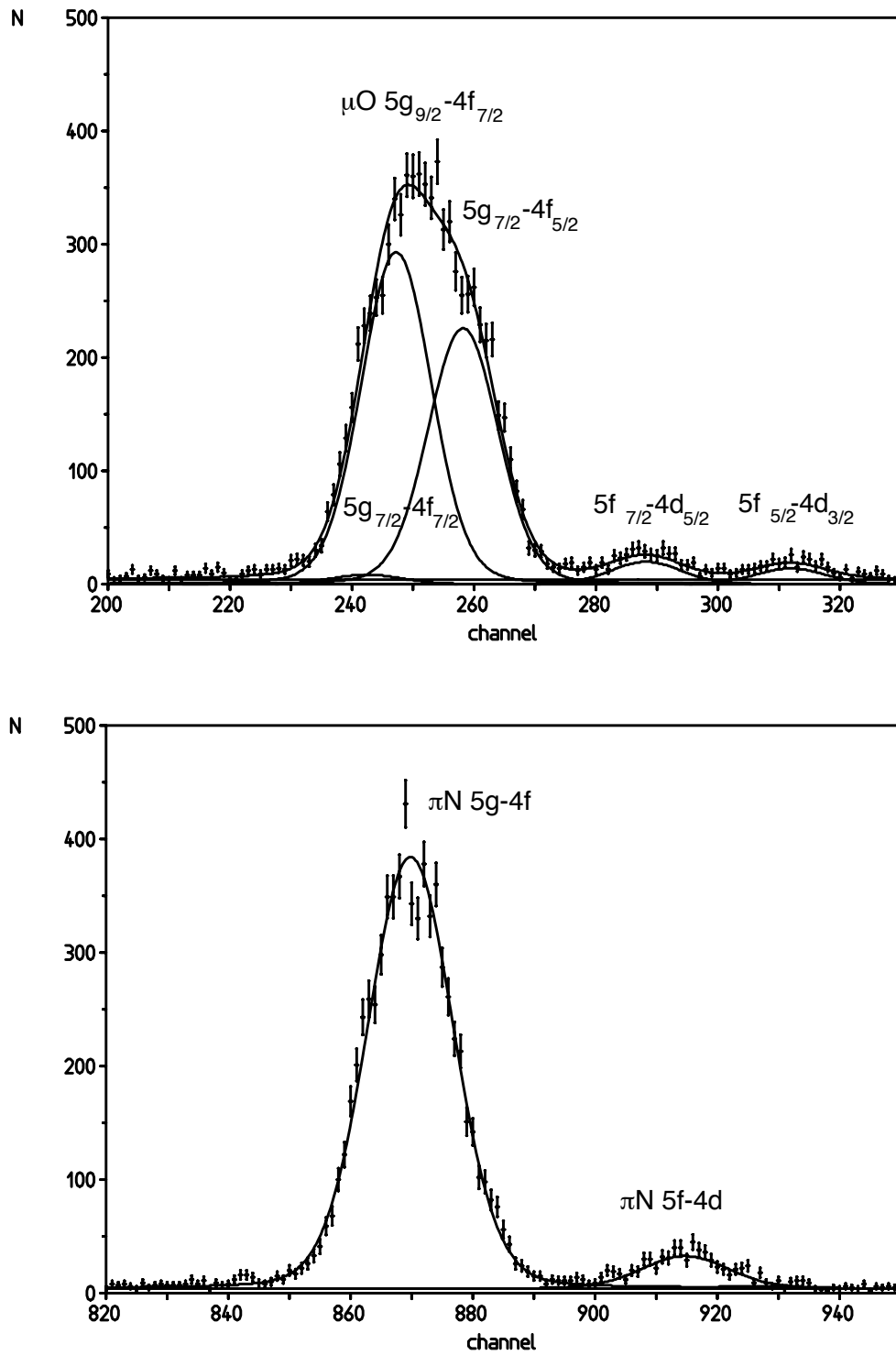


**Figure 4.11** – Experimental spectrum compared to the fit for muonic nitrogen (top) and pionic nitrogen transitions (bottom). One pixel correspond to 50 meV near the muonic oxygen lines, and 52 meV near the pionic nitrogen lines.

oxygen no high statistics spectrum was available and the intensity ratio between parallel transitions and the Doppler broadening parameters were evaluated at the same time that the peak position. The intensity ratio between fine structure components was fixed to the theoretical values 35:1:27 for  $5g_{9/2} \rightarrow 4f_{7/2}$ ,  $5g_{7/2} \rightarrow 4f_{7/2}$  and  $5g_{7/2} \rightarrow 4f_{5/2}$  transitions and 20:1:14 for  $5f_{7/2} \rightarrow 4d_{5/2}$ ,  $5f_{5/2} \rightarrow 4d_{5/2}$  and  $5f_{5/2} \rightarrow 4d_{3/2}$  transitions [60, 67].

The Doppler broadening could roughly be evaluated from a Gaussian fit of the lines. It results to be  $815 \pm 13$  meV for the pionic nitrogen and  $635 \pm 13$  meV for muonic oxygen.

The accuracy of the peak position measurement was in the order of 0.09 pixels. In addition to the error provided by the  $\chi^2$  minimization, one has to take into account the error due to the Monte Carlo redistribution of the events on the detector due to the CCD relative orientation and curvature correction. This error has been evaluated measuring the distance of the pionic and muonic peaks using two one-dimensional spectra generated with the CSDCLUSTER program (or CCDM) from the same set of data (Fig. 4.3). The event redistribution produces an error in the order of 0.01 pixels. The final distance between the Bragg reflections has been evaluated using the four sets of data and applying the required correction to take into account the temperature change effect. The final evaluation for the distance between the muonic oxygen  $5g_{9/2} \rightarrow 4f_{7/2}$  and pionic nitrogen  $5g \rightarrow 4f$  peaks is:

$$x(\pi N) - x(\mu O) = (622.537 \pm 0.121) \text{ pixels} \quad (4.3)$$

This position difference enables to calculate the Bragg angle difference between pionic and muonic lines, i.e., the energy of the pionic nitrogen  $5g \rightarrow 4f$  transition. From this energy measurement, the pion and muon mass ratio is calculated. Some corrections have to be applied before to obtain the correct evaluation of the angle difference between the Bragg reflections. These corrections, summarized in Table 4.4, are presented in detail in the next section.

## 4.4 Discussion of the corrections

### Temperature correction of the crystal d-spacing and of vacuum pipe length

The crystal d-spacing is temperature dependent:

$$d(T) = d(T_0)[1 - \alpha(T - T_0)], \quad (4.4)$$

where  $T$  is the temperature in  $^{\circ}\text{C}$ ,  $\alpha = 2.57 \times 10^{-6} \text{ }^{\circ}\text{C}^{-1}$  [128, 129] is the linear expansion coefficient at  $T = T_0$  and  $d_0 = 0.384\ 031\ 193$  nm [70] is the (110) d-spacing of silicon for a reference temperature  $T_0 = 22.5^{\circ}\text{C}$ .

A change in temperature causes a change  $\Delta d$  of the crystal spacing, that induces a modification  $\Delta\Theta_{TC}$  of the Bragg angle  $\Theta_B$ :

$$\Delta\Theta_{TC} = -\tan\Theta_B \frac{\Delta d}{d} = -\tan\Theta_B \alpha \Delta T, \quad (4.5)$$

which leads to the relative Bragg angle correction

$$\Delta\Theta_{TC}(\mu O) - \Delta\Theta_{TC}(\pi N) = [\tan\Theta_B(\pi N) - \tan\Theta_B(\mu O)] \frac{\Delta d}{d}, \quad (4.6)$$

**Table 4.2** – Corrections and systematic effects for the evaluation of the angular distance between muonic oxygen  $5g_{9/2} \rightarrow 4f_{7/2}$  and pionic nitrogen  $5g \rightarrow 4f$  transitions:  $\Theta_B(\mu O) - \Theta_B(\pi N)$ .

	Correction (")	error (")	error (ppm)
Bending correction	0.214	$\pm 0.004$	$\pm 0.015$
Penetration depth correction	-0.004	$\pm 0.001$	$\pm 0.004$
Strong interaction $45 \mu\text{eV}$	-0.003	$\pm 0.003$	$\pm 0.011$
1 K electron $< 0.16\%$	0.000	$\begin{cases} +0.050 \\ -0.000 \end{cases}$	$\begin{cases} +0.184 \\ -0.000 \end{cases}$
Curvature correction	0.000	$\pm 0.040$	$\pm 0.147$
Off-line CCD height reduction	0.000	$\pm 0.061$	$\pm 0.225$
Fit region	0.000	$\pm 0.004$	$\pm 0.015$
Model for the line fit	0.000	$\pm 0.070$	$\pm 0.258$
Detector-Crystal distance	0.000	$\pm 0.153$	$\pm 0.564$
Orientation detector + tubes $\leq 0.14^\circ$	0.000	$\begin{cases} +0.008 \\ -0.000 \end{cases}$	$\begin{cases} +0.030 \\ -0.000 \end{cases}$
Height CCD (out of plane) $\leq 20$ mm	0.000	$\begin{cases} +0.009 \\ -0.000 \end{cases}$	$\begin{cases} +0.032 \\ -0.000 \end{cases}$
Target shape	0.000	$\pm 0.027$	$\pm 0.099$
CCD alignment ("gap")	0.000	$\pm 0.090$	$\pm 0.332$
Pixel distance	0.000	$\pm 0.033$	$\pm 0.122$
$\pi N, \mu O$ energies	0.000	$\pm 0.093$	$\pm 0.343$
Temperature renormalisation of $D$	-0.003	$\begin{cases} +0.005 \\ -0.005 \end{cases}$	$\begin{cases} +0.018 \\ -0.018 \end{cases}$
Corr: sum /Errors: quadratic sum	0.207	$\begin{cases} +0.215 \\ -0.209 \end{cases}$	$\begin{cases} +0.792 \\ -0.769 \end{cases}$

where the angles  $\Delta\Theta_{TC}$  are in radians. To apply the temperature correction, we divided the data in four different groups of files, which correspond to different temperature conditions. The maximum value for this correction was for the temperature  $19.2^\circ\text{C}$  with:

$$\Delta\Theta_{TC}(\mu O) - \Delta\Theta_{TC}(\pi N) = 0.050''. \quad (4.7)$$

In the same way, it was necessary to correct the detector-crystal distance  $D$  taking into account the length change of the vacuum pipes, due to the temperature, connecting the crystal housing to the detector housing.

### Crystal bending corrections

In Sec.3.3 we have seen that the crystal bending causes a change of the lattice constant  $d$  of the crystal. As we have presented in Eq. (3.17), the effect of such changes on the X-ray reflection depends on the energy of the incident photons, i.e., on the extinction depth  $z$  inside the crystal. The extinction depth is different for  $\pi$  and  $\sigma$  polarization and, since the X-ray in the experiment are unpolarized, we use the weighted average. The extinction depth and relative intensities are calculated using the XOP code [103] and they are listed in Table 4.3.

To calculate the angular correction, we used Eq. (3.17) and (3.18), the values in Table 4.3, the Poisson's ratio for silicon with respect to the (110) direction for a spherically bent crystal  $\nu = 0.270$  (see Appendix 7.2), the half crystal thickness  $\zeta = 145 \mu\text{m}$  and the

**Table 4.3** – Crystal extinction depth, including normal absorption, and intensities for  $5g_{9/2} \rightarrow 4f_{7/2}$  muonic oxygen (first line) and  $5g \rightarrow 4f$  pionic nitrogen (second line) X-ray photons calculated with the XOP code [103].

Energy (eV)	$\pi$ -polarization		$\sigma$ -polarization		Average extinction length ( $\mu\text{m}$ )
	Extinction length ( $\mu\text{m}$ )	Relative intensity	Extinction length ( $\mu\text{m}$ )	Relative intensity	
4023.75	6.88	14.62	1.98	79.22	2.74
4055.38	7.39	12.89	1.98	77.86	2.75

radius of curvature  $R = 2981.31$  mm. We obtain the Bragg angle corrections:

$$\Delta\Theta_{LDC}(\mu O) = +9.937'' \quad \Delta\Theta_{LDC}(\pi N) = +9.723'', \quad (4.8)$$

which lead to the relative Bragg angle correction

$$\Delta\Theta_{LDC}(\mu O) - \Delta\Theta_{LDC}(\pi N) = +0.214'' \pm 0.004''. \quad (4.9)$$

The error takes into account the uncertainty on the crystal thickness and on the Poisson's ratio.

In the same way, we can calculate the effect of the penetration depth correction using Eq. (3.19). Substituting the values presented in Table 4.3, we obtain the corrections:

$$\Delta\Theta_{PDC}(\mu O) = +0.141'' \quad \Delta\Theta_{PDC}(\pi N) = 0.144'', \quad (4.10)$$

which leads to the relative Bragg angle correction:

$$\Delta\Theta_{PDC}(\mu O) - \Delta\Theta_{PDC}(\pi N) = -0.003''. \quad (4.11)$$

### Strong interaction correction

The pion mass value has been evaluated using the theoretical prediction for pionic nitrogen transition energies taking into account only the electromagnetic interaction between the charged pion and the nucleus. However, as discussed in Sec. 3.2, the presence of strong interaction force can modify the energy levels of pionic atoms. The hadronic interaction causes an energy shift  $\epsilon_{nl}$  of the atomic levels and open a capture channel, which reduces the lifetime of the level. This reaction is due to the overlap between the pion and nucleus wavefunctions and it is observable as a line broadening  $\Gamma_{nl}$  in the X-ray transition, which is larger for low-angular-momentum states.

For the pion mass evaluation we chose to measure  $5g \rightarrow 4f$  and  $5f \rightarrow 4d$  transitions because the strong interaction does not change significantly the levels energy. Only for the  $4d$  level, which has the lowest angular momentum, we could expect a detectable correction of its energy.

There is no direct measurement of the strong interaction shift for  $n = 4$  and  $n = 5$  levels in pionic nitrogen. However, these shifts can be evaluated by rescaling the available measured shift for  $2p$  levels in pionic carbon and pionic oxygen,  $\epsilon_{2p}(C)$  and  $\epsilon_{2p}(O)$ , and the shift on the  $1s$  level in pionic nitrogen,  $\epsilon_{1s}(N)$ .

Assuming that the reaction probability weakly depends on the quantum numbers, the strong interaction shifts  $\epsilon_{nl}$  for different orbitals are related by the formula [130]:

$$|\epsilon_{nl}| \approx \left(\frac{R}{a_0}\right)^{2l} |\epsilon_{ns}|, \quad (4.12)$$

where  $R$  is the typical range of strong interaction and  $a_0$  of the Bohr radius of pionic atom:

$$a_0 = \frac{\hbar c}{\mu c^2 \alpha Z} \approx \frac{192 \text{ fm}}{Z}, \quad (4.13)$$

with  $Z$  is the atomic number. Equation (4.12) is deduced assuming a potential  $V$  with a short range  $R$  and comparing expected values  $\langle nl|V|nl\rangle$  for different wavefunctions.

The shift for the  $4s$  and  $5s$  levels can be calculated using the Deser formula [85, 98]:

$$\epsilon_{ns} = -\frac{2\pi\hbar^2}{\mu} |\Psi_{ns}(0)|^2 \mathcal{R}e(a_s) = -\frac{2\hbar^2}{\mu} \frac{\mathcal{R}e(a_s)}{a_0^3 n^3}, \quad (4.14)$$

where  $a_s$  is the  $s$ -wave pion-nucleus scattering length due to the strong interaction and  $\mu$  is the reduced mass of the system.

Using the experimental value  $\epsilon_{1s}(N) = -11.72 \pm 0.22 \text{ keV}$  [131], we obtain:

$$\epsilon_{4s}(N) = \frac{1}{64} \epsilon_{1s}(N) = (-183.1 \pm 3.4) \text{ eV} \quad \epsilon_{5s}(N) = \frac{1}{125} \epsilon_{1s}(N) = (-93.8 \pm 1.8) \text{ eV} \quad (4.15)$$

The term  $(R/a_0)$  in Eq. (4.12) required the evaluation of  $\epsilon_{np}$  shifts that can be deduced using the formula [98, 132]:

$$\epsilon_{np} = -\frac{6\pi\hbar^2}{\mu} |\nabla\Psi_{np}|^2 \mathcal{R}e(a_p) = -\frac{6\hbar^2}{\mu} \frac{\mathcal{R}e(a_p)}{a_0^5} \frac{n^2 - 1}{3n^5}, \quad (4.16)$$

where  $a_p$  is the  $p$ -wave pion-nucleus scattering volume due to the strong interaction.

Before calculating  $\epsilon_{4p}(N)$  and  $\epsilon_{5p}(N)$ , we have to evaluate  $\epsilon_{2p}$  for pionic nitrogen from the experimental values for pionic carbon and oxygen using the empirical relationship [133]:  $\epsilon_{2p} \propto Z^{5.5}$ . For pionic carbon we have  $\epsilon_{2p}(C) = 3.16 \pm 0.10 \text{ eV}$ , and for pionic oxygen  $\epsilon_{2p}(O) = 15.5 \pm 0.16 \text{ eV}$  [133]. For pionic nitrogen we obtain the value  $\epsilon_{2p}(N) = 7.30 \pm 0.15 \text{ eV}$ . Using equation (4.16), we have

$$\epsilon_{4p} = 1141 \pm 23 \text{ meV} \quad \epsilon_{5p} = 598 \pm 12 \text{ meV}. \quad (4.17)$$

We can now evaluate the term  $R/a_0$  for  $n = 4$  and  $n = 5$  levels of pionic nitrogen:

$$\left(\frac{R}{a_0}\right)_{n=4}^2 = \frac{\epsilon_{4p}}{\epsilon_{4s}} = 0.00623 \pm 0.00018 \quad \left(\frac{R}{a_0}\right)_{n=5}^2 = \frac{\epsilon_{5p}}{\epsilon_{5s}} = 0.00638 \pm 0.00018 \quad (4.18)$$

From these values, we can calculate the strong interaction shifts  $\epsilon_{nl}$  for the pionic nitrogen levels used for the pion mass measurement. The results are summarized in Table 4.4.

As expected, we have the largest strong interaction shift for the  $4d$  level (between the measured transitions)  $\epsilon_{4d}(N) = +7.10 \text{ meV}$ . This shift has to be taken into account for the spectrum analysis for the pion mass measurement because it produces an increase of  $+7.10 \text{ meV}$  of  $5f \rightarrow 4g$  pionic nitrogen transition energy. In opposite, for the other levels, the effect of the attraction between the pion and the nucleus is completely negligible.

In the same way, we can demonstrate that the strong interaction width  $\Gamma_{nl}$  is always  $\ll 0.5 \text{ eV}$ , the spectrometer resolution.

**Table 4.4** – Calculation of the strong interaction shift in pionic nitrogen levels. The shift is evaluated from the experimental data for pionic carbon and oxygen  $2p$  levels and for pionic nitrogen  $1s$  level using the formula in the text. The corrected energy is:  $E_{nl} = E_{nl}(QED) + \epsilon_{nl}$ , with  $E_{nl} > 0$ .

Atomic level	$\epsilon_{nl}$		
4p	+ 1.14	$\pm 0.03$	eV
4d	+ 7.10	$\pm 0.40$	meV
4f	+ 44.2	$\pm 3.7$	$\mu\text{eV}$
5d	+ 3.81	$\pm 0.22$	meV
5f	+ 24.3	$\pm 0.21$	$\mu\text{eV}$
5g	+ 0.155	$\pm 0.017$	$\mu\text{eV}$

## 4.5 Discussion of the systematic errors

In this section we evaluate the systematic errors, not discussed in the previous section, in the evaluation of the Bragg angle difference between the pionic nitrogen and muonic oxygen lines

$$\Delta\Theta_B = \Theta_B(\mu O) - \Theta_B(\pi N). \quad (4.19)$$

### Pixel distance

The distance between the two Bragg reflections on the CCD array is measured in pixels. To obtain the correspondent energy difference, we have to know accurately the horizontal distance between pixels, along the dispersion direction (x-axis in Fig. 4.2). The CCD devices were fabricated using a  $0.5 \mu\text{m}$  technology, which means that the uncertainty over the full size is  $0.5 \mu\text{m}$ , i. e., an error of 0.8 nm for the pixel distance of  $40 \mu\text{m}$  at room temperature. As the CCD is operated at  $-100^\circ\text{C}$ , the knowledge of the pixel distance at this temperature is essential for crystal spectroscopy. This distance cannot be calculated precisely using the thermal expansion coefficient of silicon, the chip substrate material, and INVAR<sup>2</sup>, the metallic support material. For this reason a specific measurement was set-up in September 2003 to measure the pixel distance with an accuracy in the order of 0.5 nm. This measurement, described in the article in Appendix 7.2, used a high-precision quartz mask (fabricated using a  $0.1 \mu\text{m}$  technology) positioned in front of the CCD and illuminated with visible light. It was possible, fitting the quartz mask pattern in the two-dimensional detector images, to measure the average pixel distance with a precision of 15 ppm and it results in  $39.9775 \pm 0.0006 \mu\text{m}$ , while the nominal value is  $40 \mu\text{m}$ .

The error on the pixel distance introduces a systematic error proportional to the distance, of about 623 pixel, between the pionic nitrogen and muonic oxygen lines on the CCD array. This error is  $0.0006 \times 623 = 0.37 \mu\text{m}$ , which corresponds to an angular uncertainty:

$$\delta(\Delta\Theta_B)_{\text{PD}} = 0.033'', \quad (4.20)$$

<sup>2</sup>INVAR is an alloy of iron (64% ) and nickel (36%) with some carbon and chromium. Sometimes small amounts of selenium are added to improve machinability. Due to its small coefficient of thermal expansion (about  $10^{-6} K^{-1}$  in length; some formulations have negative CoE) it is used in precision instruments (clocks, physics laboratory devices, seismic creep gauges, shadow-mask frames, valves in motors, etc.). Definition provided by Wikipedia: <http://wikipedia.org>

**Table 4.5** – CCDs relative position and orientation with CCD 2 as reference. The orientation of CCD 2 relative to itself provides a check of the validity of the measurement method.

CCD	$\Delta x$ (pixels)	$\Delta y$ (pixels)	$\Delta\Theta$ (mrad)
CCD2-CCD1	$-1.251 \pm 0.029$	$11.404 \pm 0.023$	$-0.587 \pm 0.035$
CCD2-CCD2	$0.000 \pm 0.000$	$0.000 \pm 0.000$	$-0.002 \pm 0.003$
CCD2-CCD3	$0.509 \pm 0.012$	$-11.021 \pm 0.021$	$-0.677 \pm 0.074$
CCD2-CCD4	$-12.850 \pm 0.041$	$10.279 \pm 0.023$	$0.801 \pm 0.130$
CCD2-CCD5	$-13.579 \pm 0.009$	$1.738 \pm 0.016$	$2.233 \pm 0.130$
CCD2-CCD6	$-15.963 \pm 0.041$	$-9.435 \pm 0.021$	$5.530 \pm 0.011$

i.e., to a systematic error of 0.12 ppm on the pion mass measurement.

### CCDs relative orientation

As described in section 3.4, the position sensitive detector we used for the pion mass measurement is composed of 6 CCD devices. The relative orientation of the CCD chips has to be known to the same level of accuracy as the average pixel distance for the correct measurement of the position difference of Bragg reflections.

A first attempt to obtain the relative position of the CCDs has been made using a wire eroded aluminum mask illuminated by sulfur fluorescence X-rays produced by means of an X-ray tube. The alignment of the mask pattern allowed to estimate the relative CCD position to an accuracy of about 0.05–0.1 pixel and the relative rotation to slightly better than 100  $\mu\text{rad}$  [66]. In September 2003 we obtained, using the high-precision quartz wafer described in the previous section, a new evaluation of the CCD orientation to an accuracy of about 0.02 pixel. Both methods are described in the article in Appendix 7.2.

The fluorescence X-ray and optical measurement provides compatible values of the CCD orientation. However, for the final spectrum reconstruction, we used the set of values obtained with the quartz mask, which have a better accuracy. The results of this measurement are presented in Table 4.5.

The uncertainty of the CCDs relative orientation provides a systematic error of 0.025 pixels on the distance between the pionic nitrogen and muonic oxygen lines, which corresponds to an angular uncertainty:

$$\delta(\Delta\Theta_B)_{\text{DRO}} = 0.090'', \quad (4.21)$$

and to 0.33 ppm in the pion mass value.

### Curvature correction error

Curvature corrections were obtained using pionic nitrogen experimental data line. To set the error introduced, we measured the position distance between the two Bragg reflection in two cases: using the curvature correction deduced using the pionic nitrogen and using the muonic oxygen. The distance difference from the two evaluation provides an evaluation of the systematic error equal to:

$$\delta(\Delta\Theta_B)_{\text{CC}} = 0.040''. \quad (4.22)$$

### Fit region

The curvature correction parameters are obtained from the parabolic fit of the spectral line in the position two-dimensional plot (Fig. 3.19). The influence of the background events in the fit results is minimized applying a recursive method. For successive fits, only events than are horizontally close enough to the previous calculated parabola are taken into account. In this way, the selected zone is curved and it follows the tendency of the line intensity maximum. However, a first fit region around the spectral line has to be selected to evaluate the first fit guesses. A particular choice of this fit region could have an effect on the final curvature values. This effect has been estimated observing the changes on the line separation after having applied the curvature correction calculated from different fit regions. The resulting systematic error is:

$$\delta(\Delta\Theta_B)_{FR} = 0.004'' . \quad (4.23)$$

### Off-line detector height reduction

At the top and bottom extremes of the reflection on the CCD array, the line profiles begin broaden (due to the spherical curvature of the crystal) and can have an significant effect on the determination of the curvature correction, as the selection of the fit region in the precedent paragraph. To estimate this effect, the heights of the reflection were trimmed to determine whether this would make any improvement to the curvature correction fit. A number of symmetrical reduction were made and the associated systematic error has been estimated observing the changes on the lines separation after having applied the curvature correction. We obtain:

$$\delta(\Delta\Theta_B)_{DHR} = 0.061'' . \quad (4.24)$$

### Model of the line fit

The one-dimensional spectra have been fit using the line model provided by the Monte Carlo simulation. To calculate the dependence on this choice, we fit the same spectra using a Voigt distribution (convolution between a Lorentzian and Gaussian distribution) as line model. The distance between the pionic nitrogen and the muonic oxygen lines obtained with this fit was compatible with the distance obtained with the Monte Carlo simulation line profiles. The difference between the two evaluation was 0.04 pixels for the total distance of about 623 pixels, when the statistic error is about 0.1 pixel. This difference has been taken into account as systematic error due to the choice of line profile for the fit. We have:

$$\delta(\Delta\Theta_B)_{LP} = 0.070'' . \quad (4.25)$$

### Detector orientation

Ideally, the CCD array should be oriented perpendicular to the direction of the incoming X-ray path from the crystal and the center of the detector should be on the plane defined by the crystal planes and the source. However, mechanical tolerances from the spectrometer tubes, the cryostat flange and the CCD cold-finger all introduce a deviation from this ideal. If the offset angle  $\beta$  of the CCD array is measured, the error can be represented as

the apparent change  $\delta l$  in the separation of the reflections  $l$ :

$$\frac{\delta l}{l} = 1 - \cos \beta \approx \frac{\beta^2}{2}. \quad (4.26)$$

The offset angle was measured to be  $\beta < 0.14^\circ$ , The correspondent angular systematic error is:

$$\delta(\Delta\Theta_B)_{DO} = 0.008''. \quad (4.27)$$

In the same way, mechanical tolerances allows for a detector vertical shift  $\delta y$  up to 20 mm with respect to the horizontal crystal-source plane. This shift causes an apparent change  $\delta l$  in the separation of the reflections  $l$ . Using the Monte Carlo simulations we estimate the change on the Bragg angle difference to be:

$$\delta(\Delta\Theta_B)_{DS} = 0.009''. \quad (4.28)$$

### Detector-Crystal distance

The uncertainty on the detector-crystal distance provides the largest contribution to the systematic errors. This distance has been measured to  $2388.192 \pm 0.166$  mm using the mechanic survey of the spectrometer components and from the focal position measurement of the pionic neon and nitrogen (Sec. 4.2). The associate error is:

$$\delta(\Delta\Theta_B)_{DCD} = 0.153'', \quad (4.29)$$

that correspond to an error of 0.56 ppm on the pion mass value.

### Target window shape

The X-ray distribution on the detector plane depends on the form of the window of the target cell. As we can see in Fig. 4.3, the shape of window boundary defines diagonal cuts of the apparent X-rays emission surface. These cuts produce correspondent cuts on the line on the CCD array causing a shift of the line barycenter. As the defocusing, this effect is taken into account by the model of the line profile used in the fit, which is provided by the Monte Carlo simulation assuming a certain position of the emission surface on the target window. This position has been determined experimentally by the target scan with an accuracy of 1 mm. From this uncertainty, it corresponds a systematic effect on the evaluation of the Bragg reflection distance that is evaluated to be:

$$\delta(\Delta\Theta_B)_{TW} = 0.027''. \quad (4.30)$$

## 4.6 Final results

If we take into account all the corrections discussed in Sec. 4.4 and in Table 4.2, we obtain an angular difference between muonic  $5g_{9/2} \rightarrow 4f_{7/2}$  and pionic  $5g \rightarrow 4f$  Bragg reflections:

$$\Theta_B(\mu O) - \Theta_B(\pi N) = 0^\circ 35' 46.25'' \pm 0.41''_{\text{stat.}} \pm 0.22''_{\text{syst.}}. \quad (4.31)$$

The first error is due to the statistics and the second error is due to the systematic errors.

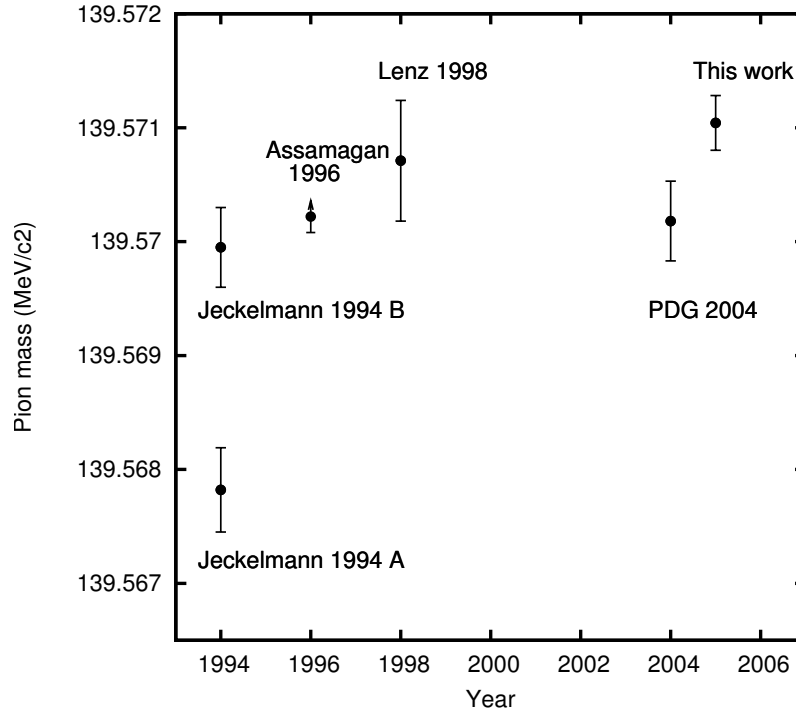


**Figure 4.12** – Comparison between different measurement of the pion mass. The Particle Data Group value [69] is the results of the average of the solution B of “Jeckelmann 1994” [9], which used a solid magnesium target, and the value from “Lenz 1998” [3], which used a target of gaseous nitrogen. The “Assamagan 1996” pion mass lower limit has been obtained from the measurement of the momentum of the muon produced by the disintegration of a pion at rest [125] .

Using the muonic oxygen  $5g_{9/2} \rightarrow 4f_{7/2}$  transition as reference line ( $E = 4023.75025$  eV), we can evaluate the energy of the pionic nitrogen  $5g \rightarrow 4f$  transition. From the transition energy dependency on the reduced mass of the atom, it is possible to evaluate the mass of the negatively charged pion:

$$m_{\pi^-} = (139.571\,042 \pm 0.000\,210_{\text{stat.}} \pm 0.000\,110_{\text{syst.}}) \text{ MeV}. \quad (4.32)$$

The first error is due to the statistics and the second to the systematic errors.

This evaluation provides the most accurate measurement of the charged pion mass up to now. As we can see from Fig. 4.12, our measurement is completely in agreement with Ref. [3], and with the Particle Data Group [69] value within two standard deviations, which is the average of the Ref. [3] value and the solution B of Ref. [9] that use a solid magnesium target. In addition, our value is not in contradiction with the pion mass lower limit evaluated from the pion decay measurement [125]. The presence of two solutions of Ref. [9] is due to the difficulty to determine the number of remaining K-shell electrons in the pionic magnesium. In the work presented here and in the Ref. [3] experiment this ambiguity is not present because of the gaseous target, and in particular, we proved that less than 0.16% of pionic nitrogen has a remaining electron in the K-shell (Sec. 4.3). For this reason, this new value of the pion mass is a good candidate to be the new world reference.

**Table 4.6** – Energy difference between  $5g \rightarrow 4f$  and  $5f \rightarrow 4d$  pionic nitrogen transitions. The calculation of the pionic nitrogen levels has been presented in Sec. 2.4. The strong interaction shift is evaluated in Sec. 4.4.

Source	Difference (eV)
QED (Ch. 2)	2.3137
QED + $\epsilon_{4d}$	$2.3208 \pm 0.0004$
Lenz 1998 [3]	$2.3082 \pm 0.0097$
This work	$2.3002^{+0.0137}_{-0.0069}$

## 4.7 Test of the Klein-Gordon equation

The fit of the pionic nitrogen transition has been performed while fixing the distance of the parallel transition using QED predictions. On other hand, if we keep this distance free, we can measure the energy difference between the  $5g \rightarrow 4f$  and  $5f \rightarrow 4d$  pionic nitrogen transitions and we can compare it to the theoretical prediction to test Klein-Gordon equation validity.

Previous tests of the Klein-Gordon equation has been obtained from the observation of pionic titanium transitions [15] with an accuracy of 2%, and from the observation of pionic nitrogen transitions [3].

The analysis of the high statistics pionic nitrogen spectrum provides a new value of the  $5g \rightarrow 4f$  and  $5f \rightarrow 4d$  pionic nitrogen transitions energy difference. We obtain:

$$E(5f \rightarrow 4d) - E(5g \rightarrow 4f) = (2.3002 \pm 0.0069^{+0.0119}_{-0.0000}) \text{ eV}. \quad (4.33)$$

The first error comes from the fit results. The second error is systematic and it is due to the contribution from pionic nitrogen  $5f \rightarrow 4d$  with a remaining electron in the K-shell estimated to be lower than 2%. Using the high statistics pionic nitrogen spectrum, we estimated this contribution to be lower than 0.16% for the  $5g \rightarrow 4f$  transition. However, the cascade model for non-circular transitions is completely different from the circular ones because in this case radiative transitions can be more probable than Auger transitions (see Sec.3.2). We estimated that less than 2% of the pionic atoms emitting a  $5f \rightarrow 4d$  photon have a remaining electron in the K-shell.

As we can observe in Table 4.6, our value is in agreement inside one standard deviation with the previous experiment [3], with the pure Quantum Electrodynamics prediction, and inside two standard deviation with theoretical value with the strong interaction correction of +7.10 meV (Sec.4.4). We should note that the value from Ref. [3] has a slightly better accuracy but its error evaluation does not take into account the possibility of a line contamination from pionic nitrogen with a remaining electron in the K-shell. We can conclude that this new measurement confirm the predictions from Quantum Electrodynamics for spin-0 particles, with an accuracy of 0.6%.

## **Part II**

### **Highly charged ions**



# Chapter 5

---

## Electron-Cyclotron-Resonance ion sources and traps

---

### Introduction

The characterization of the Bragg crystal spectrometer, described in Sec. 3.3, is an essential operation for pionic atoms spectroscopy and is particularly important for the measurement of the strong interaction broadening in the pionic hydrogen  $1s$  level. [3, 5, 6, 7, 8], and more generally, for high precision X-ray spectroscopy. This broadening is measured by evaluation of the width of the transition  $np \rightarrow 1s$  with the help of the crystal spectrometer. The width of the experimental line is the combination of the strong interaction effect, of the Doppler broadening and of the spectrometer resolution. For this reason, the accurate measurement of the strong interaction width depends critically on the evaluation of the spectrometer response function. In the same way, the correct response function has to be used for the precise evaluation of the Bragg reflection in the CCD detector, taking into account the asymmetry of the peak on the one-dimensional spectra due to the crystal rocking curve and the Johann aberration.

Fluorescence sources, generally characterized by a high intensity X-ray emission, are not adapted for this task because their emission spectrum is complex and the line width is in the order of some eV, much larger than the typical resolution of our spectrometer  $\approx 0.5$  eV. As an alternative, pionic atoms obtained by monoatomic gases can be used instead of fluorescence X-rays. For example, the natural width of  $6h \rightarrow 5g$  pionic neon transition (4.5 keV) is 12 meV [33]. Nevertheless, the low photon rate from these sources (about 100 counts/hour) doesn't allow for an accurate characterization of the spectrometer because the statistics is too low.

An alternative high intensity X-ray source is available from Electron-Cyclotron-Resonance Traps and Sources<sup>1</sup> (ECRIT and ECRIS). These X-ray sources can produce and traps considerable quantities of highly charged ions. For low- to medium-Z atoms, the X-rays from hydrogen-like ions and helium-like ions have an energy of few keV, with a natural width,

---

<sup>1</sup>Both apparatus produce multicharged ions by collision between atoms and electrons accelerated via electron-cyclotron-resonance mechanism. The difference of the two kinds of device is the presence of ion extraction.

less than 50 meV, that is negligible compared to the expected resolution of the Bragg crystal spectrometer. The ion kinetic energy in an ECRIS is small, on the level of about 1 eV [37]. Because of this, a Doppler broadening of less than 40 meV can be expected in He-like argon M1 line (a 3 keV transition).

These qualities make ECRIT and ECRIS ideal X-ray sources for Bragg spectrometer characterization. In addition, they are particularly adapted for bent crystal spectrometers that require an extended source, because the X-rays are emitted from a plasma that occupies an extended volume inside these type of sources. For this reason, since 1999, our collaboration developed an ECRIT using the super-conducting coils of the cyclotron trap [134] (described in Sec. 3.1), and we observed the first X-rays from the ion plasma in 2002. Using this device, we characterized our Johann-type spectrometer measuring accurately the response function relative of several bent crystals. These measurements have been performed during Spring 2002, Spring-Summer 2004 and Summer 2005 periods.

On the other hand, the high X-ray intensity of these sources allows to perform highly charged ions spectroscopy measurements with a precision never reached before. Highly charged ions spectroscopy provides a unique instrument to test Quantum Electrodynamics and in particular it enables to test the electron-electron interaction and electron self-energy prediction in strong field condition (high  $Z$ ) [32, 135, 136, 137]. During the spectrometer characterization, it was possible to use the Paul Scherrer Institut ECRIT to acquire X-ray spectra of atomic physics interest. The result of these measurements are presented in Chapter 6.

If we assume that QED calculations are correct at the required level of accuracy, X-rays from ECR sources can be used as standards instead of the traditional fluorescence sources. The definition of such standard requires the measurement of the absolute X-ray wavelength with an accuracy  $< 1$  ppm. A systematic study of highly charged and X-ray standards definition require long periods of spectra acquisition. These periods cannot be guaranteed by the PSI ECRIT, which shares certain components with the cyclotron trap for pionic and muonic atom production. For these reasons, the Metrology of Simple Systems and Fundamental Tests group of the Laboratoire Kastler Brossel bought an Electron-Cyclotron-Resonance (ECR) ion source in 2002. I spent my 1<sup>st</sup> year of research installing and testing this ion source with Prof. Indelicato and a technician's help. This source can now produce intense quantities of hydrogen- and helium-like argon, some tens of pA, and highly charged ions of several elements as shown in the following sections. The development of a double crystal spectrometer [138, 139, 140] is also in progress in the group. This instrument will enable the absolute measurement of X-ray energy with an expected precision  $< 1$  ppm. This device requires high intensity sources as X-ray tubes or, in our case, the plasma from an ECRIS.

This chapter is dedicated to the ECR ion sources and traps. In Sec. 5.1 I will give a general description of the ECR ion sources. In Sec. 5.2 I will describe, in particular, the ECR ion trap developed at the Paul Scherrer Institut for the Bragg crystal characterization, describing in particular the data acquisition period during my Ph.D thesis. The discussion of the atomic spectroscopy results obtained with this source will be presented extensively in Chapter 6. Section 5.3 is dedicated to SIMPA<sup>2</sup> ECR ion source mounted at the Laboratoire Kastler Brossel in Paris.

---

<sup>2</sup>Source d'Ions Multichargé de Paris

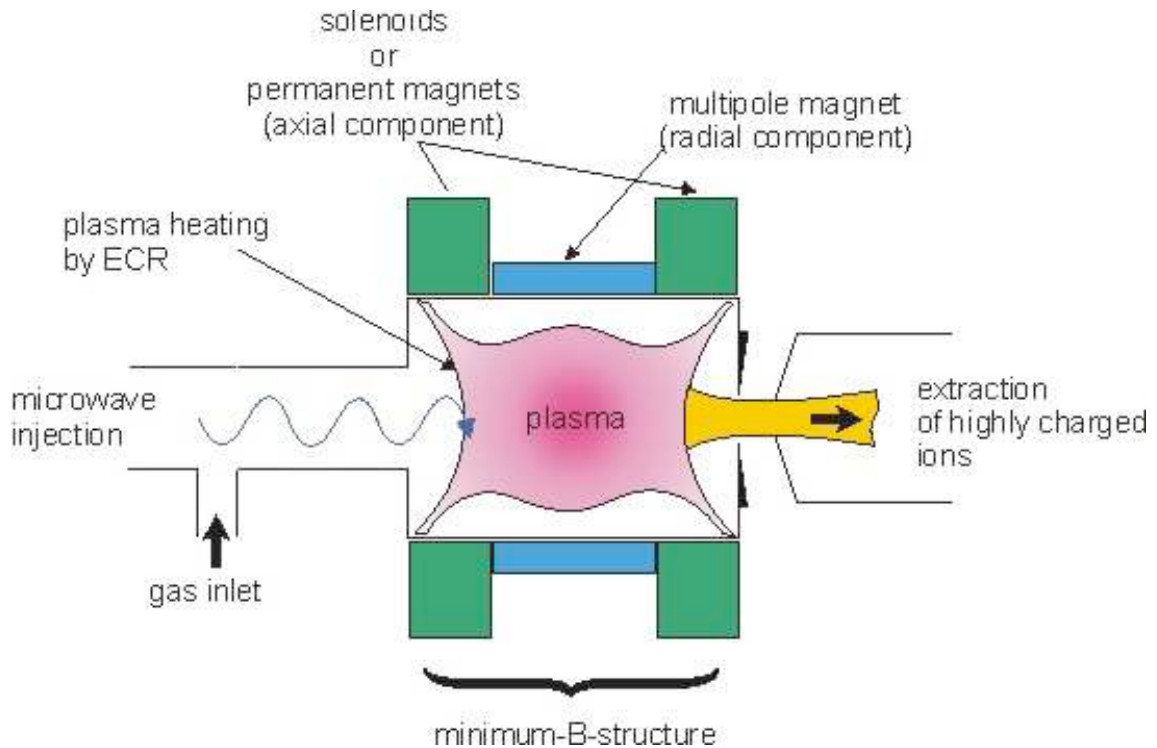


**Figure 5.1** – Schematic of a generic ECR ion source. The plasma electrons are trapped in a minimum-B-field structure and they are heated by microwaves in resonance at the Electron-Cyclotron magnetic surface.

## 5.1 General description of the Electron-Cyclotron-Resonance ion sources and traps

In 1965, R. Geller proposed to produce a confined atomic plasma heated by Electron-Cyclotron-Resonance of the free electrons inside a magnetic field. Using their experience with mirror machines for fusion plasma studies, Geller and his collaborators developed the first ECR ion source in 1971 [36, 141]. The Electro-Cyclotron-Resonance ion sources can deliver ions of many different elements and the radiation emission from the plasma can be used as an intense source of X-rays. Today's ECR ion sources are very reliable low-cost machines and they are used in the principal accelerator facilities in the world (Berkeley 88-inch cyclotron, TRIUMF, CERN, GSI, Ganil, ...). Moreover, ECRIS are used also in small experimental research facilities as ion-surface interaction study or atomic and plasma studies.

### Operation principle

The Electron-Cyclotron-Resonance ion source consists of a plasma confined in a magnetic bottle. The plasma is made of electrons and ions with different charge states. The atoms are ionized by collision with energetic electrons. The electrons are accelerated inside the device by the microwave radiation injected into the confined plasma. The microwave

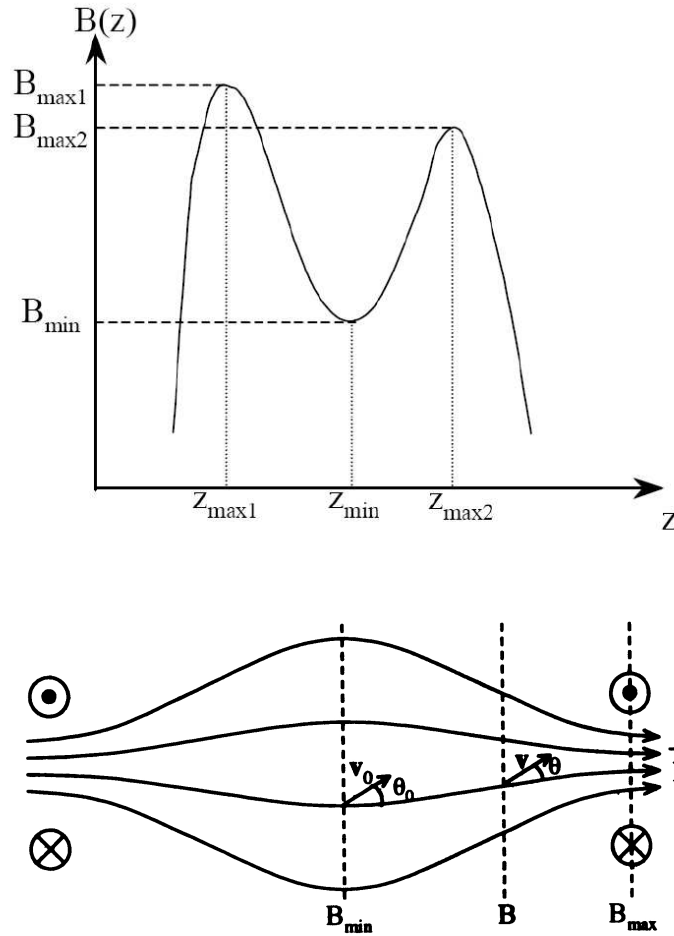


**Figure 5.2** – Top: axial field along to the ECR source axis. The magnetic field minimum at the center allows for the ions trapping long the source axis. Bottom: magnetic field lines in the source. A particle is trapped in the minimum-B-field structure if  $\sin \theta_0 \geq \sqrt{B_{\min}/B_{\max}}$ , where  $B_{\max}/B_{\min}$  is the mirror ratio of magnetic field of the source. The increasing of the mirror ration value corresponds to a high electron confinement efficiency.

frequency is chosen to be resonant with the cyclotron frequency of the electrons for a certain magnetic field value to accelerate the electrons inside the magnetic bottle (the plasma chamber).

The principal components of a ECR ion source are:

- a plasma chamber
- a set of solenoids and/or permanent magnets
- a microwave generator
- a gas injection
- an ion extraction

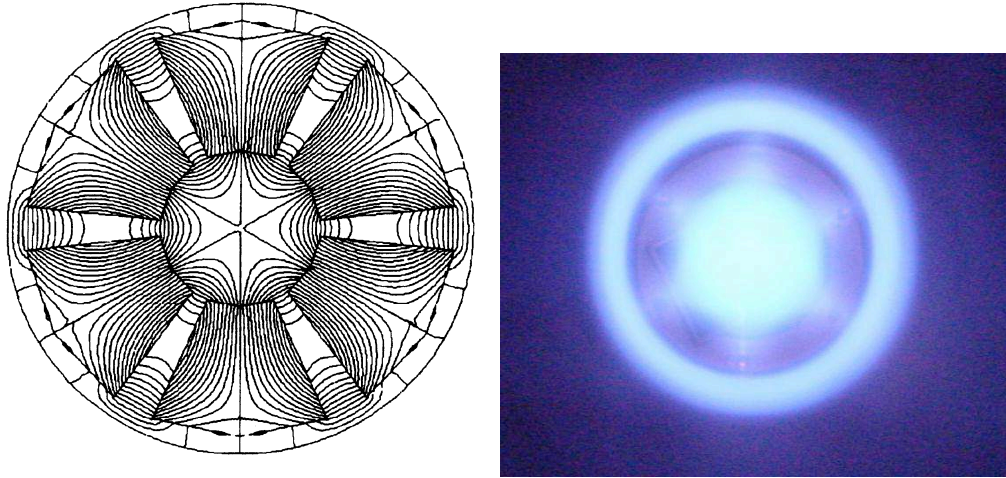


**Figure 5.3** – Left: Cross-section view of the open hexapole of the PSI ECRIT and the corresponding magnetic field lines. Internal radius = 45 mm, external radius = 120 mm, length = 300 mm, magnetic field at the hexapole surface = 1.28 Telsa. Right: picture of the plasma inside the chamber. The ions follow the field lines of the hexapole.

The ions are produced inside a vacuum chamber and they are confined axially and radially by a minimum-B-field structure inside the source. The axial confinement is provided by a longitudinal strong magnetic field, which has a minimum value at the center of the source (see Figs. 5.1 and 5.2). This field is usually produced by a pair of solenoids or by permanent magnets. In the same way, a hexapole structure (or more generally a n-pole structure) provides a radial magnetic field with a minimum along the source axis to confine the plasma in the center of the vacuum chamber. In Fig. 5.3, we can observe as example the magnetic field lines produced by the hexapole of the PSI ECRIT next to the corresponded burning plasma picture.

Charged particles inside the chamber have a helicoidal movement around the magnetic field lines and they are reflected from the zones with high B-field value if their kinetic energy is not sufficiently high. Particles moving in a magnetic field are characterized, in fact, by a velocity parallel,  $v_{\parallel}$ , and perpendicular,  $v_{\perp}$ , to the B-field. The perpendicular movement defines the magnetic moment of the particle  $\mu_p$ :

$$\mu_p = \frac{mv_{\perp}^2}{2B} \quad (5.1)$$

where  $m$  is the mass of the particle and  $B$  is the local magnetic field. If there is no additional external electric field, the kinetic energy  $E_k$  of the ions and electrons remains constant along the charged particle trajectory and the magnetic moment  $\mu_p$  is an invariant of the motion. Due to the conservation of  $\mu_p$ , a particle, moving from a zone with a low value of B-field to a zone with a higher value, transfers gradually the parallel kinetic energy  $(1/2)mv_{\parallel}^2$  to the perpendicular kinetic energy  $(1/2)mv_{\perp}^2$  to keep the magnetic moment constant. When  $B = E_k/\mu_p$  we have that  $E_k = (1/2)mv_{\perp}^2$ , and  $v_{\parallel} = 0$ , the particle stop its parallel movement and it changes the direction of its parallel velocity: the particle is reflected and go back in the direction of the magnetic field minimum and it can not

have access to spatial zones where  $B > E_k/\mu_p$ . This condition can be written using the parallel-perpendicular velocity ratio: the particle is trapped when

$$\left| \frac{v_{\perp}}{v_{\parallel}} \right|_{B=B_{\min}} = \sin \theta_0 \geq \sqrt{\frac{B_{\min}}{B_{\max}}}, \quad (5.2)$$

where  $\theta_0$  is the angle between the particle velocity and the B-field line at the minimum of the magnetic field (see Fig 5.2). The quantity  $B_{\max}/B_{\min}$  is defined as the mirror ratio of the magnetic field. This is an essential characteristic of an ECR ion source: an elevate mirror ratio value corresponds to a high electron confinement efficiency. Typical values of the mirror ratio are 1 to 5, depending on the characteristics of the magnets.

The ionization of the gas inside the ECR source is produced by collision of the electrons with the atoms:



To obtain an ion  $X^{n+}$ , it must be present an electron population with energies equal or bigger than the  $n^{\text{th}}$  level ionization potential for the atom  $X^{(n-1)+}$ . For example, to obtain  $Ar^{17+}$ , it must be present in the plasma electrons with a kinetic energy of, at least, 4.12 keV, the ionization energy of an electron in the K-shell of  $Ar^{16+}$ .

To heat the electrons in the plasma, a high frequency (HF) electromagnetic wave is injected in the chamber. The electron acceleration is obtained when the electron-cyclotron frequency  $\omega_c$  is equal to the injected HF wave frequency, i.e., when we have the electronic-cyclotron-resonance:

$$\omega_c = \frac{eB}{m_e}, \quad (5.4)$$

where  $e$  and  $m_e$  are the charge and the mass of the electron. This condition is satisfied for a specific magnetic field value. For this reason the resonance takes place on a magnetic equipotential surface in the plasma chamber. For a magnetic field of 0.5–1.5 Tesla, a typical resonance frequency is in the order of 2–20 GHz (microwave band). The electrons, confined by the magnetic field, can pass through the resonance surface several times and they are accelerated in the direction perpendicular to the B-field favoring the electrons trapping efficiency [36] as we can deduce from Eq. (5.2). These “hot” electrons are accumulated near the magnetic field minimum and they create a negative well in the plasma potential where the positive ions are attracted (see Fig. 5.4).

Neutral atoms are provided by an axial or radial injection of gas in the vacuum chamber. The presence of the free electrons can be enhanced by negatively polarized electrode inside the chamber, as in the ECR source in Paris, or by coating the plasma chamber walls with a very efficient secondary-electron emitter as the alumina. With the help of a special oven, metallic atoms can also be used in ECR ion sources. The typical gas pressure inside the plasma chamber is in the order of  $10^5 - 10^7$  mbar depending of the source requirements. High pressures are ideal to extract intense low-charged ion beam. Lower pressure are required to produce highly charged ions to prevent, inside the plasma, electron recapture from the atoms.

The production of more highly charged ions can be improved significantly by adding a gas lighter than the main gas into the plasma. For example, for argon (main gas) the mixing with oxygen (support gas) shows the best results [141]. The most widely accepted model for gas mixing effect is a cooling of the highly charged ions by the low charged ions. Using kinematic consideration, the mixing gas cooling should be optimal when the atomic

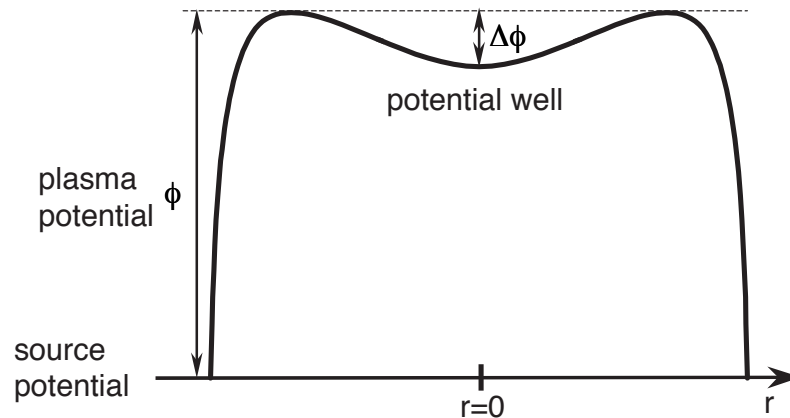


**Figure 5.4** – Shape of the plasma potential along the radial direction. The potential  $\phi$  between the source and the plasma is due to the positive ions trapped by the magnetic field in an extended region. A typical value of the plasma potential is in the order of some tens of volts. In opposite, the electrons are mostly trapped near the center of the source and then caused a depletion  $\Delta\phi$  on the plasma potential. Consequently, highly charged ions are principally attracted and trapped in this region.

mass of the main gas is about twice the atomic mass of the support gas. The cooling of the highly charged ions increases the confinement time of them giving a chance for additional ionizing collision with energetic electrons. However, this is only a hypothesis and it has not been confirmed by our observation in 2005 when we tried to cool down xenon with  $CHClF_2$ . Xenon has an atomic mass of 131 a.u., and  $CHClF_2$  has a molecular mass of 66 a.u., and it has been used as support gas instead of oxygen, which has a molecular mass of 32 a.u.. We did not observe any changes on the intensity of the highly charged xenon when we changed the support gas.

The ions can be extracted from the plasma using an extraction electrode put to a potential of several kV with respect to the source potential. The ion beam can be used for many types of experiments and it can be used also to analyze the plasma characteristics, as the ions charge states and the plasma potential [142].

Many types of ECR ions sources have been developed since the 1970's. In the following sections, two of them are described. The first one is a ECR ion trap (without ions extraction) characterized by a new design based on the presence of two superconducting coils for the axial confinement designed specifically to characterize our Bragg crystal spectrometer. The radial confinement is provided by a open hexapole structure. The second one is the ECR ion source installed in Paris. This ECRIS is a commercial source produced by PANTECHNIK and it has permanent magnets with a closed hexapole structure for the radial confinement. The ions can be extracted and analyzed in a dedicated beam line.

## 5.2 Electron-Cyclotron-Resonance ion trap at the Paul Scherrer Institute

ECR ion trap at the PSI has been projected in 1999-2000 in collaboration with S. Biri from the Institute of Nuclear Research of the Hungarian Academy of Sciences (ATOMKI) in Hungary and with D. Hitz from the Commissariat à l'Énergie Atomique (CEA) in Grenoble (France) [134]. In spring 2002, before the beginning of my Ph.D thesis, our collaboration obtained the first plasma light (see Fig. 5.3) and it was possible to observe X-rays from highly charged argon. After the source optimization on the intensity of the  $1s2s\ ^3S_1 \rightarrow 1s^2\ ^1S_0$  M1 X-ray transition in He-like argon, we measured the response function of the Bragg crystal spectrometer with quartz (10.1) and silicon (111) crystals [111, 112].

In spring 2004, the characterization of the spectrometer was completed with the test of our whole set of crystals (quartz (10.1), quartz (100) and silicon (111)) using the M1 transition line from He-like argon, chlorine and sulphur [143]. In the following section I will present principally the results obtained in 2004, during my Ph.D..

During the characterization of the crystal spectrometer in 2004, it was possible to acquire high intensity spectra of several type of multicharged ions. Using different gas mixtures in the ECRIT plasma, we measured in particular the transition energies of He-like argon, sulphur and chlorine with unprecedented statistics and resolution.

### Device description

The ECRIT developed at PSI consists (Fig. 5.2) of a pair of superconducting magnets (which, together with special iron inserts, provides the mirror field configuration), of an AECR-U-style permanent hexapole magnet, and of a 6.4 GHz power regulated HF emitter. The mirror field parameters provide one of the highest mirror ratios for ECR sources, with a value of 4.3 over the length of the plasma chamber. This high ratio provides a high electron confinement efficiency, which allows for an ionization probability increase of the ions into the plasma.

The hexapole is cooled by a forced flow of demineralised water along the internal parts of the magnets (see Fig. 5.6). The plasma chamber is formed by a 0.4 mm thick stainless steel tube of inner diameter of 85 mm and a length of 265 mm axially limited by copper inserts. At the position of the hexapole gap, the stainless steel tube is perforated by a series of holes with a diameter of 2.5 mm allowing for radial pumping in addition to the axial pumping. The pumping system is composed of three 3000 l/s turbomolecular pumps and of a 1000 l/s cryo-pump.

A reference pressure (without plasma) of  $3 \times 10^{-8}$  mbar ( $6 \times 10^{-8}$  mbar without the cryo-pump) was reached in 2004, after reducing the surface of the iron insertion pieces from the 2002 set-up and installing a cryo-pump; this pressure was  $1.7 \times 10^{-7}$  mbar in 2002. Gas injection is supplied radially through the gaps in the open structure hexapole. The gas composition is routinely controlled and stabilized with a quadrupole mass spectrometer.

### Spring-Summer 2004 measurements

#### Set-up

During Spring 2004 (see Fig. 5.7), we injected different kinds of gases in the ECRIT in order to obtain X-ray spectra from highly-charged argon, chlorine and sulphur. For this

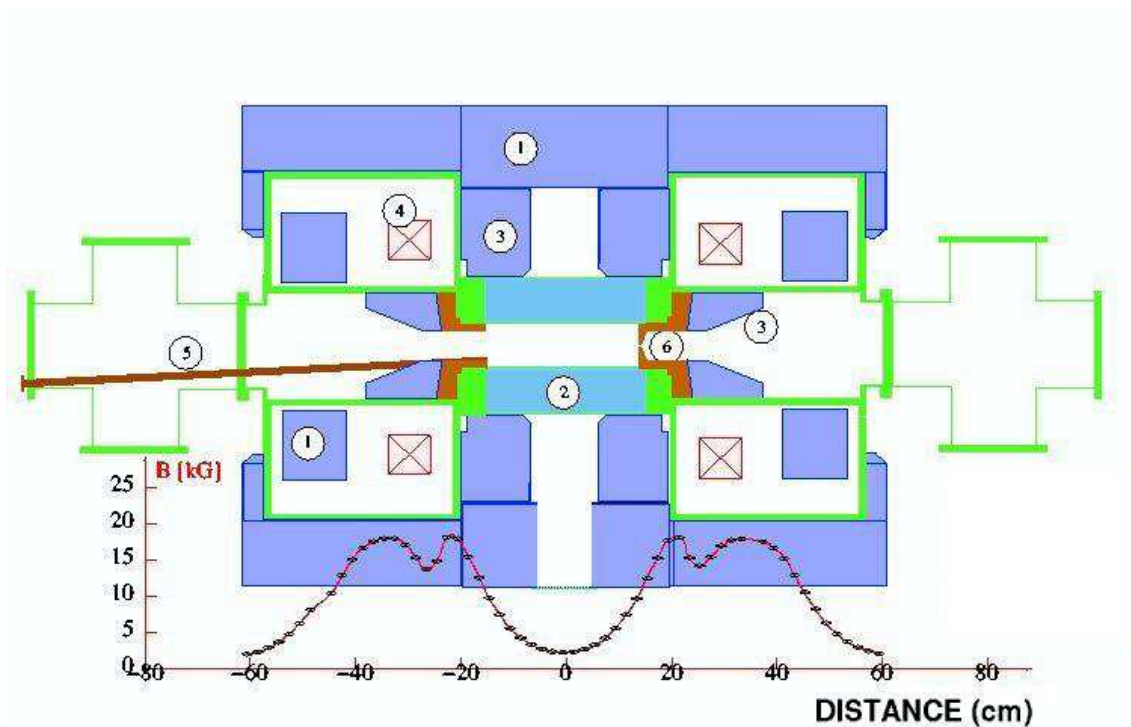


**Figure 5.5** – Schematic of the PSI ECRIT, with axial field values superimposed. 1) Iron return yoke and force balance iron. 2) Hexapole. 3) Field forming iron. 4) Superconducting coils. 5) high frequency (HF) wave guides. 6) Copper inserts.

propose, we used a gas mixture of  $O_2$  and, respectively,  $Ar$ ,  $CHClF_2$  and  $SO_2$ . Using the experience acquired in the previous run, we adjusted a mixing ratio of around 1:9, with a total pressure in the plasma chamber of  $3 - 4 \times 10^{-7}$  mbar. In order to recognize the different charge states, we used as an initial reference the  $K\alpha$  or  $K\beta$  lines of the neutral gas, which are easily recognizable: they are the brightest when only a few watts of HF power are injected. Using known energy intervals, we were then able to move the spectrometer to the region of the nearby  $1s2s \ ^3S_1 \rightarrow 1s^2 \ ^1S_0$   $M1$  transition in the He-like ion, and to observe it. We then optimized the different ECRIT and spectrometer parameters in order to maximize the line intensity in the detector.

### Data analysis

As for the pionic atoms, the energy spectra are obtained from the two-dimensional information from the X-rays detected by the CCD array, as described in Sec. 3.4. The background characteristic for highly charged ions spectroscopy is completely different from pionic atom spectroscopy. For this reason, a slightly different data analysis has to be used. Pionic atoms background was caused principally by  $\gamma$ -rays and neutrons produced by the interaction between pion and solid matter. This radiation produces tracks or cluster of excited pixels in the CCD chips. For pionic atoms, the rejection of the background events requires the use of the cluster analysis, which can be applied because, for each frame, only 1 to 10% of the image area is illuminated by X-rays and background radiation. In the case

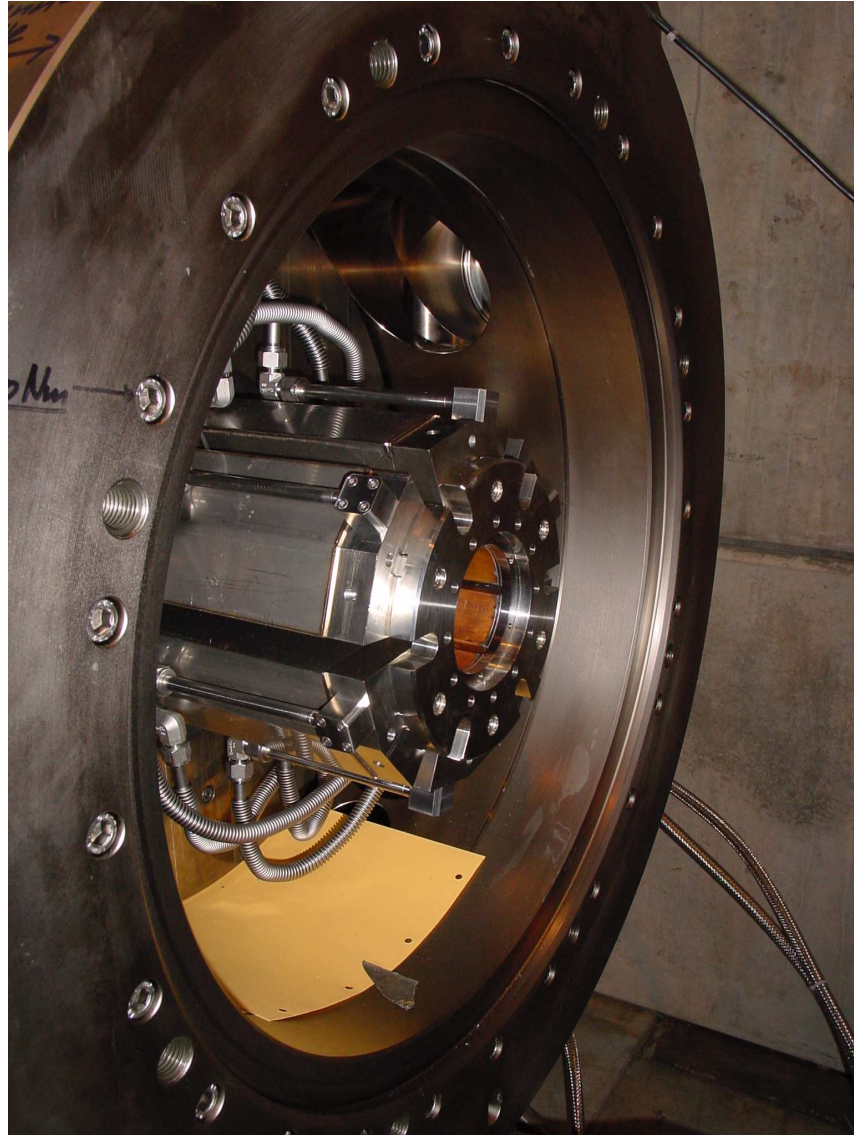


**Figure 5.6** – Picture of the PSI ECRIT during the maintenance: the superconducting coils are separated and the hexapole magnet is visible at the center of the trap with the water cooling connections. The A4 foil inside the source gives an idea of the dimensions of the device.

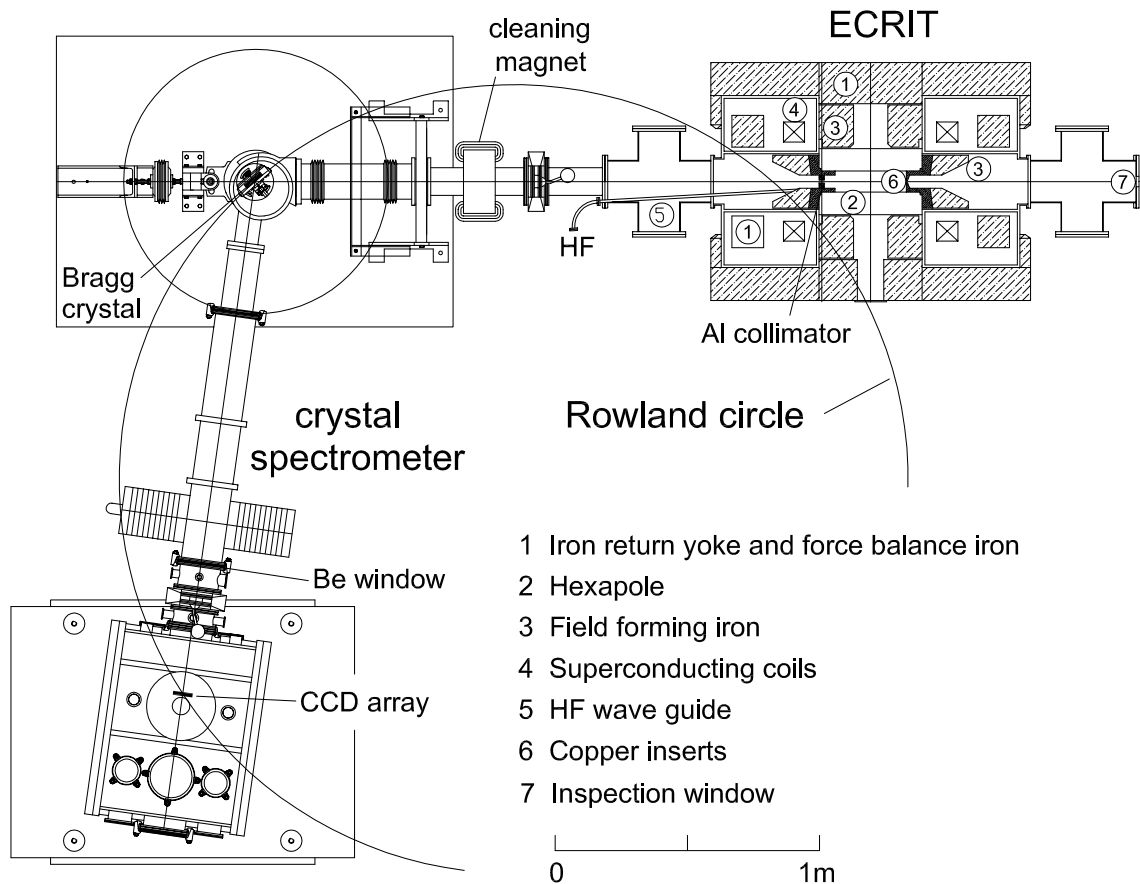
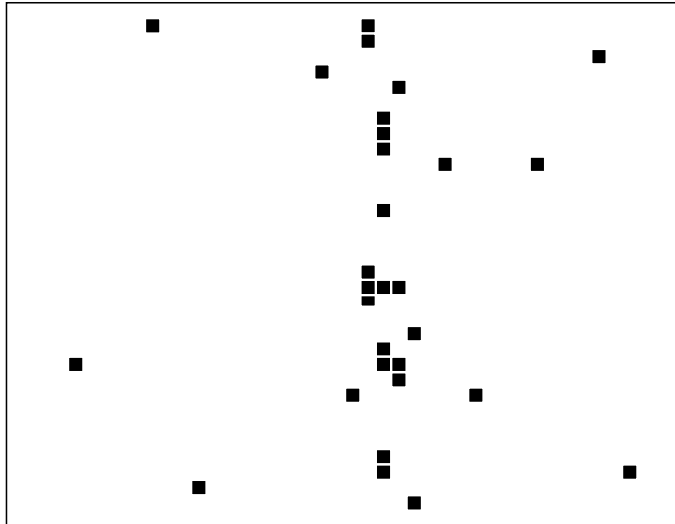


Figure 5.7 – Set-up of the experiment in 2002.

of an Electron-Cyclotron-Resonance ion trap radiation, the main source of background is the bremsstrahlung radiation due to collision of energetic electrons with ions or with the vacuum chamber walls. This radiation has a broad energy spectrum and it cannot be distinguished from X-rays of the same energy emitted by the ions. The typical illumination time per frame of the CCD chips is 30 s. Due to the high intensity of the X-rays, this allows for a sizeable probability of double hits for pixels near the line peaks and it requires a special analysis to include these events. For the same reason, the high probability to have neighboring pixels excited from different X-rays render useless the cluster analysis (see Fig. 5.8): along the line maximum we can observe clusters formed by several excited pixels. The cluster analysis algorithm detects and interprets this group of excited pixel as a unique event with an energy several time bigger than the energy of a single atomic X-ray. In opposite, if we analyze each pixel independently, it is possible to reconstruct correctly the detected events. The deposited charge in each excited pixels is usually produced from one or two photons, and it has to be considered as a single event. However, this raw analysis doesn't allow for the detection of the events that involves two or more pixels,

In order to reduce this effect and improve the peak-to-background ratio, a densimet<sup>®3</sup>

<sup>3</sup>Machinable tungsten alloy



**Figure 5.8** – Typical charge distribution on the CCD pixels near one of line peak after 30 seconds integration time. The intensity of the brightest transition from the ECRIT plasma is so strong that the cluster analysis is useless because the probability to have two or more neighboring pixels excited is too high near the peak maximum.

collimator was inserted at a distance of 150 mm from the center of the plasma, leaving an aperture of 28 mm(h)  $\times$  4 mm(v) or 28 mm(h)  $\times$  1 mm(v), depending on the configuration.

During the different runs the (double hits)-to-(single hits) ratio was always below 5%, which is small enough to properly handle double hits in the final analysis, and to neglect triple hit processes. The high accuracy energy spectra are obtained from the two-dimensional data from the CCD array as described in Sec. 3.4.

### Source characterization

During the optimization of the apparatus, we studied the M1 line intensity as a function of the injected HF power. As expected, we observed a strong dependence between the M1 intensity and the HF power (see Fig. 5.9). In contrast, we noted an unexpected behavior of the maxima of the curves, whose HF intensity does not increase with the ionization energy of the He-like ion, which is 3.2 keV for argon, 2.8 keV for the chlorine and 2.5 keV for the sulphur. This can be due to the different type of gas we used to inject the different atoms: for chlorine as example we used a molecular gas,  $CHClF_2$ . The introduction of different types of atoms at the same time could alter the normal dynamic of the ECR ion trap. Moreover, for all the elements, we noted an improvement on time of the ECRIT performances due to cleaner condition inside the plasma chamber. The condition of the plasma chamber changed any time we changed the gas mixture and when we vented the ECRIT. For this reason it is difficult to compare and to interpret correctly these data. A more detailed study could be done with specific and controlled experimental conditions.

During the ECRIT parameters adjustment, we observed a non-trivial dependency of the M1 intensity against the longitudinal magnetic field. As shown in fig. 5.9, we observe the presence of two distinct maxima in the M1 intensity-coil current relationship. These

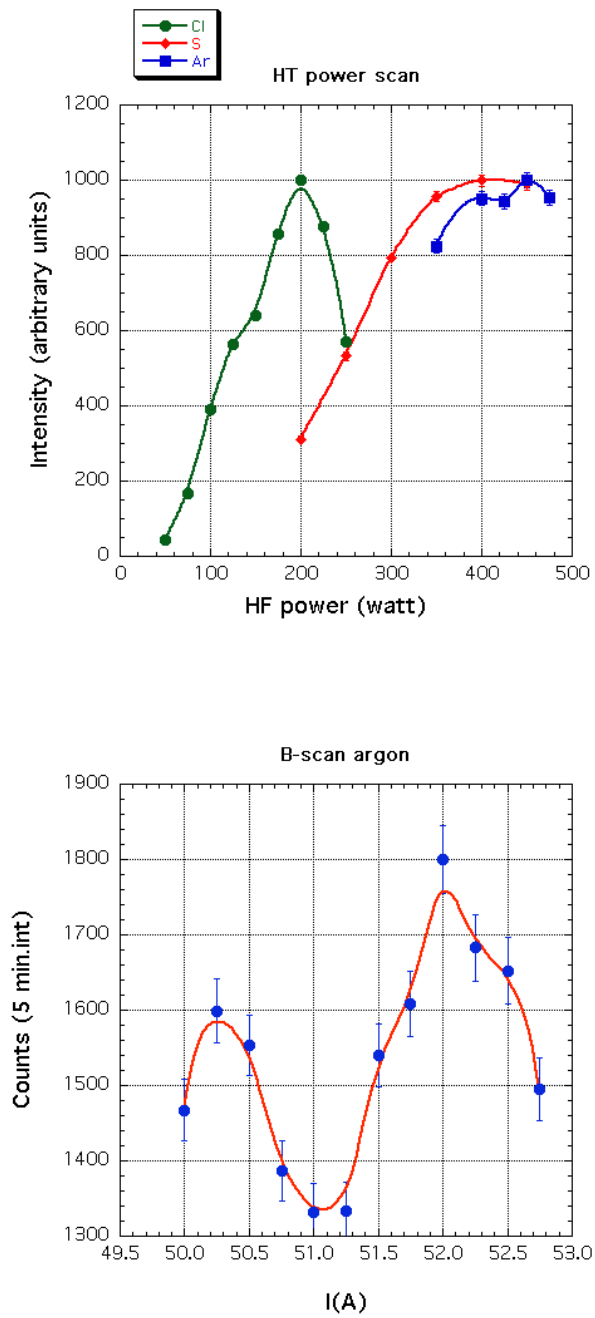


**Figure 5.9** – Up: injected HF power scan for argon, chlorine and sulphur versus the He-like M1 intensity (in arbitrary units). Down: He-like argon M1 line intensity dependency versus the superconducting coils current. 55 A corresponds to a magnetic field value of 2.35 kGauss at the center of the ECRIT. These maxima are due to the resonance between the longitudinal length of the resonance surface and the microwave wavelength.

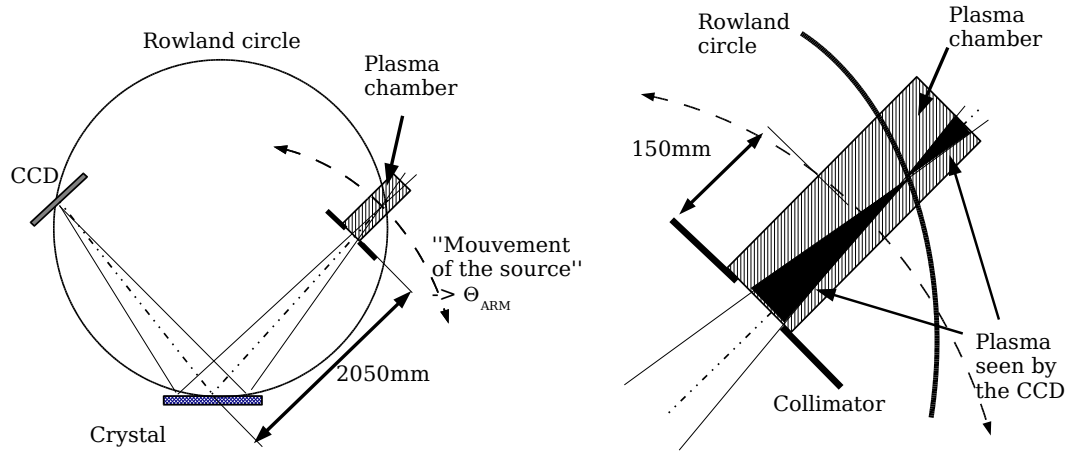


**Figure 5.10** – Target scan of the ECR ions trap. The change of the angle  $\Theta_{ARM}$  on the spectrometer is equivalent to change the zone of the plasma that emit the photons detected by the CCD array. The volume of this zone depends on the set-up geometry: the distance between the center of the plasma chamber with respect to the Rowland circle and to the collimator (28 mm width). The intensity of the X-ray emission could depend on the zone observed in the plasma, but it depends also on the value of the observed solid angle that can be reduced by the presence of the collimator. The drawing presented here corresponds to the measurement of the  $M1$  transition from He-like sulphur with a quartz ( $10.\bar{1}$ ) crystal. In this case we had the focal position 77 mm from the center of the plasma chamber.

maxima are due to the resonance between the longitudinal length of the resonance surface and the microwave wavelength.

Changing the angle of the crystal planes with respect to the axis of the source, it is possible to look at different parts of the plasma. Studying the dependency of the He-like  $M1$  line it is possible to measure the He-like ions longitudinal distribution. With our set-up, presented in Fig. 5.10, we could approximately have the spectrometer focus, i.e., the Rowland circle, on the plasma in just few cases because the plasma-crystal distance was fixed at 2200 mm by the set-up and the focalization condition imposes a plasma-crystal distance equal to  $R \sin \Theta_B$ , where  $R$  is the crystal curvature radius and  $\Theta_B$  is the Bragg angle. Moreover, the collimator positioned at 150 mm of the center of the plasma can influence the target scan at the plasma borders. The best condition to operate a target scan had been obtained using quartz ( $10.\bar{1}$ ) crystal with the sulphur spectrum  $R \sin \Theta_B = 2277 \text{ mm}$ . As show in Fig. 5.11, we can observe a small position dependence on the  $M1$  line intensity which, decreases slightly in correspondence of the plasma center. As in Ref. [144], our measurement confirms the suspicions of a highly charged ion population hole in the center of the plasma. A more accurate investigation could be done with a collimator with a smaller horizontal extension and with a set-up with position of the Rowland circle corresponding to the central position of the plasma chamber.

As we can see from Fig. 5.11 (top), the intensity of the  $M1$  line is very sensitive to the pressure values. Changing the total pressure of the gas, we change the density of free electrons inside the plasma, but also probability of electron-ion collision due to the

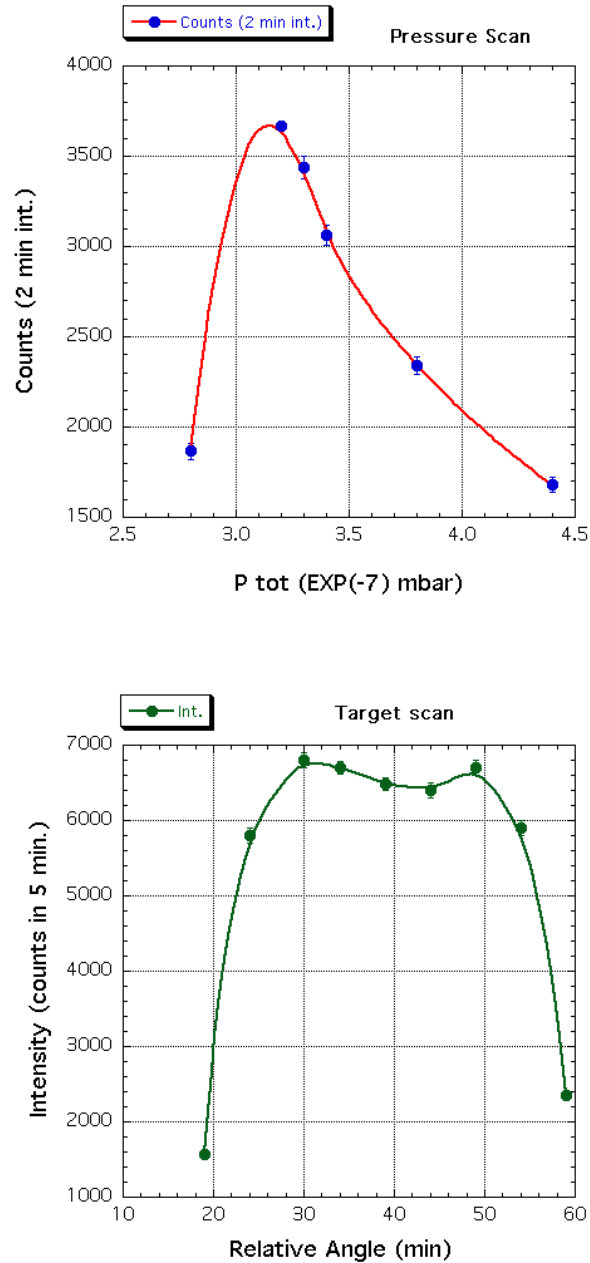


**Figure 5.11** – Pressure scan (top) and target scan (bottom) of the ECR plasma with sulphur, using quartz (10.1) crystal. The target scan enables to study the spatial distribution of ionized ions in the plasma. The total pressure of the gas in the source is a critical parameter and the optimal condition comes from a compromise between ionization and electron recapture probability.

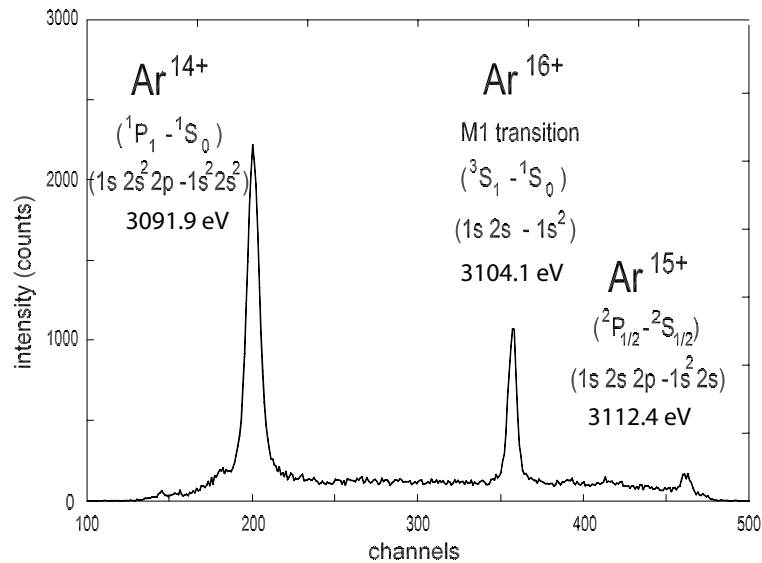


**Figure 5.12** – The spectral region for argon X-rays from  $Ar^{14+}$ ,  $Ar^{15+}$  and  $Ar^{16+}$  (M1 transition) measured with a Si (111) crystal in 2002 on the PSI ECRIT. One channel (pixel) correspond to 79 meV.

increasing or decreasing ion density. The increase of high energy electrons density favors the atom ionization and trapping, but also increase the probability of electron recapture by the ions. The ideal condition comes from a compromise of these two mechanisms. In any set-up, we found an optimal condition at total pressure of about  $3 - 4 \times 10^{-7}$  mbar, as presented in Fig. 5.11. A scan on the main gas partial pressure confirmed the optimal mixing ratio of 1:9 between the support and the main gas.

### Crystal characterization

The main goal of the ECRIT runs in 2002 and 2004 was the characterization of the crystal spectrometer used for pionic atoms experiments. In 2002, with the ECR ion source, a number of 20000 events detected by the CCD array was reached for the narrow M1 transition of He-like argon in about 30 minutes time, to be compared with a number of 5000 counts reached after 40 hours with X-rays from pionic carbon. This number of events is necessary to measure the response function for a fixed value of the crystal-detector distance. However, the accurate determination of the spectrometer response function requires variations in the detector-crystal distance (focal scan) and changes of apertures in front of the crystals. For the complete characterization of one crystal is necessary a period of about 10 hours.

The measurements (Figs. 5.12 and 5.14) are compared with theoretical prediction using a Monte Carlo simulation that is used to fit the real data. This analysis is performed principally by three collaborators: L. Simons and D. Covita at PSI and A. Hirtl at the Stefan

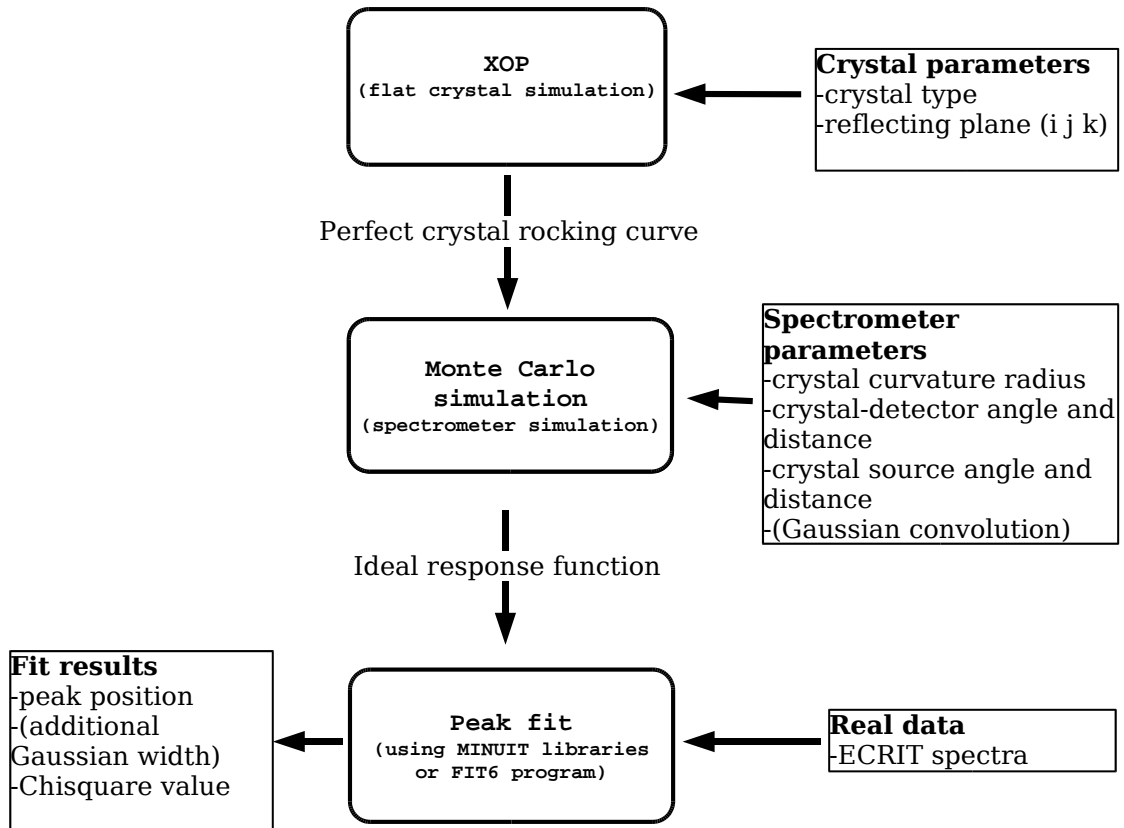


**Figure 5.13** – Schematic of the analysis to characterize the Bragg crystal spectrometer. Simulation and fit to real data are used at the same time.

Meyer Institut (Vienna, Austria). A schematic of the procedure used in the analysis is shown in Fig. 5.13. For each crystal, the program XOP [103] is used to obtain the rocking curve for an ideal flat crystal (see Fig. ??). The rocking curve is used as input for a Monte Carlo X-ray tracking routine, which takes into account the crystal spherical curvature and the geometrical condition of specific set-up parameters: source and collimator position, detector position and crystal aperture. The Monte Carlo simulation produces as result a two-dimensional plot, which correspond to the spatial event distribution detected by the position sensitive detector (CCD array image) in the real experiment. In addition, this simulation can take into account an arbitrary kinetic energy distribution of the source, which can produce a Doppler broadening of the line, and the natural width of the energy transition with the convolution with a Lorentzian distribution. These features are particular important for the study of the pionic atoms spectra.

Using the same procedure described in Sec. 3.4, the two-dimensional data are corrected in curvature and they are projected on the x-axis (dispersion axis), defined in Fig. 4.2, to provide the simulated final position spectrum, i.e., the response function of the spectrometer. In ideal circumstances, this response function would reproduce the real data.

Experimental data are fitted with the theoretical profile by  $\chi^2$  minimization. The method of  $\chi^2$  minimization can be used in this case because we have enough statistics for

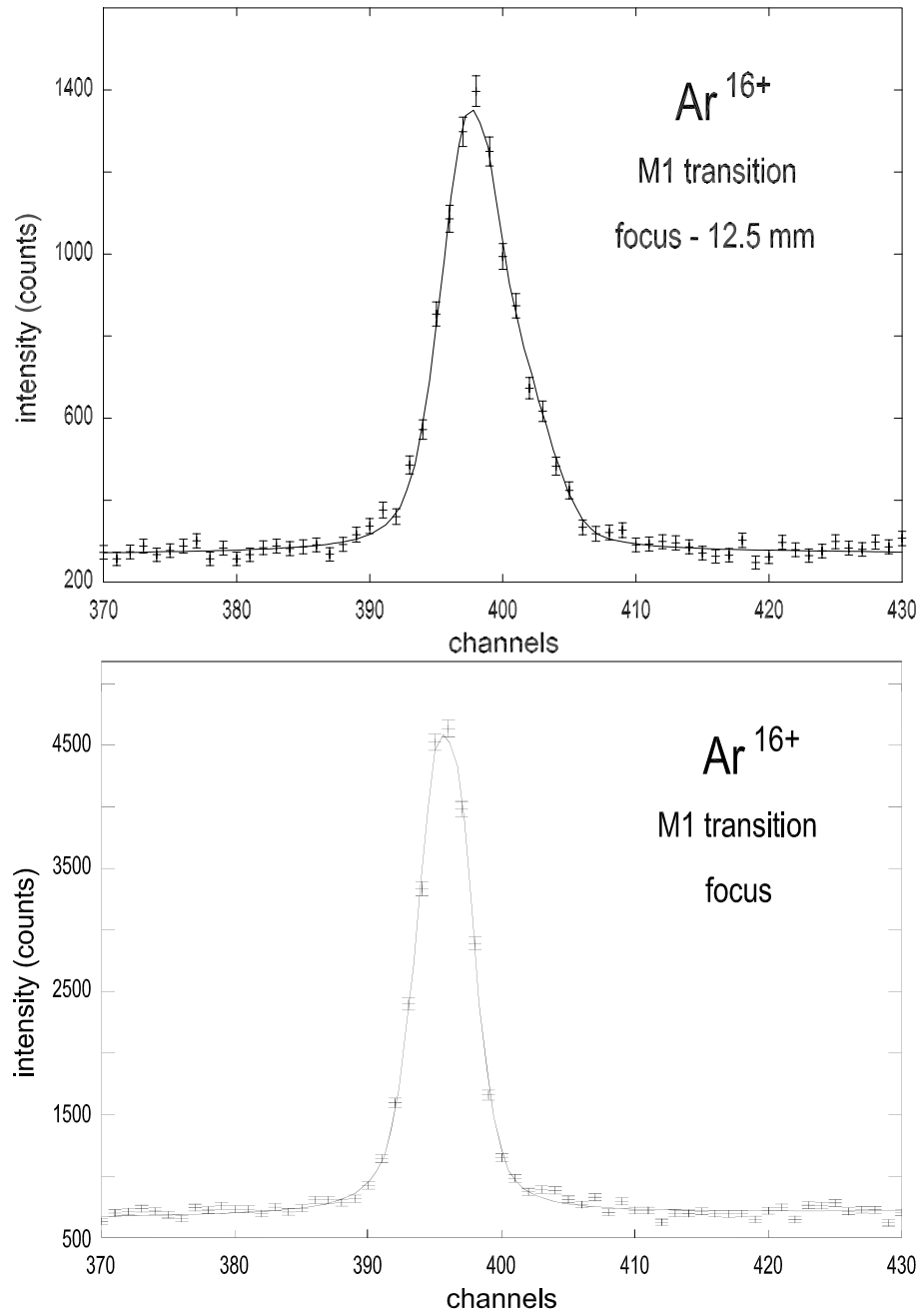


**Figure 5.14** – Spectra of the  $Ar^{16+} 1s2s\ ^3S_1 \rightarrow 1s^2\ ^1S_0$  M1 line observed with quartz ( $10.\bar{1}$ ) crystal, together with a fit for a detector position of 12.5 mm out of focus in direction of the crystal (top) and in focal position (bottom). A circular aperture with a diameter of 60 mm had been applied. One channel (pixel) corresponds to 93 meV.

each channel in the spectra. This can be performed with the program FIT6 or with the analog program FITIT developed by L. Simons that use the program package MINUIT [117] from the CERN program library<sup>4</sup>. Both programs are described in Sec. 3.5. In order to consider a possible additional broadening, the simulated response function can be folded with a Gaussian distribution.

During the experiment, two types of changes in the set-up were investigated. First, spectra were acquired for different distances of the CCD detector from the crystal (focal scan). In a second step, with the detector located at the focal position, different apertures were mounted in front of the crystal.

Each real spectra was fitted using a set of simulated profile corresponding to different set of geometrical parameters for the Monte Carlo routine. With this procedure is it possible to study several feature of the Bragg spectrometer:

- Determination of the optimum focal position.
- Measurement of the line shape variation as a function of the detector-crystal distance.
- Determination of the differences between real and simulated response functions.

The focal position and the line shape variation are determined by moving the CCD array in steps of 2-3 mm toward and away from the crystal. The application of different apertures in front of the crystal allows for the comparison of real and simulated profiles and the study of possible irregularities in the response function due to the crystal material imperfection and/or deviation from the spherical shape.

In 2002 we studied two crystals: silicon (111) and quartz (10. $\bar{1}$ ) using the M1 line of He-like argon (Figs. 5.12 and 5.14). From the data analysis described above, it was possible to test crystals and the validity of the X-ray tracking simulation program. Moreover, we measured an additional Gaussian contribution to the response function caused by the crystal imperfections for 3 keV X-rays [112].

In 2004 the investigation was extended to six additional crystals, two quartz (10. $\bar{1}$ ), two (100), and two silicon (111). In addition we explored different X-rays range using the M1 line of He-like argon (3.10 keV), chlorine (2.76 eV) and sulphur (2.43 keV) [143]. These energy ranges are chosen because they correspond to the energy of the  $4p \rightarrow 1s$ ,  $3p \rightarrow 1s$  and  $2p \rightarrow 1s$  transitions in pionic hydrogen. We have to remember that the characterization of the crystals is essential to measure the strong interaction broadening in pionic hydrogen ground level.

The analysis are not yet completed. Anyhow, the partial results available at present enables the detection of some problem of the bent crystal fabrication. Comparing the optimum focal position, deduced by the spectra fit, with the real crystal-detector distance, it was possible to observe a discrepancy between the nominal radius of curvature values (provided by the bent crystal fabrication company ZEISS) and the real radius of curvature value. The crystal radius of curvature and cut angle have limited, up to now, the accuracy of our investigation. The cut angle between the surface and the crystal planes has been measured for few crystals during Summer 2005 using the reflection of light from a laser, and X-ray from a fluorescence target from the crystal surface. With this measurement, we found, for some crystals, a cut angle of several tens of minutes instead to be less than a minute. Only the crystal used for the measurement of the pion mass has a cut angle smaller

---

<sup>4</sup><http://seal.web.cern.ch/seal/snapshot/work-packages/mathlibs/minuit/home.html>

than 1'. An additional accurate study of these effects is actually in progress (November 2005).

This analysis enables to test the reliability of the Monte Carlo simulation to describe real data. As consequence, this simulation has been used to provide the more adapted profile for the fit of the pionic nitrogen and muonic oxygen spectrum, for the measurement of the pion mass. In this case, the peaks on the one-position spectrum are strongly distorted because they are not in the focal position. This distortion is taken into account in the fit using as line model the line profile provided by the Monte Carlo simulation for specific experimental set-up. In the same way, the analysis of the highly charged ion spectra in Ch. 6 uses the simulated profile, adapted for each set-up, as line model for the fit.

### 5.3 Electron-Cyclotron-Resonance ion source at the Laboratoire Kastler Brossel

In September 2002, the Laboratoire Kastler Brossel, in collaboration with the Institut des NanoSciences de Paris (INSP) bought a second hand, almost new, permanent magnets ECR ion source from the bankrupt X-Ions company. As mentioned before, our group was interested in the ECR ion source as potential X-ray source for high precision spectroscopy for QED test in few-electrons atoms. On the other hand, the INSP would use highly charged ions to study ion-surface interaction and ion-ion collision.

The collaboration of these two laboratories has lead to the creation of the SIMPA project: Source d'Ions Multichargés de PARIS.

#### Electron-Cyclotron-Resonance ion source and analyze line description

The scheme of the SIMPA installation in Paris is presented in Fig. 5.15 and 5.16. The set-up is composed by the ECR ion source, by an ion extraction system and by a series of magnetic elements to focus and to analyze the extracted ions. Differently from the PSI ECRIT, this ECR ion source can provide intense ion beams. The composition of the extracted ions can be analyzed with the help of a magnetic dipole and by a Faraday cup. The plasma inside the source can be also studied by the direct detection of the emitted radiation. In particular, our installation is equipped by a series of X-ray detectors. The ion beam can be used also to study collision between the ions and a target. In the following paragraphs I will describe more in details the different components of the SIMPA installation.

#### Electron-Cyclotron-Resonance ion source set-up

The SIMPA ECR ion source is a SUPERNANOGAN commercial source (Fig. 5.3) developed by the society PANTECHNIK<sup>5</sup>. The permanent magnets create a longitudinal magnetic field up to 1.2 Tesla with a mirror ratio of about 2.4. The chamber is made of copper, has a diameter of 45 mm and is cooled by a forced flow of de-ionized water. The HF electromagnetic waves are produced by a Klystron generator at 14.5 GHz, which can provides microwaves up to a power of 2000 watt. The microwaves are transported to

<sup>5</sup><http://www.pantechnik.net>.

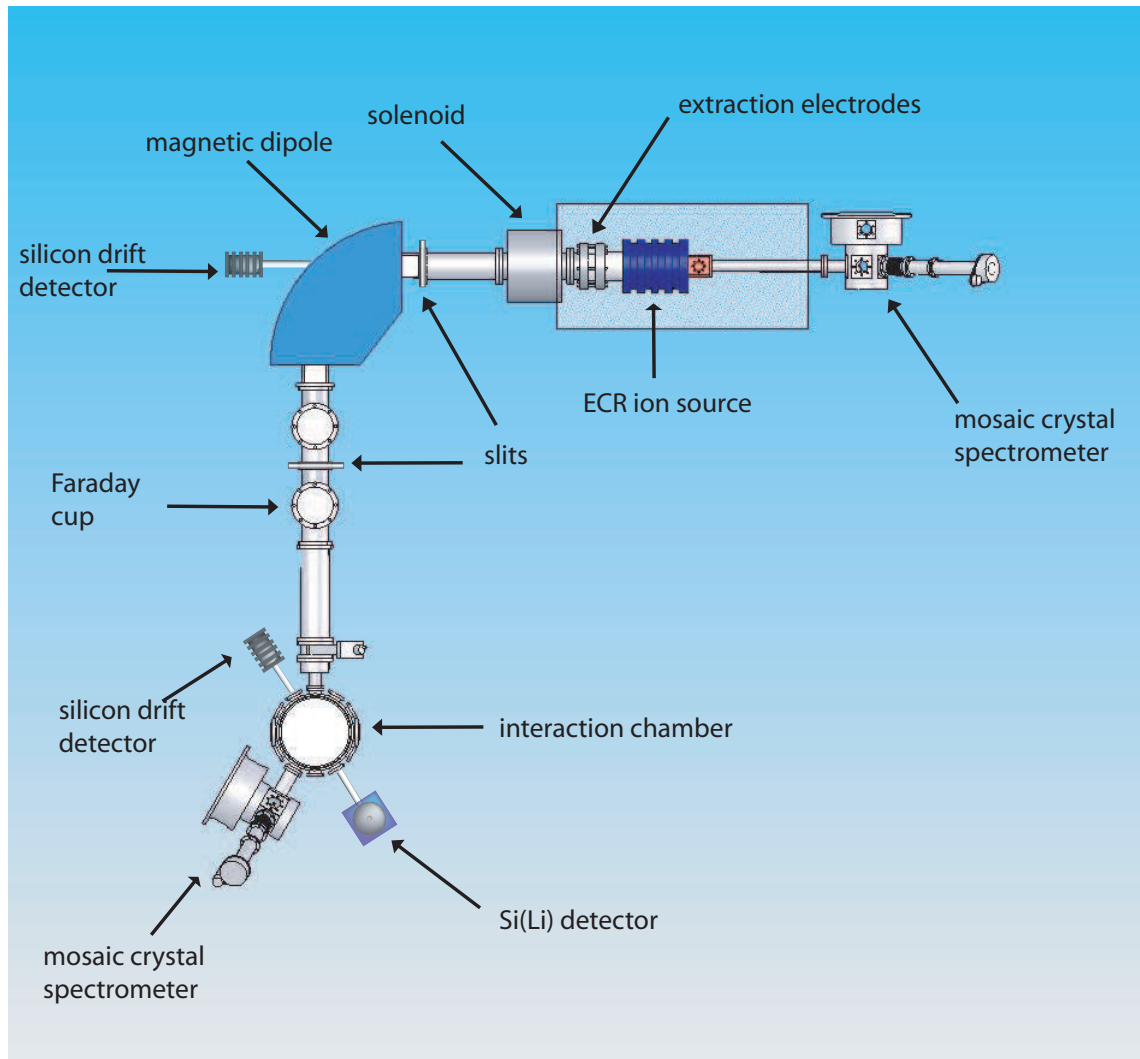


**Figure 5.15** – Set-up of the ECRIS and the vacuum line installation in Paris.

the source by a rectangular WR62<sup>6</sup> wave-guide. The injection in the vacuum chamber is obtained using a multimode cavity with Jacquot's coaxial feeder<sup>7</sup>. The copper multimode cavity enables the transition from the rectangular wave-guide, coming from the Klystron, to the coaxial line composed by two concentric tubes with different diameters. The coaxial line brings the microwaves into the plasma chamber as shown in Fig. 5.18 and 5.19. The inner tube can be polarized to a negative potential with respect to the source, and it can be used as an electron emitter: it is the so called polarization electrode [36]. An adjustable tuner is used to control the microwave coupling to the plasma (see Fig. 5.3).

In Fig. 5.19 we show a simulation of the microwave propagation inside the SIMPA ECR ion source. The simulation has been made by A. Bleiker and L. Stingelin of the High

<sup>6</sup>Rectangular waveguide for transverse electric 10 mode (TE<sub>01</sub>). They are made generally in copper or aluminum. Dimensions:  $0.622 \times 0.311$  (inches)<sup>2</sup>. Standard frequency range: 12.4 to 18.0 GHz.

<sup>7</sup>B. Jacquot, *French patent* 86 03583 (1984).

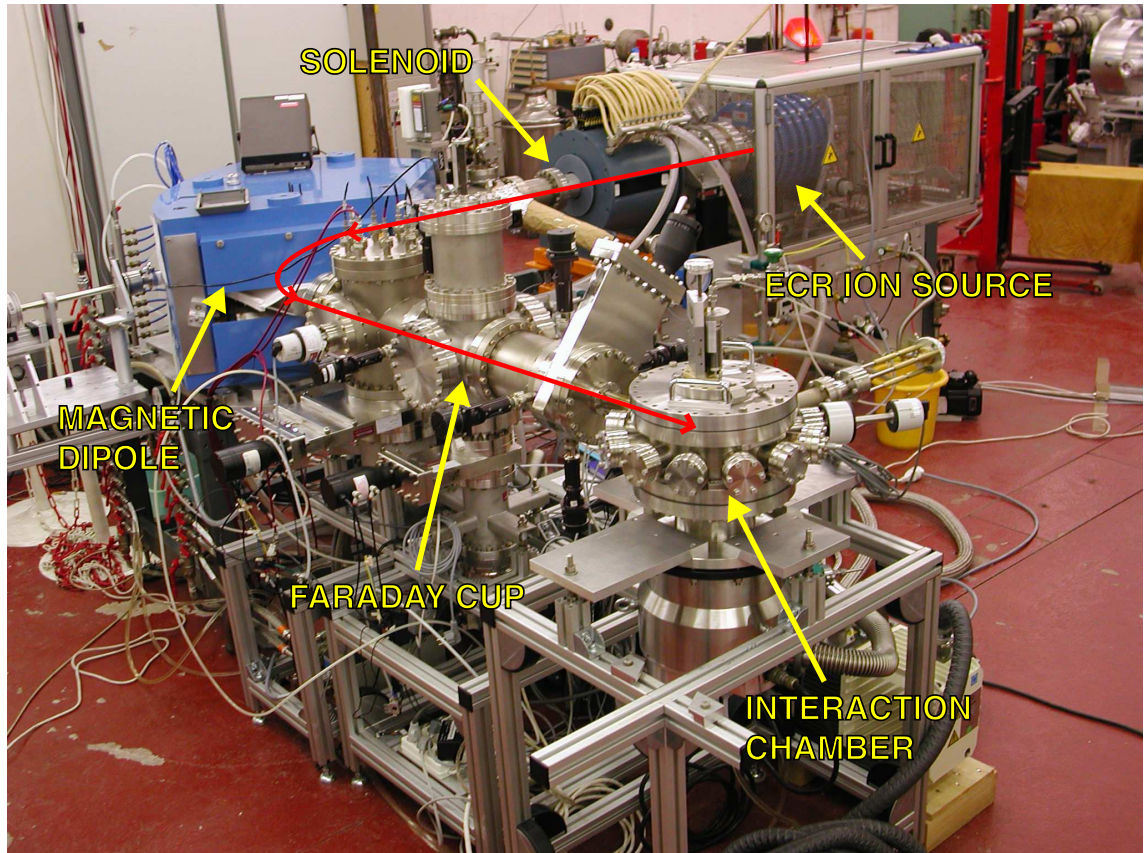


**Figure 5.16** – Picture of the SIMPA source and the vacuum line. The ion beam follows the red trajectory in the image.

Frequencies Group of PSI using the ANSYS program<sup>8</sup>[145].

### Extraction system and solenoid

The ions are extracted from the plasma by an electric field. The presence of a set of plastic and ceramics isolations, allows for setting the ECR ion source on a high voltage up to 20 kV. The ions, passing through a 10 mm diameter hole in the plasma chamber wall, are extracted from a system of two coaxial electrodes, the extraction electrodes. The electrode nearest to the plasma can be set to a negative potential up to 14 kV to produce a potential difference between the plasma up to 34 kV to increase the extraction efficiency. The second electrode is set at the mass potential and, with the first electrode, determine the shape and the angular divergence, i.e., the emittance, of the extracted ion beam. The ions can be accelerated to a kinetic energy up to 20 keV/q (q: charge of the ion). The beam is focalized by a solenoid which can produce a longitudinal magnetic field up to 0.4 Tesla.

<sup>8</sup><http://www.ansys.com>.

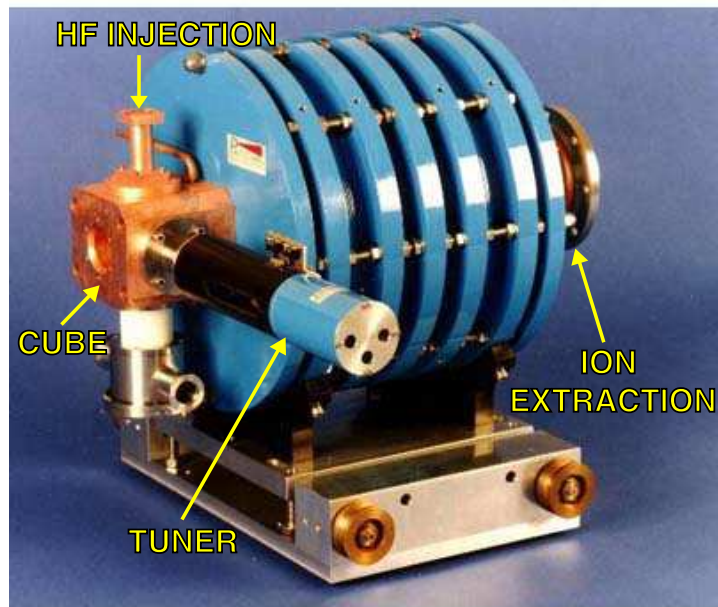


Figure 5.17 – Picture of the Supernanogan ECR ion source produced by PANTECHNIK.

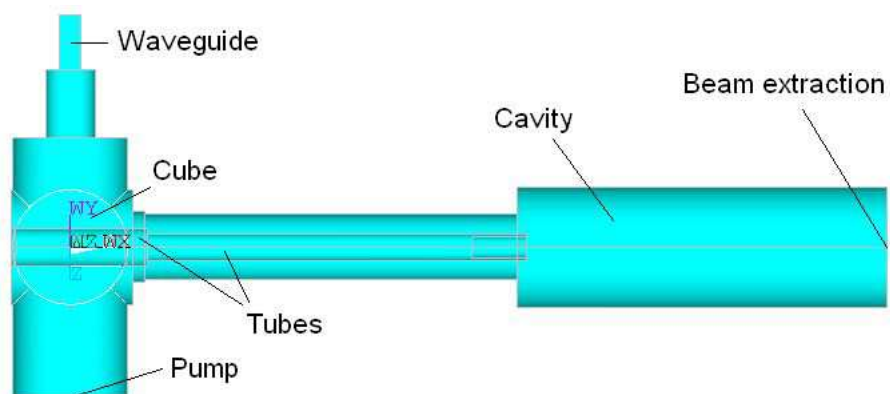
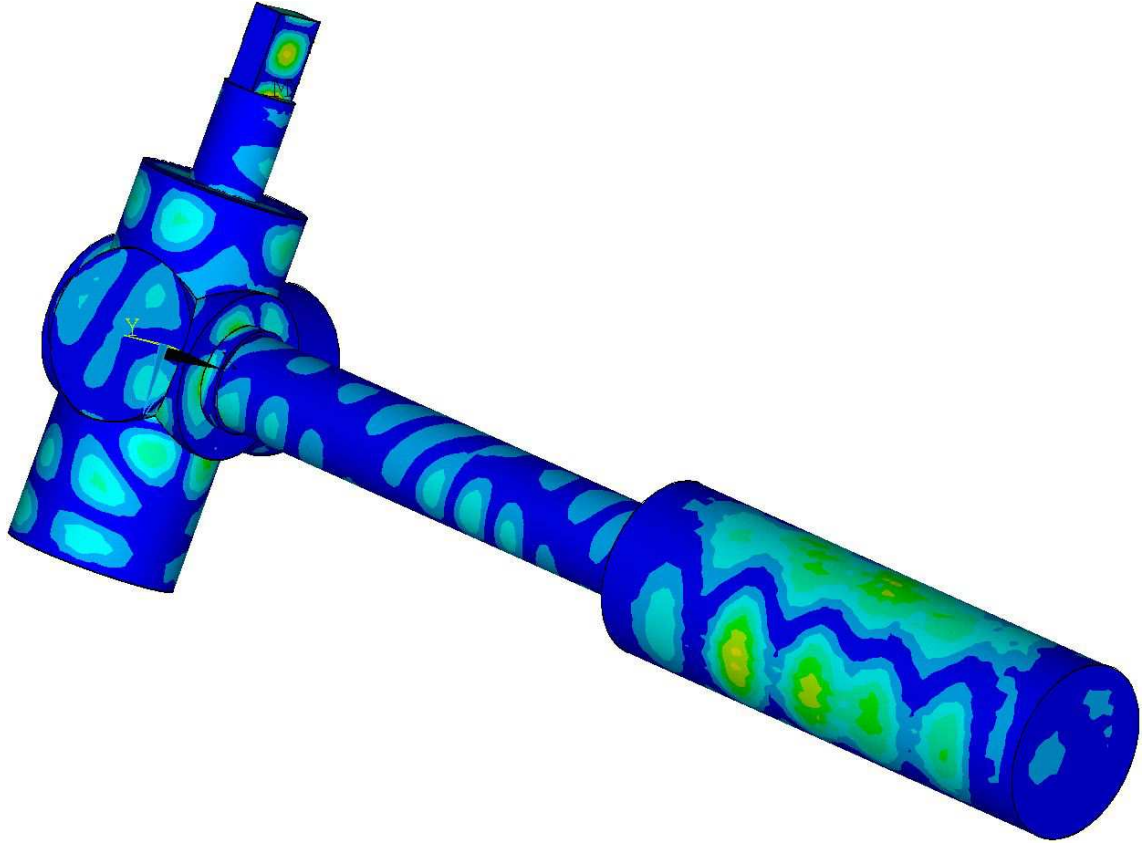


Figure 5.18 – Cut of the ECR ion source as modeled in a simulation [145]. The hole in the vacuum chamber for the beam extraction is supposed to be closed.



**Figure 5.19** – Simulation of the microwave propagation in the copper multimode cavity and in the plasma chamber [145]. The TE<sub>10</sub> mode can be identified in the waveguide. The coaxial tube guides the high-frequency waves inside the chamber. The hole in the vacuum chamber for the beam extraction is supposed to be closed.

### Magnetic dipole and Faraday cup

After the solenoid, the beam is injected into the analyzer magnet. This system is composed by a dipole magnet and of two pairs of metallic slits. The dipole produces a strong magnetic field  $B$  (up to 0.3 Tesla) perpendicular to the beam axis that forces the ions in a bent trajectory with a radius of curvature  $r$ , which depends on  $B$ , on  $\frac{q}{M}$  ratio (ion charge over ion mass) and on kinetic energy of the ions. Using the slits, it is possible to select a precise value of radius of curvature and changing the value of the magnetic field is possible to select ions with a precise  $\frac{q}{M}$  value:

$$B \propto \frac{1}{r} \sqrt{\frac{MV}{q}}, \quad (5.5)$$

where  $V$  is the extraction voltage of the ion (the voltage of the ECRIS). The current of the ions coming out from the analyzer magnet can be measured with a Faraday cup. Changing continuously the magnetic field, it is possible to study the  $\frac{q}{m}$  distribution of the beam observing the evolution of the ion current on the Faraday cup. An example of such distribution is presented in Fig. 5.20 where a beam of argon and oxygen ions is analyzed.

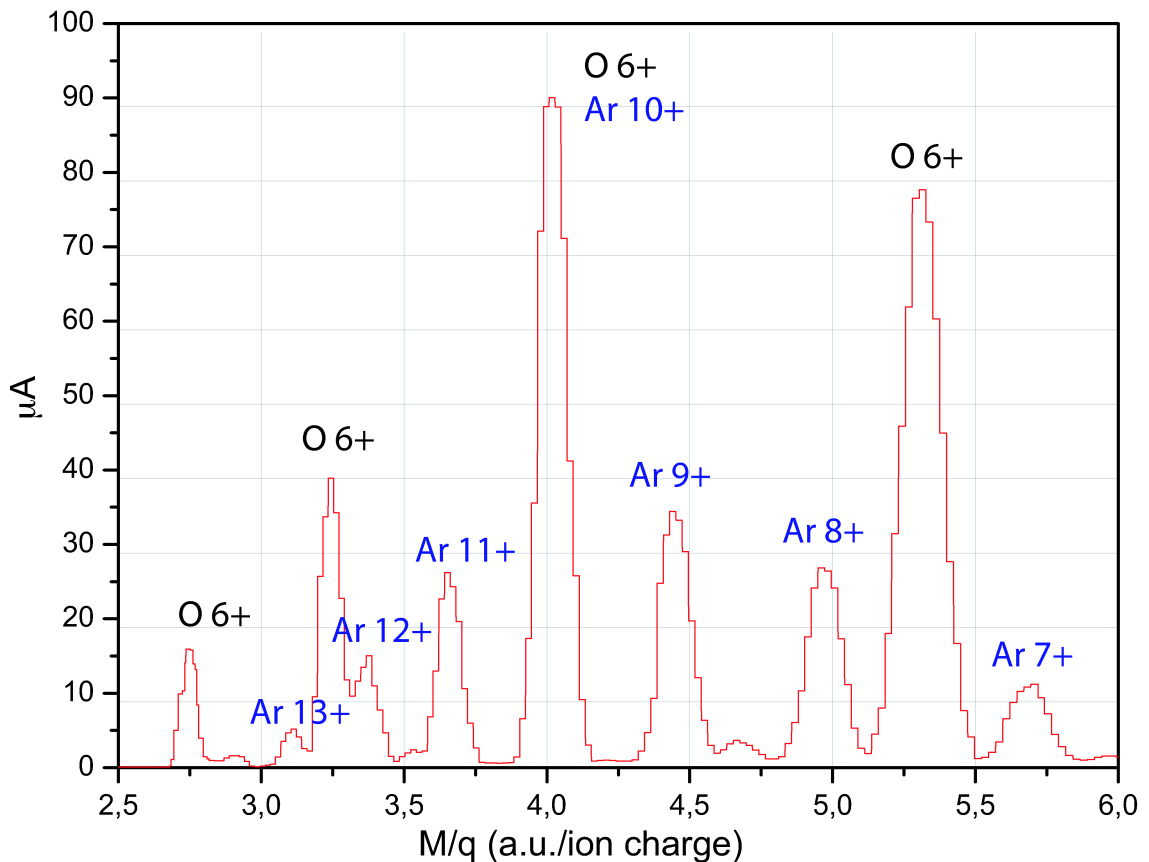


**Figure 5.20** – Magnetic scan of the charged state of the ion beam. The microwave injected power was 400 w and the ions were extracted with a tension of 14 kV.

The Faraday cup doesn't allow to detect directly currents lower than  $0.5 \mu\text{A}$ . The sensitivity of the beam current can be increased accumulating the charges into the Faraday cup for a long period, in the order of some tens of minutes. At the end of this period, the total deposited charge is measured using a current integrator and it allows for the detection of beam current in the order of some tens of pA.

### Interaction chamber

After the Faraday cup, it is present line a multiproposal interaction chamber on the beam. In this chamber, the ion beam can interact with a target: a solid plate, a gas jet or a cluster jet. The ion-target interaction allows for studies of ion-surface and ion-atom collision, but it can be also used to analyze the composition of the ion beam by observing of the radiation emitted during the collision. When the ion interact with the target, it captures one or more electrons that produce a radiative cascade inside the atom with the emission of photons. The energy of the photons depends strongly on the charged state of the interacting ion, and it can be used to identify the ion type. This method is very useful to detect low intensity ion beams and to distinguish ions with a similar  $\frac{q}{m}$  ratio, which are difficult to detect with the Faraday cup and to separate with the dipole magnet.

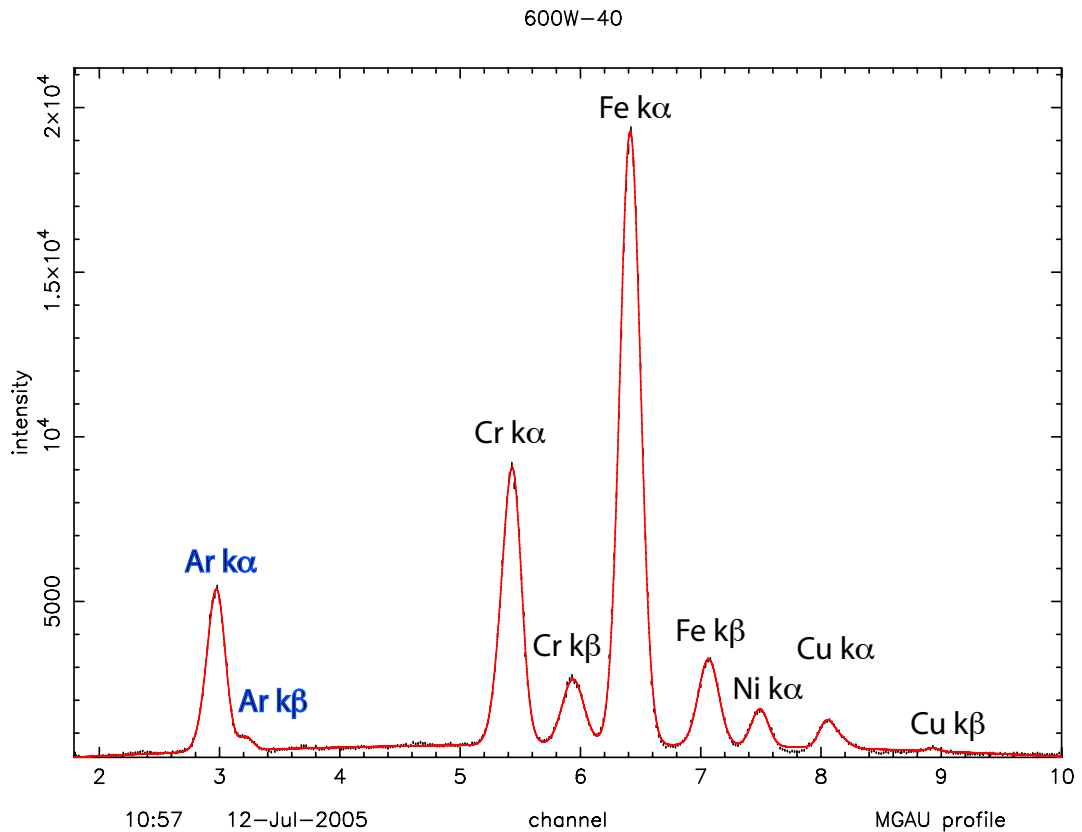


**Figure 5.21** – Spectrum of the plasma inside the source acquired with the silicon drift detector next to the dipole magnet. The injected gas was argon and oxygen, the microwave power was 600 w and the ions were extracted with a tension of 14 kV. On the left the argon  $K\alpha$  and  $K\beta$  lines are clearly visible.

Using X-ray detection, it was possible to measure the presence of  $Ne^{9+}$  and  $Ne^{10+}$  ion beam interacting with a nitrogen gas jet observing the transitions  $1s2p \rightarrow 1s^2$  and  $2p \rightarrow 1s$ , respectively. In the same way, it was possible to detect  $Ar^{17+}$  and  $Ar^{18+}$  using a denser target as a metallic plate. For this propose, we used a silicon drift detector<sup>9</sup> with resolution of 150 eV at 3 keV and an energy range of 1 – 20 keV. Using known cross-sections and geometry we can deduce the intensity of the beam.

### X-ray plasma detection

In addition to the ion beam analysis, the plasma characteristics are studied using X-ray spectroscopy. A silicon drift detector is placed on the beam axes behind the dipole magnet and it can measure X-rays coming in direct line of sight to the plasma. The silicon drift detector has a typical energy resolution of 150 eV and it can easily distinguish X-rays coming from different elements in the plasma (see Fig. 5.21).

As we saw in the previous section, the drift detector can be used also to distinguish X-rays coming from different charged states as  $Ar^{17+}$  and  $Ar^{18+}$ , which have  $K\alpha$  transition

<sup>9</sup>RÖNTEC XFLASH 2001 detector. Web site: <http://www.rontec.com>

energy of 3.1 and 3.3 keV, that interact with a solid target after the analyze magnet selection. The X-ray radiation coming from the plasma is emitted from all the charged states and it makes difficult to distinguish X-rays produced from different charged ions. For this reason, a mosaic crystal spectrometer has been installed next to the source, near the microwave injection.

Analogously to the spectrometer described in Sec. 3.3, this spectrometer is composed of a crystal, a mosaic crystal, which reflect X-rays according to the Bragg law (Eq. 3.2), and by a position sensitive detector. Mosaic crystals consist of an ensemble of microcrystals randomly oriented around a main direction according to a Gaussian distribution ( $\sigma = 1^\circ$ ). Like a flat crystal spectrometer this geometry requires a point-like source [146]. A graphite mosaic crystal is used instead of a flat crystal because the mosaic structure enables the reflection of X-rays from a bigger crystal surface than in a mono crystal, increasing the intensity of the reflected photons. The Bragg angle is measured using a position sensitive detector developed by the INSP group. This device is a gas detector filled with  $Xe(CH_4)$ . The X-rays that hit the detector produce the ionization of the gas. The released electrons are accelerated in direction of the high voltage anode and produce an avalanche, as in any proportional counters. The position sensitivity is obtained by the detection of the positive charge on the resistive cathode [146]. This instrument has an energy resolution of some about 2 eV for 3 keV X-rays. An example of a typical spectrum obtained with this instrument is presented in Fig. 5.22. The high energy part of this spectrum can be compared with the analog spectrum in Fig. 5.12 obtained with the Johann-type spectrometer and the PSI ECRIT.

An similar spectrometer is located near the interaction chamber for X-rays produced by the interaction the charged ions and the target. This enables the precise measurement of the radiation produced by the interaction between the ions and a target. In particular, for ion-surface interaction studies, such targets could consist in a solid surface or atomic clusters.

### Vacuum system

The vacuum system of the ECRIS is composed of two turbomolecular pumps: one 40 l/s pump on the gas injection side and one 500 l/s pump on the ion beam extraction side. We achieved a pressure of about  $1 - 2 \times 10^{-7}$  mbar when no gas injected.

The vacuum system of the beam line is composed, in addition to the pump near the ECR source, by a 200 l/s turbomolecular pump and a 4000 l/s cryopump. With this system we achieved a pressure of about  $5 - 10 \times 10^{-10}$  mbar. In addition, a ionic pump and a titan sublimator can be installed in the order to obtain a reference pressure in the order of  $10^{-11}$  mbar.

### Controls of the ion source and of the beam line

Almost all of the source controls are remotely connected to a computer. Using a Labview interface, it is possible to change the parameters of the source like the microwave power, the gas injection flux, the microwave tuner position and the solenoid and dipole magnetic field. Modification to the original Pantechnik design ables to change also the position of the polarization electrode.

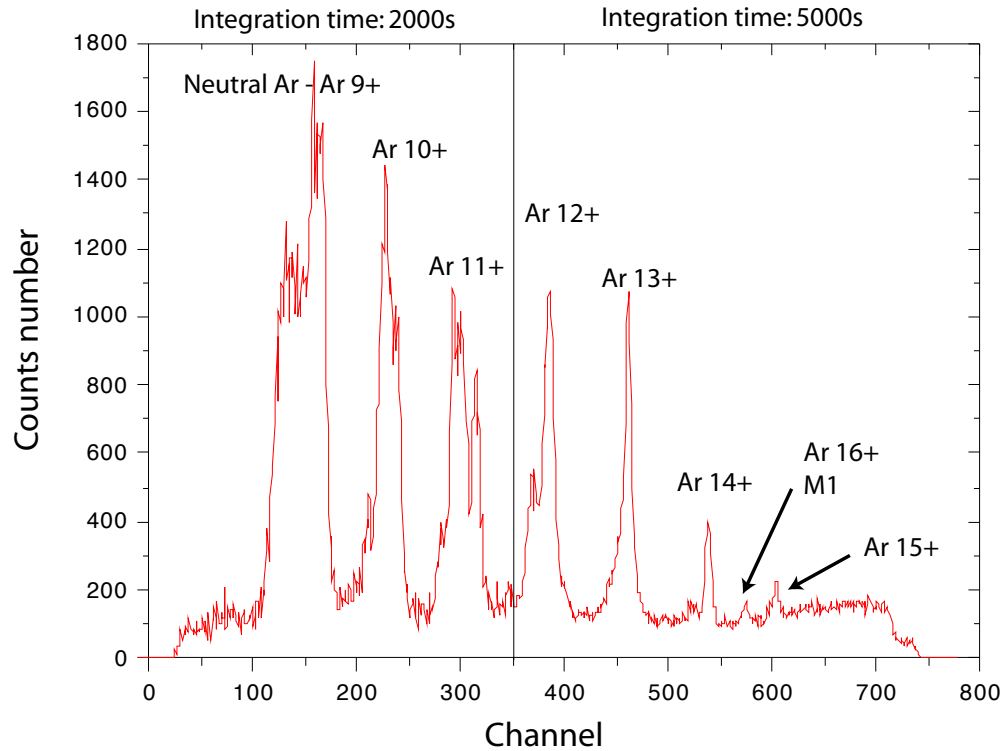


**Figure 5.22** – Spectrum of the plasma inside the source acquired with the mosaic spectrometer near the microwave injection. The injected gas was argon and oxygen, the microwave power was 400 w and the ions were extracted with a tension of 14 kV. On the left of the spectra (lower energies), it is possible to see the neutral argon  $K\alpha$ . This line and the  $K\alpha$  lines form argon ions up to  $Ar^{9+}$  are not resolved due to the small energy difference. On the right of the spectra (higher energies), it is possible to recognize the He-like argon  $1s2s\ ^3S_1 \rightarrow 1s^2\ ^1S_0$   $M1$  transition. This part of the spectrum can be compared with the similar spectrum obtained at PSI with the ECR ion trap: Fig. 5.12.

## Installation and first results

The installation of the SIMPA ECR ion source started at the end of 2002. During the first period, we placed the main components of the installation: the support of the vacuum line, the magnetic dipole (1.5 tons), the solenoid and, of course, the ECR ion source. In Spring 2003 we continued the installation connecting all the electronic devices to the computer controls and tests them. In the same period, we constructed a heat exchange system and a demineralised water cooling circuit, connected to the university cooling facility. Moreover, we placed special resins on the circuit to keep the water de-ionized. The de-ionization of the water is essential to obtain a sufficient electric isolation when the source is at high voltage.

The installation continued with the ignition and calibration of the Klystron HF generator. After a measurement of the magnetic field inside the source, we finally produced the first plasma in July 2003. In the first period of operation, we could inject only few watts of HF in the source before the source current would go to maximum. This was due to the presence of impurities on the electrode and on the plasma chamber surfaces. During the period of a few months, we cleaned the source by a gradually increasing of the injected microwave power that produced ions and radiation sputtering on the chamber surfaces.

The main interest of the ECR ion source installation is to use the plasma X-ray radiation for atomic physics studies. The original microwave injection didn't allow for the direct visual access to the plasma due of the presence of the cooling system of the polarization electrode. For this reason we modified the microwave coaxial line to enable the observation of light and X-rays coming directly from the plasma. Firstly, we changed the diameter of the polarization electrode (inner tube of the coaxial line): from 10 mm to 14 mm. Secondly, we replaced the air copper radiator by a water cooling.

After the source was commissioned in July 2003, we started to characterize the ECR ion source. In a first phase, after the cleaning of the source, we used a gas mixture of argon and oxygen and we tried to obtain the highest possible state by changing the parameters of the source. In this first period, most of the modification of the source were performed to achieve the best possible experimental conditions. These modifications enable new regulations of the ECRIS that allowed for a considerable increasing of the source performances.

Only in August 2004, we observed  $Ar^{17+}$  and  $Ar^{18+}$  in beam from the source for the first time. Subsequent optimizations allow to obtain a 50 pA current of H-like argon, which correspond to about  $1.8 \times 10^7$  ions/s.

In parallel to the ion beam detection, it was possible to observe the X-ray plasma spectrum using the silicon drift detector near the dipole magnet (see Fig. 5.15). In a typical spectrum, as in Fig. 5.21, the argon  $K\alpha$  and  $K\beta$  lines are clearly visible. In addition, there are present other  $K\alpha$  and  $K\beta$  lines of other elements. These lines are principally produced by fluorescence excitation from the plasma X-rays from different elements present in the devices in the vacuum line (electrodes, slits, ...).

The resolution of the solid state detector (about 150 eV) doesn't allow for the distinction of the different transition that have energy differences of some tens of eV. However, the contribution of the ionized atoms can shift the centroid of the argon  $K\alpha$  line. Observing the position and shape of the  $K\alpha$  line it is possible in principle to have a rough idea of the plasma degree of ionization. In practice, the interpretation of the spectra was ambiguous due to the vicinity of the  $K\beta$  to the highly charged ions  $K\alpha$  line.

A more powerful investigation was possible by the use of the mosaic crystal spectrometer. The resolution of this spectrometer at 3 KeV is about 2 eV, which is by far sufficient to distinguish the transitions from different ionized states as it is possible to see in Fig. 5.22.

Using this spectrometer we could observe clearly the He-like argon transitions, and in particular the  $1s2s\ ^3S_1 \rightarrow 1s^2\ ^1S_0$   $M1$  transition previously observed with the ECR ion trap at PSI (see Fig. 5.12).

Using the information from the ion beam and the crystal spectrometer, it was possible, at the end of 2004, to observe the plasma characteristics against different parameters of the source. In particular we studied the ionization state dependency on the injected microwave power, on the gases pressure and other parameters. The analysis are still in progress and it will be a part of the Ph.D. work of Nacer Adrouce.

## Outlook

The detection of the He-like argon  $1s2s\ ^3S_1 \rightarrow 1s^2\ ^1S_0$   $M1$  from the SIMPA ECRIS is very important because it demonstrate the possibility to measure the absolute energy of this transition with the double crystal spectrometer in development in the group. This measurement will enable the evaluation of absolute energy of the highly charged argon transitions with the recent relative energy measurement performed at PSI and presented in Ch. 6. Using the Johann Bragg spectrometer we measured, in fact, He- and Li-like  $K\alpha$  transitions with respect to the He-like argon  $1s2s\ ^3S_1 \rightarrow 1s^2\ ^1S_0$   $M1$  line, used as reference (see Ch. 6).

Since autumn 2004, we started to study other kind of highly charged ions as krypton and xenon. The study of the spectra of these two elements is very important to understand the dynamics of the plasma in the interstellar medium and in laboratory plasma, as in the ECR ion sources or other devices. The data acquisition and analysis for these elements is in progress.

# Chapter 6

---

## Highly charged ion spectra and QED tests

---

### Introduction

In chapter 5, I presented the ECR ion trap of the Paul Scherrer Institut, and in particular we saw the results of the characterization of this X-ray source and of the spectrometer, using the  $1s2s\ ^3S_1 \rightarrow 1s^2\ ^1S_0$   $M1$  transition of He-like ions. These measurements were done, principally, during the period Spring–Summer 2004. At the same time, it was possible to acquire X-ray spectra of atomic physics interest. More precisely, during this period, we obtained high accuracy spectra of highly charged argon, chlorine and sulphur. As mentioned in Ch. 1, the precise measurement of helium and lithium-like atoms with medium-high  $Z$  allows to test the relativistic interaction between electrons in strong field condition (the Coulomb potential of the nucleus). For this reason these measurements are essential to compare experimental results with predictions from different theoretical approaches.

In Sec. 3.3, I already presented the method to measure the energy difference between two X-ray transitions using a Johann-type crystal spectrometer. This method has been used to measure the energy difference between the  $5 \rightarrow 4$  muonic oxygen and pionic nitrogen transitions to evaluate the mass of the charged pion (see Ch. 4). In this case, the two atomic lines were visualized simultaneously on the CCD array to avoid the necessity to change the detector position and the crystal angles because the energy difference of the two transitions was sufficiently small (32 eV) (see Fig. 4.2). Highly charged ions spectra are, in contrast, characterized by a broader spectrum and the CCD array has to be moved to observe the ensemble of the X-ray transitions. As example,  $K\alpha$  lines from different charged states of argon, have energies that vary from 2.957 keV for the neutral atoms, to 3.320 keV for the H-like ions. These lines cannot be visualized simultaneously on the CCD array, and the CCD position and the crystal spectrometer angles have to be changed to observe a broader energy range. The change of the spectrometer set-up introduces an additional complication in the measurement of the energy differences, but it can easily be handled by simple geometrical reflections.

Contrary to the pionic nitrogen and muonic oxygen transitions, characterized by a Doppler broadening of several hundreds meV, multicharged ion transitions have a typical

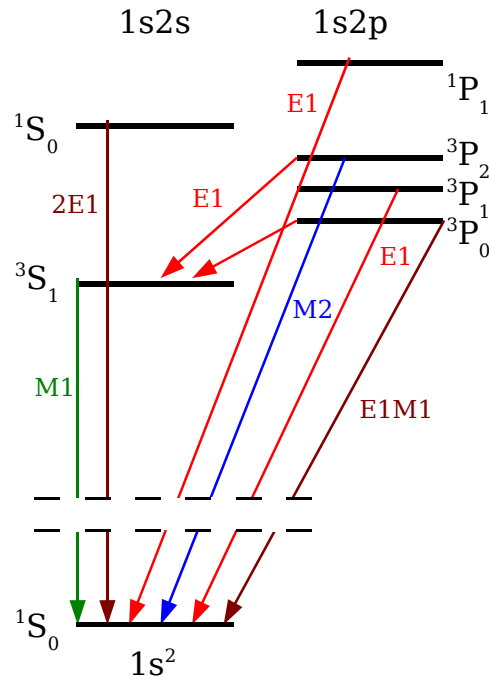


**Figure 6.1** – Energy level and decay scheme for the low-lying states of He-like ions.

width below 40 meV, almost 10 times smaller than the spectrometer resolution. For this reason, the line shape on the CCD array is mostly due to the crystal spectrometer response function. In particular, this response function can be slightly asymmetric if the detector is not at the focal point, and the data analysis requires a specific treatment to take into account this asymmetry and avoid the introduction of systematic effects in the measurement.

In Sec. 6.1, I will present the experimental condition and the procedure to obtain X-ray atomic spectra with our crystal spectrometer. In Sec. 6.2, the data analysis is described in detail. This analysis is preliminary and it allows to investigate possible systematic effects due to the spectrometer defocusing. It was possible to obtain a preliminary values for the transition energies of He-like argon and sulphur, which are, up to now, ones of the most accurate relative X-ray measurements for this energy range. The results are presented in Sec. 6.3, where they are compared to theoretical predictions and to previous measurements. The final section, Sec.6.4, is dedicated to the discussion of the systematic effects and I will present a new method for the spectra analysis, in development in the group, for a more accurate measurement of the highly charged ion transitions.

## 6.1 Helium-like ions spectra

The Electron-Cyclotron-Resonance ion trap at the Paul Scherrer Institut was originally designed to characterize accurately the crystal spectrometer used for the study of pionic

**Table 6.1** – Principal characteristics of the different experimental set-up for the acquisition of atomic spectra of argon, chlorine and sulphur.

Element	Argon	Chlorine	Sulphur
Gas mixture	$Ar - O_2$	$CHClF_2 - O_2$	$SO_2 - O_2$
Total pressure (mbar)	$3 - 4 \times 10^{-7}$	$3 - 4 \times 10^{-7}$	$3 - 4 \times 10^{-7}$
Pressure ratio (main gas)/ $O_2$	$\sim 9$	$\sim 9$	$\sim 9$
Crystal name	Z20, Z21	Z13	Z11
Crystal type	Qz (10.1)	Si (111)	Qz (10.0)
2d (nm)	0.66862	0.62712	0.85110
M1 energy (eV)	3104.14	2756.85	2430.34
$\Theta_B$ (°)	36.6814	45.8186	36.8271
Crystal-Detector distance (mm)	1783.75	2141.88	1789.46
$\frac{dE}{dx}$ (eV / pixels)	0.093	0.050	0.094
Microwave injected power (watt)	450	250	400

atoms. During spring and summer 2004, we have obtained high-precision measurements of the X-ray spectra of argon, chlorine and sulphur, which are particularly interesting to investigate atomic physics in relatively strong Coulomb fields. These spectra have been acquired using set-up with crystals of different type: silicon (111) and quartz (10.0) and (10.1). Each of them has a nominal radius of curvature of about 2985 mm. The injected microwave power was always around 200–400 watts, and the total pressure in the vacuum chamber was in the range of 3 to  $4 \times 10^{-7}$  mbar. For any set of measurements, the ECR ion trap has been optimized on the intensity of the He-like ions  $1s2s \ ^3S_1 \rightarrow 1s^2 \ ^1S_0$  M1 transition. Each time a new crystal was inserted in the spectrometer, a focal scan was performed to determine precisely the position of the focal plan. More details for the experimental condition are presented in Table 6.1 and in Sec. 5.2.

The typical data acquisition time for the He-like and Li-like ions spectra was in the order of 15 minutes, 30 frames of 30 s each (see Sec. 3.4 for the definition of “frame”). For less intense transitions, like the He-like  $1s2p \ ^1P_1 \rightarrow 1s^2 \ ^1S_0$  and  $1s2p \ ^3P_n \rightarrow 1s^2 \ ^1S_0$  transitions (Fig. 6.1), we acquired data for a period up to a maximum of 2 hours. In Figs. 6.2 and 6.3 we show atomic spectra near the region of the  $1s2p \ P \rightarrow 1s^2 \ ^1S_0$  He-like argon transitions. It is interesting to note the remarkable intensity differences between  $1s2s \ ^3S_1 \rightarrow 1s^2 \ ^1S_0$  M1 line and the other transitions in He-like ions. This difference on the transition line intensities ECR ion sources and traps is due to processes of the ion formation in the plasma. Helium-like ions are mostly ionization in the 1s shell of a Li-like ion [147]. Lithium-like ions are generally in ground state, as the majority of the ions in a ECR plasma, which has the electronic configuration  $1s^2 \ 2s$ . When a Li-like ion is ionized by ejection of a K-shell electron, the newly created He-like ion can be in either one of the excited levels  $1s2s \ ^3S_1$  or  $1s2s \ ^1S_0$ , which are metastable with a typical lifetime of some  $\mu s$ . Due to the angular momentum conservation, the  $1s2s \ ^1S_0 \rightarrow 1s^2 \ ^1S_0$  transition is possible only by emission of two E1 photons ( $L = L' = 0$  and  $|J - J'| \neq 1$ ). The dominant process for the  $1s2s \ ^3S_1 \rightarrow 1s^2 \ ^1S_0$  transition is the emission of a M1 photon ( $L = L' = 0$  and  $|J - J'| = 1$ ). The energy of the two E1 photons is distributed in a range between 0 eV and the energy difference between the levels, and it is impossible to distinguish it

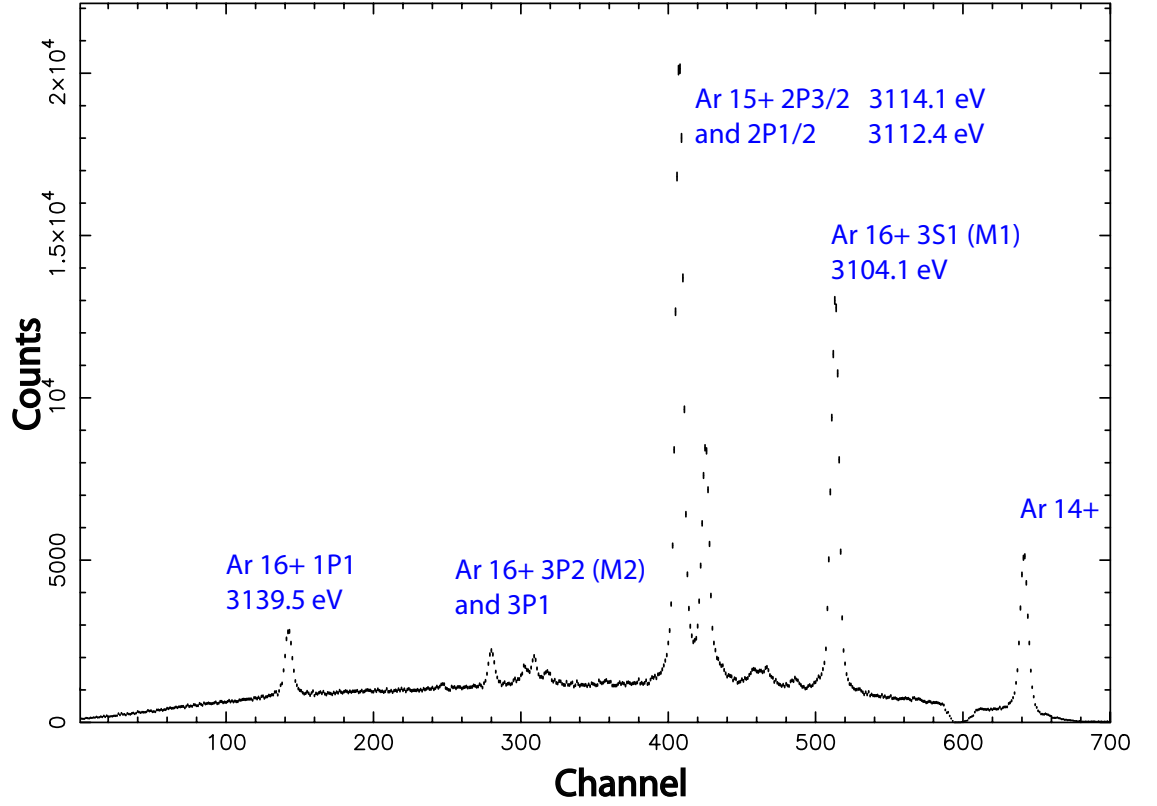


**Figure 6.2** – He-like and Li-like argon spectrum using quartz ( $10.\bar{1}$ ) crystal. HF power injected  $P = 400\text{ W}$ . Argon partial pressure  $p_{Ar} = 5 \times 10^{-9}\text{ mbar}$ , total pressure  $p_{tot} = 5 \times 10^{-7}\text{ mbar}$ . This spectrum has been obtained with an integration time of 2 hours. The focal position of this spectrum was in correspondence to the  $1s2p\ ^3P_n \rightarrow 1s^2\ ^1S_0$  peak, near ch. 310. The energy decreases with the increase of the channel number.

from the bremsstrahlung background, especially with a high resolution spectrometer. In contrast, the  $M1$  transition produces a peak with an intensity that is directly dependent on the number of created He-like ions in the plasma.

The transitions  $1s2p\ P \rightarrow 1s^2\ ^1S_0$  are principally produced by the excitation of He-like ions in the ground state due to collision with an electron:  $1s^2 \rightarrow 1s2p$ . For this reason, the intensity difference between the  $1s2p\ P \rightarrow 1s^2\ ^1S_0$  and  $1s2s\ ^3S_1 \rightarrow 1s^2\ ^1S_0$  transitions is proportional to the difference between the number of He-like ions ( $1s^2$ ) and the Li-like ions ( $1s^22s$ ) into the plasma [147].

## 6.2 Data acquisition and analysis

### Measurement of energy differences using two or more spectra

With the  $M1$  line in the focal position, the energy range of the visible spectrum is limited to some tens of eV due to the finite horizontal size of the collimator (28 mm) in front of

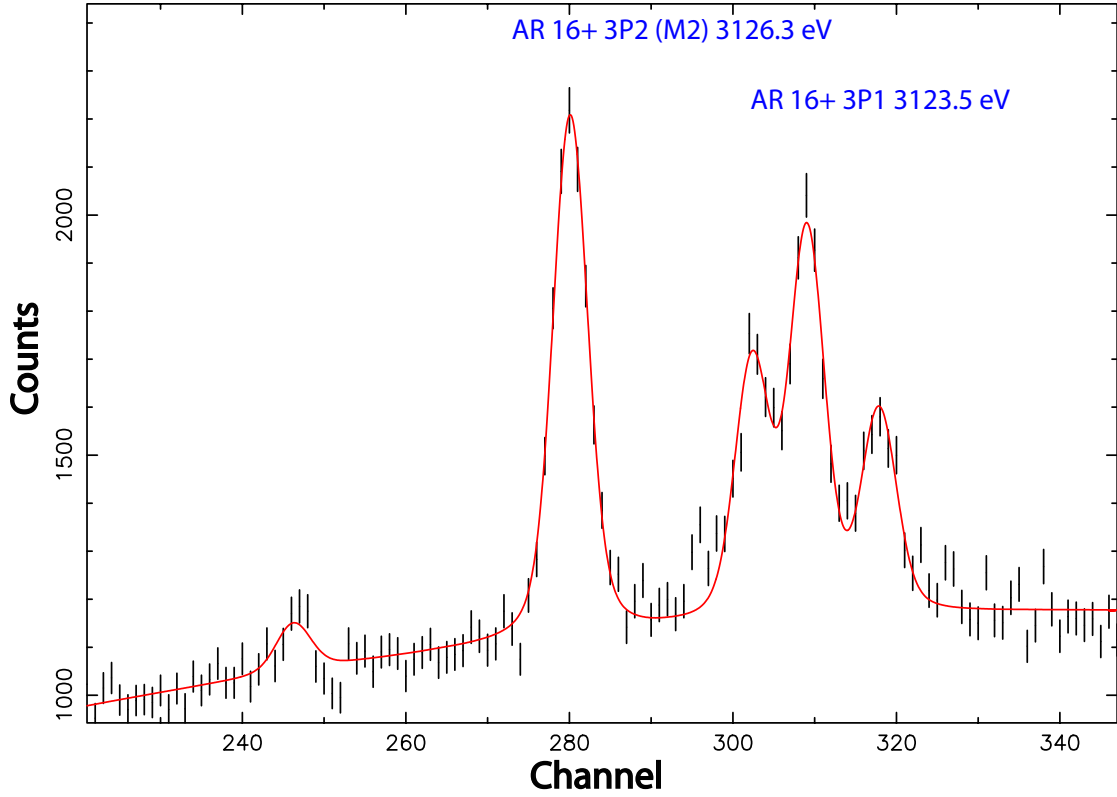


**Figure 6.3** – Detail of the spectrum in figure 6.2 around the  $1s2p\ ^3P_n \rightarrow 1s^2\ ^1S_0$  transitions. The energy decrease with the increasing of the channel number. The two lines next to the  $3P_1$  peak are due to Li-like transitions with an electron in  $n = 3 - 5$  orbitals.

the source (see Fig. 5.10) and due to the detector size. The presence of the collimator is essential to increase the peak-to-background ratio, reducing the bremsstrahlung radiation from the source, which is indistinguishable from the X-rays emitted by the ions. It is possible to explore broader energy ranges changing  $\Theta_{\text{ARM}}$ ,  $\Theta_{\text{CRY}}$  ( $\delta\Theta_{\text{ARM}} = 2 \times \delta\Theta_{\text{CRY}}$ ) and the crystal-detector distance. The change of these two angles corresponds to observe an other range of Bragg angle, i.e., a different energy range. To maintain the CCD array on the Rowland circle, it is necessary to adjust the distance between crystal and the detector at each angle (see also Sec. 3.3). As an example, we consider the  $1s2s\ ^3S_1 \rightarrow 1s^2\ ^1S_0$  and  $1s2p\ ^1P_1 \rightarrow 1s^2\ ^1S_0$  transitions in He-like argon, which have an energy difference of about 34 eV. As we can see on Fig. 6.2, both lines can be visualized in the same spectrum. However, the  $M1$  transition is significantly away from the focal position of the detector near ch. 310, and for this reason it is preferable to measure the energy difference between these lines using at least two different spectra with the CCD in two different positions (more details about the defocusing effect are presented in Sec. 6.4). As presented in Fig. 6.4 and 6.5, we consider a set-up with the  $M1$  transition on the focal position, *Set-up 1*, and a set-up with the  $1s2p\ ^3P_1 \rightarrow 1s^2\ ^1S_0$  transition in the focal position, *Set-up 2*. In correspondence of these two set-up, we obtain two spectra, *Spectrum 1* and *Spectrum 2*,

respectively. In *Spectrum 2*,  $1s2p\ ^1P_1 \rightarrow 1s^2\ ^1S_0$  transition is at only 150 channels (6 mm) from the position of the focus near ch. 310.

In principle, we could measure the energy difference between the M1 line (line A in Fig. 6.5), observed in *Set-up 1*, and  $1s2s\ ^1P_1 \rightarrow 1s^2\ ^1S_0$  line (line C in Fig. 6.5), observed in *Set-up 2*, considering the position of the peaks and the spectrometer angles  $\Theta_1$ ,  $\Theta_2$ , and the crystal-detector distance  $D_1$ ,  $D_2$  corresponding to *Set-up 1* and *2*, respectively. The precision of the measurement depends, of course, on the  $\Theta_i$  and  $D_i$  accuracy. At present, it is easy to obtain an error smaller than 0.1 mm for the distance value, and modern angular encoders can easily reach a precision of about  $0.2'' \approx 1\ \mu\text{rad}$ , accurate enough for our intents.

Unfortunately, our angular encoder and/or the rotating mechanical parts in the spectrometer are affected by an ‘‘hysteresis’’ of unknown origin: if we move the detector to a certain angle, the position of the peaks on the spectrum depends on the direction we moved the spectrometer to reach this angle. This ‘‘hysteresis’’ can produce a deviation of several minutes between the real value and the measured angles,  $\Theta_1$  and  $\Theta_2$ , just after a direction change, which makes the angular encoder readout for the energy measurement useless.

To avoid this problem, we employed a special technique in the analysis of the spectra. For the measurement of the energy difference between a peak A, in *Spectrum 1* and a peak C in *Spectrum 2*, we managed to have a third peak B in *Spectrum 1* **and** in *Spectrum 2* to be used as reference peak. In our example, one of the  $K\alpha$  line from Li-like argon can be used for this intent. The Li-like argon transitions are, in fact, present in *Spectrum 1* and *Spectrum 2* as we can see in Fig. 6.4.

The energy difference between two lines in different spectra requires a slightly more complicated formula than for the case of two lines in the same spectra (Eq. 3.8). The energy difference  $\Delta E_{AC}$ , between the line A and C, can be evaluated by the sum of the angular differences  $\Delta\Theta_{AB}$  between the line A and line B, and the angular difference  $\Delta\Theta_{BC}$  between line B and line C. The angular difference  $\Delta\Theta_{AB}$  is evaluated from the peak positions in *Spectrum 1* (see Fig. 6.5), where the crystal-detector distance is  $D_1$ , and  $\Delta\Theta_{BC}$  is evaluated from the peak positions in *Spectrum 2* (see Fig. 6.5), where the crystal-detector distance is  $D_2$ . In this case we have:

$$\begin{aligned} \Delta\Theta_{AB} &= \arctan\left(\frac{x_A^{(1)} - x_F^{(1)}}{D_1}\right) - \arctan\left(\frac{x_B^{(1)} - x_F^{(1)}}{D_1}\right) \\ &\approx \frac{x_A^{(1)} - x_B^{(1)}}{D_1} + \mathcal{O}\left[\left(\frac{x_{A,B}^{(1)} - x_F^{(1)}}{D_1}\right)^3\right] \end{aligned} \quad (6.1)$$

and

$$\begin{aligned} \Delta\Theta_{BC} &= \arctan\left(\frac{x_B^{(2)} - x_F^{(2)}}{D_2}\right) - \arctan\left(\frac{x_C^{(2)} - x_F^{(2)}}{D_2}\right) \\ &\approx \frac{x_B^{(2)} - x_C^{(2)}}{D_2} + \mathcal{O}\left[\left(\frac{x_{B,C}^{(2)} - x_F^{(2)}}{D_2}\right)^3\right], \end{aligned} \quad (6.2)$$

where  $x_i^{(1)}$  are the line positions when we have *Set-up 1*, and  $x_i^{(2)}$  are the line positions when we have *Set-up 2*.

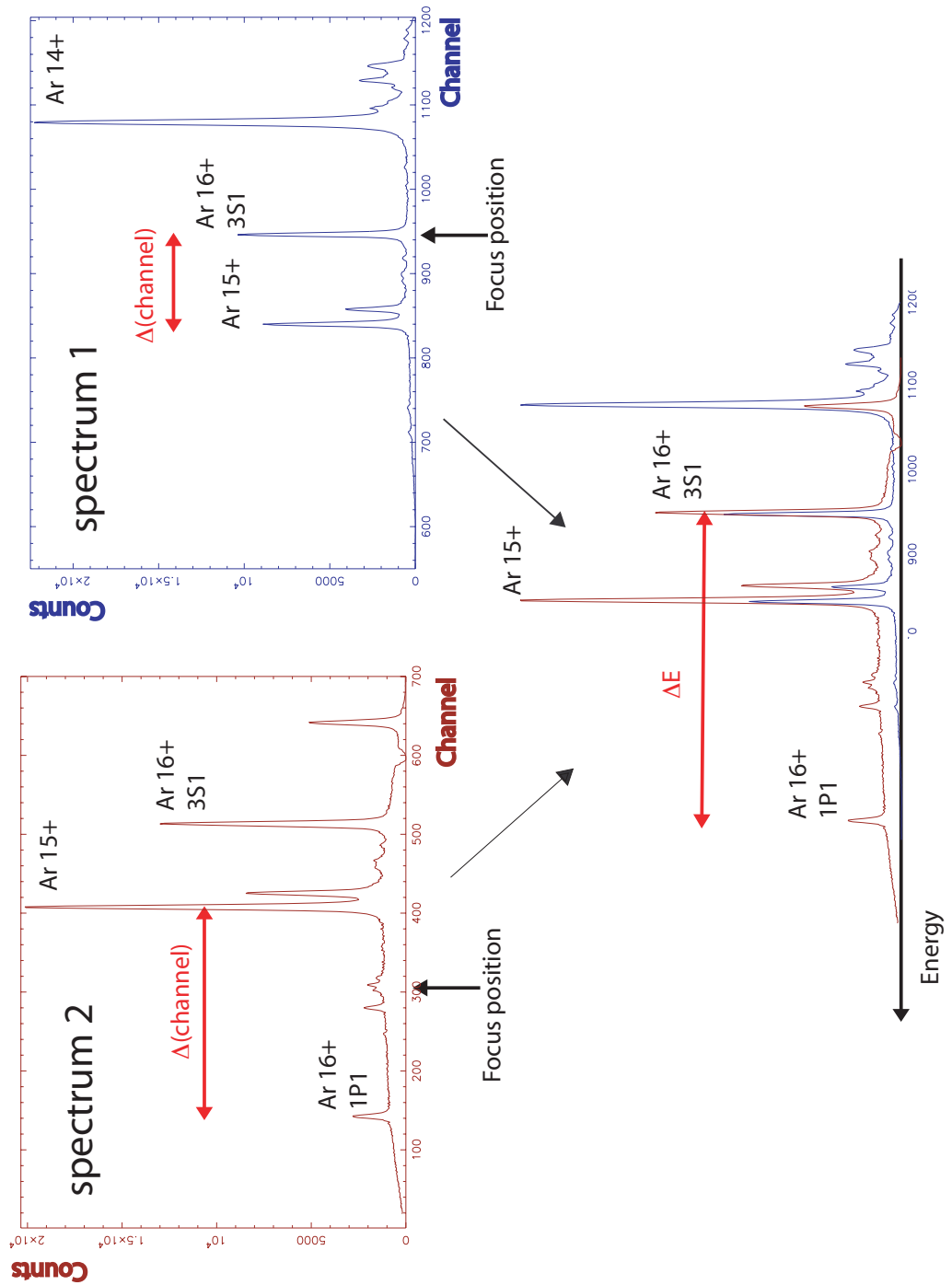


**Figure 6.4** – Measurement of the energy differences between two transitions using a third reference line. The energy difference between  $1s2s\ ^3S_1 \rightarrow 1s^2\ ^1S_0$  and  $1s2p\ ^1P_1 \rightarrow 1s^2\ ^1S_0$  transitions (peak A and C in the text) is evaluated by measuring the corresponding peak position with respect to the position of the  $K\alpha$  Li-like argon peak (peak B in the text) in *Spectrum 1* and in *Spectrum 2*. See also Fig. 6.5.

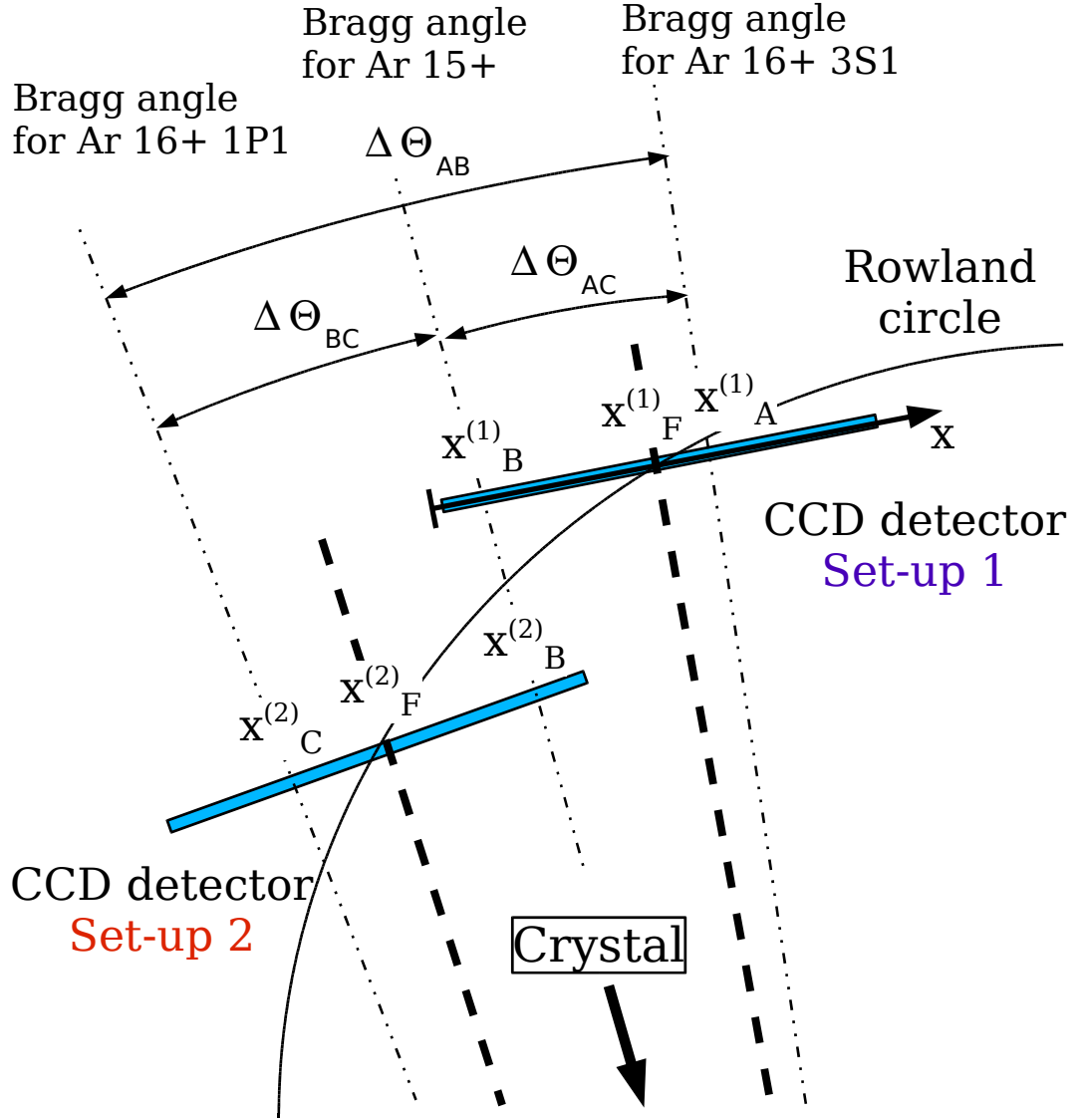


**Figure 6.5** – Measurement of the energy differences between two transitions using a third reference line. The energy difference between  $1s2s\ ^3S_1 \rightarrow 1s^2\ ^1S_0$  and  $1s2p\ ^1P_1 \rightarrow 1s^2\ ^1S_0$  transitions is deduced from the corresponding Bragg angle difference  $\Delta\Theta_{AB}$ . This difference is measured by the evaluation of the position of the different lines on the CCD array with the help of a third transition, the  $K\alpha$  transition from Li-like argon in our case. Measuring the correspondent peak position  $x_A^{(1)}$  and  $x_B^{(1)}$  in *Spectrum 1*, which correspond to the *Set-up 1*, it is possible to measure  $\Delta\Theta_{AB}$ . In the same way, measuring the peak positions  $x_B^{(2)}$  and  $x_C^{(2)}$  in *Spectrum 2*, which correspond to the *Set-up 2* of the detector, it is possible to measure  $\Delta\Theta_{BC}$ . From  $\Delta\Theta_{AB}$  and  $\Delta\Theta_{BC}$  we can evaluate the angular difference  $\Delta\Theta_{AC} = \Delta\Theta_{AB} + \Delta\Theta_{BC}$ , which allows for the energy difference measurement between the line A,  $1s2s\ ^3S_1 \rightarrow 1s^2\ ^1S_0$  transition, and line C,  $1s2p\ ^1P_1 \rightarrow 1s^2\ ^1S_0$  transition.

The energy difference between line A and line C, ( $1s2s^3S_1 \rightarrow 1s^2^1S_0$  and  $1s2s^1P_1 \rightarrow 1s^2^1S_0$  transition He-like argon in our example) can be calculated using Eq. (3.7) for the energy differences  $\Delta E_{AB}$  and  $\Delta E_{BC}$ :

$$\begin{aligned}
\Delta E_{AC} &= E_A \left( 1 - \frac{1}{\cos \Delta\theta_{AB} + \cot \theta_A \sin \Delta\theta_{AB}} \right) \\
&\quad + (E_A + \Delta E_{AB}) \left[ 1 - \frac{1}{\cos \Delta\theta_{BC} + \cot(\theta_A + \Delta\theta_{AB}) \sin \Delta\theta_{BC}} \right] \\
&= E_A \left\{ \left( 1 - \frac{1}{\cos \Delta\theta_{AB} + \cot \theta_A \sin \Delta\theta_{AB}} \right) \right. \\
&\quad \left. + \frac{1}{\cos \Delta\theta_{AB} + \cot \theta_A \sin \Delta\theta_{AB}} \left[ 1 - \frac{1}{\cos \Delta\theta_{BC} + \cot(\theta_A + \Delta\theta_{AB}) \sin \Delta\theta_{BC}} \right] \right\} \\
&\approx -E_A \cot \theta_A \left\{ \Delta\theta_{AB} + \Delta\theta_{BC} + \mathcal{O} \left[ (\Delta\theta_{AB,BC})^2 \right] \right\} \\
&\approx -E_A \cot \theta_A \left\{ \left( \frac{x_A^{(1)} - x_B^{(1)}}{D_1} \right) + \left( \frac{x_B^{(2)} - x_C^{(2)}}{D_2} \right) + \mathcal{O} \left[ \left( \frac{x_{A,B,C}^{(1),(2)} - x_F^{(1),(2)}}{D_{1,2}} \right)^2 \right] \right\}, \quad (6.3)
\end{aligned}$$

In the data analysis we used the complete formula without any approximation. However, the approximated form provides an easier understanding of the formulas that can be compared to the expected spectrometer dispersion relationship (Eq. (3.9)).

This technique leads to an accuracy of few meV on the energy differences, depending on the statistic and on the set-up. This method can be used only when we dispose of an atomic spectrum sufficiently dense to have always at least two visible lines in each spectrum. This condition can easily be accomplished with the overlapping of two or more emission spectra from different ions.

### Peak fit on the high accuracy position spectrum

As for the pionic atoms, the line positions on the CCD array are measured by fitting the one-dimensional spectrum, produced by the projection of the two-dimensional plot on the x-axis, the dispersion axis, (see Fig. 4.2). In the preliminary analysis during the optimization of the ECR ion trap, the lines intensity was measured using a simple profile model for the fit, like Gaussian or Lorentzian distributions. For the precise energy measurement, the peaks are fitted with the theoretical response function of the spectrometer convoluted with a Gaussian distribution. The theoretical rocking curve of the crystal is obtained from XOP code [103]. The response function is obtained from Monte Carlo simulations, which takes into account the experimental set-up geometry and the type of crystal. The reliability of the simulation had been tested previously during the characterization of the spectrometer, as discussed in Sec. 5.2 and in Ref. [112]. The convolution with a Gaussian distribution enables to take into account the imperfection of the crystal. The fit is performed using the FIT6 program and the typical accuracy of the position evaluation is in the order of some percent of pixel. This line shape reproduces very well the real data with a typical reduced  $\frac{\chi^2}{\nu} \approx 1$  even for high statistics spectra as that presented in Fig. 6.2.

**Table 6.2** – Energy transition in He-like argon. The energy difference to the ground level have been evaluated using as calibration the  $1s2s\ ^3S_1 \rightarrow 1s^2\ ^1S_0$  transition with the theoretical value evaluated with the multiconfiguration Dirac-Fock method [67, 148]. The first error represents the error due to the statistic. The second one is due to the systematic effects.

Transition	Measured energy (eV)
$1s2p\ ^3S_1 \rightarrow 1s^2\ ^1S_0$	3104.129 Reference line
$1s2p\ ^3P_1 \rightarrow 1s^2\ ^1S_0$	$3123.483 \pm 0.006 \pm 0.004$
$1s2p\ ^3P_2 \rightarrow 1s^2\ ^1S_0$	$3126.256 \pm 0.005 \pm 0.005$
$1s2p\ ^1P_1 \rightarrow 1s^2\ ^1S_0$	$3139.511 \pm 0.003 \pm 0.008$
$1s2p\ ^3P_1 \rightarrow 1s2p\ ^3S_1$	$19.354 \pm 0.006 \pm 0.004$
$1s2p\ ^3P_2 \rightarrow 1s2p\ ^3S_1$	$22.127 \pm 0.005 \pm 0.005$
$1s2p\ ^1P_1 \rightarrow 1s2p\ ^3S_1$	$35.382 \pm 0.003 \pm 0.008$
$1s2p\ ^1P_1 \rightarrow 1s2p\ ^3P_1$	$16.028 \pm 0.010 \pm 0.004$
$1s2p\ ^1P_1 \rightarrow 1s2p\ ^3P_2$	$13.255 \pm 0.008 \pm 0.003$
$1s2p\ ^3P_1 \rightarrow 1s2p\ ^3P_2$	$2.773 \pm 0.011 \pm 0.000$

**Table 6.3** – Energy transition in He-like sulphur. The energy difference to the ground level have been evaluated using as calibration the  $1s2s\ ^3S_1 \rightarrow 1s^2\ ^1S_0$  transition with the theoretical value evaluated with the multiconfiguration Dirac-Fock method [67, 148]. The first error represents the error due to the statistic. The second one is due to the systematic effects.

Transition	Measured energy (eV)
$1s2p\ ^3S_1 \rightarrow 1s^2\ ^1S_0$	2430.336 Reference line
$1s2p\ ^3P_1 \rightarrow 1s^2\ ^1S_0$	$2447.116 \pm 0.007 \pm 0.004$
$1s2p\ ^3P_2 \rightarrow 1s^2\ ^1S_0$	$2448.737 \pm 0.013 \pm 0.004$
$1s2p\ ^1P_1 \rightarrow 1s^2\ ^1S_0$	$2460.632 \pm 0.011 \pm 0.007$
$1s2p\ ^3P_1 \rightarrow 1s2p\ ^3S_1$	$16.780 \pm 0.007 \pm 0.004$
$1s2p\ ^3P_2 \rightarrow 1s2p\ ^3S_1$	$18.401 \pm 0.013 \pm 0.004$
$1s2p\ ^1P_1 \rightarrow 1s2p\ ^3S_1$	$30.296 \pm 0.011 \pm 0.007$
$1s2p\ ^1P_1 \rightarrow 1s2p\ ^3P_1$	$13.516 \pm 0.018 \pm 0.003$
$1s2p\ ^1P_1 \rightarrow 1s2p\ ^3P_2$	$11.895 \pm 0.024 \pm 0.003$
$1s2p\ ^3P_1 \rightarrow 1s2p\ ^3P_2$	$1.621 \pm 0.019 \pm 0.000$

### 6.3 Results and comparison with theoretical predictions

In this section, I will present the result of the energy measurement of the argon and sulphur spectra. The analysis presented in this thesis is not final and its main propose was to investigate the simulation and fit techniques, required to reach a good accuracy, and to study systematic effects. For this reason the chlorine spectra have not yet been analyzed. For the same reason, I restrict the analysis to the He-line transitions. The study of the atomic transition of ions with a smaller charged state requires a more refined analysis because they are characterized by more complicated structures, and the Auger broadening cannot be neglected. The preliminary results obtained from He-like argon and sulphur spectroscopy have a precision of the order of 10 meV and they agree with

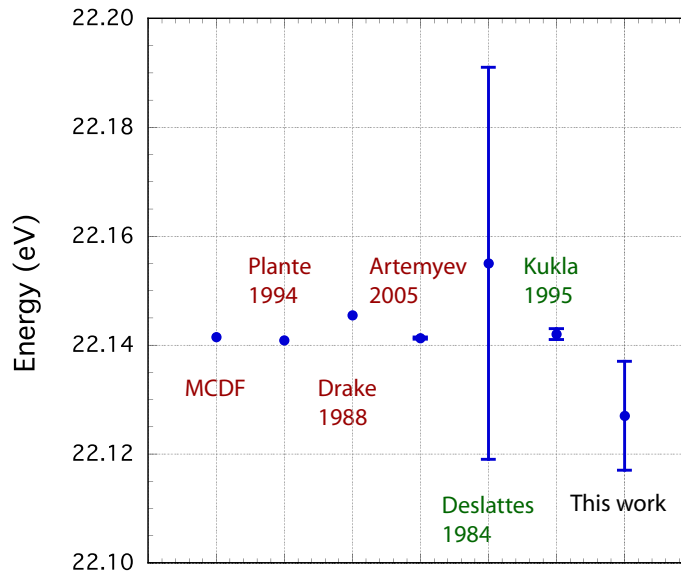


**Figure 6.6** – Comparison of the theoretical and experimental values for the  $1s2p\ ^3P_2 \rightarrow 1s2s\ ^3S_1$  transition in He-like argon. “Deslattes1984” [149] value has been obtained using X-ray crystal spectroscopy. “Kukla1995” [150] has been obtained using UV spectroscopy.

the previous experimental values and theoretical predictions. The value of the measured He-like transition are resumed in Tables 6.3 and 6.3. The absolute evaluation of the  $1s2p\ P \rightarrow 1s^2\ ^1S_0$  transitions have been obtained using as reference the theoretical value of the  $1s2s\ ^3S_1 \rightarrow 1s^2\ ^1S_0$   $M1$  transition evaluated with the multiconfiguration Dirac-Fock method [67, 148]. In these tables, the first error is due to the statistics and it is provided by the error analysis of the fit. The second contribution comes from the systematic error due principally to accuracy of the detector-crystal distance value. The accuracy of this distance is actually limited by the knowledge of the vacuum pipe length used into the set-up. This length, at ambient temperature, is known at present with an error of about 0.5 mm, and it introduces a systematic error of about 0.03% on the energy differences. This error can be reduced with a more accurate measurement of the vacuum pipes length. With the present technology, an accuracy better than 100  $\mu\text{m}$  can easily be reached. This measurement will be done in the next few months.

A complete error analysis requires the study of the systematic errors due to the pixel distance, the CCD orientation, the curvature correction and other effects. These effects have been already estimated for the pion mass measurement (Sec. 4.5) and they are sufficiently small (in the order of 10-20 ppm on the energy difference values) to be neglected for this preliminary analysis, where the error due to the detector-crystal distance is much larger than other systematic effects.

In Tables 6.4 and 6.5 and in Figs. 6.6 and 6.7 we compare the obtained results with the available values provided by previous experiments and theoretical predictions. As we can observe, our results confirm the older measurement on X-ray spectroscopy of He-like argon

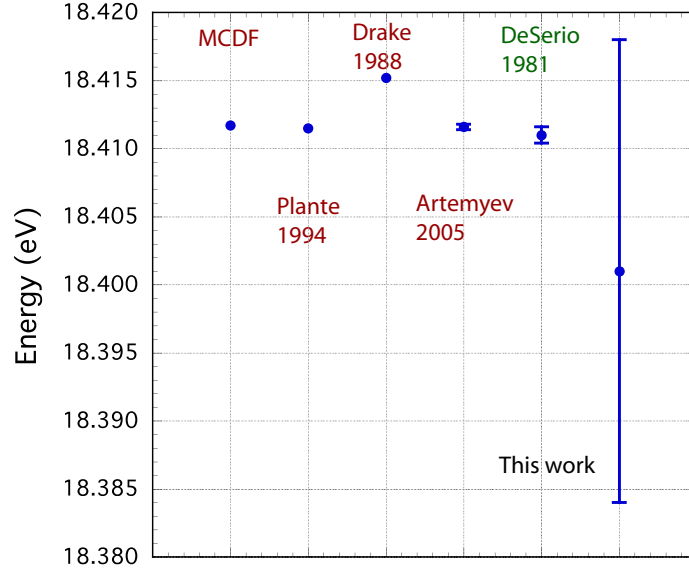


**Figure 6.7** – Comparison of the theoretical and experimental values for the  $1s2p\ ^3P_2 \rightarrow 1s2s\ ^3S_1$  transition in He-like sulphur. “DeSerio1981” [151] has been obtained using UV spectroscopy.

and sulphur [149, 152] with a significant increase of the experimental accuracy. Our values are also in agreement with the direct UV measurement of the  $2\ ^3P_2 \rightarrow 2\ ^3S_1$  transition [150, 151], which are characterized by an accuracy one order of magnitude better than X-ray spectroscopy. Contrary to the UV spectroscopy, which is limited to study transitions with  $|J - J'| = 1$  (as  $2\ ^3P_2 \rightarrow 2\ ^3S_1$ ), X-ray spectroscopy can evaluate the energy differences between almost all the He-like  $n = 2$  levels. This is possible because we compare the energy of  $2 \rightarrow 1$  transitions. In opposite, with this method it is not possible to evaluate the energy of the levels  $1s2s\ ^1S_0$  and  $1s2p\ ^3P_0$  because they decay to the ground level by emission of two photons (see Fig. 6.1).

As we can observe in Tables 6.4 and 6.5, our results are also in agreement with the theoretical evaluation from different methods: the multiconfiguration Dirac-Fock (MCDF) [148, 67], the relativistic many-body problem theory (RMBPT) [25, 26], the unified method [30] and recent calculation for He-like atoms from Artemyev [32]. However, the experimental accuracy does not allow to test the validity of the different predictions.

## 6.4 Outlook and further analysis

### The further analysis

As written in the previous sections, the accuracy of the previous measurement can be improved by an accurate measurement of the vacuum line pipes. Their length value introduces, at present, the largest systematic effect on the energy evaluation. A decrease

**Table 6.4** – Comparison of the theoretical and experimental values for the  $n = 2$  inner-shell transition in He-like argon. “Destlattes1984” value has been obtained using X-ray crystal spectroscopy. “Kukla1995” has been obtained using UV spectroscopy.

1s2p 3P1-1s2p 3P2	MCDF [67]	Plante [25]	Drake [30]	Artemyev2005 [32]	Deslattes1984 [149]	Kukla1995 [150]	This work
$1s2p\ ^3P_1 \rightarrow 1s2p\ ^3S_1$	19.3875	19.3858	19.3910	$19.3861 \pm 0.0002$			$19.354 \pm 0.011$
$1s2p\ ^3P_2 \rightarrow 1s2p\ ^3S_1$	22.1415	22.1409	22.1455	$22.1413 \pm 0.0002$		$22.1422 \pm 0.0006$	$22.127 \pm 0.010$
$1s2p\ ^1P_1 \rightarrow 1s2p\ ^3S_1$	35.4379	35.4342	35.4415	$35.4338 \pm 0.0002$			$35.382 \pm 0.011$
$1s2p\ ^1P_1 \rightarrow 1s2p\ ^3P_1$	16.0505	16.0484	16.0505	$16.0477 \pm 0.0002$	$16.031 \pm 0.072$		$16.028 \pm 0.013$
$1s2p\ ^1P_1 \rightarrow 1s2p\ ^3P_2$	13.2964	13.2933	13.2960	$13.2925 \pm 0.0002$	$13.269 \pm 0.072$		$13.255 \pm 0.011$
$1s2p\ ^3P_1 \rightarrow 1s2p\ ^3P_2$	2.7540	2.7551	2.7545	$2.7552 \pm 0.0010$	$2.762 \pm 0.072$		$2.773 \pm 0.011$

**Table 6.5** – Comparison of the theoretical and experimental values for the  $n = 2$  inner-shell transition in He-like sulphur. “Schleinkofer1982” value has been obtained using X-ray crystal spectroscopy. “DeSerio1981” has been obtained using UV spectroscopy.

Transition	MCDF [67]	Plante [25]	Drake [30]	Artemyev2005 [32]	Schleinkofer1982 [152]	DeSerio1981 [151]	This work
$1s2p\ ^3P_1 \rightarrow 1s2p\ ^3S_1$	16.7935	16.7926	16.7967	$16.7927 \pm 0.0002$			$16.780 \pm 0.010$
$1s2p\ ^3P_2 \rightarrow 1s2p\ ^3S_1$	18.4117	18.4115	18.4152	$18.4116 \pm 0.0002$		$18.4108 \pm 0.0006$	$18.401 \pm 0.017$
$1s2p\ ^1P_1 \rightarrow 1s2p\ ^3S_1$	30.2810	30.2783	30.2845	$30.278 \pm 0.0002$			$30.296 \pm 0.018$
$1s2p\ ^1P_1 \rightarrow 1s2p\ ^3P_1$	13.4875	13.4857	13.4878	$13.4853 \pm 0.0002$	$13.62 \pm 0.20$		$13.516 \pm 0.021$
$1s2p\ ^1P_1 \rightarrow 1s2p\ ^3P_2$	11.8692	11.8668	11.8693	$11.8664 \pm 0.0008$			$11.895 \pm 0.027$
$1s2p\ ^3P_1 \rightarrow 1s2p\ ^3P_2$	1.6182	1.6189	1.6185	$1.6189 \pm 0.0008$			$1.621 \pm 0.020$

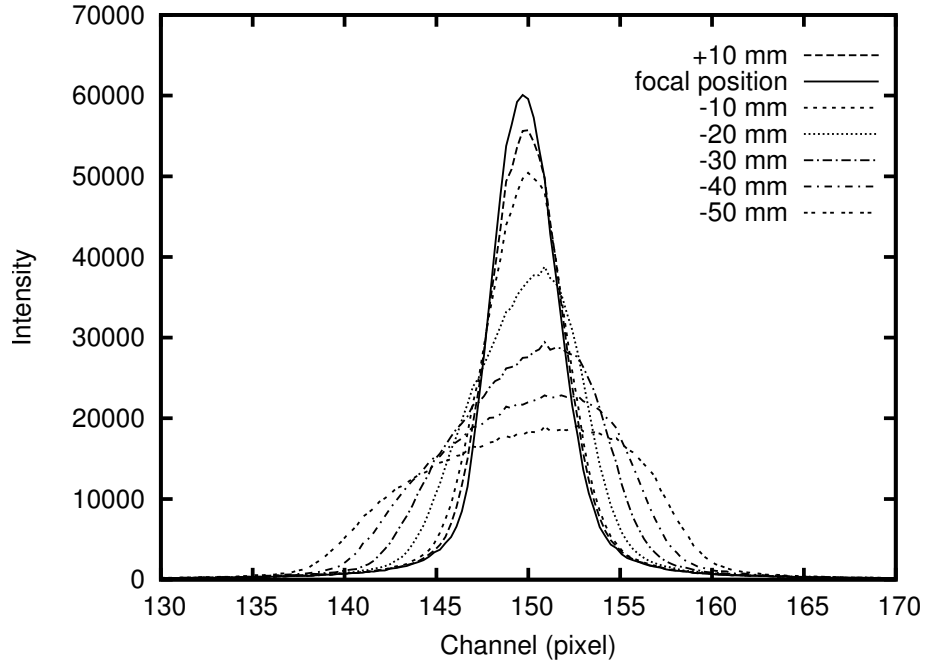


**Figure 6.8** – Deformation of the peak on the one-dimensional position spectra as a function of the distance between the detector plane and the Rowland circle. These profiles have been simulated for X-ray of about 3.1 keV energy and a quartz ( $10\bar{1}$ ) crystal. The energy decreases with the increase of the channel number.

of this error requires a more accurate analysis of the data. In the pion mass measurement, a refinement of the spectra analysis requires to take into account the deformation of the response function due to the defocusing. Up to now, the peaks in the highly charged ions spectra have been fitted using the theoretical response function in focus convoluted with a Gaussian distribution. This profile is perfectly adapted for lines near the focal position on the CCD, but it is not suited for lines far from there: for each energy transition, the focal position for the Johann-type crystal spectrometer is on the Rowland circle. However, the spectral lines are detected using a flat two-dimensional detector (the CCD array in our case), which intersects the Rowland circle in only one point (see Fig. 6.4 and 6.5). It is only at this position that we can observe an exact focusing. Transitions with a focal position outside the detector plane corresponds to a deformed peak on the one-dimensional position spectrum.

The larger the distance between the focus and the detector, the larger the peak width and asymmetry be. As we can see on Fig. 6.9, this distance  $z_F$  is related to the peak position on the detector  $x_P$  and to the Bragg angle by the simple formula:

$$z_F \simeq \Delta x \tan\left(\frac{\pi}{2} - \Theta_B\right), \quad (6.4)$$

where  $\Delta x = x_P - x_F$  and  $x_F$  is the detector focal position (the intersection point of the Rowland circle and of the detector). The defocusing effect is minimum for  $\Theta_B = \pi/2$  and is maximum for small Bragg angles. The peak asymmetry can introduce a shift of the barycenter position of the line, i.e., a systematic effect on the energy difference

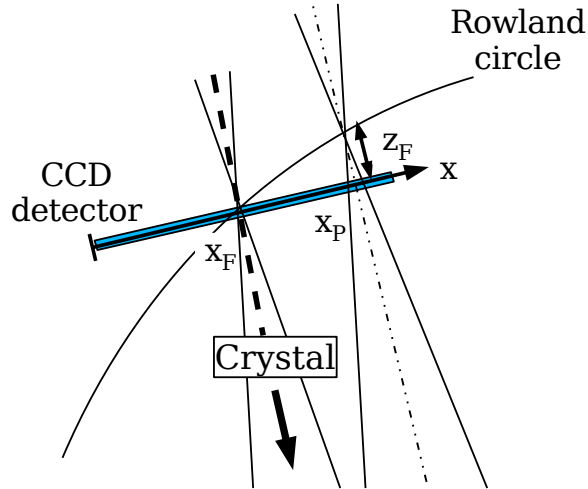


**Figure 6.9** – Correspondence between the position of the peak and the distance between the Rowland circle and the detector plane. Only a peak with a position  $x_F$  on the CCD array is in the focal position. Peaks with  $x_P \neq x_F$  are out of focus.

**Table 6.6** – Discrepancies between energy differences of He-like argon transition evaluated using the Li-like argon  $K\alpha$  transition as reference line between two spectra (*Spectrum 1* and *Spectrum 2* in Fig. 6.4) and evaluated directly using one spectrum (*Spectrum 2* in Fig. 6.4). The errors considered in this table are due only to the statistics. The energy difference discrepancies are produced from the asymmetric shape of the  $M1$  transition in *Spectrum 2* in Fig. 6.4.

Transition	Measured energies (eV)		Difference	Error sum
	using 2 spectra	using 1 spectrum		
$1s2p\ ^3P_1 \rightarrow 1s^2\ ^1S_0$	$3123.472 \pm 0.006$	$3123.483 \pm 0.006$	-0.012	0.012
$1s2p\ ^3P_2 \rightarrow 1s^2\ ^1S_0$	$3126.244 \pm 0.004$	$3126.256 \pm 0.005$	-0.012	0.009
$1s2p\ ^1P_1 \rightarrow 1s^2\ ^1S_0$	$3139.499 \pm 0.003$	$3139.511 \pm 0.003$	-0.012	0.006
$1s2p\ ^3S_1 \rightarrow 1s2p\ ^3P_1$	$19.343 \pm 0.006$	$19.354 \pm 0.006$	-0.012	0.012
$1s2p\ ^3S_1 \rightarrow 1s2p\ ^3P_2$	$22.116 \pm 0.004$	$22.127 \pm 0.005$	-0.012	0.009
$1s2p\ ^3S_1 \rightarrow 1s2p\ ^1P_1$	$35.371 \pm 0.003$	$35.382 \pm 0.003$	-0.012	0.006
$1s2p\ ^3P_1 \rightarrow 1s2p\ ^1P_1$	$16.028 \pm 0.009$	$16.028 \pm 0.010$	0.000	0.018
$1s2p\ ^3P_2 \rightarrow 1s2p\ ^1P_1$	$13.255 \pm 0.007$	$13.255 \pm 0.008$	0.000	0.015

measurement. This systematic error can be estimated by the evaluation of the energy difference between two away lines, A and C, choosing two different lines, line B and B', as intermediate reference. In principle, the energy difference between two lines is independent on the choice of the intermediate line B used to connect the two different spectra. In the real world, if we don't take into account the defocusing effect, this is not true and the energy evaluated depends on the position of the lines with respect to the focus in each spectrum. The difference between the two values obtained with the two methods can give an estimation of the systematic effects due to the unsuited profile model used for the peak fit. These differences are compared to the statistics error to estimate the defocusing effect.

Considering the spectra of the He-like argon in Fig. 6.4, we can evaluate the energy difference between the  $1s2s\ ^3S_1 \rightarrow 1s^2\ ^1S_0$  M1 and the  $1s2p\ P \rightarrow 1s^2\ ^1S_0$  transitions using just one spectrum, *Spectrum 2* or using two spectra, *Spectrum 1* and *Spectrum 2*, by the intermediate of the Li-like peaks, as showed in Fig. 6.4. The results using only *Spectrum 1* must be more affected by the defocusing, due to the large distance between the M1 transition and the focal position on the CCD. To test this hypothesis, we can evaluate the energy differences using both methods and compare the results. The values are presented in Tab. 6.4, where only the statistics error have been taken into account.

As we can observe, the two different evaluations bring two values, which differ significantly from each other. This difference comes from the asymmetry of the peaks far from the focus, as the  $1s2p\ P \rightarrow 1s^2\ ^1S_0$  peaks in *Spectrum 2* in Fig. 6.4, and it must be taken into account in a more precise analysis.

This source of systematic error can be estimated to roughly 10 meV, which is of the same order of magnitude as the statistical error and the systematic errors already considered.

However, this error can be eliminated with a more accurate analysis. For this reason, Eric-Olivier Le Bigot and me we developed a new program for the proper analysis of the highly charged ion spectra. As in the previous study, this program uses the Monte Carlo simulation developed by Leopold M. Simons (see also Sec. 5.2) to simulate the line profiles. In this new analysis we generate a set of profiles at different position of the detector instead of a single profile corresponding to the focus position. Each profile will be adapted for a finite range of the x-position of the peaks in the one dimensional spectra. The profile corresponding to the response function in focus will now be used only to fit peaks in proximity of the focal position.

The set of theoretical profiles has to be generated for each experimental spectrum and the fit program, FIT6, modified to choose the best adapted profile as a function of the peak position on the spectrum. An example of such a set of profiles is presented in Fig. 6.10. The shape of each peak on the position sensitive detector is simulated as a function of its relative distance from the focus position, which is, in this case, at proximity of channel 1170.

The following operations have to be accomplished for this new analysis:

- Determination of the focal position on the CCD.
- Generation of the set of profiles for this specific CCD position using, as input, the crystal characteristics (radius of curvature, crystal type,...) and the geometry condition of the set-up.

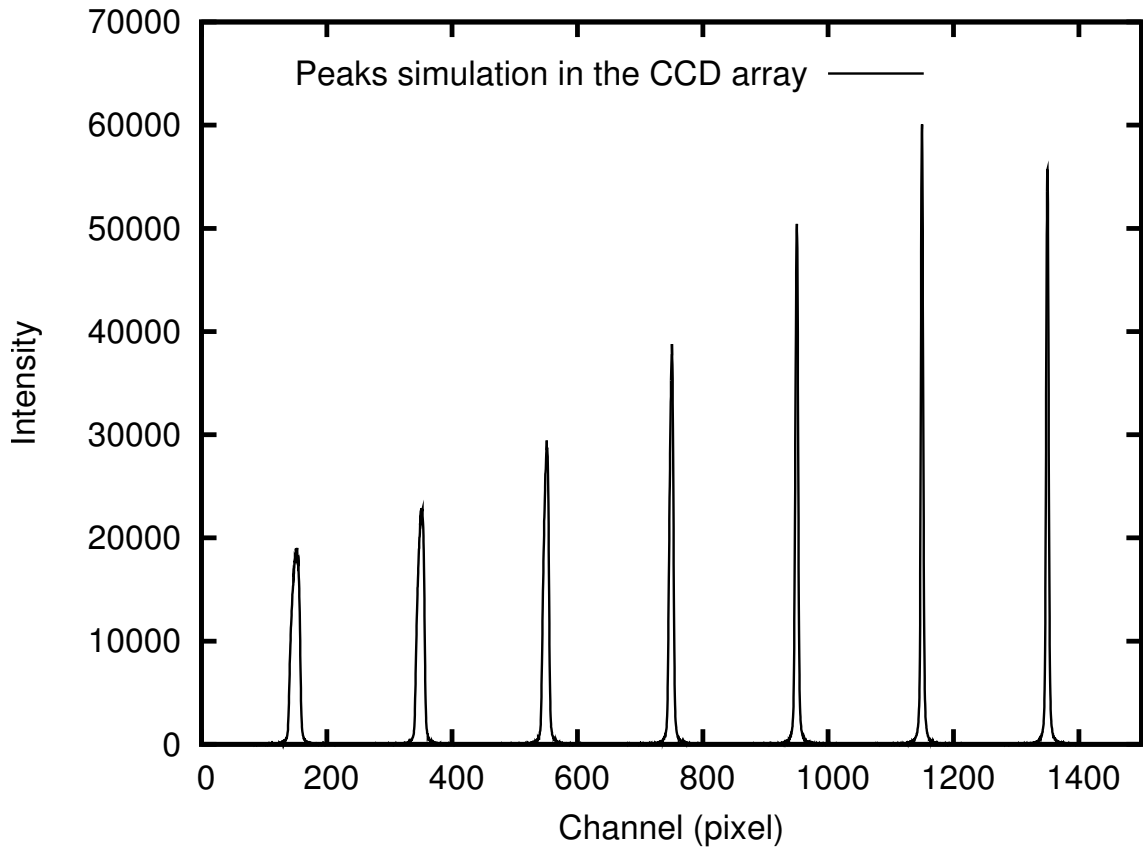


**Figure 6.10** – Simulated profiles in the one-dimensional position spectrum for X-rays with energy of about 3.1 keV reflected by a quartz ( $10.\bar{1}$ ) crystal. The focal position in this figure is near channel 1170. The amount of 1204 channels correspond to the total width of the CCD array. Experimental spectra occupied usually about 600 channels. Each profile is used by the program FIT6 to fit peaks distant by at least 100 channels from its position.

- Fit of the spectrum using the adapted profile for each position of the CCD, convoluted with a Gaussian distribution.

The evaluation of the focal position on the CCD is essential to determine the detector position with respect to the Rowland circle. This position is measured for each crystal by the focal scan using the  $1s2s\ ^3S_1 \rightarrow 1s^2\ ^1S_0$  M1 transition from He-like ions. A rough analysis for the focal position has been done on-line during the data acquisition. A more refined analysis has been performed using the Monte Carlo simulation and requires the precise knowledge of the radius of curvature of the bent crystal.

Once the focal position obtained, the set of theoretical response functions is generated using the Monte Carlo simulation. For each peak, the program chooses the more adapted profile to take into account correctly the defocusing of the line, following the same procedure described in Sec. 3.5. In this way, the angular differences between two lines can be evaluated without the possible energy shifts, due to the peak asymmetry.

**Present situation: problems**

The program has been finished and tested and the data are ready to be analyzed. But we discovered a problem, which stopped our analysis. As presented in Sec.5.2, during the focal scan analysis, the PSI group found in spring 2005 that the bent crystals used in the experiments have a radius of curvature different from the nominal value and that, in addition, most of them have a cut angle between the crystal surface and the crystal planes significantly different from zero (some tens of minutes) as it supposed to be.

These derivations from the nominal values can cause differences of several millimeters between the theoretical focal position (without taking into account the real radius of curvature and cut angle value) and the experimental focal position deduced from the focal scan. For this reason, the cut angle and the real radius of curvature have to be taken into account in the the simulation of the theoretical response functions for the fit of the ions and pionic atoms spectra. At present, the analysis of the highly charged ions cannot be completed because the measurement of the cut angle is still in progress. Once this measurement will be finished, the measured cut angle will be included into the Monte Carlo simulation to produce the correct theoretical profiles.

However, this analysis is very promising. As we saw in Tables 6.4 and 6.5, our results have an error 5 to 10 times smaller than the previous X-ray spectroscopy measurement. The new measurement of the vacuum pipes and the new analysis with the correct Monte Carlo simulation will reduce by an additional factor of 2–3 the experimental error. This will allows to a more accurate comparison between experimental and theoretical values for highly charged ions transitions.

# **Part III**

## **Conclusion and appendices**



# Chapter 7

---

## Conclusion

---

*“È che Diotallevi, e io stesso, stiamo progettando una riforma del sapere. Una Facoltà di Irrilevanza Comparata, dove si studino materie inutili o impossibili.(...) Ecco pertanto Morfematica del Morse, Storia dell’Agricoltura Antartica, Storia della Pittura nell’Isola di Pasqua, Letteratura Sumera Contemporanea, Istituzioni di Docimologia Montessoriana, Filatelia Assiro-Babilonese, Tecnologia della Ruota degli Imperi Precolombiani, Iconologia Braille, Fonetica del Film muto...”*

---

Umberto Eco, *Il Pendolo di Foucault*, 1988

### 7.1 Results summary

The aim of this thesis was to increase the accuracy on X-ray spectroscopy of pionic atoms and highly charged ions, to provide quantities of fundamental interest and to test fundamental theories.

Pionic nitrogen has been used to provide a new precise measurement of the mass of negatively charged pion. This measurement required a reduction of the error on the theoretical prediction of the atomic energies and an accurate measurement of the  $5 \rightarrow 4$  pionic nitrogen transitions.

To improve the theoretical calculation, based on the Klein-Gordon equation, it was necessary to investigate new energy corrections. For this reason, I calculated the Hyperfine Structure (HFS) for pionic atoms, that causes a shift of the transition energy due to the difference in transition probabilities between HFS sublevels. The formalism I developed in Ch. 2 consists in new perturbation expansion of the Klein-Gordon equation and, for this reason, it includes automatically relativistic corrections. In the case I presented, the perturbation was due to the interaction between the pion orbital moment and the magnetic moment of the nucleus. The perturbation term has been deduced using a multipole expansion of the nuclear electromagnetic potential. The results obtained with this

method have been compared with the Breit-Pauli Hamiltonian predictions for a spin- $\frac{1}{2}$  nucleus. This comparison allowed to obtain additional recoil corrections to the HFS structure. The results presented in Ch. 2 are also confirmed by theoretical predictions that uses the Bethe-Salpeter equations for a spin- $\frac{1}{2}$  nucleus, but the KG equation perturbation method can be used for arbitrary values of the nuclear spin.

Using this formalism, it was possible to increase the precision of the theoretical prediction for pionic atoms with low or medium atomic numbers. In particular we calculated the pionic nitrogen transition energies with an accuracy in the order of 0.2 ppm producing a negligible effect on the pion mass measurement. Moreover, the QED  $np \rightarrow 1s$  pionic hydrogen transition energies have been predicted with and unprecedented accuracy that lead to a reduction of about 30% of the systematic error in the evaluation of the strong interaction shift on the pionic hydrogen.

With this new theoretical predictions, the pionic nitrogen spectroscopy presented in Ch. 4 provides, at present, the most accurate value of the negatively charged pion mass with an error of 1.7 ppm, 32% less than the world average value accuracy (2.5 ppm).

Pionic nitrogen spectroscopy enables, in addition, to test the Quantum Electrodynamics prediction for a spin-0 particle in a bound system. By measuring the energy difference between the  $5g \rightarrow 4f$  and  $5f \rightarrow 4d$  parallel transitions, it was possible to test the validity of the Klein-Gordon equation with an accuracy in the order of 0.6%.

This new pion mass value did not cause any error decrease on the strong interaction shift measurement because the  $6 \rightarrow 5$  pionic oxygen transition, the energy of which is proportional to the pion mass, was used as reference line for the  $3p \rightarrow 1s$  pionic hydrogen transition. However, a decrease of the pion mass error provides an increase of accuracy of the X-ray standards using pionic atoms transitions. The precision of these transition energies prediction is limited in fact by the experimental error in the pion mass value.

The high accuracy of the pion mass has been obtained using several experimental improvements. In particular we used the muonic oxygen transition as a calibration line instead of fluorescence X-ray sources, and we characterized accurately the crystal spectrometer used in the experiment.

The measurement of the spectrometer response function has been made possible by the development of a new ECR ion trap for the production of highly charged ions. The relativistic M1 transitions  $1s2s \ ^3S_1 \rightarrow 1s^2 \ ^1S_0$  in He-like argon, chlorine and sulphur have been used for the systematic study of the spectrometer bent crystals. This study allowed also for the development and test of the Monte Carlo simulation of the instrument and of specific fit programs as FIT6 and FITIT, which use such simulations for the fit to the experimental spectra.

The simulation and the fit routines constitute an important set of tools for the precise analysis of the X-ray spectra. Thanks to this tools it was possible to use appropriate line profile for the determination of the pion mass and for the measurement of the strong interaction width of pionic hydrogen ground state, but also for the measurement of the He-like ion transitions. Highly charged ions produced in the ECR ion trap have been used not only to characterize the spectrometer, but also for atomic spectroscopy in strong field. The preliminary analysis of the He-like argon and sulphur spectra provides the most accurate value, in the order of 10 meV, of  $1s2p \ P \rightarrow 1s^2 \ ^1S_0$  transition energies with respect to the  $1s2s \ ^3S_1 \rightarrow 1s^2 \ ^1S_0$  M1 using X-ray spectroscopy, with a reduction of a factor of 3 to 10 of the uncertainty with respect to the precedent experiments. In particular, this new

measurements enable to test accurately the theoretical predictions for highly charged ions with few electrons.

## 7.2 Outlook

The perturbation method for the Klein-Gordon equation has been used for the calculation of the HFS due to the nuclear magnetic moment, but it can be applied for different type of perturbation. For pionic atoms with high  $Z$ , the nuclear quadrupole moment may not be negligible. The effect of such moments can be easily evaluated using the same perturbation method. In this case, HFS due to the quadrupole moment can be predicted using the multipole development of the electric potential to calculate the correspondent perturbation operator. In the same way, strong interaction effects can be taken into account introducing the optical potential [39, 40] as perturbation. These two applications are very important for calculation of the atomic levels in heavy pionic ions, where the relativistic effect, automatically taken into account by the KG equation, are not negligible.

An additional improvements of this formalism will be the introduction of the pion and the nucleus finite size in the HFS formula. A correct approach to the problem requires in fact a modified expression of the vector potential to take into account the spatial distribution of the nuclear magnetic moment and to lead to the Bohr-Weisskopf correction [41, 42].

As written above, the analysis of the He-like ions presented in this thesis is only preliminary. Several improvement must be done to increase the accuracy of the measurement. At present, the largest source of uncertainty is the evaluation of the crystal-detector distance of the X-ray spectrometer. In addition, the line profile model used up to now does not take into account the defocusing of the peak on the one-dimensional spectra, for lines not at the focal position. A more correct analysis is in progress. This new study simulated the most adapted profile for each peak on the one-dimensional spectra and uses the new features of the Monte Carlo simulation to take into account the recently measured cut angle of the bent crystals.

This analysis will also be extend to lower charge states spectra as the Li- and Be-like transitions. The study of these transitions will require an additional effort to study properly the contribution from satellites transition due to the more complex atomic spectra. For this reason a study of the dependence of the spectra characteristic on the injected microwave power and gas pressure in the ECRIT plasma chamber will be required. Such studies have already started using the new SIMPA ECRIS in Paris. The SIMPA installation is provided at the moment with a mosaic spectrometer that, due to the limited energy resolution, can not distinguish such satellite transitions. However, in our group a new double crystal spectrometer is in construction. This instrument is characterized by an energy resolution of 0.27 eV at 3 keV for Si(111) and it can measure the absolute value of the transition energy. With the double crystal spectrometer it will be possible to measure energies of transitions as the  $1s2s\ ^3S_1 \rightarrow 1s^2\ ^1S_0$   $M1$  in He-like argon, with an error smaller than 0.5 ppm, which will allow to test the different theoretical predictions for few electrons highly charged ions with unprecedented accuracy.



---

# Hyperfine structure in atomic and natural units

---

To pass to the atomic units we have to transform firstly the formula presented in Ch. 2 in Gaussian units from the International System of Units (SI). Using the conversion formulas in Ref. [153], we have:

$$\begin{cases} (\mathbf{E})_{SI} = \sqrt{4\pi\epsilon_0} (\mathbf{E})_{\text{gauss}} \Rightarrow e_{SI} = \sqrt{4\pi\epsilon_0} e_{\text{gauss}} \\ (\mathbf{B})_{SI} = \sqrt{\frac{\mu_0}{4\pi}} (\mathbf{B})_{\text{gauss}} \Rightarrow (\hat{t}_q^i)_{SI} = \sqrt{\frac{\mu_0}{4\pi}} (\hat{t}_q^i)_{\text{gauss}} \end{cases} . \quad (1)$$

The expression for  $\hat{T}_q$  in Eq. (2.46) becomes <sup>1</sup> :

$$\hat{T}_q = \frac{2e\hbar}{c} r^{-3} \hat{L}_q, \quad (2)$$

$$\langle n'l'IF'M' | \hat{W} | nllIFM \rangle = \delta_{FF'} \delta_{MM'} \delta_{ll'} \delta_{II'} \frac{e\hbar}{c} \frac{F(F+1) - I(I+1) - l(l+1)}{I} \langle n'l | \hat{r}^{-3} | nl \rangle. \quad (3)$$

Before to move to the atomic units it will be useful to express the energy correction terms in terms with the binding energy. In fact, the total energy  $E_{(0)}$  can be composed in the mass energy and the binding energy  $\mathcal{E}_{(0)}$ :  $E_{(0)} = \mu c^2 + \mathcal{E}_{(0)}$ . In that case Eq.(2.35) becomes:

$$E_{(1)} = \frac{\langle \hat{W} \rangle}{\mu \left( 1 + \frac{\mathcal{E}_{(0)}}{\mu c^2} \right) \left[ 1 + \left( 1 + \frac{\mathcal{E}_{(0)}}{\mu c^2} \right)^{-2} \right]} \quad (4)$$

The last step is to pass to the atomic units (a.u.) where  $-e = \hbar = m_{\text{electron}} = 1$ . Using

---

<sup>1</sup>In practice it sufficient to substitute in all the  $\hat{T}_q$  expression  $e/c$  at the place of  $(\mu_0 e)/(4\pi)$

these units we have  $\alpha = 1/c$  and the equation above become:

$$\hat{T}q = 2\alpha\hat{r}^{-3}\hat{L}_q, \quad (5)$$

$$\langle n'l'IF'M'|\hat{W}|nlIFM\rangle = -\delta_{FF'}\delta_{MM'}\delta_{ll'}\mu_I\mu_N\alpha\frac{F(F+1) - I(I+1) - l(l+1)}{I}\langle n'l|\hat{r}^{-3}|nl\rangle, \quad (6)$$

$$E_{(1)} = \frac{\langle\hat{W}\rangle}{\mu\left(1 + \frac{\alpha^2\mathcal{E}_0}{\mu}\right)\left[1 + \left(1 + \frac{\alpha^2\mathcal{E}_0}{\mu}\right)^{-2}\right]}, \quad (7)$$

where now  $\mu$  is expressed in electron mass units. In the natural units (n.u.) we have  $c = \hbar = 1$  and we have:

$$\hat{T}q = 2\sqrt{\alpha}\hat{r}^{-3}\hat{L}_q, \quad (8)$$

$$\langle n'l'IF'M'|\hat{W}|nlIFM\rangle = \delta_{FF'}\delta_{MM'}\delta_{ll'}\mu_I\mu_N\sqrt{\alpha}\frac{(F(F+1) - I(I+1) - l(l+1))}{I}\langle n'l|\hat{r}^{-3}|nl\rangle, \quad (9)$$

$$E_{(1)}^{nlF} = \frac{\langle\hat{W}\rangle}{\mu(1 + \frac{\mathcal{E}_0}{\mu})(1 + (1 + \frac{\mathcal{E}_0}{\mu})^{-2})}. \quad (10)$$

It is interesting to note than if we use explicitly the formula for the expression of the nuclear magneton, we find the same expression in both unit systems. The nuclear magneton is:

$$\mu_N = \frac{e\hbar}{2m_p} = \left(\frac{1}{2m_p}\right)_{a.u.} = \left(\frac{\sqrt{\alpha}}{2m_p}\right)_{n.u.}. \quad (11)$$

The expression for  $\langle\hat{W}\rangle$  becomes for both cases:

$$\langle n'l'IF'M'|\hat{W}|nlIFM\rangle = \delta_{FF'}\delta_{MM'}\delta_{ll'}\mu_I\frac{\alpha}{2m_p}\frac{F(F+1) - I(I+1) - l(l+1)}{I}\langle n'l|\hat{r}^{-3}|nl\rangle. \quad (12)$$

---

# Non-relativistic transition probability calculation

---

The transition probability in a non-relativistic framework can be easily found in the classical literature [60, 62, 154]. If we don't take into account the polarization of the emitted photon, the transition probability between the level  $|nl\rangle$  and  $|n'l'\rangle$  is given by the formula:

$$A_{nl \rightarrow n'l'} = \frac{4k^3}{3(2l+1)} |\langle nl || \hat{\mathbf{D}} || n'l' \rangle|^2, \quad (13)$$

where  $k = (E_{nl} - E_{n'l'})/(c\hbar)$  is the wave vector of the emitted photon, and  $\langle nl || \hat{\mathbf{D}} || n'l' \rangle$  is the reduced matrix of the dipole operator  $\hat{\mathbf{D}} = q\hat{\mathbf{r}}$ . The selection rules impose that  $l - l' = \pm 1$ . Reduced matrix elements can be expressed as function of the integrals  $R_{nl}^{n'l' \pm 1}$ :

$$R_{nl}^{n'l'} = \frac{1}{a_0^2} \int_0^\infty \psi_{nl}(r)\psi_{n'l'}(r)r^3 dr, \quad (14)$$

where  $\psi_{nl}$  are the radial part of the hydrogen-like atoms wave-functions.  $a_0 = \hbar/(mcZ\alpha)$  is the Bohr radius, the characteristic atomic length. In the case  $l' = l - 1$  Eq. (13) becomes:

$$A_{nl \rightarrow n'l-1} = \frac{4\alpha(E_{nl} - E_{n'l-1})^3}{3\hbar^3 c^2} \frac{l}{2l+1} a_0^2 (R_{nl}^{n'l-1})^2. \quad (15)$$

Replacing  $a_0$  with its value, we have:

$$A_{nl \rightarrow n'l-1} = \frac{4(E_{nl} - E_{n'l-1})^3}{3m^2 c^4 \hbar} \frac{\alpha}{(Z\alpha)^2} \frac{l}{2l+1} (R_{nl}^{n'l-1})^2. \quad (16)$$

From this expression, the transition probability for the hyperfine sub-level can be calculated using the angular momentum addition properties [62]:

$$A_{nlIF \rightarrow n'l'IF'} = \frac{(2F+1)(2F'+1)}{2I+1} \left\{ \begin{matrix} l' & F' & I \\ F & l & 1 \end{matrix} \right\}^2 A_{nl \rightarrow n'l-1}, \quad (17)$$

where  $F$  is the total angular momentum resulting from the addition of  $L$  and the nuclear angular momentum  $I$ .



---

# Calculation of the lattice deformation for a spherically bent crystal

---

In X-ray Bragg spectrometer that use curved crystal, the surface shape is predetermined by pressing the crystal plate to the highly precise glass former with a defined curvature characterized by two radius of curvature  $R_1$  and  $R_2$ . In the case of a cylindrically bent crystal we have  $R_1 = \infty$  or  $R_2 = \infty$  and for a spherically bent crystal  $R_1 = R_2 < \infty$ . The “forced bending” makes that the given surface shape with curvature radii  $R_1$  and  $R_2$  produces a “hidden” bending moment along the direction perpendicular to the surface. A value of  $R_3 \neq \infty$  correspond to a change of the d-spacing between planes parallel to the surface that is proportional to  $1/R_3$ . As presented in Ch. 3.3, this deformation produces a correction for X-ray spectroscopy with bent crystals. The exact expression for  $R_3$  is [155]:

$$\frac{1}{R_3} = \frac{1}{R_1} \frac{s_{13} s_{22} - s_{12} s_{23}}{s_{11} s_{22} - s_{12}^2} + \frac{1}{R_2} \frac{s_{23} s_{11} - s_{12} s_{13}}{s_{11} s_{22} - s_{12}^2}, \quad (18)$$

where  $s_{ij}$  are the compliance coefficients are defined as the proportionality constants between stress and strain by the generalized Hooke’s law [156]:

$$\epsilon_i = \sum_j s_{ij} \sigma_j \quad (i, j = 1, 2, \dots, 6), \quad (19)$$

where  $\sigma_j$  and  $\epsilon_i$  are the engineering stress and strains, respectively. The value of the  $s_{ij}$  coefficients depends of the choice of the coordinate system. When the crystal-axis coordinate system is used for a cubic crystal, as germanium and silicon, the compliance coefficients reduce to the following matrix:

$$S_{ij} = \begin{pmatrix} S_{11} & S_{12} & S_{12} & 0 & 0 & 0 \\ S_{12} & S_{11} & S_{12} & 0 & 0 & 0 \\ S_{12} & S_{12} & S_{11} & 0 & 0 & 0 \\ 0 & 0 & 0 & S_{44} & 0 & 0 \\ 0 & 0 & 0 & 0 & S_{44} & 0 \\ 0 & 0 & 0 & 0 & 0 & S_{44} \end{pmatrix}. \quad (20)$$

The compliance coefficients for rotated axes in cubic crystals can be calculated from

the formulas:

$$\begin{aligned}
s_{11} = s_{22} = s_{33} &= S_{11} + S_c(l_1^4 + m_1^4 + n_1^4 - 1), \\
s_{12} = s_{13} = s_{23} &= S_{12} + S_c(l_1^2 l_2^2 + m_1^2 m_2^2 + n_1^2 n_2^2), \\
s_{14} = s_{24} = s_{34} = s_{15} = s_{25} \\
= s_{35} = s_{16} = s_{26} = s_{36} &= 2S_c(l_1^2 l_2 l_3 + m_1^2 m_2 m_3 + n_1^2 n_2 n_3), \\
s_{45} = s_{46} = s_{56} &= 4S_c(l_1^2 l_2 l_3 + m_1^2 m_2 m_3 + n_1^2 n_2 n_3), \\
s_{44} = s_{55} = s_{66} &= S_{44} + 4S_c(l_1^2 l_2^2 + m_1^2 m_2^2 + n_1^2 n_2^2),
\end{aligned} \tag{21}$$

where  $[l_i, m_i, n_i]$  are the miller indexes for the direction  $\hat{x}_i$  and  $S_c = S_{11} - S_{22} - \frac{1}{2}S_{44}$ .

In the case of the isotropic elasticity model for the two-dimensional forced bending,  $R_3$  does not depend on the orientation of the bending curvature and surface normal directions and Eq. (18) becomes:

$$\frac{1}{R_3} = \left( \frac{1}{R_1} + \frac{1}{R_2} \right) \frac{\nu}{1 - \nu}, \tag{22}$$

with the Poisson's ratio  $\nu = -S_{12}/S_{11}$ .

We consider now the effect of the spherically forced bending of a crystal,  $R_1 = R_2 = R$ , with crystal planes  $(l_3 m_3 n_3)$  parallel to the surface, i.e., perpendicular to the direction  $\hat{x}_3 \equiv [l_3 m_3 n_3]$ , and spaced with a distance  $d$ . We have [109]:

$$\frac{\Delta d}{d} = -\frac{2\nu_{[l_3 m_3 n_3]}}{1 - \nu_{[l_3 m_3 n_3]}} \frac{z - \zeta}{R}, \tag{23}$$

where  $z$  is the distance along the  $x_3$ -axis from the crystal surface, and  $\zeta$  is half of the thickness of the crystal. When  $z = \zeta$  we are on the neutral plane, the crystal plane where the d-spacing does not change, located in the middle of the crystal (Fig. 3.11). For an isotropic material

$$\nu_{[l_3 m_3 n_3]} = \nu = -S_{12}/S_{11} \tag{24}$$

In the general case  $\nu_{[l_3 m_3 n_3]}$  depends on the direction  $\hat{x}_3$  and from Eq. (18) and (22):

$$-\frac{\nu_{[l_3 m_3 n_3]}}{1 - \nu_{[l_3 m_3 n_3]}} = \frac{s_{11} s_{12} - s_{12}^2}{s_{11}^2 - s_{12}^2}, \tag{25}$$

according to Eq. (18) and (21).

As an example we determine the Poisson's ratio  $\nu_{[110]}(Si)$  for a spherically bent silicon crystal with the surface parallel to the (110) planes. In this case we can take  $\hat{x}_1 \equiv [100]$ ,  $\hat{x}_2 \equiv [1\bar{1}0]$  and  $\hat{x}_3 \equiv [110]$ . The  $s_{ij}(Si)$  coefficients can be calculated from Eq. (21) using the values in Ref. [156]:

$$\begin{aligned}
S_{11} &= +0.768 \\
S_{11} &= -0.214, \\
S_{11} &= +1.26
\end{aligned} \tag{26}$$

and using Eq. (25), we obtain  $\nu_{[110]}(Si) = 0.270$ .

---

**Measurement of the pixel distance  
and the CCD relative orientation  
(preprint article physics/0602159)**

---

## Characterization of a CCD array for Bragg spectroscopy

Paul Indelicato, Eric-Olivier Le Bigot, and Martino Trassinelli\*

*Laboratoire Kastler Brossel, Unité Mixte de Recherche du CNRS n° 8552,  
Université Pierre et Marie Curie, Case 74,  
4, Place Jussieu, F75005 Paris, France.*

Detlev Gotta and Maik Hennebach

*Institut für Kernphysik, Forschungszentrum Jülich, D-52425 Jülich, Germany*

Nick Nelms

*Space Research Center, Department of Physics and Astronomy,  
University of Leicester, University road,  
Leicester LE1 7RH, United Kingdom.*

Christian David and Leopold M. Simons

*Paul Scherrer Institut, CH-5232 Villigen, Switzerland*

(Dated: December 15, 2005)

### Abstract

The average pixel distance as well as the relative orientation of an array of 6 CCD detectors have been measured with accuracies of about 0.5 nm and 50  $\mu$ rad, respectively. Such a precision satisfies the needs of modern crystal spectroscopy experiments in the field of exotic atoms and highly charged ions. Two different measurements have been performed by illuminating masks in front of the detector array by remote sources of radiation. In one case, an aluminum mask was irradiated with X-rays and in a second attempt, a nanometric quartz wafer was illuminated by a light bulb. Both methods gave consistent results with a smaller error for the optical method. In addition, the thermal expansion of the CCD detectors was characterized between  $-105^{\circ}\text{C}$  and  $-40^{\circ}\text{C}$ .

PACS numbers: 07.85.Nc, 14.40.Aq, 29.40.Wk, 36.10.Gv, 39.30.%2Bw, 65.40.De

Keywords: X-ray spectroscopy, Exotic atoms, Multicharged ions, CCD detector

---

\*Corresponding author. Electronic address: [martino.trassinelli@spectro.jussieu.fr](mailto:martino.trassinelli@spectro.jussieu.fr).

## I. INTRODUCTION

Charge-coupled devices (CCDs) are ideally suited as detectors for X-ray spectroscopy in the few keV range, because of excellent energy resolution and the inherent two-dimensional spatial information. In particular, they can be used as focal-plane detectors of Bragg crystal spectrometers for studies of characteristic X-radiation from exotic atoms with ultimate energy resolution [1].

The detector described in this work was set-up for a bent crystal spectrometer used in three ongoing experiments at the Paul Scherrer Institut: the measurement of the charged pion mass [2, 3], the determination of the strong-interaction shift and width of the pionic hydrogen ground state [4, 5] and highly charged ion spectroscopy [6]. The detector is made of an array of two vertical columns of 3 CCDs each [7] (Fig. 1). Each device has  $600 \times 600$  square pixels with a nominal dimension of  $40 \mu\text{m}$  at room temperature. Each pixel is realized by an open-electrode structure. For this reason, the dimension characterizing the detector is rather the average distance between pixels centers than the size of the individual pixel.

As the CCD is usually operated at  $-100^\circ\text{C}$ , the knowledge of the inter-pixel distance at the working temperature is essential for crystal spectroscopy, because any angular difference is determined from a measured position difference between Bragg reflections. Furthermore, for an array like the one described here, the relative orientation of the CCDs has to be known at the same level of accuracy as the average pixel distance.

A first attempt to determine the relative positions has been made using a wire eroded aluminum mask illuminated by sulphur fluorescence X-rays produced by means of an X-ray tube. The alignment of the mask pattern made it possible to estimate the relative CCD position with an accuracy of about  $0.05 - 0.1$  pixel and the relative rotation to slightly better than  $100 \mu\text{rad}$  [8]. In order to obtain in addition a precise value for the average pixel distance a new measurement was set-up using a high-precision quartz wafer in front of the CCD illuminated with visible light. Using this method, the relative CCD devices' position was evaluated with an accuracy of about  $0.02$  pixel. The temperature dependence of the pixel distance was also determined.

Section II is dedicated to the description of the optical measurement set-up. In section III, we describe the measurement of the pixel distance. Section IV we present the measurement of the CCD orientation using the aluminum mask (Sec. IV A) and using the quartz mask

(Sec. IV B). In section V we describe the measurement of the inter-pixel distance temperature dependence.

## II. SET-UP OF THE OPTICAL MEASUREMENT

The quartz wafer is an optical cross grating manufactured by the Laboratory of Micro- and Nanotechnology of the Paul Scherrer Institut. The grating is 40 mm wide and 70 mm high. It is composed of vertical and horizontal lines of 50  $\mu\text{m}$  thickness separated from each other by 2 mm (Fig. 2). The linearity of the lines is of order 0.05  $\mu\text{m}$  in the horizontal direction. In the vertical direction, the lines become slightly parabolic with a maximum deviation of 0.15  $\mu\text{m}$  from the average value (Fig. 3).

The wafer was positioned 37 mm in front of the CCD array. It was illuminated with short light pulses using a point-like light source, which was approximated by a collimator of one millimeter in diameter located in front of a light bulb at a distance of 6.43 m from the CCDs to reduce parallax effects distorting the wafer image (Fig. 4-5). The wafer temperature was monitored and remained at room temperature during the measurements. The integration time per picture was 10 s with the bulb shining for 6 s for each selected temperature of the CCDs. The temperature was varied between  $-105^\circ\text{C}$  and  $-40^\circ\text{C}$ .

## III. MEASUREMENT OF THE AVERAGE PIXEL DISTANCE

For the determination of the pixel distance, a simultaneous linear fit of two adjacent lines was performed under the constraint that the two lines are parallel.

After cutting out the crossing points, the diffraction pattern of the straight sections linking them (zones) was fitted to a superposition of 5 Gaussian profiles: central peak, first and second side maxima, and left and right backgrounds (Fig. 6-7). The parabolic shape of the grating was taken into account in the analysis of the images recorded with the detector.

For the fit of two parallel lines we have to consider two sets of data at the same time:  $(x1_i, y1_i, \Delta y1_i)$  and  $(x2_i, y2_i, \Delta y2_i)$ , and the lines are described by the equations:

$$\begin{cases} y1 = a1 + b x1 \\ y2 = a2 + b x2 \end{cases} . \quad (1)$$

The best determination of the parameters  $a_1$ ,  $a_2$  and  $b$  is obtained by minimization of the  $\chi^2$  merit function following the same procedure as described in Ref. [9]. In this case, the  $\chi^2$  merit function is:

$$\chi^2(a_1, a_2, b) = \sum_{i=1}^{N_1} \left( \frac{y_{1i} - a_1 - b x_{1i}}{\Delta y_{1i}} \right)^2 + \sum_{i=1}^{N_2} \left( \frac{y_{2i} - a_2 - b x_{2i}}{\Delta y_{2i}} \right)^2. \quad (2)$$

Considering two parallel lines that are at a distance  $L$  (in  $\mu\text{m}$ ) on the CCD, the average pixel distance is obtained from the formula:

$$\text{pixel dist.} = \frac{L}{|a_1 - a_2| \cos(\arctan b)} = L \frac{\sqrt{1 + b^2}}{|a_1 - a_2|}. \quad (3)$$

The presence of the cosine term takes into account the fact that the lines are generally not parallel to the CCD edge. The detailed formulas for the  $\chi^2$  minimization are presented in Appendix A.

For each CCD, we obtained about 180 independent evaluations of the pixel distance from straight sections of different line pairs. The average value of the pixel distance was obtained by a Gaussian fit to the histogram obtained from individual values (Fig. 8-9). Two series of images were available and the final value was calculated from the sum of the two distributions.

It is interesting to observe that the vertical and horizontal distributions have different dispersions (Fig. 8-9 and Table I). The horizontal pixel distance distribution is characterized by a FWHM of 80 nm, compared to 50 nm for the vertical one. Accordingly, the error on the Gaussian peak position for the vertical distance is half that for the horizontal one (0.9 nm and 1.8 nm, respectively). We have no clear-cut explanation for this difference. It is unlikely that this difference could come from the accuracy of the mask fabrication. As seen from Fig. 3, the line distances show similar fluctuations in the order of  $0.05 \mu\text{m}$  for both directions and they should produce a dispersion of about  $0.05 \mu\text{m} / 50 = 1 \text{ nm}$  on the vertical and horizontal pixel distance (50 is the average number of pixels between two lines in the wafer image).

The CCD devices were fabricated using a  $0.5 \mu\text{m}$  technology, which means that the uncertainty over the full size is  $0.5 \mu\text{m}$  (at room temperature). Such an inaccuracy could introduce an average difference of order 0.8 nm for the inter-pixel distance of various CCDs.

This assumption was tested applying *Student's t-test* [9] to distributions from different CCDs. The only significant difference in the obtained distributions comes from CCD 2 and CCD 5. However, for these two CCDs we observe a parasitic image of the mask superimposed on the normal one, probably due to a reflection between the detector and the mask itself. Therefore, the final value of the pixel distance is given by the weighted average of the individual CCD values excluding CCD 2 and CCD 5 (Table I).

The overall precision of the quartz wafer is quoted to be  $\pm 0.0001$  mm over the full width of 40 mm. Hence, the uncertainty of the wafer grid contributes on average  $0.1 \mu\text{m} / 1000 = 0.1$  nm per pixel. As horizontal and vertical pixel distances are in good agreement, a weighted average is calculated. Taking the wafer uncertainty of 0.1 nm into account, the average pixel distance reads  $39.9775 \pm 0.0005 \pm 0.0001 \mu\text{m}$ , where the nominal value is  $40 \mu\text{m}$ .

#### IV. MEASUREMENT OF THE RELATIVE ORIENTATION OF THE CCDS

##### A. X-ray method

An aluminum mask was installed 37 mm in front of the CCD array; this mask has a slit pattern chosen to provide an unambiguous connection between all CCDs (Fig. 11). The mask has a thickness of 1 mm, the slits are wire eroded with a width of about 0.1 mm and the linearity is about  $50 \mu\text{m}$  over the full height. The detector array, shielded by the mask, was irradiated with sulphur X-rays of 2.3 keV produced with the help of an X-ray tube; this energy is low enough to keep charge splitting effects small [5]. The sulphur target was placed at about 4 m from the detector. A collimator with a diameter of 5 mm was placed close to the target to provide a point-like source. In total, about 600 000 X-ray events were collected.

The relative rotations of the CCDs are determined by performing linear fits to sections of the mask slit images. Because of the slit arrangement, CCD 3 (CCD 6 would be equivalent) is the best choice to serve as reference frame. In this case, the relative rotations of CCDs 1, 2 and 6 are established directly. The values for CCD 4 and CCD 5 are the weighted average of results with CCD 1 and CCD 6 as intermediate steps.

The fit is done by calculating the center of gravity (COG) for each CCD row (or column for fitting a horizontal line) and then making a linear regression through them. The error of

the COGs is based upon a rectangular distribution with a width equal to the width of the slits of the mask. With  $N$  as the number of events and  $w$  as the slit width,  $\Delta_{COG} = \frac{w}{\sqrt{12} \cdot \sqrt{N}}$ . A width  $w$  of 4 pixels for the horizontal/vertical lines and 6 pixels for the diagonals is assumed. From the inclinations (in mrad) of the mask slits relative to the perfect horizontal, vertical or diagonal ( $45^\circ$ ), the rotations  $\Delta\Theta$  of individual CCDs are calculated. Results (relative to CCD 3) are given in Table II.

After the rotations have been determined and corrected for, the lines were fitted again to determine the crossing points of each slit with the CCD edge. The relative offsets  $\Delta x$  and  $\Delta y$  can be determined only if there are at least two lines crossing from one CCD to the other (Fig. 12). With CCD 3 as the starting point, the only other CCD fulfilling this condition is CCD 6. The position of all other CCDs has to be calculated relative to all CCDs shifted so far. The correct order for this is CCD 2, then CCD 5, CCD 1 and CCD 4.

The correct values for the vertical offsets follow from the condition that both lines should continue from one CCD to the other (CCD A and CCD B in Fig. 12). For case i) in Fig. 12, one horizontal and one diagonal line:

$$\begin{cases} A_1 + \Delta y + B_1 \cdot \Delta x = A_2 \\ A_3 + \Delta y + B_2 \cdot \Delta x = A_4 \end{cases}, \quad (4)$$

where  $A_i$  are the y-coordinate of the crossing point between the lines of equation  $y = B_i \cdot x + (\text{constant})$  and the CCD edge. From this, one derives:

$$\Delta x = \frac{(A_2 - A_4) - (A_1 - A_3)}{B_1 - B_2}, \quad (5)$$

and the associate error is:

$$\delta(\Delta x) = \left[ \frac{(\delta A_1)^2 + (\delta A_2)^2 + (\delta A_3)^2 + (\delta A_4)^2}{(B_1 - B_2)^2} + \frac{((\delta B_1)^2 + (\delta B_2)^2) \cdot (A_2 - A_4 - A_1 + A_3)^2}{(B_1 - B_2)^4} \right]^{1/2} \quad (6)$$

For case ii), one horizontal and one vertical line,

$$\begin{cases} A_1 + \Delta x + B_1 \cdot \Delta y = A_2 \\ A_3 + \Delta y + B_2 \cdot \Delta x = A_4 \end{cases} \quad (7)$$

(note that  $B_1$  is defined as  $x = B_1 \cdot y + (\text{constant})$ ). Here, the equations are:

$$\Delta x = \frac{A_1 - A_2 - B_1(A_3 - A_4)}{B_1 \cdot B_2 - 1}, \quad (8)$$

$$\begin{aligned}
(\delta(\Delta x))^2 = & \frac{(\delta A_1)^2 + (\delta A_2)^2 + (\delta B_1)^2((\delta A_3)^2 + (\delta A_4)^2)}{(B_1 \cdot B_2 - 1)^2} \\
& + (\delta B_1)^2 \left( \frac{A_4 - A_3}{B_1 \cdot B_2 - 1} - \frac{B_2(A_1 - A_2 - B_1(A_3 - A_4))}{(B_1 \cdot B_2 - 1)^2} \right)^2 \\
& + (\delta B_2)^2 \left( \frac{B_1(A_1 - A_2 - B_1(A_3 - A_4))}{(B_1 \cdot B_2 - 1)^2} \right)^2. \quad (9)
\end{aligned}$$

Values for  $\Delta y$  are derived by inserting  $\Delta x$  in either of the starting equations Eq. (4). The final horizontal and vertical displacements (which depend on the previously determined set of rotations) are given in Tab. II.

The analysis of the mask data assumes that the slits on the mask are perfectly straight; the given uncertainties are then purely statistical. However, a detailed study of the vertical slit to the right (on CCD 1 to CCD 3) shows that the mechanical irregularities of the mask are big enough to be noticeable. Fig. 13 shows the centers of gravity calculated for this slit subtracted from the fit through these points. Both the sudden jump (left arrow) and the inclination change (right arrow) are substructures on a scale of roughly 1/10th of a pixel ( $4 \mu\text{m}$ ). This fits well with the mechanical accuracy of  $5 \mu\text{m}$  quoted for the mask slits. Consequently, a further improvement in accuracy is not limited by statistics, but by the mechanical precision of the mask itself. More details may be found in [8].

## B. Optical method

By using the nanometric quartz wafer, the precision for the CCD offsets was improved beyond 1/20 of the pixel width of  $40 \mu\text{m}$ , which was envisaged for measuring the charged pion mass. The knowledge of the line positions on the wafer allows one to infer the relative position between pairs of CCDs from the image. As for X-rays, the image, when visualized without position and rotation correction, shows discontinuities at the boundaries of adjacent CCDs: lines are not parallel and a part of the mask image is missing due to the spatial separation of the CCDs (Fig. 14 bottom-left). Again, one CCD has to be chosen as a reference.

The unambiguous calculation of relative horizontal and vertical shift ( $\Delta x$  and  $\Delta y$ ) and rotation ( $\Delta\Theta$ ) of two CCDs requires the information coming from at least one pair of perpendicularly crossing lines per CCD. Using the line parameters, it is possible to build a function depending upon  $\Delta x$ ,  $\Delta y$  and  $\Delta\Theta$ , which is minimal when the shift and rotation values are optimal. The idea is to compare the coordinates of a crossing point using the

reference frame of the reference CCD  $(x_p, y_p)$  and of the selected CCD  $(x'_p, y'_p)$ . The values of  $\Delta x$  and  $\Delta y$  are unequivocally determined by first applying a rotation of the coordinate system of the selected CCD around the CCD center. The value of the rotation angle  $\Delta\Theta$  is chosen to have the lines parallel to the ones of the reference CCD (Fig. 14 bottom-middle side). In this new frame, the coordinates  $(X_p, Y_p)$  of the crossing point depend on the line parameters and on the value of  $\Delta\Theta$ . The differences  $X_p - x_p$  and  $Y_p - y_p$  provide exactly the shift values  $\Delta x$  and  $\Delta y$ . A function  $F$  may be defined as:

$$F(\Delta x, \Delta y, \Delta\Theta) = (X_p - x_p - \Delta x)^2 + (Y_p - y_p - \Delta y)^2 \quad (10)$$

In the ideal case,  $F = 0$ , the values of  $\Delta x$ ,  $\Delta y$  and  $\Delta\Theta$  are the correct ones. In reality we assume that, for a selected set of lines, the best estimate of  $\Delta x$ ,  $\Delta y$  and  $\Delta\Theta$  is found when  $F$  is minimal. The full expression used for  $F$  is given in appendix B.

A whole set of values was obtained by randomly selecting line pairs. For different choices of line pairs, different values are obtained for the position parameters. Hence, the final values of  $\Delta x$ ,  $\Delta y$  and  $\Delta\Theta$  are given again by a Gaussian fit to the distribution of the individual values. The accuracy of this method can be increased by forcing the simultaneous minimization of coordinate differences for several crossing points instead of only one. Here, four crossing points and a set of 100 different choices of line pairs were used. In this case the function  $F$  reads

$$F(\Delta x, \Delta y, \Delta\Theta) = \sum_{i=1}^4 (X_p^i - x_p^i - \Delta x)^2 + (Y_p^i - y_p^i - \Delta y)^2 \quad (11)$$

where  $i = 1$  to 4 corresponds to the crossing point number arbitrarily ordered. Figure 16 shows the distribution data for  $\Delta y$  obtained for the full set of line pairs.

The final result for the relative CCD positions was obtained from three series of 10 images each: two at  $-100^\circ\text{C}$  and one at  $-105^\circ\text{C}$ . The precision for each series is around 0.001 pixels for  $\Delta x$  and  $\Delta y$ , and  $3 \mu\text{rad}$  for the relative rotation  $\Delta\Theta$ , and it can be reduced using a function  $F$  with more crossing points. The systematic errors were estimated by comparing the results from the three series of data acquisition. However, the differences between values from different series are of order 0.01–0.03 pixels for  $\Delta x$  and  $\Delta y$ , and  $50 \mu\text{rad}$  for  $\Delta\Theta$ . This large spread, compared to the precision of each series, has two possible explanations: differences of the wafer illumination condition (affecting the line fit), or a mechanical change of the CCD array position during warming up and cooling of the detector. The second hypothesis is more likely, because only small differences were observed between the series at

$-105^{\circ}\text{C}$  and the first series at  $-100^{\circ}\text{C}$ , where no warming up between the two measurements was performed. In contrast, before the second series at  $-100^{\circ}\text{C}$ , the detector was at room temperature for a short period. This hypothesis is also confirmed by the observation of a small change in time of the  $\Delta y$  values in Fig. 16, where a significant change is observed between points obtained from different images. These differences could be attributed to a mechanical change in time due to the not yet attained thermal equilibrium of the CCD array during the measurement.

For each CCD, the final position and rotation parameters are calculated as the average of the three series (Table III). The systematic effect from the temperature difference of the image series is negligibly small compared to the spread of values. The systematic error is estimated using the standard deviation formula for a set of values. For CCD 4, only one series of measurements was available. In this case, the largest value of all other CCDs was chosen.

The fabrication of the grating introduces a systematic error due to the slightly parabolic shape of the vertical lines (Fig. 3). The error is estimated to be of order of  $9\mu\text{rad}$  for  $\Delta\theta$  and 0.009 pixels for  $\Delta x$  for CCD 1, CCD 3, CCD 4 and CCD 6, which is negligible compared with other systematic errors.

The values presented in Table III are in very good agreement with the results obtained using the aluminum mask, taking into account the different reference CCD. As an example, for the  $\Delta x$  shift between CCD 5 and CCD 2 we obtain  $-13.548 \pm 0.045$  pixels with the X-ray method, and  $-13.579 \pm 0.009$  pixels with the optical method.

## V. TEMPERATURE DEPENDENCE OF THE PIXEL DISTANCE

For the determination of the temperature dependence, images between  $-105^{\circ}\text{C}$  and  $-40^{\circ}\text{C}$  were acquired. For each condition the same analysis method as described in Sec. III was applied. As expected, the pixel distance increases with increasing temperature except for the vertical pixel distance at  $-40^{\circ}\text{C}$  (Table IV). This effect may be caused by the high CCD read-noise level at this temperature. The values obtained at  $-40^{\circ}\text{C}$  have been ejected for the measurement of the temperature dependence.

The average of the thermal expansion coefficient is obtained by a simple linear extrapolation of the data between  $-105^{\circ}\text{C}$  and  $-60^{\circ}\text{C}$ . The results are:  $(2.8 \pm 1.0) \cdot 10^{-6} \text{K}^{-1}$  for

the horizontal distance and  $(1.3 \pm 0.4) \cdot 10^{-6} K^{-1}$  for the vertical distance. These values are in the range of the thermal expansion coefficient of silicon, the CCD substrate material, and INVAR, the metallic support material for the temperatures considered: literature values are  $0.8 - 1.6 \cdot 10^{-6} K^{-1}$  for silicon [10] and  $1 - 2 \cdot 10^{-6} K^{-1}$  for INVAR [11].

## VI. CONCLUSION

We have demonstrated that the average inter-pixel distance of a CCD detector under operating conditions can be determined to an accuracy of 15 ppm. We obtain  $39.9775 \pm 0.0006 \mu\text{m}$  for the average pixel distance at a temperature of  $-100^\circ\text{C}$ , which deviates significantly from the nominal value of  $40 \mu\text{m}$ . Also, the temperature dependence of the inter-pixel distance was studied and successfully compared to values found in the literature. The relative rotations and positions of the individual CCD devices of a  $2 \times 3$  array have been measured to a precision of about  $50 \mu\text{rad}$  and 0.02 pixel, respectively. The X-ray method was limited by the quality of the aluminum mask, i. e., by the accuracy of wire-eroding machine. With the nanometric quartz wafer no limitation occurs from the accuracy of the mask. The principal difficulty encountered in that case, is the proper description of the diffraction pattern and in particular the control of the illumination. The accuracy achieved by this method fully satisfies the requirements of a recent attempt to measure the charged pion mass to about 1.5 ppm. The X-ray method and the optical method can be used for any CCD camera sensitive to X-ray and/or visible light radiation.

### Acknowledgments

Partial travel support for this experiment has been provided by the “Germaine de Staël” French exchange program.

## APPENDIX A: FORMULAS FOR FITTING WITH A PAIR OF PARALLEL LINES

In this appendix, we present mathematical formulas for linear fitting with a pair of parallel lines, i.e. for the minimization of the  $\chi^2$  merit function defined in Eq. (2).

$\chi^2$  is minimized when its derivatives with respect to  $a_1$ ,  $a_2$ , and  $b$  vanish:

$$\begin{cases} 0 = \frac{\partial \chi^2}{\partial a_1} = -2 \sum_{i=1}^{N_1} \frac{y_1 i - a_1 - b x_1 i}{\Delta y_1 i^2} \\ 0 = \frac{\partial \chi^2}{\partial a_2} = -2 \sum_{i=1}^{N_2} \frac{y_2 i - a_2 - b x_2 i}{\Delta y_2 i^2} \\ 0 = \frac{\partial \chi^2}{\partial b} = -2 \left( \sum_{i=1}^{N_1} \frac{x_1 i (y_1 i - a_1 - b x_1 i)}{\Delta y_1 i^2} + \right. \\ \left. \sum_{i=1}^{N_2} \frac{x_2 i (y_2 i - a_2 - b x_2 i)}{\Delta y_2 i^2} \right) \end{cases} \quad (A1)$$

These conditions can be rewritten in a convenient form if we define the following sum:

$$S1 = \sum_{i=1}^{N_1} \frac{1}{\Delta y_1 i^2}, \quad S1_x = \sum_{i=1}^{N_1} \frac{x_1 i}{\Delta y_1 i^2}, \quad (A2)$$

$$S1_y = \sum_{i=1}^{N_1} \frac{y_1 i}{\Delta y_1 i^2}, \quad (A3)$$

$$S1_{xx} = \sum_{i=1}^{N_1} \frac{x_1 i^2}{\Delta y_1 i^2}, \quad S1_{xy} = \sum_{i=1}^{N_1} \frac{x_1 i y_1 i}{\Delta y_1 i^2}, \quad (A4)$$

$$S2 = \sum_{i=1}^{N_2} \frac{1}{\Delta y_2 i^2}, \quad S2_x = \sum_{i=1}^{N_2} \frac{x_2 i}{\Delta y_2 i^2}, \quad (A5)$$

$$S2_y = \sum_{i=1}^{N_2} \frac{y_2 i}{\Delta y_2 i^2}, \quad (A6)$$

$$S2_{xx} = \sum_{i=1}^{N_2} \frac{x_2 i^2}{\Delta y_2 i^2}, \quad S2_{xy} = \sum_{i=1}^{N_2} \frac{x_2 i y_2 i}{\Delta y_2 i^2}. \quad (A7)$$

With this definitions Eq. (A1) becomes:

$$\begin{cases} a_1 S1 + b S1_x = S1_y \\ a_2 S2 + b S2_x = S2_y \\ a_1 S1_x + b S1_{xx} + a_2 S2_x + b S2_{xx} = S1_{xy} + S2_{xy} \end{cases} \quad (A8)$$

The solution of these three equations with three unknowns is:

$$\begin{cases} a1 = -\frac{S2 S1_x S1_{xy} + S2 S1_x S2_{xy} + S2_x^2 S1_y - S2 S1_{xx} S1_y - S2 S2_{xx} S1_y - S1_x S2_x S2_y}{-S2 S1_x^2 - S1 S2_x^2 + S1 S2 S1_{xx} + S1 S2 S2_{xx}} \\ a2 = -\frac{S1 S2_x S1_{xy} - S1 S2_x S2_{xy} + S1_x S2_x S1_y - S1_x^2 S2_y + S1 S1_{xx} S2_y + S1 S2_{xx} S2_y}{S2 S1_x^2 + S1 S2_x^2 - S1 S2 S1_{xx} - S1 S2 S2_{xx}} \\ b = -\frac{S1 S2 S1_{xy} + S1 S2 S2_{xy} - S2 S1_x S1_y - S1 S2_x S2_y}{S2 S1_x^2 + S1 S2_x^2 - S1 S2 S1_{xx} - S1 S2 S2_{xx}} \end{cases} \quad (A9)$$

#### APPENDIX B: DEFINITION OF THE FUNCTION $F(\Delta x, \Delta y, \Delta\Theta)$

The exact form of  $F$  in Eq. (10) can be deduced using simple algebraic equations and reference frame transformation formulas. If we take any pair of perpendicular lines in the reference CCD (see Fig. 14),

$$y = a_0 + b_0 x \quad \text{and} \quad x = c_0 + d_0 y, \quad (B1)$$

the coordinates  $(x_p, y_p)$  from the line intersection can be calculated on the selected CCD. The parameters of these lines are deduced from the lines in the reference CCD (Eq. (B1)), taking into account the necessary change on  $a_0$  and  $c_0$  for the translation on the grating pattern:

$$\begin{pmatrix} x_p \\ y_p \end{pmatrix} : \begin{cases} x_p = c_0 + s y + d_0 y_p \\ y_p = a_0 + s x + b_0 x_p \end{cases} \quad (B2)$$

Here,  $s x$  and  $s y$  are the parameters of the translation that can be easily deduced from the wafer image. In this case we have:

$$\begin{cases} x_p = \frac{c_0 + d_0(a_0 + s x) + s y}{1 - b_0 d_0} \\ y_p = \frac{a_0 + b_0(c_0 + s y) + s x}{1 - b_0 d_0} \end{cases} \quad (B3)$$

In the same way we can calculate the coordinates  $(X_p, Y_p)$ : the crossing point of the lines in the selected CCD after the  $\Delta\Theta$  rotation. Before the rotation, the line coordinates on the selected CCD are:

$$y' = a + b x' \quad \text{and} \quad x' = c + d y'. \quad (B4)$$

After rotation around the CCD center  $(X_C, Y_C)$  the line equations become (see Fig. 14):

$$Y = A + BX \quad \text{and} \quad X = C + DY, \quad (\text{B5})$$

where the line parameters are given by:

$$A = \frac{a + bX_C - Y_C + (Y_C - bX_C) \cos \Delta\Theta - (X_C + bY_C) \sin \Delta\Theta}{\cos \Delta\Theta - b \sin \Delta\Theta} \quad (\text{B6})$$

$$B = \frac{b \cos \Delta\Theta + \sin \Delta\Theta}{\cos \Delta\Theta - b \sin \Delta\Theta} \quad (\text{B7})$$

$$C = \frac{c - X_C + dY_C + (X_C - dY_C) \cos \Delta\Theta + (Y_C + dX_C) \sin \Delta\Theta}{\cos \Delta\Theta + d \sin \Delta\Theta} \quad (\text{B8})$$

$$D = \frac{d \cos \Delta\Theta - \sin \Delta\Theta}{\cos \Delta\Theta + d \sin \Delta\Theta}. \quad (\text{B9})$$

With this reference change, the coordinates  $(X_p, Y_p)$  are:

$$\begin{cases} X_p = \frac{(b d - 1)X_C - [c + a d + (b d - 1)X_C] \cos \Delta\Theta + (a + b c + (b d - 1)Y_C) \sin \Delta\Theta}{b d - 1} \\ Y_p = \frac{(b d - 1)Y_C - [c + a d + (b d - 1)Y_C] \cos \Delta\Theta + (a + b c + (b d - 1)X_C) \sin \Delta\Theta}{b d - 1} \end{cases}. \quad (\text{B10})$$

The function  $F$  is defined as

$$\begin{aligned} F(\Delta x, \Delta y, \Delta\Theta) &= (X_p - x_p - \Delta x)^2 + (Y_p - y_p - \Delta y)^2 \\ &= \left( \frac{1}{(b d - 1)(b_0 d_0 - 1)} \right. \\ &\quad \left. \{ (b d - 1)(c_0 + a_0 d_0 + d_0 s x + s y - X_C + b_0 d_0 X_C) \right. \\ &\quad \left. - (b_0 d_0 - 1)[c + a d + (b d - 1)X_C] \cos \Delta\Theta \right. \\ &\quad \left. + (b_0 d_0 - 1)[a + b c + (b d - 1)Y_C] \sin \Delta\Theta \} - \Delta x \right)^2 \\ &\quad + \left( \frac{1}{(b d - 1)(b_0 d_0 - 1)} \right. \\ &\quad \left. \{ (b d - 1)(a_0 + b_0 c_0 + b_0 s y + s x - Y_C + b_0 d_0 Y_C) \right. \\ &\quad \left. - (b_0 d_0 - 1)[a + b c + (b d - 1)Y_C] \cos \Delta\Theta \right. \\ &\quad \left. + (b_0 d_0 - 1)[c + a d + (b d - 1)X_C] \sin \Delta\Theta \} - \Delta y \right)^2. \quad (\text{B11}) \end{aligned}$$

[1] D. Gotta, Prog. Part. Nucl. Phys. **52**, 133 (2004).

- [2] Pion Mass Collaboration, PSI experiment proposal R-97.02 (1997).
- [3] N. Nelms, D. F. Anagnostopoulos, M. Augsburg, G. Borchert, D. Chatellard, M. Daum, J. P. Egger, D. Gotta, P. Hauser, P. Indelicato, et al., Nucl. Instrum. Meth. A **477**, 461 (2002).
- [4] Pionic Hydrogen Collaboration, PSI experiment proposal R-98.01 (1998), URL <http://pihydrogen.web.psi.ch>.
- [5] D. F. Anagnostopoulos, M. Cargnelli, H. Fuhrmann, M. Giersch, D. Gotta, A. Gruber, M. Hennebach, A. Hirtl, P. Indelicato, Y. W. Liu, et al., Nucl. Phys. A **721**, 849 (2003).
- [6] M. Trassinelli, S. Biri, S. Boucard, D. S. Covita, D. Gotta, B. Leoni, A. Hirtl, P. Indelicato, E.-O. Le Bigot, J. M. F. dos Santos, et al., in *ELECTRON CYCLOTRON RESONANCE ION SOURCES: 16th International Workshop on ECR Ion Sources ECRIS'04* (AIP, Berkeley, California (USA), 2005), vol. 749, pp. 81–84, physics/0410250.
- [7] N. Nelms, D. F. Anagnostopoulos, O. Ayranov, G. Borchert, J. P. Egger, D. Gotta, M. Hennebach, P. Indelicato, B. Leoni, Y. W. Liu, et al., Nucl. Instrum. Meth. A **484**, 419 (2002).
- [8] M. Hennebach, Ph.D. thesis, Universität zu Köln, Köln (2004).
- [9] W. H. Press, S. A. Teukolsky, V. W. T., and B. P. Flannery, *Numerical Recipes in Fortran 77: The Art of Scientific Computing* (Cambridge University Press, New York, 2001), 2nd ed.
- [10] K. G. Lyon, G. L. Salinger, C. A. Swenson, and G. K. White, J. Appl. Phys. **48**, 865 (1977).
- [11] G. Beranger, F. Duffaut, J. Morlet, and J.-F. Tiers, *The Iron-Nickel Alloys* (Lavoisier, Paris, 1996).

## TABLES

TABLE I: Results of a Gaussian fit to the horizontal and vertical pixel distance distribution. The fabrication accuracy of the quartz wafer contributes with additionally 0.1 nm to the average pixel distance.

CCD	Hor. dist. ( $\mu\text{m}$ )	FWHM ( $\mu\text{m}$ )	$\chi^2$
1	$39.9778 \pm 0.0018$	$0.0820 \pm 0.0035$	1.11
2	$39.9743 \pm 0.0018$	$0.0810 \pm 0.0033$	1.26
3	$39.9751 \pm 0.0018$	$0.0808 \pm 0.0033$	1.41
4	$39.9753 \pm 0.0017$	$0.0808 \pm 0.0032$	1.16
5	$39.9744 \pm 0.0017$	$0.0856 \pm 0.0031$	1.01
6	$39.9777 \pm 0.0018$	$0.0913 \pm 0.0031$	1.20
weighted average $39.9764 \pm 0.0009$ without CCDs 2 and 5			
line fits			
CCD	Vert. dist. ( $\mu\text{m}$ )	FWHM ( $\mu\text{m}$ )	$\chi^2$
1	$39.9766 \pm 0.0012$	$0.0504 \pm 0.0022$	1.05
2	$39.9787 \pm 0.0008$	$0.0420 \pm 0.0014$	0.88
3	$39.9785 \pm 0.0010$	$0.0496 \pm 0.0019$	0.68
4	$39.9769 \pm 0.0009$	$0.0450 \pm 0.0016$	0.62
5	$39.9781 \pm 0.0007$	$0.0472 \pm 0.0013$	0.52
6	$39.9787 \pm 0.0007$	$0.0423 \pm 0.0014$	0.66
weighted average $39.9779 \pm 0.0004$ without CCDs 2 and 5			
line fits			

TABLE II: CCD position corrections (relative to CCD 3) from the mask measurement using sulphur fluorescence radiation.

CCD	$\Delta x$ (pixels)	$\Delta y$ (pixels)	$\Delta\Theta$ (mrad)
CCD3-CCD1	$-2.818 \pm 0.022$	$22.264 \pm 0.077$	$0.197 \pm 0.078$
CCD3-CCD2	$-1.049 \pm 0.015$	$10.901 \pm 0.085$	$0.522 \pm 0.062$
CCD3-CCD3	$0.000 \pm 0.000$	$0.000 \pm 0.000$	$0.000 \pm 0.000$

CCD3-CCD4	$-14.347 \pm 0.046$	$20.808 \pm 0.075$	$1.577 \pm 0.084$
CCD3-CCD5	$-14.597 \pm 0.043$	$12.265 \pm 0.064$	$2.940 \pm 0.109$
CCD3-CCD6	$-16.487 \pm 0.040$	$1.173 \pm 0.052$	$6.328 \pm 0.101$

TABLE III: CCD relative position and orientation with CCD 2 as reference. The orientation of CCD 2 relative to itself provides a check of the validity of the measurement method.

CCD	$\Delta x$ (pixels)	$\Delta y$ (pixels)	$\Delta\Theta$ (mrad)
CCD2-CCD1	$-1.251 \pm 0.029$	$11.404 \pm 0.023$	$-0.587 \pm 0.035$
CCD2-CCD2	$0.000 \pm 0.000$	$0.000 \pm 0.000$	$-0.002 \pm 0.003$
CCD2-CCD3	$0.509 \pm 0.012$	$-11.021 \pm 0.021$	$-0.677 \pm 0.074$
CCD2-CCD4	$-12.850 \pm 0.041$	$10.279 \pm 0.023$	$0.801 \pm 0.130$
CCD2-CCD5	$-13.579 \pm 0.009$	$1.738 \pm 0.016$	$2.233 \pm 0.130$
CCD2-CCD6	$-15.963 \pm 0.041$	$-9.435 \pm 0.021$	$5.530 \pm 0.011$

TABLE IV: Pixel distance values at different detector temperatures.

Temp. ( $^{\circ}\text{C}$ )	Hor. pixel dist. ( $\mu\text{m}$ )	Vert. pixel dist. ( $\mu\text{m}$ )
-105	$39.9796 \pm 0.0014$	$39.9779 \pm 0.0006$
-100	$39.9764 \pm 0.0009$	$39.9779 \pm 0.0004$
-80	$39.9796 \pm 0.0020$	$39.9794 \pm 0.0006$
-60	$39.9827 \pm 0.0017$	$39.9800 \pm 0.0006$
-40	$39.9837 \pm 0.0013$	$39.9762 \pm 0.0010$

## FIGURES



FIG. 1: Array of 6 CCD devices mounted on the cold head [7].



FIG. 2: Quartz wafer illuminated by light. The spacing of the grating is 2 mm both vertically and horizontally.

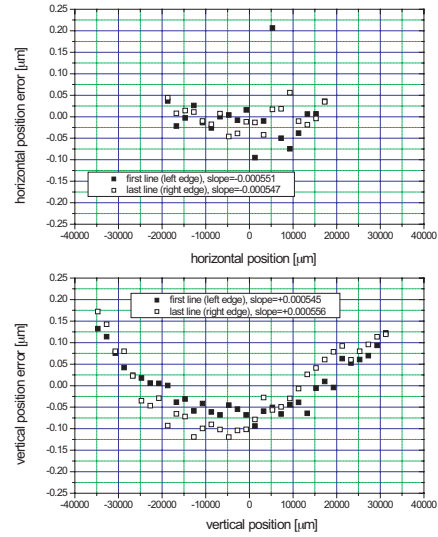


FIG. 3: Linearity of the grating in horizontal direction (top) and vertical direction (bottom).

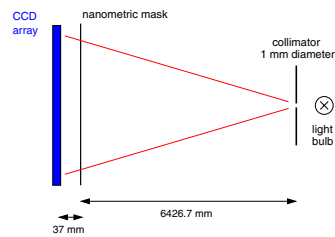


FIG. 4: Scheme of the experimental set-up.

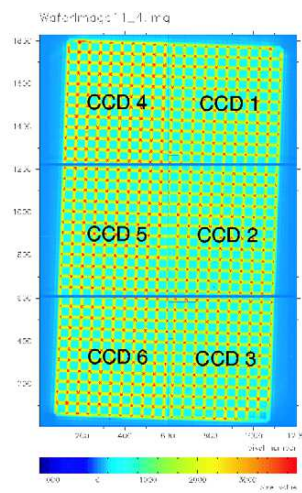


FIG. 5: Image of the quartz wafer as seen without correcting for the relative positions of the CCDs.

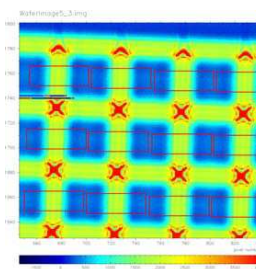


FIG. 6: Selection of the line fitting zones on the wafer image materialized by solid line rectangles.

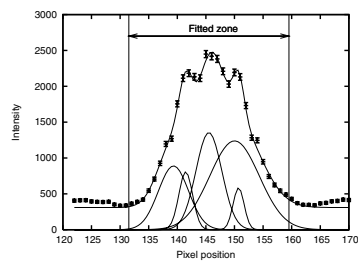


FIG. 7: Intensity profile of one pixel row of a selected zone. The line position is defined by using the average of the three central profiles. The other two profiles, normally characterized by a larger width, strongly depend on the background, i. e., on the illumination conditions of the selected zones.

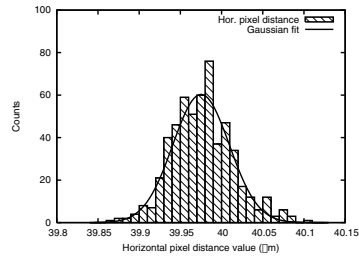


FIG. 8: Distribution of the horizontal pixel distance in CCD 3 as obtained from pairs of selected zones.

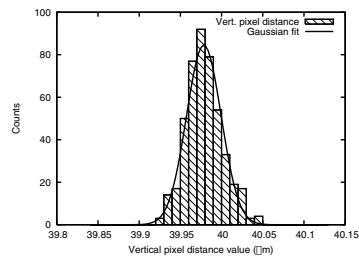


FIG. 9: Distribution of the vertical pixel distance in CCD 3 as obtained from pairs of selected zones.

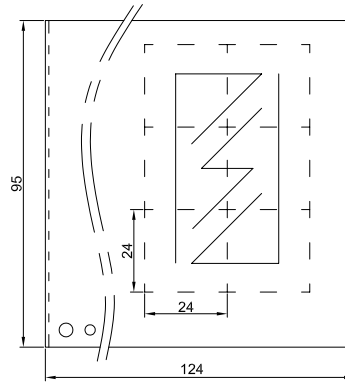


FIG. 10: Wire-eroded aluminum mask for the CCD alignment.

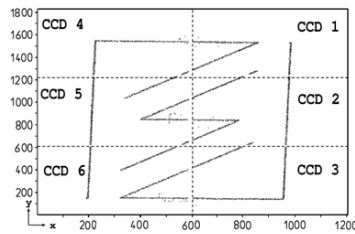


FIG. 11: Pattern produced by sulphur  $K\alpha$  radiation excited by means of an X-ray tube.

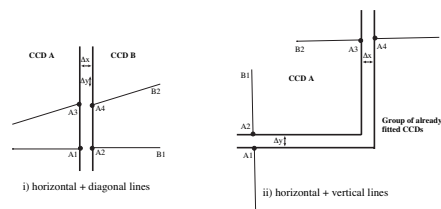


FIG. 12: Definition of crossing points for the determination of the relative offsets of the CCDs.

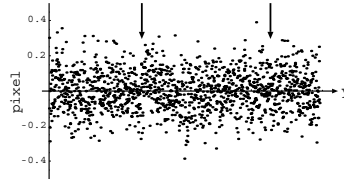


FIG. 13: Centers of gravity of the right vertical slit of the wire-eroded aluminum mask. Arrows indicate the two largest irregularities.

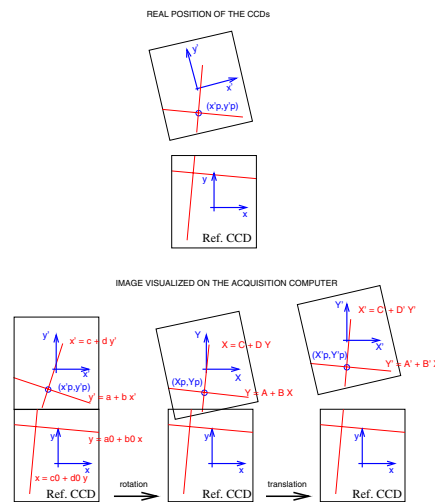


FIG. 14: Scheme of the transformation used in obtaining the orientation and shift between CCDs. In the top part, the real position of the CCDs is shown together with one crossing of the quartz grid. In the lower part, the transformation from the individual CCD coordinates (left) to the real relative position with respect to the reference CCD is displayed. The rotation is first performed (middle) and then the shift is adjusted from the known geometry of the grid (right).

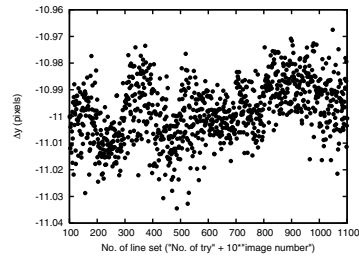


FIG. 15: Distribution of the relative shift  $\Delta y$  (gap) for CCD3 relative to reference CCD2 for various crossing points. Each point corresponds to a value of  $\Delta y$  obtained for a set of line pairs. For each of the 10 images, 100 sets of line pairs have been randomly chosen. The slope with time (corresponding approximately to the “No. of line set” axis) may be due to the CCD array not reaching the thermal equilibrium.

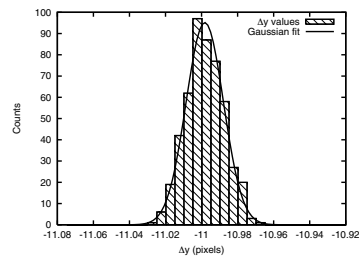


FIG. 16: Projection of the  $\Delta y$  distribution. A Gaussian fit yields the most likely value and an estimate for the uncertainty of  $\Delta y$ .



---

# Bibliography

---

- [1] R. Battesti, P. Cladé, S. Guellati-Khélifa, C. Schwob, B. Grémaud, F. Nez, L. Julien, and F. Biraben, *Bloch Oscillations of Ultracold Atoms: A Tool for a Metrological Determination of  $h/m_{Rb}$* , Phys. Rev. Lett. **92** (2004), 253001–4.
- [2] M. Fattori, G. Lamporesi, T. Petelski, J. Stuhler, and G. M. Tino, *Towards an Atom Interferometric Determination of the Newtonian Gravitational Constant*, Phys. Lett. A **318** (2003), 184–191.
- [3] S. Lenz, G. Borchert, H. Gorke, D. Gotta, T. Siems, D. Anagnostopoulos, M. Augsburg, D. Chatellard, J. Egger, D. Belmiloud, P. El-Khoury, P. Indelicato, M. Daum, P. Hauser, K. Kirch, and L. Simons, *A New Determination of the Mass of the Charged Pion*, Phys. Lett. B **416** (1998), 50–55.
- [4] M. Hori, J. Eades, R. S. Hayano, T. Ishikawa, W. Pirkl, E. Widmann, H. Yamaguchi, H. A. Torii, B. Juhász, D. Horváth, and T. Yamazaki, *Direct Measurement of Transition Frequencies in Isolated He+ Atoms, and New CPT-Violation Limits on the Antiproton Charge and Mass*, Phys. Rev. Lett. **91** (2003), 123401.
- [5] Pionic Hydrogen Collaboration, *Measurement of the Strong Interaction Width and Shift of the Ground State of Pionic Hydrogen*, PSI experiment proposal R-98.01.
- [6] D. F. Anagnostopoulos, M. Cargnelli, H. Fuhrmann, M. Giersch, D. Gotta, A. Gruber, M. Hennebach, A. Hirtl, P. Indelicato, Y. W. Liu, B. Manil, V. E. Markushin, J. Marton, N. Nelms, L. M. Simons, M. Trasinelli, and J. Zmeskal, *Precision Measurements in Pionic Hydrogen*, Nucl. Phys. A **721** (2003), 849c–852c.
- [7] Pion Mass Collaboration, *Measurement of the Pion Mass*, PSI experiment proposal R-97.02.
- [8] N. Nelms, D. F. Anagnostopoulos, M. Augsburg, G. Borchert, D. Chatellard, M. Daum, J. P. Egger, D. Gotta, P. Hauser, P. Indelicato, E. Jeannet, K. Kirch, O. W. B. Schult, T. Siems, L. M. Simons, and A. Wells, *Precision Determination of Pion Mass Using X-Ray CCD Spectroscopy*, Nucl. Instrum. Meth. A **477** (2002), 461–8.
- [9] B. Jeckelmann, P. F. A. Goudsmit, and H. J. Leisi, *The Mass of the Negative Pion*, Phys. Lett. B **335** (1994), 326–329.
- [10] A. Gumberidze, *Experimental Studies of the Ground State QED Corrections in H- and He-like Uranium*, PhD thesis, Johann Wolfgang Goethe-Universität in Frankfurt am Main, Frankfurt am Main, 2003.

- [11] W. Johnson and G. Soff, *The Lamb Shift in Hydrogenlike Atoms*,  $1 \leq Z \leq 110$ , Atomic Data and Nuclear Data Tables **33** (1985), 405.
- [12] E. Uehling, *Polarization Effects in the Positron Theory*, Phys. Rev. **48** (1935), 55–63.
- [13] G. Källén and A. Sabry, *Fourth Order Vacuum Polarization*, Det Kongelige Danske Videnskabernes Selskab Matematisk-Fysiske Meddelelser **29** (1955), 3–20.
- [14] E. Wichmann and N. Kroll, *Vacuum Polarization in a Strong Coulomb Field*, Phys. Rev. **101** (1956), 843.
- [15] D. Delker, G. Dugan, C. Wu, D. C. Lu, A. Caffrey, Y. Cheng, and Y. Lee, *Experimental Verification of the Relativistic Fine-Structure Term of the Klein-Gordon Equation in Pionic Titanium Atoms*, Phys. Rev. Lett. **42** (1979), 89–92.
- [16] M. I. Eides, H. Grotch, and V. A. Shelyuto, *Theory of Light Hydrogenlike Atoms*, Physics Reports **342** (2001), 63–261.
- [17] G. W. F. Drake, *High Precision Calculation for Helium*, in Atomic, Molecular and Optical Physics Handbook, (G. W. F. Drake, ed.), AIP Press, Woodbury, New York, 1996.
- [18] K. Pachucki and J. Sapirstein, *Contributions to Helium Fine Structure of Order  $m\alpha^7$* , J. Phys. B: At. Mol. Opt. Phys. **33** (2000), 5297.
- [19] ———, *Determination of the Fine Structure Constant From Helium Spectroscopy*, J. Phys. B: At. Mol. Opt. Phys. **35** (2002), 1783–1793.
- [20] ———, *Higher-Order Recoil Corrections to Helium Fine Structure*, J. Phys. B **36** (2003), 803–809.
- [21] C. H. Storry, M. C. George, and E. A. Hessels, *Precision Microwave Measurement of the  $2^3P_1 - 2^3P_2$  Interval in Atomic Helium*, Phys. Rev. Lett. **84** (2000), 3274–3277.
- [22] M. C. George, L. D. Lombardi, and E. A. Hessels, *Precision Microwave Measurement of the  $2^3P_1 - 2^3P_0$  Interval in Atomic Helium: A Determination of the Fine-Structure Constant*, Phys. Rev. Lett. **87** (2001), 173002.
- [23] P. C. Pastor, G. Giusfredi, P. De Natale, G. Hagel, C. de Mauro, and M. Inguscio, *Absolute Frequency Measurements of the  $2^3S_1 \rightarrow 2^3P_{0,1,2}$  Atomic Helium Transitions around 1083 nm*, Phys. Rev. Lett. **92** (2004), 023001.
- [24] T. Zelevinsky, D. Farkas, and G. Gabrielse, *Precision Measurement of the Three  $2^3P_J$  Helium Fine Structure Intervals*, Phys. Rev. Lett. **95** (2005), 203001–4.
- [25] D. Plante, W. Johnson, and J. Sapirstein, *Relativistic All-Order Many-Body Calculations of the  $n=1$  and  $n=2$  States of Heliumlike Ions*, Phys. Rev. A **49** (1994), 3519–3530.
- [26] I. Lindgren, S. Salomonson, and B. Åsén, *The Covariant-Evolution-Operator Method in Bound-State QED*, Physics Reports **389** (2004), 161–261.

- 
- [27] J. P. Desclaux, *A Multiconfiguration Relativistic Dirac-Fock Program*, Comp. Phys. Communi. **9** (1975), 31–45.
- [28] S. Boucard and P. Indelicato, *Relativistic Many-Body and QED Effects on the Hyperfine Structure of Lithium-like Ions*, Eur. Phys. J. D **8** (2000), 59–73.
- [29] J. Desclaux, J. Dolbeault, M. Esteban, P. Indelicato, and E. Séré, *Computational Approaches of Relativistic Models in Quantum Chemistry*, Vol. X, Elsevier, 2003.
- [30] G. Drake, *Theoretical Energies for the  $n=1$  and  $2$  States of the Helium Isoelectronic Sequence up to  $Z=100$* , Can. J. Phys. **66** (1988), 586.
- [31] A. N. Artemyev, V. M. Shabaev, M. M. Sysak, V. A. Yerokhin, T. Beier, G. Plunien, and G. Soff, *Evaluation of the Two-Photon Exchange Diagrams for the  $(1s)^2\ ^2P_{3/2}$  Electron Configuration in Li-like Ions*, Phys. Rev. A **67** (2003), 062506 (7).
- [32] A. N. Artemyev, V. M. Shabaev, V. A. Yerokhin, G. Plunien, and G. Soff, *QED Calculation of the  $n = 1$  and  $n = 2$  Energy Levels in He-like Ions*, Phys. Rev. A **71** (2005), 062104.
- [33] D. F. Anagnostopoulos, D. Gotta, P. Indelicato, and L. M. Simons, *Low-Energy X-Ray Standards from Hydrogenlike Pionic Atoms*, Phys. Rev. Lett. **91** (2003), 240801.
- [34] R. Deslattes, E. Kessler Jr., P. Indelicato, L. de Billy, E. Lindroth, and J. Anton, *X-Ray Transition Energies: New Approach to a Comprehensive Evaluation*, Rev. Mod. Phys. **75** (2003), 35–99.
- [35] R. D. Deslattes, R. E. LaVilla, P. L. Cowan, and A. Henins, *Threshold Studies of a Multivacancy Process in the  $K\beta$  Region of Argon*, Phys. Rev. A **27** (1983), 923–33.
- [36] R. Geller, *Electron Cyclotron Resonance Ion Sources and ECR Plasmas*, First edition, IOP Publishing, Bristol, 1996.
- [37] N. Sadeghi, T. Nakano, D. J. Trevor, and R. A. Gottscho, *Ion Transport in an Electron Cyclotron Resonance Plasma*, J. Appl. Phys. **70** (1991), 2552.
- [38] B. de Beauvoir, C. Schwob, O. Acef, L. Jozefowski, L. Hilico, F. Nez, L. Julien, A. Clairon, and F. Biraben, *Metrology of the Hydrogen and Deuterium Atoms: Determination of the Rydberg Constant and Lamb Shifts*, Eur. Phys. J. D **12** (2000), 61–93.
- [39] F. Scheck, *Leptons, Hadrons, and Nuclei*, First edition, Elsevier, North-Holland, 1983.
- [40] T. Ericson and W. Weise, *Pions and Nuclei*, Vol. 74 of *International Series to Monographs on Physics*, Oxford Science Publications, 1988.
- [41] A. Bohr and V. F. Weisskopf, *The Influence of Nuclear Structure on the Hyperfine Structure of Heavy Elements*, Phys. Rev. **77** (1950), 94–98.

- [42] I. Lindgren and A. Rosén, *Relativistic Self-Consistent-Field Calculations with Application to Atomic Hyperfine Interaction*, Case Studies in Atomic Physics **4** (1974), 93–196.
- [43] K. Cheng and W. Childs, *Ab Initio Calculation of  $4f^N 6s^2$  Hyperfine Structure in Neutral Rare-Earth Atoms*, Phys. Rev. A **31** (1985), 2775–2784.
- [44] P. Ebersold, B. Aas, W. Dey, R. Eichler, H. J. Leisi, W. W. Sapp, and F. Scheck, *Monopole and Quadrupole Strong Interaction Effects in Pionic Atoms of  $^{175}\text{Lu}$  and  $^{165}\text{Ho}$* , Nucl. Phys. A **296** (1978), 493–518.
- [45] J. Koch and F. Scheck, *Quadrupole Interaction in Pionic and Kaonic Atoms*, Nucl. Phys. A **340** (1980), 221–239.
- [46] J. L. Friar, *Feshbach-Villars Perturbation Theory for Pionic Atom Problems*, Zeitschrift für Physik **297** (1980), 147–152.
- [47] M. Leon and R. Seki, *Relativistic Corrections to Perturbation Theory for Pionic and Kaonic Atoms*, Nucl. Phys. A **352** (1981), 477–484.
- [48] D. R., P. H., and S. A., *Stationary Perturbation Theory for Non-Hamiltonian Eigenvalue Equations*, Zeitschrift für Physik D **6** (1987), 1–3.
- [49] R. N. Lee, A. I. Milstein, and S. G. Karshenboim, *Corrections to the Energy Levels of a Spin-Zero Particle Bound in a Strong Field*, Phys. Rev. A **73** (2006), 012505.
- [50] G. Austen and J. de Swart, *Improved Coulomb Potential*, Phys. Rev. Lett. **50** (1983), 2039–2042.
- [51] D. A. Owen, *On Quantum Electrodynamics of Two-Particle Bound States Containing Spinless Particles*, Found. Phys. **24** (1994), 273–96.
- [52] H. Kragh, *Equation With the Many Fathers. The Klein–Gordon Equation in 1926*, Am. J. Phys. **52** (1984), 1024–1033.
- [53] H. Yukawa, *On the Interaction of Elementary Particles*, Proc. Phys.-Math. Soc. Japan **17** (1935), 48.
- [54] J. Bjorken and S. Drell, *Relativistic Quantum Mechanics*, First edition, McGraw-Hill Book Company, San Francisco, 1964.
- [55] W. Greiner, B. Müller, and J. Rakelski, *Quantum Electrodynamics of Strong Fields*, Texts and Monographs in Physics, first edition, Springer-Verlag, Berlin, 1985.
- [56] G. Baym, *Lectures in Quantum Mechanics*, Lectures notes and Supplements in Physics, first edition, Benjamin/Cumming, 1969.
- [57] A. R. Edmonds, *Angular Momentum in Quantum Mechanics*, third edition, Princeton University Press, 1974.
- [58] D. A. Varshalovich, A. N. Moskalev, and V. K. Khersonskii, *Quantum Theory of Angular Momentum*, first edition, World Scientific, Singapore, 1988.

- 
- [59] I. Lindgren and J. Morrison, *Atomic Many-Body Theory*, Atoms and Plasmas, second edition, Springer, Berlin, 1982.
- [60] H. B. Bethe and E. E. Salpeter, *Quantum Mechanics of One- and Two-Electron Atoms*, first edition, Springer-Verlag, 1957.
- [61] C. Cohen-Tannoudji, B. Diu, and F. Laloë, *Mécanique Quantique*, second edition, Hermann, Paris, 1996.
- [62] V. Bérétetski, E. Lifchitz, and L. Pitayevsky, *Électrodynamique Quantique*, Physique Theorique, second edition, Éditions MIR, Moscou, 1989.
- [63] W. A. Barker and F. N. Glover, *Reduction of Relativistic Two-Particle Wave Equations to Approximate Forms. III*, Phys. Rev. **99** (1955), 317–324.
- [64] K. Pachucki and S. G. Karshenboim, *Nuclear-Spin-Dependent Recoil Correction to the Lamb Shift*, J. Phys. B **28** (1995), L221.
- [65] J. L. Friar, J. Martorell, and D. W. L. Sprung, *Nuclear Sizes and the Isotope Shift*, Phys. Rev. A **56** (1997), 4579–4586.
- [66] M. Hennebach, *Precision Measurement of Ground State Transition in Pionic Hydrogen*, PhD thesis, Universität zu Köln, Köln, 2004.
- [67] P. Indelicato private communication.
- [68] H. C. Schröder, A. Badertscher, P. Goudsmit, M. Janousch, H. Leisi, E. Matsinos, D. Sigg, Z. Zhao, D. Chatellard, Z. Egger, K. Gabathuler, P. Hauser, L. Simons, and A. Rusi El Hassani, *The Pion Nucleon Scattering Lengths from Pionic Hydrogen and Deuterium*, Eur. Phys. J. C **21** (2001), 473–488.
- [69] S. Eidelman, K. Hayes, K. Olive, M. Aguilar-Benitez, C. Amsler, D. Asner, K. Babu, R. Barnett, J. Beringer, P. Burchat, C. Carone, C. Caso, G. Conforto, O. Dahl, G. D’Ambrosio, M. Doser, J. Feng, T. Gherghetta, L. Gibbons, M. Goodman, C. Grab, D. Groom, A. Gurtu, K. Hagiwara, J. Hernández-Rey, K. Hikasa, K. Honscheid, H. Jawahery, C. Kolda, K. Y., M. Mangano, A. Manohar, J. March-Russell, A. Masoni, R. Miquel, K. Mönig, H. Murayama, K. Nakamura, S. Navas, L. Pape, C. Patrignani, A. Piepke, G. Raffelt, M. Roos, M. Tanabashi, J. Terning, N. Törnqvist, T. Trippe, P. Vogel, C. Wohl, R. Workman, W.-M. Yao, P. Zyla, B. Armstrong, P. Gee, G. Harper, K. Lugovsky, S. Lugovsky, V. Lugovsky, A. Rom, M. Artuso, E. Barberio, M. Battaglia, H. Bichsel, O. Biebel, P. Bloch, R. Cahn, D. Casper, A. Cattai, R. Chivukula, G. Cowan, T. Damour, K. Desler, M. Dobbs, M. Drees, A. Edwards, D. Edwards, V. Elvira, J. Erler, V. Ezhela, W. Fetscher, B. Fields, B. Foster, D. Froidevaux, M. Fukugita, T. Gaisser, L. Garren, H.-J. Gerber, G. Gerbier, F. Gilman, H. Haber, C. Hagmann, J. Hewett, I. Hinchliffe, C. Hogan, G. Höhler, P. Igo-Kemenes, J. Jackson, K. Johnson, D. Karlen, B. Kayser, D. Kirkby, S. Klein, K. Kleinknecht, I. Knowles, P. Kreitz, Y. Kuyanov, O. Lahav, P. Langacker, A. Liddle, L. Littenberg, D. Manley, A. Martin, M. Narain, P. Nason, Y. Nir, J. Peacock, H. Quinn, S. Raby, B. Ratcliff, E. Razuvaev, B. Renk, G. Rolandi, M. Ronan, L. Rosenberg, C. Sachrajda, Y. Sakai, A. Sanda, S. Sarkar, M. Schmitt, O. Schneider, D.

- Scott, W. Seligman, M. Shaevitz, T. Sjöstrand, G. Smoot, S. Spanier, H. Spieler, N. Spooner, M. Srednicki, A. Stahl, T. Stanev, M. Suzuki, N. Tkachenko, G. Trilling, G. Valencia, K. van Bibber, M. Vinciter, D. Ward, B. Webber, M. Whalley, L. Wolfenstein, J. Womersley, C. Woody, O. Zenin, and R.-Y. Zhu, *Review of Particle Physics*, Phys. Lett. B **592** (2004), 1+.
- [70] P. J. Mohr and B. N. Taylor, *CODATA Recommended Values of the Fundamental Physical Constants: 2002*, Rev. Mod. Phys. **77** (2005), 1–107.
- [71] L. W. Fullerton and G. A. Rinker, *Accurate and Efficient Methods for the Evaluation of Vacuum-Polarization Potentials of Order  $Z\alpha$  and  $Z\alpha^2$* , Phys. Rev. A **13** (1976), 1283–87.
- [72] K. N. Huang, *Calculation of the Vacuum-Polarization Potential*, Phys. Rev. A **14** (1976), 1311–1318.
- [73] B. Jeckelmann *Ein program zur berechnung von bindungsenergien in pionischen atomen* Technical report, ETHZ-IMP, 1985 (LB-85-03).
- [74] J. R. Sapirstein and D. R. Yennie, *Theory of Hydrogenlike Bound States*, Vol. 7 of *Directions in High Energy Physics*, World Scientific, 1990.
- [75] K. Pachucki, *Theory of the Lamb Shift in Muonic Hydrogen*, Phys. Rev. A **53** (1996), 2092–100.
- [76] G. Audi, A. Wapstra, and C. Thibault, *The AME2003 Atomic Mass Evaluation: (II). Tables, Graphs and References*, Nucl. Phys. A **729** (2003), 337–676.
- [77] I. Angeli, *A Consistent Set of Nuclear RMS Charge Radii: Properties of the Radius Surface  $R(N,Z)$* , At. Data Nucl. Data Tables **87** (2004), 185–206.
- [78] P. Raghavan, *Table of Nuclear Moments*, At. Data Nucl. Data Tables **42** (1989), 189–191.
- [79] C. M. G. Lattes, G. P. S. Occhialini, and C. F. Powell, *Observations on the Tracks of Slow Mesons in Photographic Emulsions. 1*, Nature **160** (1947), 453–456.
- [80] ———, *Observations on the Tracks of Slow Mesons in Photographic Emulsions. 2*, Nature **160** (1947), 486–492.
- [81] S. Tomonaga and G. Araki, *Effect of the Nuclear Coulomb Field on the Capture of Slow Mesons*, Phys. Rev. **58** (1940), 90–91.
- [82] E. Fermi and E. Teller, *The Capture of Negative Mesotrons in Matter*, Phys. Rev. **72** (1947), 399–408.
- [83] W. F. Fry, *The Capture and Decay of Mesons in Photographic Emulsions*, Phys. Rev. **83** (1951), 594–597.
- [84] M. Camac, A. D. McGuire, J. B. Platt, and H. J. Schulte, *X-Rays from Mesic Atoms*, Phys. Rev. **88** (1952), 134.

- 
- [85] S. Deser, M. L. Goldberger, K. Baumann, and W. Thirring, *Energy Level Displacements in Pi-Mesonic Atoms*, Phys. Rev. **96** (1954), 774–776.
- [86] G. Rasche and W. S. Woolcock, *Connection Between Low-Energy Scattering Parameters and Energy Shifts for Pionic Hydrogen*, Nucl. Phys. A **381** (1982), 405–418.
- [87] V. E. Lyubovitskij and A. Rusetsky,  *$\pi^-p$  Atom in ChPT: Strong Energy-level Shift*, Phys. Lett. B **494** (2000), 9–18.
- [88] J. Gasser, M. A. Ivanov, E. Lipartia, M. Mojzis, and A. Rusetsky, *Ground-State Energy of Pionic Hydrogen to One Loop*, Eur. Phys. J. C **26** (2002), 13–34.
- [89] T. E. O. Ericson, B. Loiseau, and S. Wycech, *A Phenomenological  $\pi^-p$  Scattering Length from Pionic Hydrogen*, Phys. Lett. B **594** (2004), 76–86.
- [90] L. M. Simons, *The Cyclotron Trap for Antiprotons*, Hyperfine Interactions **81** (1993), 253–262.
- [91] P. Vogel, P. K. Haff, V. Akylas, and A. Winther, *Muon Capture in Atoms, Crystals and Molecules*, Nucl. Phys. A **254** (1975), 445–479.
- [92] R. Bacher, P. Blüm, D. Gotta, K. Heitlinger, M. Schneider, J. Missimer, and L. M. Simons, *Degree of Ionization in Antiprotonic Noble Gases*, Phys. Rev. A **38** (1988), 4395–4404.
- [93] ———, *Relevance of Ionization and Electron Refilling to the Observation of the M1 Transition ( $\gamma M1 : 2s - 1s$ ) In Light Muonic Atoms*, Phys. Rev. A **39** (1989), 1610–1620.
- [94] J. S. Cohen and N. T. Padial, *Initial Distributions, Cascade, and Annihilation of  $\bar{p}p$  Atoms Formed in  $\bar{p} + H$  and  $\bar{p} + H^-$  Collisions in Near Vacuum*, Phys. Rev. A **41** (1990), 3460–3468.
- [95] K. Kirch, D. Abbott, B. Bach, P. Hauser, P. Indelicato, F. Kottmann, J. Missimer, P. Patte, R. T. Siegel, L. M. Simons, and D. Viel, *Muonic Cascades in Isolated Low-Z Atoms and Molecules*, Phys. Rev. A **59** (1999), 3375–3385.
- [96] M. Leon and H. A. Behte, *Negative Meson Absorption in Liquid Hydrogen*, Phys. Rev. **127** (1962), 636–647.
- [97] T. B. Day, G. A. Snow, and J. Sucher, *High-Orbital s-State Capture of  $\pi^-$  Mesons by Protons*, Phys. Rev. **118** (1960), 864–866.
- [98] D. Gotta, *Precision Spectroscopy of Light Exotic Atoms*, Prog. Part. Nucl. Phys. **52** (2004), 133–195.
- [99] T. S. Jensen and V. E. Markushin, *Scattering of Light Exotic Atoms in Excited States*, Eur. Phys. J. D **19** (2002), 165–181.
- [100] ———, *Collisional Deexcitation of Exotic Hydrogen Atoms in Highly Excited States. I. Cross-Sections*, Eur. Phys. J. D **21** (2002), 261–270.

- [101] ———, *Collisional Deexcitation of Exotic Hydrogen Atoms in Highly Excited States. II. Cascade Calculations*, Eur. Phys. J. D **21** (2002), 271–183.
- [102] T. S. Jensen, *Kinetic Energy Distributions in Pionic Hydrogen*, Eur. Phys. J. D **31** (2004), 11–19.
- [103] M. Sanchez del Rio and J. Dejus, *XOP: Recent Development*, in SPIE proceedings, 1998, p. 3448.
- [104] B. E. Warren, *X-ray Diffraction*, First edition, Addison-Westley Publishing Company, London, 1969.
- [105] H. H. Johann, *Die Erzeugung lichtstarker Röntgenspektren mit Hilfe von Konkavkristallen.*, Zeitschrift für Physik **69** (1931), 185.
- [106] D. Sigg, A. Badertscher, M. Bogdan, P. F. A. Goudsmit, H. J. Leisi, H. C. Schroder, Z. G. Zhao, D. Chatellard, J. P. Egger, and E. Jeannet, *The strong interaction shift and width of the ground state of pionic hydrogen*, Nucl. Phys. A **609** (1996), 269–309.
- [107] J. Eggs and K. Ulmer, *Roentgenspektroskopie mit Sphaerisch Gekruemmtten Kristallen*, Zf. angew. Phys. **20** (1965), 118–128.
- [108] L. V. Azároff, *X-Ray Spectroscopy*, International Series in pure and applied physics, MacGraw-Hill, 1974.
- [109] F. Cembali, R. Fabbri, M. Servidori, A. Zani, G. Basile, G. Cavagnero, A. Bergamin, and G. Zosi, *Precise X-Ray Relative Measurement of Lattice Parameters of Silicon Wafers by Multiple-Crystal Bragg-Case Diffractometry. Computer Simulation of the Experiment*, J. Appl. Crystallogr. **3** (1992), 424–31.
- [110] C. T. Chantler and R. D. Deslattes, *Systematic Corrections in Bragg X-Ray Diffraction of Flat and Curved Crystals*, Rev. Sci. Instrum. **66** (1995), 5123–5147.
- [111] D. F. Anagnostopoulos, S. Biri, V. Boisbourdain, M. Demeter, G. Borchert, J. P. Egger, H. Fuhrmann, D. Gotta, A. Gruber, M. Hennebach, P. Indelicato, Y. W. Liu, B. Manil, V. E. Markushin, H. Marton, N. Nelms, A. Rusi El Hassanii, L. M. Simons, L. Stingelin, A. Wasser, A. Wells, and J. Zmeskal, *Highly Charged Ions in Exotic Atoms Research at PSI*, Nucl. Instrum. Meth. B **205** (2003), 9–14.
- [112] D. Anagnostopoulos, S. Biri, H. Fuhrmann, D. Gotta, A. Gruber, P. Indelicato, B. Leoni, L. M. Simons, L. Stingelin, A. Wasser, and J. Zmeskal, *On the Characterisation of a Bragg Spectrometer with X-rays from an ECR Source*, eprint: physics/0408081.
- [113] N. Nelms, D. F. Anagnostopoulos, O. Ayranov, G. Borchert, J. P. Egger, D. Gotta, M. Hennebach, P. Indelicato, B. Leoni, Y. W. Liu, B. Manil, L. M. Simons, and A. Wells, *A Large Area CCD X-Ray Detector for Exotic Atom Spectroscopy*, Nucl. Instrum. Meth. A **484** (2002), 419–31.

- 
- [114] N. Nelms, *A New Determination of the Charged Pion Mass and Muon Neutrino Mass Upper Limit from Exotic Atom X-ray Spectroscopy*, PhD thesis, University of Leicester, Leicester, 2002.
- [115] M. Manil, *Spectroscopie X de Précision sur les Ions Lourds Multichargés et les Atomes Exotiques*, PhD thesis, Université Pierre et Marie Curie, Paris, 2001.
- [116] W. H. Press, S. A. Teukolsky, W. T. Vetterling, and B. P. Flannery, *Numerical Recipes in Fortran 77: The Art of Scientific Computing*, second edition, Cambridge University Press, New York, 2001.
- [117] F. James and M. Roos, *MINUIT—a System for Function Minimization and Analysis of the Parameter Errors and Correlations*, *Computer Physics Communications* **10** (1975), 343–67.
- [118] M. Stearns, M. B. Stearns, S. DeBenedetti, and L. Leipuner, *Limits on  $\pi^-$  Meson Mass from Mesonic X-Rays*, *Phys. Rev.* **95** (1954), 1353–1354.
- [119] R. E. Shafer, *Pion-Mass Measurement by Crystal Diffraction of Mesonic X Rays*, *Phys. Rev.* **163** (1967), 1451–1461.
- [120] V. N. Marushenko, A. F. Mezentsev, A. A. Petrunin, S. G. Skorniyakov, and A. I. Smirnov, *New Measurement of the  $\pi^-$ -Meson Mass*, *JETP Lett.* **23** (1976), 72–74.
- [121] A. L. Carter, M. S. Dixit, M. K. Sundaresan, J. S. Wadden, F. J. Watson, C. K. Hargrove, E. P. Hincks, R. J. McKee, H. Mes, H. L. Anderson, and A. Zehnder, *New Determination of the  $\pi^-$  Mass from Pionic-Atom Transition Energies*, *Phys. Rev. Lett.* **37** (1976), 1380–1383.
- [122] D. C. Lu, D. Delker, G. Dugan, C. S. Wu, A. J. Caffrey, Y. T. Cheng, and Y. K. Lee, *New High-Accuracy Measurement of the Pionic Mass*, *Phys. Rev. Lett.* **45** (1980), 1066–1069.
- [123] B. Jeckelmann, W. Beer, G. De Chambrier, O. Elsenhans, K. Giovanetti, P. Goudsmit, H. Leisi, T. Nakada, O. Piller, A. Ruetschi, and W. Schwitz, *New Precision Determination of the  $\pi^-$  Mass from Pionic X-Rays*, *Nucl. Phys. A* **457** (1986), 709–730.
- [124] M. Daum, R. Frosch, D. Heter, M. Janousch, and P.-R. Kettle, *New Precision Measurement of the Muon Momentum in Pion Decay at Rest*, *Phys. Lett. B* **265** (1991), 425–429.
- [125] K. Assamagan, C. Brnrimann, H. F. M. Daum, R. Frosch, P. Gheno, R. Horisberger, M. Janousch, P. R. Kettle, T. Spirig, and C. Wigger, *Upper Limit of the Muon-Neutrino Mass and Charged-Pion Mass From Momentum Analysis of a Surface Muon Beam*, *Phys. Rev. D* **53** (1996), 6065–6077.
- [126] G. Hölzer, M. Fritsch, M. Deutsch, J. Härtwig, and E. Förster,  *$K\alpha_{1,2}$  and  $K\beta_{1,3}$  X-Ray Emission Lines of the 3d Transition Metals*, *Phys. Rev. A* **56** (1997), 4554–68.

- [127] T. Siems, D. Anagnostopoulos, G. Borchert, D. Gotta, P. Hauser, K. Kirch, L. Simons, P. El-Khoury, P. Indelicato, M. Augsburger, D. Chatellard, and J.-P. Egger, *First Direct Observation of Coulomb Explosion During the Formation of Exotic Atoms*, Phys. Rev. Lett. **84** (2000), 4573–4576.
- [128] K. G. Lyon, G. L. Salinger, C. A. Swenson, and G. K. White, *Linear Thermal Expansion Measurements on Silicon from 6 to 340 K*, J. Appl. Phys. **48** (1977), 865–868.
- [129] Y. Okada and Y. Tokumaru, *Precise Determination of Lattice Parameter and Thermal Expansion Coefficient of Silicon between 300 and 1500 K*, J. Appl. Phys. **56** (1984), 314–320.
- [130] I. S. Shapiro, *The Physics of Nucleon-Antinucleon Systems*, Physics Reports **35** (1978), 129–185.
- [131] J. Konijn, C. T. A. M. De Laat, A. Taal, and J. H. Koch, *An Improved Parametrization of the Optical Potential for Pionic Atoms*, Nucl. Phys. A **519** (1990), 773–804.
- [132] T. L. Trueman, *Energy Level Shifts in Atomic States of Strongly-Interacting Particles*, Nucl. Phys. **26** (1961), 57–67.
- [133] G. de Chambrier, W. Beer, F. W. N. de Boer, K. Bos, A. I. Egorov, M. Eckhause, K. L. Giovanetti, P. F. A. Goudsmit, B. Jeckelmann, and K. E. Kir'yanov, *Precision Measurement of the Wavelengths and Natural Line Widths of 3d-2p Pionic X-Ray Transitions in Low-Z Atoms*, Nucl. Phys. A **442** (1985), 637–666.
- [134] S. Biri, L. Simons, and D. Hitz, *Electron Cyclotron Resonance Ion Trap: a Hybrid Magnetic System with Very High Mirror Ratio for Highly Charged Ion Production and Trapping*, Rev. Sci. Instrum. **71** (2000), 1116–18.
- [135] A. Gumberidze, T. Stöhlker, D. Banas, K. Beckert, P. Beller, H. F. Beyer, F. Bosch, X. Cai, S. Hagmann, C. Kozhuharov, D. Liesen, F. Nolden, X. Ma, P. H. Mokler, A. Orsic-Muthig, M. Steck, D. Sierpowski, S. Tashenov, A. Warczak, and Y. Zou, *Electron-Electron Interaction in Strong Electromagnetic Fields: The Two-Electron Contribution to the Ground-State Energy in He-like Uranium*, Phys. Rev. Lett. **92** (2004), 203004–4.
- [136] C. T. Chantler, D. Paterson, L. T. Hudson, F. G. Serpa, J. D. Gillaspay, and E. Takacs, *Absolute Measurement of the Resonance Lines in Heliumlike Vanadium on an Electron-Beam Ion Trap*, Phys. Rev. A **62** (2000), 042501/1–13 FTXT Phys Rev Article <http://publish.aps.org/abstract/PRA/v62/p042501>.
- [137] I. Draganić, J. R. Crespo López-Urrutia, R. DuBois, S. Fritzsche, V. M. Shabaev, R. Soria Orts, I. I. Tupitsyn, Y. Zou, and J. Ullrich, *High Precision Wavelength Measurements of QED-Sensitive Forbidden Transitions in Highly Charged Argon Ions*, Phys. Rev. Lett. **91** (2003), 183001.
- [138] A. H. Compton, *A Precision X-Ray Spectrometer and the Wave Length of Mo  $K\alpha_1$* , Rev. Sci. Instrum. **2** (1931), 365–376.

- 
- [139] R. Deslattes, *Two-Crystal, Vacuum Monochromator*, Rev. Sci. Instrum. **38** (1967), 616–620.
- [140] R. D. Deslattes, *Single Axis, Two Crystal X-Ray Instrument*, Rev. Sci. Instrum. **38** (1967), 815–820.
- [141] B. Wolf, *Handbook of Ion Sources*, First edition, CRC Press, New York, 1995.
- [142] O. Tarvainen, P. Suominen, T. Ropponen, H. Koivisto, R. C. Vondrasek, and R. H. Scott, *Plasma Potential Measurements with a New Instrument*, in ELECTRON CYCLOTRON RESONANCE ION SOURCES: 16th International Workshop on ECR Ion Sources ECRIS'04, Vol. 749 AIP, 2005, pp. 61–66.
- [143] M. Trassinelli, S. Biri, S. Boucard, D. S. Covita, D. Gotta, B. Leoni, A. Hirrtl, P. Indelicato, E.-O. Le Bigot, J. M. F. dos Santos, L. M. Simons, L. Stingelin, J. F. C. A. Veloso, A. Wasser, and J. Zmeskal, *High Resolution He-like Argon and Sulfur Spectra from the PSI ECRIT*, in ELECTRON CYCLOTRON RESONANCE ION SOURCES: 16th International Workshop on ECR Ion Sources ECRIS'04, Vol. 749, AIP, Berkeley, California (USA), 2005, pp. 81–84.
- [144] S. Biri, A. Valek, T. Suta, E. Takacs, C. Szabo, L. T. Hudson, B. Radics, J. Imrek, B. Juhasz, and J. Palinkas, *Imaging of ECR Plasma with a Pinhole X-ray Camera*, Rev. Sci. Instrum. **75** (2004), 1420–1422.
- [145] A. Bleiker and L. Stingelin *Simulation of an ECR-Ion Source with ANSYS* Technical report, Paul Scherrer Institut, 2003.
- [146] C. Prigent, *L'Émission X : un Outil et une Sonde pour l'Interaction Laser–Agrégats*, PhD thesis, Université Pierre et Marie Curie, Paris, 2004.
- [147] M. C. Martins, A. M. Costa, J. P. Santos, P. Indelicato, and F. Parente, *Interpretation of X-Ray Spectra Emitted by Ar Ions in an Electron Cyclotron Resonance Ion Source*, J. Phys. B: At. Mol. Opt. Phys. **34** (2001), 533–543.
- [148] A. M. Costa, M. C. Martins, F. Parente, J. P. Santos, and P. Indelicato, *Dirac-Fock Transition Energies and Radiative and Radiationless Transition Probabilities for  $Ar^{9+}$  to  $Ar^{16+}$  Ion Levels with K-Shell Holes*, At. Data Nucl. Data Tables **79** (2001), 223–39.
- [149] R. Deslattes, H. Beyer, and F. Folkmann, *Precision X-Ray Wavelength Measurements in Heliumlike Argon Recoil Ions*, J. Phys. B: At. Mol. Opt. Phys. **17** (1984), L689–L694.
- [150] K. Kukla, A. Livingston, J. Suleiman, H. Berry, R. Dunford, D. Gemmell, E. Kanter, S. Cheng, and L. Curtis, *Fine-Structure Energies for the  $1s2s\ ^3S - 1s2p\ ^3P$  Transition in Heliumlike  $Ar^{16+}$* , Phys. Rev. A **51** (1995), 1905–1917.
- [151] R. DeSerio and H. Berry,  *$2s-2p$  Transitions in Heliumlike Ions*, Phys. Rev. A **24** (1981), 1872–1888.

- 
- [152] L. Schleinkofer, F. Bell, H. Betz, G. Trolman, and J. Rothermel, *Precision Wavelength Determination of  $2\ ^1P_1 - 1\ ^1S_0$  and  $2\ ^3P_1 - 1\ ^1S_0$  Transitions in Heliumlike Sulfur*, Phys. Scr. **25** (1982), 917–923.
- [153] J. D. Jackson, *Classical Electrodynamics*, second edition, Jhon Wiley and Sons, 1975.
- [154] A. Messiah, *Mécanique Quantique*, First edition, Dunod, Paris, 1960.
- [155] F. N. Chukhovskii, G. Holzer, O. Wehrhan, and E. Forster, *Anisotropic Elasticity Corrections for Reflection Efficiency and X-Ray Standing-Wave Patterns Using Bent Crystals*, J. App. Crystallogr. **29** (1996), 438–445.
- [156] J. J. Wortman and R. A. Evans, *Young's Modulus, Shear Modulus, and Poisson's Ratio in Silicon and Germanium*, J. App. Phys. **36** (1965), 153–156.



---

## Résumé

---

L'objet de cette thèse est de présenter une nouvelle mesure de la masse du pion en utilisant la spectroscopie X de l'hydrogène pionique et des résultats de spectroscopie de l'argon et du soufre héliumoides. La nouvelle masse du pion a été mesurée avec une précision 30% supérieure à la moyenne mondiale actuelle, c'est-à-dire égale à 1.7 ppm. Elle a été obtenue par spectroscopie de Bragg des transitions 5 -> 4 de l'azote pionique en utilisant les prédictions théoriques de QED. Je présente le calcul de la structure hyperfine et celui de la correction de recul du noyau pour les atomes pioniques au moyen d'une nouvelle méthode de perturbation de l'équation Klein-Gordon. Le spectromètre utilisé pour cette mesure a été caractérisé grâce aux transitions relativistes des atomes héliumoides produits dans un nouveau type de source d'ions à résonance cyclotronique des électrons. Les spectres haute statistique de ces ions permettent de mesurer les énergies de transition avec une précision de quelques ppm, ce qui permet de tester, avec un degré de précision jamais atteint, les prédictions théoriques. L'émission de rayons-X des atomes pioniques et des ions multichargés peut ainsi être utilisée pour la définition de nouveaux étalons de rayons-X de quelques keV.

**Mots-clefs :** Spectroscopie de rayons-X, masse du pion, atomes pioniques, ions multichargés, tests d'électrodynamique quantique, équation de Klein-Gordon.

---

## Abstract

---

The object of this thesis is to present a new measurement of the pion mass using pionic nitrogen X-ray spectroscopy and results on helium-like argon and sulphur spectroscopy. The new pion mass has been measured with an accuracy of 1.7 ppm, 30% better than the present world average value, and it is obtained from Bragg spectroscopy of 5 -> 4 pionic nitrogen transitions using the theoretical predictions provided by QED. I present the calculation of the hyperfine structure and recoil corrections for pionic atoms using a new perturbation method for the Klein-Gordon equation. The spectrometer used for this measurement has been characterized with the relativistic M1 transitions from he-like ions produced with a new device, the Electron-Cyclotron-Resonance Ion Trap. High statistics spectra from these ions enable to measure transition energies with a precision of some ppm that allows to compare theoretical predictions with experiment. X-ray emission from pionic atoms and multicharged ions can be used to define new types of X-ray standards for energies of a few keV.

**Keywords:** X-ray spectroscopy, pion mass, pionic atoms, highly charged ions, QED tests, Klein-Gordon equation.